University of Southampton

Faculty of Engineering and Physical Sciences

Engineering and Electronics and Computer Science

Triboelectric nanogenerators for breaking water wave impact energy harvesting for self-powered applications

Volume [1] of [1]

by

Ulises Tronco Jurado

ORCID ID 0000-0002-7992-5561

Thesis for the degree of Doctor of Philosophy

October 2020

University of Southampton

Abstract

Faculty of Engineering and Physical Sciences

Engineering and Electronics and Computer Science

Thesis for the degree of Doctor of Philosophy

Triboelectric nanogenerators for breaking water wave impact energy harvesting for self-powered applications

by

Ulises Tronco Jurado

Harvesting clean and renewable energy from the ocean waves is one of the greatest attractions nowadays because it offers greater reliability than solar or wind and could potentially meet 10% of total worldwide electric demand. Numerous ocean wave assessments report the optimism of wave energy to tackle the excessive electricity demands in different countries in the world. Effective utilization and sustainability of this kind of energy can be exploited due to the effects of climate change with the rapid increase of sea levels and more recurrent flooding of coastal zones. Specifically focused on the cumulative loads of breaking water wave forces at defence structures deliver high magnitude pulse-like hydrostatic pressures with a wide frequency range of destructive oscillatory compressed air bubbles at the structure-water interfaces. Such energy can be potentially harvested to produce sustainable electricity in the future using an alternative approach of triboelectric nanogenerators (TENG). The triboelectric effect is generated as a result of periodic, non-uniform contact between a negative triboelectric material (gains electrons) and a positive triboelectric material (losses electrons). This research work describes and studies the design, finite element analysis (FEA), fabrication, selection of the best triboelectric material combination and electrical output performance characterization of different stable, easy to fabricate and lightweight single/grids of triboelectric nanogenerators and hybrid nanogenerators using contact-electrification between solid-solid and liquid-solid interfaces. As an alternative and novel approach exploiting the potential to harvest breaking water wave impact energy at a wide frequency range from lower frequencies between 0.7 Hz to 3 Hz and high frequencies between 30 Hz to 252 Hz.

The highest power density was generated with the hybrid nanogenerators by the coupling of triboelectric-piezoelectric effects with a value of 3.8 W/m^2 considering the electric output performance for a single device. Also, lower power densities were found for the water-dielectric single-electrode mode triboelectric nanogenerator (WDSE-TENG) and dielectric-metal contact-separation mode triboelectric nanogenerator (DMCS-TENG) with power densities between 1.7

W/m^2 and 0.695 W/m^2, respectively. Furthermore, the integration of the grid of the proposed energy harvesters offers an innovative approach that can work in liquid environments and it is estimated to generate output power from 3.05 W to 30.63 W if 2,812 to 11,250 devices are electrically connected with the construction of large water-nanogenerator-structure interfaces for the generation of electricity on a large scale within an area of 18 m^2 that receives wave sizes from 0.3 m to 4 m.

This research work provides a promising alternative and innovative approach to harvest breaking water wave impact energy at a broad frequency range between 0.7 to 252 Hz, with the generated power density levels implementing the proposed energy harvesters that show a stable performance. This approach represents an energy source that could be integrated for smart battery-less systems at water-structure interfaces for aquaculture applications such as fish detection, water level measurement, weather condition monitoring and sensor systems that monitor erosion and weathering in coastal defence systems at small and big scales harvesting breaking water wave impact energy using areas between 145 cm^2 and 18 m^2. Such applications having average power consumptions from 1 mW to 100 mW for small scales, and 100 W to 1 kW for large scales, respectively.

Table of Contents

Table of Contents iii

List of Tables vii

List of Figures ix

Research Thesis: Declaration of Authorship xvii

Acknowledgements xix

Nomenclature xx

Abbreviations xxiii

Chapter 1 Introduction 1

1.1 Research motivation 1

1.2 Aims and objectives 4

1.3 Layout of the report and novelty of the research 5

Chapter 2 Literature review of ocean wave energy harvesting techniques 9

2.1 Introduction 9

2.2 Ocean energy 9

2.3 Energy harvesting from ocean waves 10

2.4 Triboelectric nanogenerators (TENG) in comparison with mechanical energy harvesting technologies with potential for ocean wave energy harvesting 12

2.5 Materials for triboelectrification 16

2.6 State of the art of TENG for ocean wave energy harvesting 19

2.7 State of the art of piezoelectric generators for ocean wave energy harvesting 23

2.8 Technical barriers for ocean wave energy harvesters 25

2.9 Applications for ocean wave energy harvesters 26

2.10 Comparison of triboelectric and piezoelectric ocean wave energy harvesting techniques and their potential for self-powered systems 27

2.11 Chapter summary 28

Chapter 3 Modelling and numerical simulation of breaking water wave impact energy harvesting generators 29

3.1 Introduction 29

3.2 FEM modelling and simulation of triboelectric nanogenerators for breaking water wave impact energy harvesting 30
3.2.1 Voltage-Charge-Distance *(V-Q-x)* relationship for triboelectric nanogenerators 30
3.2.2 Maximum surface charge density calculation for triboelectric nanogenerators considering the ion injection method 34
3.3 Triboelectric nanogenerators FEM results and analysis 35
3.4 FEM and simulation of hybrid triboelectric-piezoelectric generators for water wave impact energy harvesting 42
3.5 Hybrid triboelectric-piezoelectric generators FEM results and analysis 43
3.6 Chapter summary 49

Chapter 4 Dielectric-metal triboelectric nanogenerators (DMCS-TENG) prototypes for water wave impact energy harvesting 51

4.1 Introduction 51
4.2 Triboelectric material selection using DMSE-TENG 52
4.2.1 Fabrication and characterization of arc-shaped dielectric-metal single electrode triboelectric nanogenerators (DMSE-TENG) for triboelectric material optimization 52
4.2.2 Experimental results and analysis of electrical characterization of the DMSE-TENG prototypes for triboelectric material optimization under impact test .. 53
4.3 DMCS-TENG electrical characterization under different oscillating frequencies and using breaking water wave generator tank 58
4.3.1 Fabrication and characterization of DMCS-TENG energy harvester prototypes 58
4.3.2 The dynamic operation, experimental results and analysis of the electrical characterization of the DMCS-TENG energy harvester prototypes 60
4.4 Chapter summary 69

Chapter 5 Hybrid nanogenerator for breaking water wave impact energy harvesting 71

5.1 Introduction 71

5.2 Working mechanism of electricity generation, fabrication and characterization of hybrid nanogenerators energy harvester prototypes 72
5.3 Experimental results, analysis of electrical characterization and battery-less application of the hybrid nanogenerators through breaking water wave impact test 80
5.4 Chapter summary 87

Chapter 6 Water-dielectric single electrode triboelectric nanogenerators (WDSE-TENG) for water wave impact energy harvesting 89

6.1 Introduction 89
6.2 Fabrication, working mechanism through water-dielectric interfaces for electricity generation and characterization of WDSE-TENG energy harvester prototypes 90
6.3 Experimental results and analysis of the electrical characterization of the WDSE-TENG energy harvester prototypes through water wave impact test 97
6.3.1 Water-dielectric triboelectric materials selection and optimization 97
6.3.2 Single/Grid WDSE-TENG output performance electrical characterization under different breaking water wave impact frequencies and potential battery-less applications 102
6.4 Chapter summary 110

Chapter 7 Conclusion and future work 111

7.1 Conclusion 111
7.2 Future work 115

Appendix A 117

References 155

List of Tables

Table 2.1 A comparison of advantages and possible practical limitations about the harvesting of mechanical energy using electromagnetic, electrostatic, piezoelectric and triboelectric effect [73]. 15

Table 2.2 Triboelectric series for insulators materials arranged by charge affinity based on their tendency to lose electrons (electropositive) or gain electrons (electronegative). 17

Table 2.3 Triboelectric series for some common materials arranged by the relative ease of losing (positive) or gaining (negative) electrons) [86]. 18

Table 2.4 Comparison of triboelectric, piezoelectric, electromagnetic and hybrid ocean wave energy harvesting techniques, power density, applications, challenges and recommendations.....27

Table 3.1 Parameters utilized in the FEM calculation for the dielectric-metal contact-separation TENG, through different frequencies and load resistances....38

Table 3.2 Parameters used in the FEM 45

Table 4.1 Comparison of the rankings of positive and negative triboelectric materials in terms of ease of losing or gaining electrons with data from the literature [14] versus our impact test characterization data....57

Table 6.1 Comparison of the level of positive and negative triboelectric water-dielectric interfaces in terms of ease of losing or gaining electrons through breaking water wave impact comprising (a) DI water and tap water and (b) seawater. 101

Table 6.2 Estimation of the electric output performance enhancement factor of the single WDSE-TENG and grid of five WDSE-TENG energy harvesters focused on the transferred charges (Q) at breaking water wave impact conditions with a frequency from 0.7 to 3 Hz with amplitudes of 10 cm to 12 cm. 102

List of Figures

Figure 1.1 (a-d) Hydrostatic pressure distribution of the breaking ocean wave impact at the water-structure interface and main frequencies of interest (0.7 Hz to 300 Hz) [12, 13] for breaking ocean wave impact energy harvesting generated by (a) the water wave impact and (d) the impact of oscillatory compressed air bubbles flows at the water-structure interface exploited using triboelectric nanogenerators..... 3

Figure 1.2 Main frequencies of interest in pressure signal for breaking ocean wave energy harvesting generated by the impact and the oscillatory compressed air bubbles flows at the structural-water interfaces [12]. 4

Figure 2.1 Global distribution of wave energy density [44]. 10

Figure 2.2 Current technologies for breaking water wave energy harvesting integrating robust water energy converters with breakwater structures (a) overtopping [47-49], (b) oscillating water column [47, 50, 51] and (c) piston type [47, 52] configurations aimed at harvesting water wave energy in large scales.....12

Figure 2.3 The four fundamental modes of triboelectric nanogenerators: (a) vertical contact-separation mode, (b) in plane contact-sliding mode, (c) single-electrode mode, and (d) freestanding triboelectric-layer mode [69, 77].....16

Figure 2.4 TENG with solid-solid triboelectric interfaces for ocean wave energy harvesting. (a) Schematic of the TENG based on a wavy-structured layer. (b) Set-up for the packaged TENG to harvest water wave energy and turn on LEDs [24]. (c) Schematic diagram of RF-TENG and (d) digital image of the device operating in a water wave system [25]. (e) Schematic of single unit of Arc-shaped TENG and (f) network of four devices (12cm x 12cm x 6cm) [26]. (g) Schematic diagram of the TS-TENG and (h) TS-TENG array for water wave energy harvesting [27].....20

Figure 2.5 TENG with liquid-solid triboelectric interfaces for water wave energy harvesting. (a) Schematic description of LSEG with the electrification layer with two electrodes on the back. (b) Scanning electron microscopy image of the polymer nanowires on the electrification layer. (c) Schematic description of a substrate supported LSEG in water waves [37]. (d) Schematic diagram and (e) set-up of the water tank triboelectric nanogenerator [32].....21

Figure 2.6 Coupling between TENG-EMG to form a hybrid device. (a) Schematic diagram of THNG in motion in real ocean environment and (b) digital photo of THNG acting as power source to turn on LEDs [39]. (c) Structural design of How-NG, (d) digital image of How-NG integrated with two units and (e) turning on 108 LEDs by water wave energy harvesting [40]..... 22

Figure 2.7 (a) Modelling of a piezoelectric power generator [87], (b) Piezoelectric flag [97], (c) Heaving based harvester [93] and (d) Design of piezoelectric beam bodies fixed for the ocean bottom [95, 96]. 24

Figure 2.8 (a) The piezoelectric flexible membrane in operation [98] and (b) hydrodynamic piezoelectric system [99]. 25

Figure 3.1 First order lumped-parameter equivalent circuit model of triboelectric nanogenerators..... 31

Figure 3.2 Theoretical models for (a) dielectric-to-dielectric contact separation mode TENG and (b) conductor-to-dielectric contact separation mode TENG. 32

Figure 3.3 Equivalent circuit model of the whole TENG system loaded by a load resistor [65, 66]..... 34

Figure 3.4 (a) FEM simulation model builder of the DMCS-TENG by coupling electromechanics and electrical circuit interfaces. (b) Two-dimensional sketch of the DMCS-TENG prototype..... 36

Figure 3.5 Theoretical relationship between maximum surface charge density (σ_{max}) using the ion injection method and the thickness (d_{D1}) at different gap distance (x) (a) between the polyimide dielectric layer with different thicknesses, and (b) polyimide vs PDMS layers of different thicknesses at different gap distance. 37

Figure 3.6 The influence of the load resistance divided into three working regions on the magnitude of the peak output voltage (V), peak output current (I) and maximum output power performance of the DMCS-TENG prototypes with a structure of L = 8 cm composed with (a) PDMS-Al and (b) Polyimide-Al layers at the oscillation frequency of 150 Hz. Structure of L = 5 cm with (c) PDMS-Al and (d) Polyimide-Al layers and (e-f) structure of L = 2.5 cm..... 40

Figure 3.7 DMCS-TENG under oscillatory frequency and deformation. (a) Two-dimensional shape showing the two triboelectric layers in contact, (b) Al layer released, which will raise a much higher potential. 41

Figure 3.8 Maximum instantaneous output power of simulated DMCS-TENG prototypes with (a) L = 8 cm, (b) L = 5 cm, and (c) L = 2.5 cm as a function of the main oscillatory frequencies of 30, 80, 150, 180, 200, 219 and 252 Hz with an amplitude of 1 mm (t = 0.12s). 42

Figure 3.9 (a) FEM simulation model builder of the hybrid nanogenerator by coupling solid mechanics, electrostatics and electrical circuit interfaces. (b) Two-dimensional schematic of the hybrid nanogenerator (coupling triboelectric-piezoelectric effects). (c) Two-dimensional schematic of the simulated hybrid nanogenerator and direction of the applied horizontal periodic motions to the modelled structure in COMSOL Multiphysics.....44

Figure 3.10 Electric potential model and simulated electric circuit diagram of (a) TENG, (b) PENG, and (c) simultaneous coupling of triboelectric-piezoelectric effects (hybrid nanogenerator). Simulation of the influence of the load resistance in the output voltage, current and power of (d) TENG, (e) PENG and (f) Hybrid prototype. 46

Figure 3.11 (a) Output power of the simulated hybrid devices with different lengths (3 cm, 6 cm and 8 cm) under different frequencies (0.7 Hz to 3 Hz) that highlights the optimum load resistance for every structure. Simulation of the influence of the load resistance in the output power performance of the hybrid nanogenerator prototype at different frequencies (0.7 Hz to 3 Hz) with different length structures (b) *L* = 4 cm, (c) *L* = 6 cm and (d) *L* = 8 cm).....48

Figure 4.1 (a) Two-dimensional schematic of the arc-shaped DMSE-TENG. (b) Cross-sectional digital photo of the arc-shaped DMSE-TENG.....52

Figure 4.2 Experimental set-up of impact test using a 40 mm ball bearing on the arc-shaped DMSE-TENG prototypes (connected to a 5 MΩ load resistor) with different triboelectric material combinations.....53

Figure 4.3 Instantaneous output (a) voltage and (b) current of the top-five arc-shaped DMSE-TENG prototypes (connected to a 5 MΩ load resistor) using dielectric-metal contact electrification under the impact of a 40 mm ball bearing for 0.7 seconds. 54

Figure 4.4 Comparison of the output voltage (V_{RMS}), current (I_{RMS}) and power effective values of the top five arc-shaped DMSE-TENG fabricated prototypes (connected to a 5 MΩ load resistor) with silver conductive cloth tape and aluminium foil, under impact test through a 40 mm ball bearing. 56

Figure 4.5 Selected triboelectric materials for the DMCS-TENG fabrication, electrical characterization and the study of the effect of surface morphology. 58

Figure 4.6 (a) Fabricated DMCS-TENG, (b) DMCS-TENG mounted on the mechanical shaker table for the output performance measurements at different frequencies of oscillation. (c) The average measurements of acceleration, velocity, and displacement of the top dielectric layer when contacts the conductor layer of the energy harvester measured with a PDV-100 Portable Digital Vibrometer. 59

Figure 4.7 Insulated DMCS-TENG prototype placed on the water wave generator tank for its output performance measurements. 60

Figure 4.8 Open-circuit voltage generated by the DMCS-TENG in one cycle of external vibration at 150 Hz. The open-circuit voltage sinewave looks distorted for the range of data points acquired during its measurement through the Agilent Technologies N6705B power analyser. 62

Figure 4.9 DMCS-TENG with polyimide-flat Al and polyimide-honeycomb patterned Al instantaneous (a-b) voltage-time, (c-d) current-time and (e-f) transferred charge-time response through simulated resonant frequencies of 30 Hz, 80 Hz, 150 Hz, 180 Hz, 200 Hz, 219 Hz and 252 Hz. 63

Figure 4.10 (a) Acceleration, (b) velocity and (c) displacement of the top dielectric layer when in contacts the conductor layer of the DMCS-TENG prototype during the vibration frequency swept from 25 to 300 Hz with an increasing step of 5 Hz for 55 seconds. (d) Average acceleration, velocity and displacement of the top dielectric layer measured with a PDV Portable Digital Vibrometer. 65

Figure 4.11 (a) DMCS-TENG output power, ECE % and average acceleration measured at the main compressed air bubble frequencies generated during wave impact with polyimide (Kapton), PDMS, FEP, silicone rubber, PET – flat Al foil/honeycomb-patterned Al foil. (b) Zoom of the output power generated for the DMCS-TENG devices with silicone rubber and PET. 66

Figure 4.12 (a) Power up of 62 serially-connected white LEDs instantaneously and continuously with the DMCS-TENG prototype (polyimide-honeycomb patterned Al foil). Measured average instantaneous power consumption by the LEDs was around 13.48 mW. (b) Output power generated by the DMCS-TENG prototype (polyimide-honeycomb patterned Al foil), when the dielectric-metal layers are in contact and released exposed to water wave impact with an amplitude of 10.5 cm and frequency of 1.2 Hz. 68

Figure 5.1 Two-dimensional schematic of the (a) Hybrid nanogenerator, (b) PENG with charge distribution when it is under an external force. (c) The arc-shaped DMCS-TENG, and (d) the DMCS-TENG self-resetting system. (e) Digital photo and a cross-sectional digital photo of the hybrid nanogenerator. Digital photo of the (f) PENG, (g) arc-shaped DMCS-TENG and (h) DMCS-TENG self-resetting system. 74

Figure 5.2 (a-e) Working mechanism of the piezoelectric nanogenerator under water wave impact….. 75

Figure 5.3 (a-e) Working mechanism of the Arc-shaped TENG at water wave impact conditions.76

Figure 5.4 (a-e) Working mechanism of the DMCS-TENG at water wave impact conditions.....76

Figure 5.5 (a-e) The working mechanism of the hybrid nanogenerator with a simultaneous operation and electricity generation of triboelectric-piezoelectric effects at water wave impact conditions. Digital photos of the grid of hybrid nanogenerators in the breaking wave impact generator tank (f) before receiving water wave impact, (g) contacted and pressed, (h) contacted and released, and (i) releasing. 78

Figure 5.6 (a) Circuit diagram of the hybrid nanogenerators for the load matching and capacitor charging experiments. (b) Grid of hybrid nanogenerators placed in the water wave generator tank for its output performance measurements. 79

Figure 5.7 (a) Average rectified instantaneous output current, (b) output voltage and (c) transferred charges of hybrid nanogenerator. In comparison with (d-f) arc-shaped TENG, (g-i) DMCS-TENG, and (j-l) PENG average rectified instantaneous output current, output voltage, and transferred charges connected to a 1 MΩ load resistor tested in a water wave impact generator tank under different frequencies of impact between 0.7 Hz to 3 Hz (Data acquired during approximately 3 seconds). 81

Figure 5.8 (a) Rectified average instantaneous output power and its standard deviation analysis calculated (10 measurements performed for each sample) of Hybrid device compared

with TENG and PENG devices connected to a 1 MΩ resistor at water wave impact conditions (0.7 Hz to 3 Hz). (b) Charging performance of a single hybrid device, arc-shaped TENG, PENG, and DMCS TENG connected to a 2.2 µF capacitor. (c) Load resistance matching analysis to reach the highest output power performance of the hybrid device tested in the water generator tank. 82

Figure 5.9 (a) Charging performance of a single hybrid device, and (b) a grid of 4 hybrid devices connected in parallel to different capacitors (2.2 µF – 100 µF). (c) Rectified instantaneous output current, (d) output voltage, (e) transferred charges (Data acquired during approximately 3 seconds), and (f) output power of a grid of hybrid devices compared with a single hybrid device unit connected to a 1 MΩ load resistor..... 84

Figure 5.10 (a) Set-up for powering the wireless transmitter with the grid of hybrid nanogenerators under the water wave impact. (b) Electrical circuit diagram of the hybrid nanogenerators to charge the capacitor of 47 µF for powering the wireless transmitter. (c) Capacitor charging and discharging process for powering the wireless transmitter under the water wave impact with a frequency of 1.2 Hz. (d) Energy stored in the capacitor of 47 µF for the grid of hybrid devices, and the power generated for the capacitor during the discharging process for powering the wireless transmitter to send a signal to a receiver with a transmission distance from 2 m to 8 m. 85

Figure 5.11 Maximum average instantaneous output current generated by the hybrid nanogenerator during different periods (30 min to 180 min) and cycles of operation (2168 to 19512) at water wave impact conditions. 86

Figure 5.12 Two-dimensional schematic illustration of the configuration of the proposed large water-hybrid nanogenerators-structure interfaces to escalate the energy harvesting of water wave impact (Ocean water wave adapted from [132]). 87

Figure 6.1 Two-dimensional schematic and digital images of the three configurations of fabricated WDSE-TENG prototypes (a) WDSE-TENG with one dielectric layer, (b) full device covered with two dielectric layers, and (c) split electrode-two dielectric layers. Molecular structure of d) FEP, e) PTFE, f) Silicone rubber (Acetoxy, elastomer) and PDMS and g) Kapton..... 91

Figure 6.2 (a-g). Working mechanism of the WDSE-TENG with one-dielectric layer by the contact electrification of dielectric layers with breaking water wave impact. 93

Figure 6.3 (a-g). Working mechanism of the WDSE-TENG with two-dielectric layers by the contact electrification of dielectric layers with breaking water wave impact.....93

Figure 6.4 Working mechanism of the split-electrode WDSE-TENG with two-dielectric layers by the contact electrification of dielectric layers from breaking water wave impact. 94

Figure 6.5 (a) Digital image of the single WDSE-TENG attached and under breaking water wave impact in the water wave impact generator tank. (b) Circuit diagram of the WDSE-TENG for the load matching and charging of different capacitors. (c) Digital image of the grid of five WDSE-TENG devices attached and under breaking water wave impact in the water wave impact generator tank. (d) Digital image of the back view of the grid of five WDSE-TENG devices under breaking water wave impact that illustrates the contact of the water wave in both of their faces. 96

Figure 6.6 (a) Instantaneous output current generation of the WDSE-TENG in two cycles of operation at breaking water wave impact conditions (with a frequency and amplitude of 1.2 Hz and 10.5 cm). (b) The average instantaneous output current of the WDSE-TENG with different configurations and materials in contact with tap water (Data acquired during 15 seconds for each sample).....97

Figure 6.7 The average instantaneous output voltage (Data acquired during 2.5 s for each sample), output current and transferred charge (Data acquired during 15 seconds for each sample) of the WDSE-TENG with different configurations and materials in contact with (a-c) DI water, (d-f) tap water and (g-i) artificial seawater.....99

Figure 6.8 Comparison of the output power calculated for each of the three WDSE-TENG prototypes when exposed to 10.5 cm amplitude waves at 1.2 Hz (with 1 MΩ load)..... 100

Figure 6.9 Transferred charges of (a) a single WDSE-TENG and (b) grid of five WDSE-TENG devices through different breaking water wave frequencies (0.7 Hz to 3 Hz) in proportion to the total mechanical energy of the breaking water wave impact consisting of potential and kinetic energy that contacts on the WDSE-TENG (Data acquired during 3 seconds for each sample).....103

Figure 6.10 (a) The Instantaneous output voltage, (b) current and (c) transferred charges of a single WDSE-TENG with two-dielectric layers of silicone rubber compound. (d) Instantaneous output voltage, (e) current and (f) transferred charges of the grid of five WDSE-TENG devices through different breaking wave impact frequencies (0.7 Hz to 3 Hz) with a load resistance of 3.8 MΩ (Data acquired during 5 seconds for each sample). (g) Load

resistance matching analysis to obtain the highest output power performance with the WDSE-TENG devices. (h) Charging performance of a single WDSE-TENG energy harvester, and (i) a grid of five WDSE-TENG energy harvesters connected in parallel to different capacitors (4.7 µF to 470 µF) tested in the water generator tank..... 104

Figure 6.11 (a) Average instantaneous output power, energy and energy conversion efficiency of a single WDSE-TENG with two-dielectric layers of silicone rubber compound over 15 seconds. (b) Average instantaneous output power, energy and energy conversion efficiency of the grid of five WDSE-TENG devices through different breaking wave impact frequencies (0.7 Hz to 3 Hz) and amplitudes (10 cm to 12 cm) with a load resistance of 3.8 MΩ, for 15 seconds. (c) Maximum average instantaneous output current generated by the WDSE-TENG during different periods and cycles of operation from 30 min to 210 min and 2160 cycles to 15120 cycles under breaking water wave impact..... 106

Figure 6.12 (a) Electrical circuit diagram of the grid of WDSE-TENG energy harvesters under breaking water wave impact to charge the 47 µF and 470 µF capacitors to power-up (b) the wireless transmitter to turn (c) a Therma-hygrometer and (d) an ultrasonic ranger sensor (Ocean water wave adapted from Refs. [132]). 108

Figure 6.13 Capacitor charging and discharging process for powering the (a) wireless transmitter to power-up the therma-hygrometer, and (b) ultrasonic range sensor under the breaking water wave impact with a frequency of 1.2 Hz. (c) Energy stored in the 47 µF capacitor for the grid of WDSE-TENG devices, and the power supplied by the capacitor during the discharging process for powering the wireless transmitter to turn on a therma-hygrometer. (d) Integration of the grid of WDSE-TENG with an LT8303 micropower high-voltage insolated flyback converter to form a power management control circuit (PMCC). (e) Digital image of the PMCC circuit with the grid of WDSE-TENG. (f) Energy transfer from Ct to Cs from harvesting the breaking water wave impact for 200 seconds.. 109

Figure 7.1 Power density generated by the DMCS-TENG [124, 125] (Results can be found in section 4.3.2 and section 5.3), hybrid nanogenerators [136] (section 5.3) with contact electrification between solid-solid materials, and WDSE-TENG [158-160] (section 6.3.2) with contact electrification between liquid-solid materials for breaking water wave impact energy harvesting. The power density of energy harvesters based in TENG, Hybrid TENG-EMG and liquid-solid-enabled generator (LSEG) for shallow water wave energy harvesting using solid-solid and liquid-solid contact electrification [19-40]. 114

Research Thesis: Declaration of Authorship

Print name: Ulises Tronco Jurado

Title of thesis: Triboelectric nanogenerators for breaking water wave impact energy harvesting for self-powered applications

I declare that this thesis and the work presented in it are my own and has been generated by me as the result of my own original research.

I confirm that:

1. This work was done wholly or mainly while in candidature for a research degree at this University;
2. Where any part of this thesis has previously been submitted for a degree or any other qualification at this University or any other institution, this has been clearly stated;
3. Where I have consulted the published work of others, this is always clearly attributed;
4. Where I have quoted from the work of others, the source is always given. With the exception of such quotations, this thesis is entirely my own work;
5. I have acknowledged all main sources of help;
6. Where the thesis is based on work done by myself jointly with others, I have made clear exactly what was done by others and what I have contributed myself;
7. Parts of this work have been published as:

[124] U. T. Jurado, S. H. Pu, and N. M. White, "A contact-separation mode triboelectric nanogenerator for ocean wave impact energy harvesting," in 2017 IEEE SENSORS, 2017: IEEE, pp. 1-3.

[125] U. T. Jurado, S. H. Pu, and N. M. White, "Dielectric-metal triboelectric nanogenerators for ocean wave impact self-powered applications," IEEE Sensors Journal, vol. 19, no. 16, pp. 6778-6785, 2019.

[136] U. T. Jurado, S. H. Pu, and N. M. White, "Grid of hybrid nanogenerators for improving ocean wave impact energy harvesting self-powered applications," Nano Energy, vol. 72, p. 104701, 2020.

[158] U. T. Jurado, S. H. Pu, and N. M. White, "Water-dielectric single electrode mode triboelectric nanogenerators for ocean wave impact energy harvesting," in Multidisciplinary Digital Publishing Institute Proceedings, 2018, vol. 2, no. 13, p. 714.

[159] U. T. Jurado, S. H. Pu, and N. M. White, "Wave impact energy harvesting through water-dielectric triboelectrification with single-electrode triboelectric nanogenerators for battery-less systems," *Nano Energy,* vol. 78, p. 105204, 2020.

Signature: ..... Date:.....

Acknowledgements

Firstly, I would like to thank and express my gratitude to my supervisors Dr Suan Hui Pu and Dr Neil M. White for the wealth of knowledge and experience which they imparted to me over the duration of this doctoral research study, which in pulse me to overcome all the confronted challenges on this path. I wish to thank my fiancée Daniela Ivanova for all her help support and accompanying me to achieve this dream. I wish to thank my family without whose support this would not have been possible. I would like to acknowledge all my colleagues and the great friends whom I have met over the last three years at the University of Southampton. The staff at the Faculty of Engineering and Physical Sciences, especially in the Smart Electronic Materials and Systems proved most helpful from the time I arrive in Southampton. I would like to thank my examiners, Dr Paul Chappell, Dr Swee Leong Kok and Dr Sze Sing Lee. Finally, I would like to thank CONACYT for the fellowship awarded to me to study this Doctoral degree.

Nomenclature

A	Constant determined by the gas pressure (V/(atm·m))
a	Acceleration (mm/s^2)
A_c	Cross-sectional area of the piezoelectric layer (cm^2)
$A_{waterwave}$	Amplitude of the water wave impact (cm)
B	Constant determined by the gas pressure
b	Width of the piezoelectric material (cm)
C	Capacitance (F)
Cs	Storage capacitor (μF)
Ct	Pre-storage capacitor (μF)
d_A	Thickness of conductive acrylic adhesive (μm)
d_{D0}	Effective dielectric thickness (μm)
d_{D1}	Thickness of dielectric layer 1 (μm)
d_{D2}	Thickness of dielectric layer 2 (μm)
d_{E1}	Thickness of electrode 1 (μm)
d_{E2}	Thickness of electrode 2 (μm)
d_{E3}	Thickness of electrode 3 (μm)
d_P	Thickness of the piezoelectric material (μm)
E	Young's modulus (Pa)
E_1	Electric field inside dielectric 1 (kg·m/s^2·C)
E_2	Electric field inside dielectric 2 (kg·m/s^2·C)
E_{air}	Electric field inside the air gap (kg·m/s^2·C)
$E_{elastic}$	Elastic energy (mJ)
$E_{electric}$	Electric energy (J)
$E_{kinetic}$	Kinetic energy (mJ)
$E_{mechanical}$	Mechanical energy (mJ)
$E_{waterwave}$	Energy produced by the water wave impact (J)
f	Frequency (Hz)
f_0	Resonant frequency (Hz)
F	Force (N)
F_0	External force amplitude (N)
g	Acceleration of gravity (m/s^2)
I	Current (μA)
I_{RMS}	Effective value of current (μA)
k	Spring constant (N/m)
k_P	Spring constant due to the stiffness in stretching the piezoelectric layer (N/m)
k_T	Spring constant due to the flexural stiffness of the arc-shaped triboelectric layer (N/m)
L	Length of the structure (cm)
m	Mass (g)
min	Minutes
N	Number of springs
η	Energy conversion efficiency

P	Gas pressure for the air at standard atmospheric pressure of 101 kPa
Q	Transferred charges (nC)
Q_{SC}	Short-circuit transfer charge (nC)
R_L	Load resistance (Ω)
R_P	External resistive load of piezoelectric generator (Ω)
R_T	External resistive load of triboelectric nanogenerator (Ω)
S	Area size (cm^2)
t	Time (s)
$T_{1/2}$	Time of the generated open-circuit voltage (s)
V	Voltage (V)
v	Velocity (m/s)
$V_{a\text{-}b}$	Threshold voltage for the air breakdown (V)
V_{gap}	Voltage drop across the air gap (V)
V_{OC}	Open-circuit voltage (V)
V_{ocmax}	Maximum open-circuit voltage (V)
V_{RMS}	Effective value of voltage (V)
W	Work done due to pressing/pulling of the piezoelectric layer (J)
x	Distance (m)
$x1$	Piezoelectric polarization ($\mu C/m^2$)
X_t	Displacement of the top plate (layer) (mm)
x_P	Distance due to the stress of the piezoelectric layer for the water wave impact (mm)
ΔL	Length change of the piezoelectric material (mm)
ε_0	Permittivity of vacuum (F/m)
ε_P	Permittivity of the piezoelectric material (F/m)
ε_{r1}	Dielectric constant of dielectric layer 1
ε_{r2}	Dielectric constant of dielectric layer 2
ρ	Density of water (kg/m^3)
σ	Triboelectric-charges (Surface charge density) ($\mu C/m^2$)
σ_{max}	Maximum surface charge density ($\mu C/m^2$)
σ_P	Tensile stress of the piezoelectric layer (Pa)
ζ	Damping coefficient
ϕ	Phase angle
~	Approximately

Abbreviations

AC	Alternating Current
CS-TENG	Contact-Separation mode Triboelectric Nanogenerator
DC	Direct Current
DI	Deionized Water
DMCS-TENG	Dielectric-Metal Contact-Separation mode Triboelectric Nanogenerator
DMSE-TENG	Dielectric-Metal Single-Electrode Triboelectric Nanogenerator
ECE	Energy Conversion Efficiency
EDL	Electric Double Layer
EMG	Electromagnetic Generators
FEA	Finite Element Analysis
FEM	Finite Element Method
FEP	Fluorinated Ethylene Propylene
How-NG	Honeycomb-like three-electrode Nanogenerator
LSEG	Liquid-Solid Electrification-Enabled Generator
MSCD	Maximum Surface Charge Density
OBREC	Overtopping breakwater for energy conversion
OWC	Oscillating water column
PDMS	Polydimethylsiloxane
PDV	Portable Digital Vibrometer
PENG	Piezoelectric Nanogenerator
PET	Polyethylene Terephthalate
PMCC	Power Management Control Circuit
PMM	Power Management Module
PTFE	Polytetrafluoroethylene
PVDF	Polyvinylidene
PZT	Lead Zirconate Titanate
RF-TENG	Rolling-Spherical Freestanding Triboelectric Nanogenerator
SC	Short-Circuit
SEV	Self-Excited Vibrations
TENG	Triboelectric Nanogenerator
TENG-EMG	Triboelectric Nanogenerator and Electromagnetic Generator
TENGs	Triboelectric Nanogenerators
THNG	Teeterboard-like Hybrid Nanogenerator
TS-TENG	Torus Structured Triboelectric Nanogenerator
UUV	Unmanned Underwater Vehicles
WDSE-TENG	Water-Dielectric Single-Electrode mode Triboelectric Nanogenerator

Chapter 1 Introduction

This first chapter describes the research project motivation, as well as the aims and objectives of this study. Additionally, it includes a brief overview of the followed methodology about how the objectives were achieved. The layout of the report and the novelty of performed research work is subsequently described.

1.1 Research motivation

Ocean energy represents one of the largest renewable resources available on the planet and is an emerging industry that has the potential to satisfy the worldwide demand for electricity, water, and fuels when coupled with other energy generation methods. Harvesting clean and renewable energy from ocean waves is one of the greatest attractions nowadays because it offers greater reliability than solar or wind, lower auditory impact than wind, and could potentially meet 10% of total demand worldwide electric demand [1]. Among different types of ocean energy, wave energy represents the highest density resource [2]. Numerous ocean wave assessments report the optimism of wave energy to tackle the excessive electricity demands in different countries in the world. For example, it is estimated that wave energy would meet ~60, 20, and 33% of the total electricity demands in the US, UK, and Denmark, respectively [3, 4]. However, due to technological and economical complexity, it is not straightforward to implement the majority of these energy harvesters in the real ocean environment. Effective utilization and sustainability of this kind of energy can be exploited due to the effects of climate change with the rapid increase of sea levels and more recurrent flood coastal zones. UK coastlines have become highly vulnerable to floods with a significant impact on critical infrastructure (roads, railway tracks, ports, etc.) and coastal communities [5-8]. Their critical vulnerability is unresolved simply because their design does not fundamentally take into account the long-term effects of penetrative high magnitude wave forces inflicted upon the constituent material structure of coastal defences. In order to reduce ocean wave damage effects on in-shore structures, wave breakers are constructed. For example, the total length of breakwaters in Japan is more than 800 km [9]. Therefore, specifically focused on the cumulative loads of breaking water wave forces at defence structures deliver high magnitude pulse-like hydrostatic pressures with a wide frequency range of destructive oscillatory compressed air bubbles at the structure-water interfaces. The fluid-structure interaction has been predicted for the understanding and quantification of wave impact energy transfer process at porous structures by means of a compressible fluid simulation [10-13].

The surging flow front impacts the structure, which spreads vertically upwards as shown in Figure 1.1 (a) and produces the first hydrostatic pressure oscillations peak between 0.7 Hz to 80 Hz with an amplitude range of 57 Pa to >400 Pa (Figure 1.2). After the wave collapses a plunging breaker is formed (Figure 1.1 (b)) and many air bubbles are entrained (Figure 1.1 (c)), which compresses and dilates in a high-frequency oscillatory manner, impinging upon the coastal protective structure as shown in Figure 1.1 (d)). This yields a cyclic hydrostatic pressure response between 150 to 252 Hz with an amplitude range of 148 to 348 Pa, predicted through a fluid-structure simulation [10-13] (Figure 1.2). Such energy can be potentially harvested and exploited to produce sustainable electricity in the future at small and large scales, using triboelectric nanogenerators (TENG) as an alternative and new approach for breaking ocean wave impact energy harvesting (Figure 1.1 (a)). This aim, in harvesting the breaking wave impact at a broad range of low frequencies between 0.7 Hz to 3 Hz and at high frequencies between 30 Hz to 300 Hz is to harvest the major energy [10-13]. The integration of TENG with wave breakers-structure interfaces to extract the wave energy that breaks in a vertical structure. It is a promising alternative to energize a variety of battery-less marine sensing platforms at water-structure interfaces in aquaculture applications as smart fish farms, environmental monitoring, and the utilization to prevent critical damage in coastal defence systems.

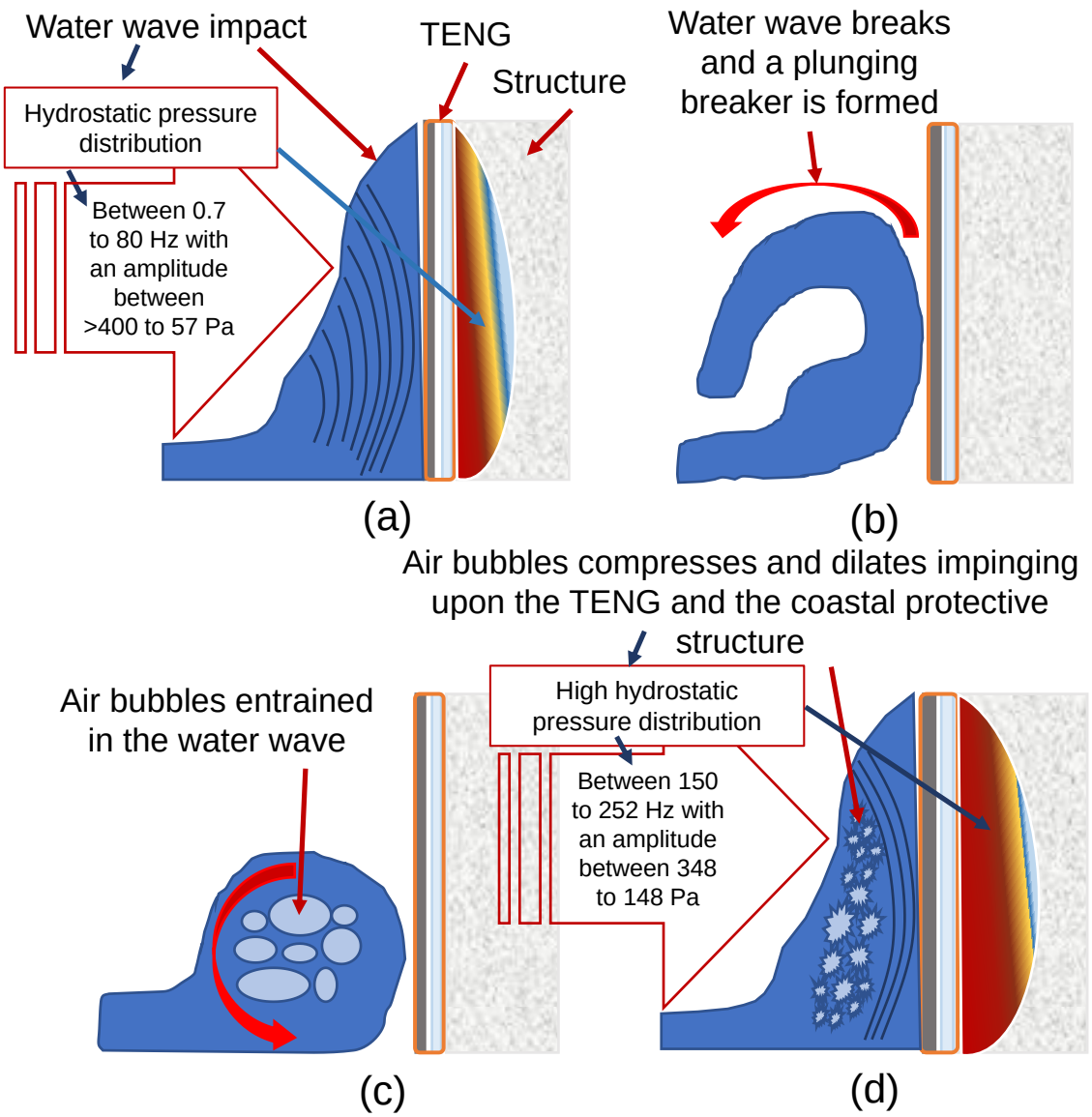

Figure 1.1 (a-d) Hydrostatic pressure distribution of the breaking ocean wave impact at the water-structure interface and main frequencies of interest (0.7 Hz to 300 Hz) [12, 13] for breaking ocean wave impact energy harvesting generated by (a) the water wave impact and (d) the impact of oscillatory compressed air bubbles flows at the water-structure interface exploited using triboelectric nanogenerators.

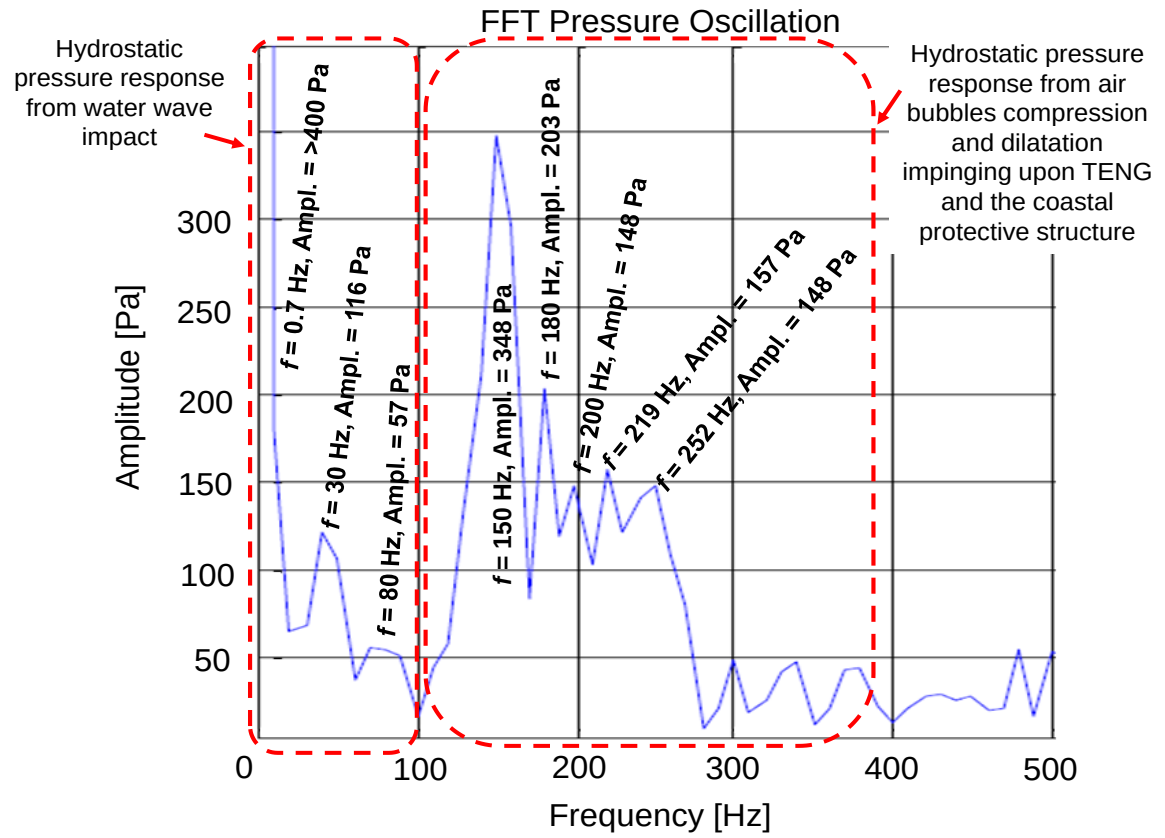

Figure 1.2 Main frequencies of interest in pressure signal for breaking ocean wave energy harvesting generated by the impact and the oscillatory compressed air bubbles flows at the structural-water interfaces [12].

1.2 Aims and objectives

This study aims to investigate the harvesting of the energy of the combined loads of the breaking ocean wave impact forces and air bubbles oscillatory frequencies at coastal defence structures. Mainly because the high energy density of breaking waves compared to other ocean waves for the production of clean and renewable electricity at coastal defences by using triboelectric nanogenerators (TENG) energy harvesters which converts the external mechanical energy into electricity by a combination of triboelectric effect and electrostatic induction, based on contact electrification between two materials and charge transfer between their electrodes [14-17]. Their advantages include broadband behaviour, lightweight, good energy density, and easy fabrication process exploiting low-cost abundant choice of materials [16, 18].

The first objective is to obtain a quantitative understanding of the breaking water wave impact energy harvesting technology of triboelectric nanogenerators prototypes using COMSOL Multiphysics finite element analysis (FEA) software. The electromechanical behaviour and output performance of the entire system of triboelectric nanogenerators in terms of the range of cumulative loads by the resonant oscillatory frequencies due to ocean wave impact forces will be

evaluated using finite element modelling. It would be of interest to characterize the output voltage (V), current (I), and output power using resistors as external loads to maximize the device output performance and parameter optimization.

The second objective is to develop and characterize actual prototypes for the TENG for breaking water wave impact energy harvesting. In order to maximize the device output performance through changing parameters such as different triboelectric materials combinations, dimensions, operation mode design, surfaces, shape, and so on, under the broad oscillatory frequency range between 0.7 Hz to 300 Hz and 50 Pa to >400 Pa of amplitude will be studied. Three different approaches based on contact electrification between solid-solid, liquid-solid and hybrid device studying the coupling between triboelectric-piezoelectric effects of the fabricated triboelectric nanogenerators will be studied. For the testing and analysis of the electric output performance potential of each approach with the measurement of the generated output voltage (V), current (I), transferred charges (Q), charging performance by charging different capacitors, output power, power density and energy conversion efficiency (ECE), with resistors utilized as external loads under similar experimental conditions.

The third objective is to study and analyse the potential of the fabricated TENG devices as an energy harvesting mechanism for breaking water wave impact to drive small electronic devices that could enable future advancement for powering a variety of battery-less applications at small and large scales. Finally, a conclusion will be made through the analysis of the experimental results comparing each studied energy harvesting technique based on solid-solid and liquid-solid interfaces. Focused on the most important findings of the alternative approach of triboelectric nanogenerators used to realize a new type of energy harvester for generating electrical power from breaking water wave impacts and after the wave collapses, where the air bubbles are formed (Figure 1.2). Nevertheless, finding optimum trade-offs to maximize the energy harvested from the flow is required, focusing on triboelectric nanogenerators technique, methods to improve robustness, long-term durability and efficient energy coupling will be recommended.

1.3 Layout of the report and novelty of the research

A literature review of the potential for ocean wave energy harvesting, the current state of the art in the development and detailed background of the proposed technology of triboelectric nanogenerators to harvest the mechanical energies generated by breaking ocean wave impact and the oscillatory compressed air bubbles flows at the structural porous water-interfaces is reported in chapter 2. Also included in the literature review is a brief explanation of the triboelectric nanogenerators in comparison with mechanical energy harvesting technologies with the potential

for ocean wave energy harvesting, as well as technical barriers, potential applications and comparison for ocean wave energy harvesters.

Following the above, modelling and numerical simulation results are reported in chapter 3. It includes a description and explanation of the theoretical background for the triboelectric nanogenerators. The model and FEA simulation parameters settled to perform and obtain a quantitative understanding for the working mechanism and analysing the output performance of the entire system of TENG technique for breaking water wave impact energy harvesting purposes is explained in detail. Additionally, chapters 4, 5 and 6 report the fabrication and characterization of water wave impact energy harvesting generators in detail. Where the fabricated TENG prototypes through different approaches using solid-solid, liquid-solid triboelectric interfaces and hybrid coupling, which electric output performance is characterized through different experiments. Such as impact test over the prototypes with different triboelectric materials combinations, the reproduction of oscillatory frequencies due to water wave impact forces through a mechanical shaker and using a breaking water wave generator tank. Furthermore, the results obtained through the experimental electrical characterization of the triboelectric energy harvesting prototypes are then presented, analysed and summarized. Chapter 7 summarizes the key findings from the simulations and the experimental electrical characterizations of the proposed energy harvesters. Proposals for future development work for this research project are also highlighted in the final chapter.

The novelty of this research will be to study, analyse and employ the triboelectric nanogenerators using different triboelectrification configurations as an alternative approach to realize a new type of energy harvester for the collection of cumulative loads by the breaking ocean wave impact hydrostatic pressures, and air bubbles oscillatory frequencies that can be integrated into defence porous structures water-interfaces, for the production of clean and renewable electricity at coastal defences. Furthermore, it is expected that the proposed energy harvesting devices will enable future advancement in energy harvesting at porous water interfaces to prevent critical damage, and as an energy harvesting mechanism for breaking ocean wave monitoring applications that require self-powering. Additionally, the novelty of this research study differs from the developed studies using different TENG based on contact electrification of solid-solid [19-28] and liquid-solid interfaces [29-38], and hybrid devices combined with TENG-electromagnetic generators (EMG) [39,

40], which are focused in harvesting the irregular motions at low frequencies between 0.5 Hz to 10 Hz, generated by the shallow ocean wave energy.

Chapter 2 Literature review of ocean wave energy harvesting techniques

2.1 Introduction

The analysis of the potential for harvesting energy from ocean waves is described in the next section. Furthermore, a comparison of triboelectric nanogenerators (TENG) with mechanical energy harvesting technologies with the potential for ocean wave energy harvesting is described. The state of the art of the current energy harvesting devices and techniques from ocean waves are explained. Focusing on different triboelectric nanogenerators that mainly are oriented in collecting the energy generated by the random motions of shallow ocean waves at low-frequency range from 0.5 Hz to 10 Hz, based on contact electrification of solid-solid and liquid-solid interfaces [19-27, 29-38], and hybrid devices combined with TENG-electromagnetic generators (EMG) [39, 40]. Additionally, a brief description of piezoelectric generators harvesting ocean wave energy are described. Additionally, potential applications and characteristics for applications are explained. To sum up, the comparison of ocean wave energy harvesting techniques and their potential for self-powered systems, which are relevant for this study are described and summarized.

2.2 Ocean energy

The ocean energy represents one of the largest renewable resources on the planet and is an emerging industry that has a potential to satisfy the worldwide demand for electricity, water and fuels when coupled with other energy generation methods. Its theoretical energy potential as a global resource is estimated as follows [41, 42]:

- Wave energy is represented by surface and subsurface motion of waves (8,000 – 80,000 TWh/year).
- Hydrokinetic energy that harvests the energy of ocean currents and tides (800 TWh/year).
- Ocean thermal energy conversion using the temperature differential between cold water from the deep ocean current and tides (10,000 TWh/year).
- Osmotic energy is the pressure differential between salt and freshwater (2,000 TWh/year).

Among different types of ocean energy, wave energy represents the highest density resource. When a meteorological process in the ocean concentrate solar and wind energy that in turn create waves as the winds blow across the oceans, travelling thousands of kilometres with little energy losses, unless they encounter headwinds [43]. The energy available from the oceans in various

forms can be put into perspective by comparing them to the world's electricity consumption of 22,347 TWh/year [44]. The graphical distribution of annual mean power density around the world is illustrated in Figure 2.1. The best mean direction of the power density vectors is shown with the arrows. Wave energy with the maximum distribution is concentrated and recorded between the 40th and 60th lines of latitude north and south [44].

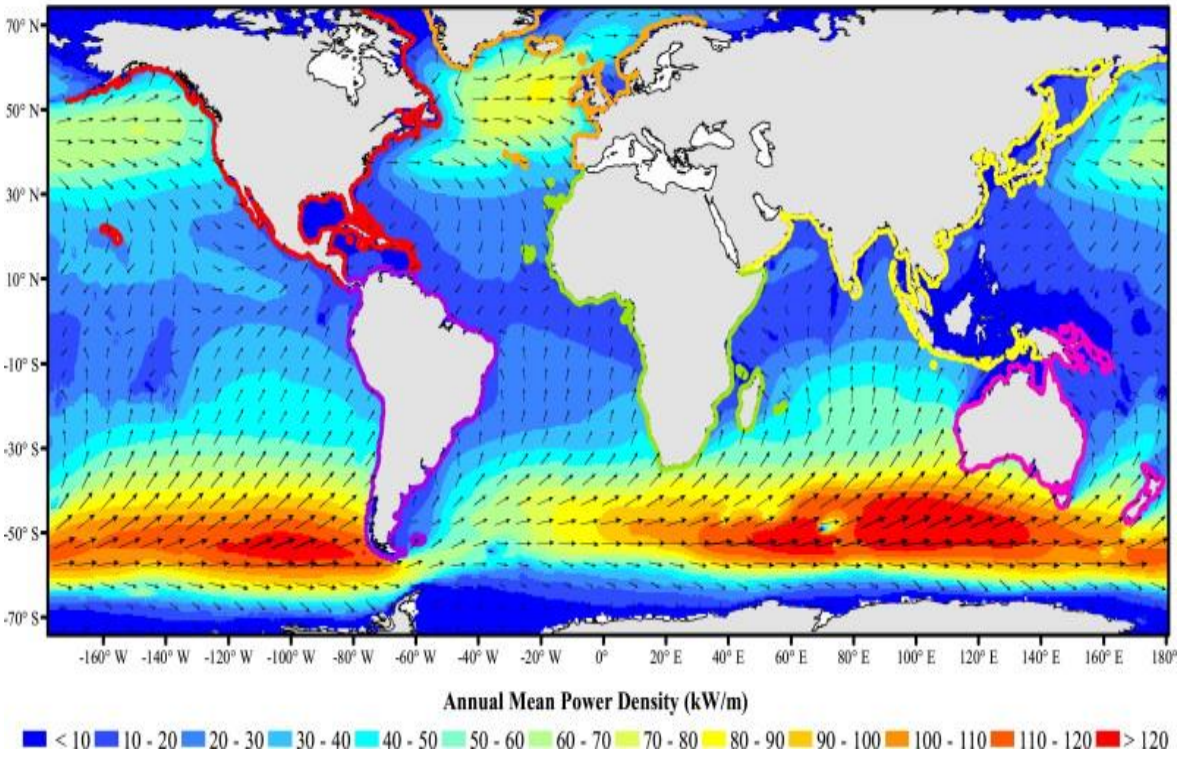

Figure 2.1 Global distribution of wave energy density. Reproduced with permission from Elsevier [44].

2.3 Energy harvesting from ocean waves

Harvesting energy from ocean waves is one of the greatest attractions for energy engineers and scientists. To date, plenty of methods have been adopted to harvest the energy from the ocean waves. However, due to technological challenges, it is not possible to use the majority of these energy harvesters in the real ocean environment. Effective utilization and sustainability of any wave energy harvester depend upon its adaptability to irregular seasonal waves, high energy extraction and finally overcoming the economic barriers. Many different concepts to capture wave energy have been proposed in recent times. However, the technical and conceptual convergence has not been obtained to achieve designs that are well-suited for wave energy application [45].

Ocean wave power has the potential to produce clean, renewable energy in an environmentally sound manner that offers greater reliability than solar or wind power, and lower visual and auditory

impact than wind power generation. Further, this energy tends to be available near many population centres with significant industrial activity [1]. The Electric Power Research Institute estimates that wave energy could potentially meet 10% of total worldwide electric demand [46]. Ocean wave power is yet to be used for electrical power generation to any significant degree. Widespread adoption of wave power harvesting is hampered by certain economic and environmental factors. For instance, the primary converter structure of conventional ocean wave power-harvesting systems must be over-engineered to deal with high sea events (such as storms that cause high wave activity) and, as a result, these systems are very expensive [1]. Numerous attempts have been unsuccessful as the device failed to survive the severe and corrosive marine environment.

At the present, different kinds of technology integrating robust and large water wave energy converters with breakwater structures have been studied and presented named overtopping, oscillating water column and piston type configurations focused on harvesting water wave energy in large scales [47]. The **overtopping breakwater for energy conversion (OBREC)** it is a device that uses an overtopping effect caused by the breaking ocean waves that fill a tank, then causes the movement of a turbine that converts the potential energy into electricity as illustrated in Figure 2.2 (a). For this device, if the breaking wave is below the breakwater device wall, no overtopping effect will occur, which is a disadvantage to produce electricity with this device [47-49].

The **oscillating water column (OCW)** uses the change in pressure level caused in a chamber due to two openings, one for the circulation of the breaking water wave and the second for the expansion and retraction of the air horizontally, which moves a turbine to produce electricity (Figure 2.2 (b) [47, 50, 51]. The **piston-type water energy harvester** collects breaking wave energy by reducing the impact of the wave. Such a system produces electricity absorbing the wave impact that is transferred to mechanical energy with the horizontal movement of a piston system as depicted in Figure 2.2 (c) [47, 52]. The previously described devices are estimated to produce output power levels between 6 kW to 30,000 kW with structure lengths from 250 m to 1176 m [47]. Although their high estimated output power, these devices utilize electromagnetic generators (EMG) to generate electricity, comprising turbines, metal coils, bulky and heave magnets, which are very expensive and technically complicated to fabricate [53]. Consequently, different challenges should be addressed like the proposal of an alternative integration concept of wave energy harvesters and breakwater structures for breaking water wave impact energy harvesting.

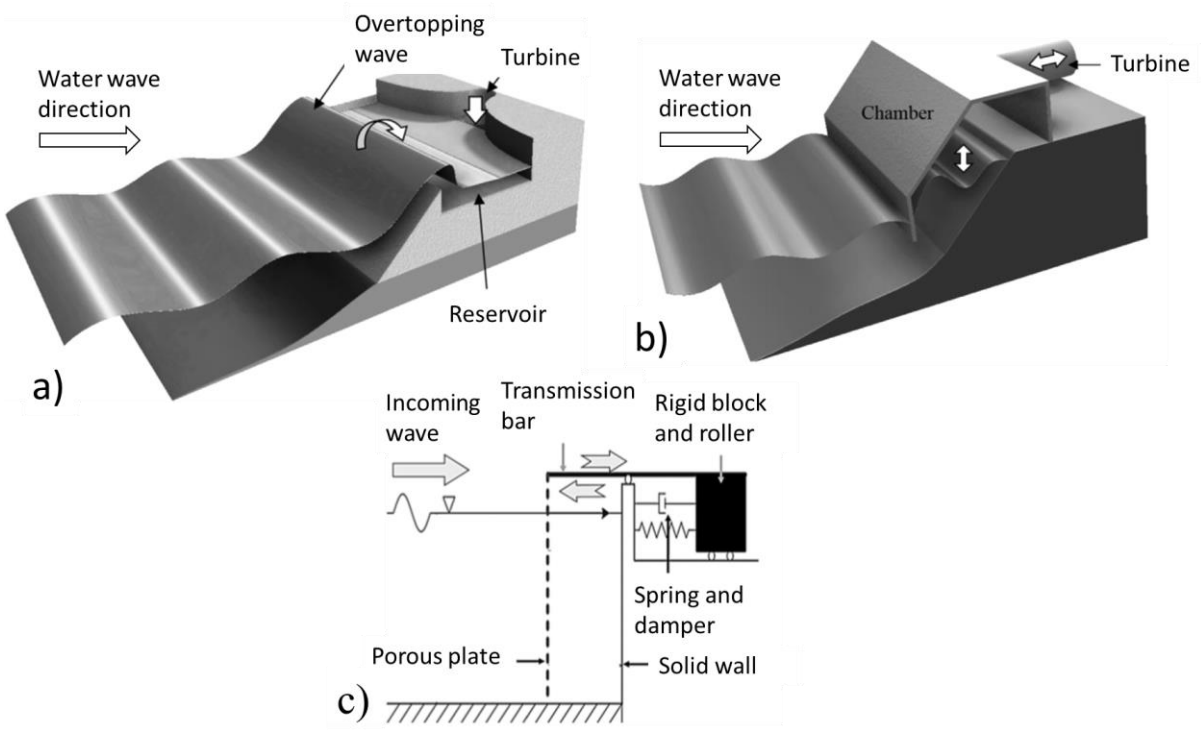

Figure 2.2 Current technologies for breaking water wave energy harvesting integrating robust water energy converters with breakwater structures (a) overtopping [47-49], (b) oscillating water column [47, 50, 51] and (c) piston type [47, 52] configurations aimed at harvesting water wave energy in large scales. Reproduced with permission from Elsevier [47].

2.4 Triboelectric nanogenerators (TENG) in comparison with mechanical energy harvesting technologies with potential for ocean wave energy harvesting

In contrast to other renewable energy sources, the number of concepts for wave energy conversion is very large. Although over 4000 wave energy conversion techniques have been patented worldwide. It can be classified by its basic principles of energy conversion [43]. This study is focused in triboelectric nanogenerators focus on mechanical energy harvesting of the breaking ocean wave impact that varies between slowly-acting pulsating loads, and more intense impulsive loads [12] which can be exploited as a source of electrical energy. To date, the mechanisms of mechanical energy harvesting have been mainly based on electromagnetic effect, electrostatic effect, and piezoelectric effect, which are likely to be shadowed by possible limitations in the field of harvesting mechanical energy. Each of these effects has its uniqueness and applications, as summarized in Table 2.1.

To get started, the piezoelectric effect-base generator, an insulator piezoelectric material is covered by a top and bottom electrode on its two surfaces. A vertical mechanical deformation results in the

generation of piezoelectric polarization charges at the two ends of the material due to distortion of the crystal lattice. An increase in the applied force results in higher polarization charge density. The electrostatic potential created by the polarization charges is balanced by the flow of electrons from one electrode to the other through an external load. This is the process of converting mechanical energy into electric power [54]. With simple structure design, the piezoelectric effect-based generator is characterized by a longer life span and lower cost. Numerous piezoelectric materials including zinc oxide (ZnO), lead zirconate titanate (PZT), polyvinylidene (PVDF), etc. have been utilized to fabricate high-performance piezoelectric generators [54-56]. However, it has low power output, which greatly limits its practical application as a sustainable power source [57, 58].

For electromagnetic effect-based generator is the current and most popular technology for large-scale mechanical energy harvesting. It requires interaction between a hard magnet and conductive coils, which has a bulky structure since the output power heavily depends on such factors as the number of coils turns, the diameter of metal coils, and coil geometry. The shrinkage in size results in substantial deterioration in output power due to insufficient electromagnetic coupling and other parasitic effects. Therefore, it normally needs a relatively large size and weight for delivering a decent output power [59, 60]. However, mechanical energy is usually associated with factors such as human body motions, engine/machine running, water waves, acoustic waves, and so on. With little adaptability on structural design and high manufacturing cost is also a concern in developing a wide range of applications using the electromagnetic generators (EMG).

Traditional electrostatic generators require “pre-charging” of electric plates, while recent electrostatic generators based on electrets suffer decay of implanted surface charge [61]. For energy harvesting, electrostatic generators need external DC voltage to maintain the static charge, which is not convenient for mechanical energy harvesting. Similar to an electromagnetic effect-based generator, the electrostatic generator still suffers from its poor adaptability on structural design, low power output when miniaturized, and high manufacturing cost for sophisticated structure.

In the triboelectric nanogenerators, the device converts the external mechanical energy into electricity by a combination of **contact electrification** (triboelectric effect) found everywhere in nature, especially for the earth-abundant and commonly used polymer materials which are coupling with **electrostatic induction.** The triboelectric effect is the phenomenon that material becomes electrically charged after it contacts a different material through friction and has been known for thousands of years. Therefore, TENG are based on contact electrification between two materials and charge transfer between their electrodes due to electrostatic induction [14-17] and they typically utilize a polymer-metal pair as the friction layers [62, 63]. The periodic contact separation or back and forth sliding replenishes the surface triboelectric charges during each

physical contact, which contributes to the long-term stable electrical output of TENG. Since the most fundamental device based on electrostatics is a capacitor, fundamentally TENG will have inherent capacitive behaviour [64].

Though the aforementioned electromagnetic generators, they have a crucial limitation for ocean wave energy conversion. Indeed, the output voltage of EMG can be impractically low at the low frequencies of ocean waves. In contrast, TENG are highly suitable for ocean wave energy harvesting as they can effectively harvest mechanical energies with a wide range of amplitude and from low frequencies (<1 Hz) to relatively high frequencies (~kHz). Additionally, to practically power electronics such as wireless sensors, energy harvesters are usually implemented in places with the harsh environment and extreme conditions, such as high humidity, contamination, and even around corrosive chemicals. Therefore, easy packaging and sealing are significantly important for real applications. The unique operating principle of TENG enables easy packaging of the device compared with other technologies. To obtain above 90% total charge transfer rate, it only needs a tiny gap distance that is 10-times the thickness of the dielectric layer to physically separate the charged triboelectric surfaces [65, 66]. The development of TENGs opens new possibilities for materials scientists, chemists and engineers to use nanogenerators to convert mechanical energy at high efficiency, offering an innovative and alternative approach of technology for energy harvesting.

In brief, the TENG holds wider adaptability on structural design and are also low-cost, lightweight, and easy to fabricate and offer an abundant choice of materials [18, 67], which help the TENG to overcome the challenges of traditional approaches, with superior total energy conversion efficiency up to 85% [68]. TENG can be adapted well to various mechanical energy types or are suitable for different applications by different modes of operations such as vertical contact-separation mode, lateral sliding mode, single-electrode mode and freestanding triboelectric-layer mode (Figure 2.3) [17, 69]. Remarkably, TENGs can harvest energy over a broad frequency range, including vibration, human walking, body motions and ocean waves [70]. Additionally, TENGs can be integrated with other energy-harvesting forms, such as piezoelectric effect, electromagnetic effect, and biochemical energy, to form hybrid TENGs, which can be utilized to harvest multiple kinds of energy simultaneously [68, 71, 72].

Table 2.1 A comparison of advantages and possible practical limitations about the harvesting of mechanical energy using electromagnetic, electrostatic, piezoelectric and triboelectric effect [73].

Mechanical energy harvesting	Electromagnetic	Electrostatic	Piezoelectric	Triboelectric
Harvesting principle	Electromagnetic induction	Electrostatic induction	Piezoelectric effect and Electrostatic induction	Contact electrification and Electrostatic induction
Impedance type	Resistive	Capacitive	Capacitive	Capacitive
Pros	High efficiency, easy to scale up	Light weight	Easy to scale down to nanoscale	High output power, high efficiency, low weight, cost effective materials, simple fabrication
Cons	Heavy magnet required, low output for small-scale devices	Precharge required, low output, high matched impedance	Low output and low efficiency, pulse output, high matched impedance	Pulsed output, high matched impedance

The four basic modes of TENG are described as follows. To begin with **vertical contact-separation mode** (Figure 2.3 (a)), two dissimilar dielectric films face with each other, and there are electrodes deposited on the top and the bottom surfaces of the stacked structure. Physical contact between the two dielectric films creates oppositely charged surfaces. Once the two surfaces are separated by small gap under the lifting of an external force, a potential drop is created, if the two electrodes are connected with a load, free electrons in one electrode would flow to the other electrode to build an opposite potential in order to balance the electrostatic field. Once the gap is closed, the triboelectric charge created potential disappears, the electrons flow back.

Lateral sliding mode (Figure 2.3 (b)), when two dielectric films are in contact, a relative sliding in parallel to the surface also creates triboelectric charges on the two surfaces [74, 75]. A lateral polarization is thus introduced along the sliding direction, which drives the electrons on the top and bottom electrodes to flow in order to fully balance the field created by the triboelectric charges. The sliding can be planar motion, a cylindrical rotation, or disc rotation. In some cases, the object that is part of the TENG cannot be electrically connected to the load because it is a mobile object, such as human walking on a floor. In order to harvest energy from that case, a **single electrode mode** TENG (Figure 2.3 (c)) is functional, in which the electrode on the bottom part of the TENG is grounded. If the size of the TENG is finite, the approaching or departing of the top object from the

bottom one would change the local electrical field distribution, so that there are electron exchanges between the bottom electrode and the ground to maintain the potential change of the electrode.

In nature, a moving object is naturally charged due to its contact with air or other objects, such as our shoes walking on floors that are usually charged. The charges remain on the surface for hours and the contact or friction is unnecessary within this period of time because the charge density reaches a maximum. A pair of symmetric electrodes underneath a dielectric layer and the size of the electrodes and the gap distance between the two are on the same order as the size of the moving object, the object's approaching or departing from the electrodes create an asymmetric charge distribution in the media, which causes the electrons to flow between the two electrodes to balance the local potential distribution [76] (**Freestanding triboelectric layer mode** (Figure 2.3 (d)). The oscillation of the electrons between the pair electrodes produces power. The moving object does not have to directly touch the top dielectric layer of the electrodes, so that, in rotation mode, a free rotation is possible without direct mechanical contact, so that the wearing of the surfaces can be drastically reduced.

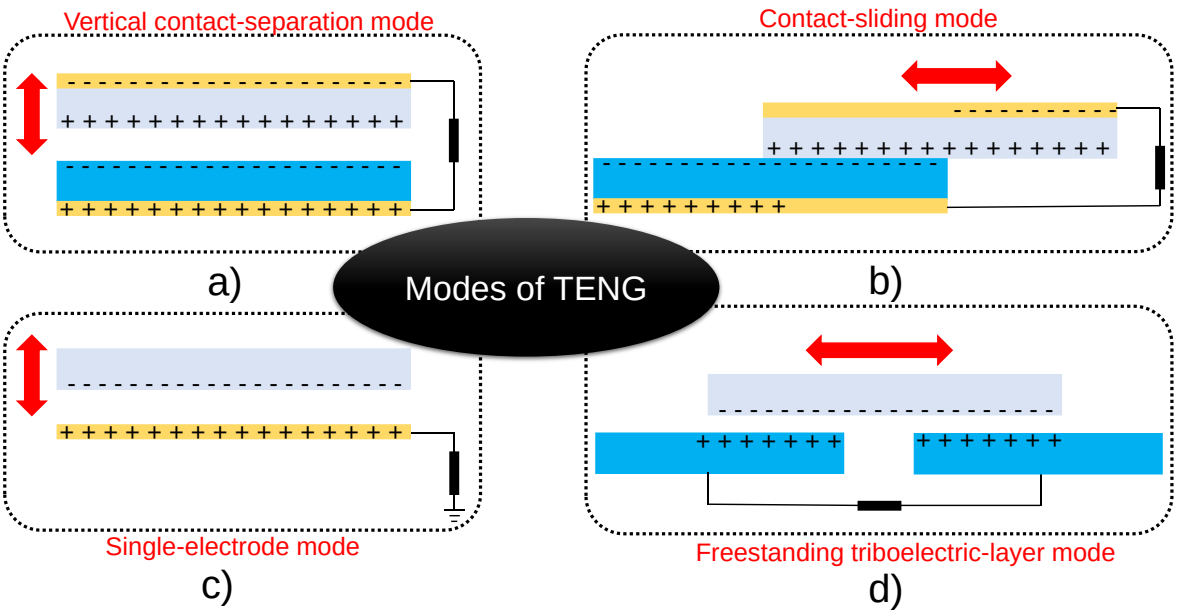

Figure 2.3 The four fundamental modes of triboelectric nanogenerators: (a) vertical contact-separation mode, (b) in plane contact-sliding mode, (c) single-electrode mode, and (d) freestanding triboelectric-layer mode [69, 77].

2.5 Materials for triboelectrification

Almost all materials exhibit the triboelectrification effect, from metals to polymers, to silk and to wood, almost everything. All of these materials can be candidates for fabricating TENG so that the material choices for TENG are huge. When two materials with different electron affinity are brought

into contact with one another, charges transfer at the interface. The triboelectric charge density is largely determined by the electron affinity difference (triboelectric series) between two contact materials [78-81]. Under identical environmental conditions and the nature of the contact, choosing two materials with closer electron affinity, the relative ability to acquire/lose charges is very close. Then, it is very hard for charge transfer, and thus, the amount of generated charges is small. In contrast, when the electron affinity difference of triboelectric pairs is very large, the relative ability to acquire/lose electrons is very large. In other words, one material is easy to acquire electrons (electronegative), while the other is easy to lose electrons (electropositive). Then, it is very easy for charge transfer at the interface, and the amount of generated charges are very big. Therefore, the larger the relative difference of triboelectric pairs in the triboelectric series, the better the output performance of TENG. Table 2.2 is a triboelectric table, which was tested by Bill Lee (© 2009 by AlphaLab, Inc). This table lists the common insulator materials based on their tendency to gain electrons or lose electrons [82, 83].

Table 2.2 Triboelectric series for insulators materials arranged by charge affinity based on their tendency to lose electrons (electropositive) or gain electrons (electronegative).

Insulator Name	Charge Affinity (nC/J)		Insulator Name	Charge Affinity (nC/J)
Polyurethane foam	+60		Sorbothane	+58
Hair, oily skin	+45		solid polyurethane	+40
Magnesium fluoride	+35		nylon, dry skin	+30
Machine oil	+29		Nylatron	+28
Glass (soda)	+25		paper	+10
Wood (pine)	+7		cotton	+5
Nitrile rubber	+3		wool	0
Polycarbonate	−5		acrylic	−10
Epoxy	−32		styrene-butadiene rubber	−35
PET (mylar) solid	−40		EVA rubber	−55
Gum rubber	−60		polystyrene	−70
Polyimide	−70		silicones	−72
Vinyl: flexible	−75		LDPE	−90
Polypropylene	−90		HDPE	−90
Cellulose nitrate	−93		UHMWPE	−95
Polychloroprene	−98		PVC (rigid vinyl)	−100
Latex (natural) rubber	−105		Viton, filled	−117
Epichlorohydrin rubber	−118		Santoprene rubber	−120
Hypalon rubber, filled	−130		butyl rubber, filled	−135
EDPM rubber, filled	−140		PTFE (Teflon)	−190

Additionally, researchers have already tried many materials to enhance the output performance of TENG. Table 2.3 lists the common conductive and insulators materials according to the ability of acquire/lose electrons during the triboelectric effect [84, 85].

Table 2.3 Triboelectric series for some common materials arranged by the relative ease of losing (positive) or gaining (negative) electrons) [86].

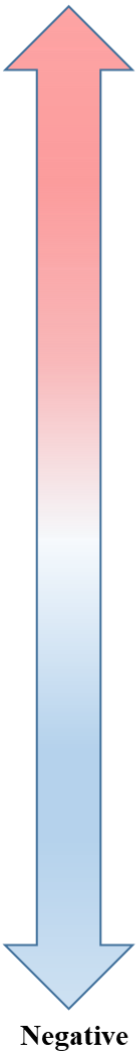

Polyformaldehyde 1.3 - 1.4
Etylcellulose
Polyamide 11
Polyamide 6 - 6
Melanine formol
Wool, knitted
Silk, woven
Aluminum
Paper
Cotton
Steel
Wood
Hard rubber
Copper
Sulfur
Silver
Acetate
Polymethyl methacrylate (Lucite)
Polyvivyl alcohol
Polyester (Dracon)
Polyisobutylene
Polyuretane flexible sponge
Polyethylene Terephthalate
Polyvinyl butyral
Polychlorobutadiene
Natural rubber
Polyacrilonitrile
Acrylonitrile-vinyl chloride
Polystyrene
Polyethylene
Polypropylene
Polyimide (Kapton)
Polyvinyl Chloride (PVC)
Polydimethylsiloxane (PDMS)
Polytetrafluoroethylene (Teflon)

Although the triboelectric series is somewhat useful for material selection, it is a qualitative indication on the capability of a material to gain or lose an electron, but it lacks a quantitative standard of calibration. The choice of material combinations, surface structuring, and surface functionalization need to be further studied.

By introducing nanomaterials and possibly nanocomposites, it is possible to tailor the mechanical, dielectric and surface properties of materials to achieve better power output. Besides the choice of the materials in the triboelectric series, the morphologies of the surfaces can be modified by physical techniques with the creation of pyramids-square or hemisphere based micro or nano-patterns, which are effective for enhancing the contact area and possibly the triboelectrification.

The surfaces of the materials can be functionalized chemically using various molecules, nanotubes, nanowires or nanoparticles, in order to enhance the triboelectrification effect [86].

2.6 State of the art of TENG for ocean wave energy harvesting

Different triboelectric nanogenerators have been developed aiming at harvesting the irregular motions at low frequencies generated by the shallow ocean wave energy between 0.5 Hz to 10 Hz, based on contact electrification of solid-solid [19-27] and liquid-solid interfaces [29-38], and by combining of TENG-EMG [39, 40]. Firstly, utilizing TENG with solid-solid triboelectrification in environmental conditions as humidity working in interaction with water can have a negative effect on their output performance. Due to that reason such devices must be fully enclosed to work under harsh conditions. Xiaonan Wen fabricated a sliding contact electrification mode TENG comprising a wavy structure [24] (Figure 2.4 (a)) for water wave energy harvesting using copper, Kapton and PTFE triboelectric materials. Such wavy-electrode structure TENG sealed into a rubber pocket (Figure 2.4 (b)) could reach peak output current, voltage, power and power density of approximately 6 μA, 24 V and 0.144 mW and 0.4 W/m^2 respectively, at artificial wave conditions with a wave speed of 1.2 m/s^2 with a wave height of 0.2 m [24].

Furthermore, X. Wang reported a rolling-spherical freestanding TENG (RF-TENG) [25] that was fabricated using a full-enclosed spherical shell and triboelectric materials like Kapton attached to Al electrodes in contact with a nylon ball (Figure 2.4 (c)). Such a device working at water wave movement at low frequencies of approximately 1.43 Hz generated instantaneous output current and power of 1 μA and 10 mW, respectively. Which was able to power up tens of LEDs and charge a set of supercapacitors (Figure 2.4 (d) [25]. Additionally, J. Chen proposed the integration of contact-separation mode arch-shaped TENGs (Figure 2.4 (e)) and metal ball into a box-structure for the harvesting of ocean waves at large-scale with a network of TENGs (Figure 2.4 (f)) [26]. Such energy harvesters are fabricated using contact electrification between metal (aluminium)-dielectric (polyethylene terephthalate (PTFE)) with copper as back electrodes. The metallic balls collide with the arc-shaped TENGs, due to the water wave mechanical energy to produce output power. A network of four arc-shaped TENGs was demonstrated to produce approximately open-circuit voltage, short-circuit current and peak power of 200 V, 320 μA and 60 mW, respectively at water wave conditions of 2 Hz. It is estimated that over an area of 1km^2 of the water's surface, the network of TENGs can potentially produce an average power output of 1.15 MW [26]. Moreover, a torus structured TENG (TS-TENG) array was reported by W. Liu (Figure 2.4 (g) and figure 2.4 (h)) that consist in a shell and an inner ball using dielectric-dielectric contact electrification to scavenge large-scale water wave energy, with an ocean wave agitation of 2 Hz it is expected to generate a

maximum peak power density of 0.21 W/m^2 [27]. Such a device was presented as a power source to powering electronic devices and charging capacitors.

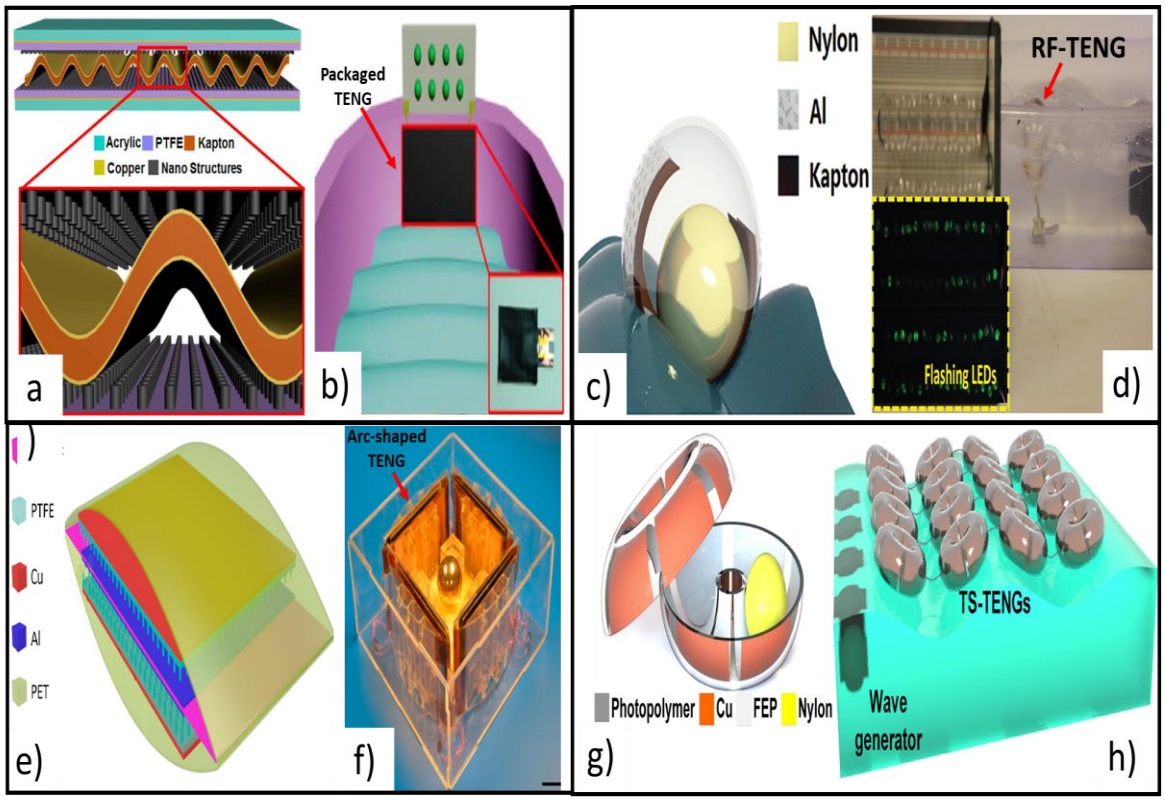

Figure 2.4 TENG with solid-solid triboelectric interfaces for ocean wave energy harvesting. (a) Schematic of the TENG based on a wavy-structured layer. (b) Set-up for the packaged TENG to harvest water wave energy and turn on LEDs. Adapted with permission from [24]. Copyright 2014 American Chemical Society. (c) Schematic diagram of RF-TENG and (d) digital image of the device operating in a water wave system. Adapted with permission from Wiley [25]. (e) Schematic of single unit of Arc-shaped TENG and (f) network of four devices (12cm x 12cm x 6cm). Adapted with permission from [26]. Copyright 2015 American Chemical Society. (g) Schematic diagram of the TS-TENG and (h) TS-TENG array for water wave energy harvesting. Reproduced with permission from Elsevier [27].

Secondly, G. Zhu proposed a liquid-solid electrification-enabled generator (LSEG) for harvesting shallow water wave energy [37] as illustrated in Figure 2.5 (a) that was fabricated using a nanotextured fluorinated ethylene propylene (FEP) friction layer attached to copper electrodes at its back (Figure 2.5 (b)). The nanotextured hydrophobic FEP layer engages and increases the contact area when the contact electrification with the water waves occurs. The LSEG with a size of 6cm x 3cm is able to produce an average output power and power density of 0.12mW and 0.066 W/m^2 at the wave velocity of 0.5 m/s [37] (Figure 2.5 (c)). To scale up, multiple LSEGs can be interconnected to form a network for harvesting energy from water waves on a large scale. Furthermore, X. Yang

presented a contact-separation mode water tank triboelectric nanogenerator fabricated of polytetrafluoroethylene (PTFE) layer attached to a copper electrode for harvesting water wave energy as illustrated in Figure 2.5 (d) and Figure 2.5 (e) at low frequencies from 0.1 Hz to 10 Hz [32]. Such a device generated a maximum power density of 9.62 W/m^2 with an energy conversion efficiency of 63.2 % with a rhombic patterned surface-modified PTFE at contact frequency of 0.1 Hz [32].

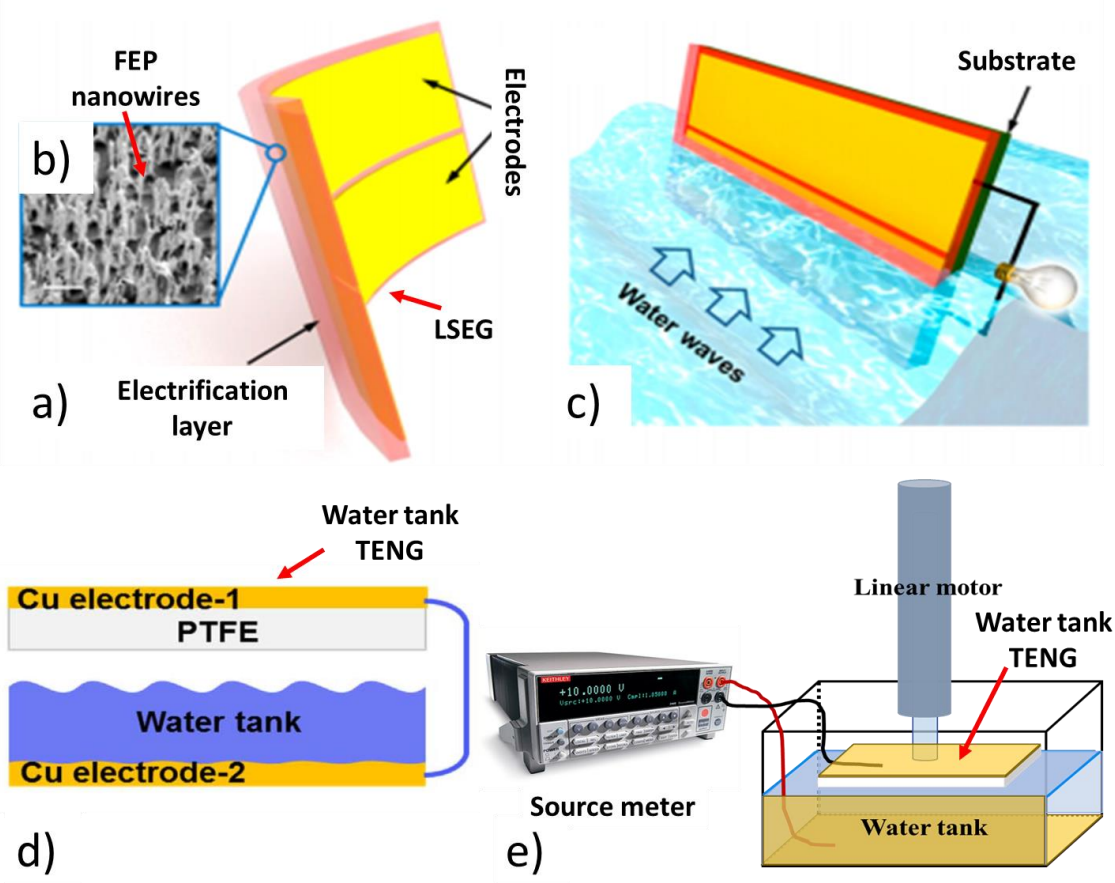

Figure 2.5 TENG with liquid-solid triboelectric interfaces for water wave energy harvesting. (a) Schematic description of LSEG with the electrification layer with two electrodes on the back. (b) Scanning electron microscopy image of the polymer nanowires on the electrification layer. (c) Schematic description of a substrate supported LSEG in water waves. Adapted with permission from [37]. Copyright 2014 American Chemical Society. (d) Schematic diagram and (e) set-up of the water tank triboelectric nanogenerator. Reproduced with permission from Elsevier [32].

Thirdly, by coupling TENG-EMG, effects for harvesting ocean wave energy have been studied. Y. Wu proposed a teeterboard-like hybrid nanogenerator (THNG), composed of two systems an EMG at one end and a multi-layered TENG at the other end (Figure 2.6 (a)) [39]. The motion amplitude of EMG system can be adjusted that helps to move it with a reasonable amplitude generating an electrical output, which overcomes the problem of low efficiency of EMG working at low

frequencies. This THNG device generates a maximum output voltage, current and power density of 760 V and 10 mA and 55 mW/m^2 respectively harvesting ocean waves at low-frequencies from 0.17 Hz to 1.25 Hz. Such a device is able to light up 200 LEDs and drives a rain-drop sensor (Figure 2.6 (b)) [39]. Further, combining the aforementioned effects, with a TENG working in sliding and contact-separation modes a honeycomb-like three-electrode nanogenerator (How-NG) has been studied by L. Feng (Figure 2.6 (c)) [40] for harvesting shallow water wave energy. The maximum output power and energy of the How-NG assembled into a sealed acrylic cylinder reached 8.23 µW and 21.7 µJ respectively under water wave frequency of 4 Hz and sliding displacement of 3.5 cm. Such a device is able to turn-on 108 LEDs and can be integrated with networks (Figure 2.6 (d) and Figure 2.6 (e)) to harvest large-scale shallow ocean wave energy [40].

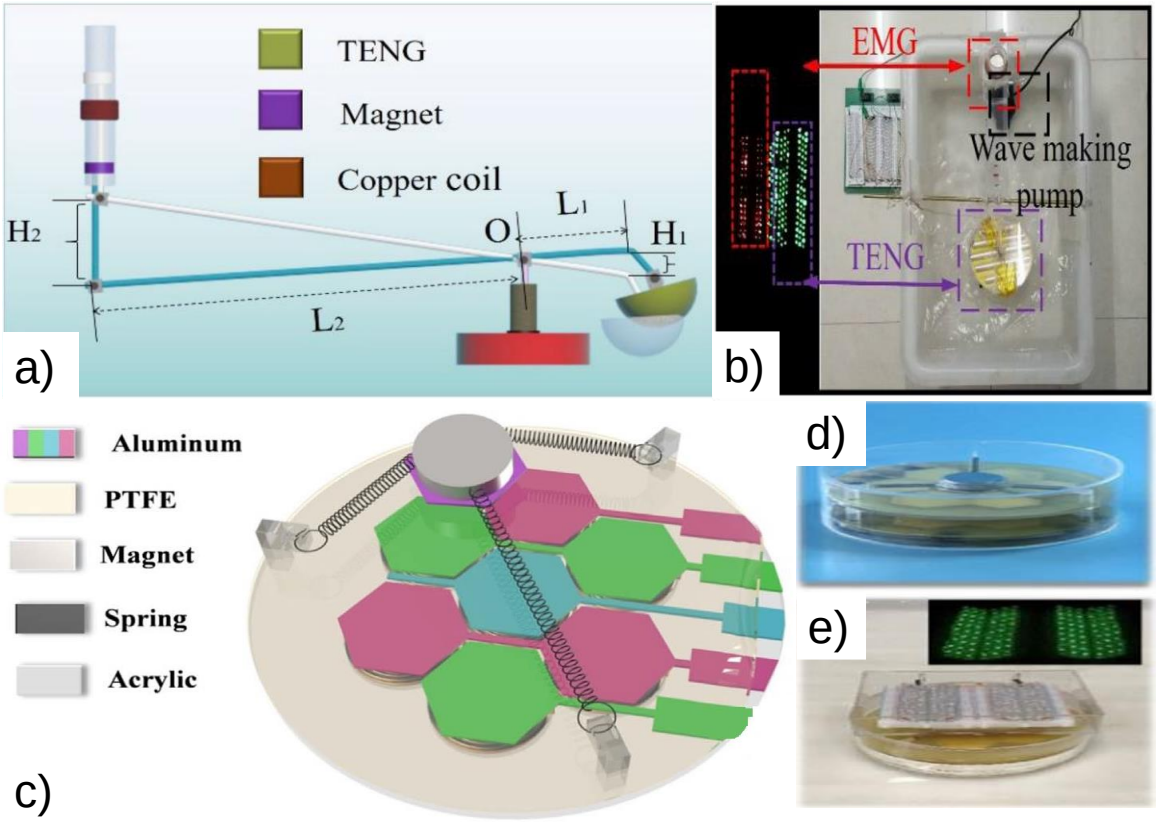

Figure 2.6 Coupling between TENG-EMG to form a hybrid device. (a) Schematic diagram of THNG in motion in real ocean environment and (b) digital photo of THNG acting as power source to turn on LEDs. Reproduced with permission from Elsevier [39]. (c) Structural design of How-NG, (d) digital image of How-NG integrated with two units and (e) turning on 108 LEDs by water wave energy harvesting. Reproduced with permission from Elsevier [40].

2.7 State of the art of piezoelectric generators for ocean wave energy harvesting

Piezoelectric generators consist of a piezoelectric element coupled to a mechanical structure. The model generator is shown in Figure 2.7 (a) can be excited by the forces generated by passing waves when installed in the ocean. The oscillations of the mass induce strains in the piezoelectric element, which lead to the generation of an electric voltage that can be extracted through electrical equipment connected to the electrodes [87]. PZT and PVDF are the two most commonly used materials in ocean-energy extraction devices. PZT, called lead zirconate titanate [88] is a poled ferroelectric ceramic that has a perovskite structure. PVDF is a polarised electroactive polymer with the name polyvinylidene fluoride and has an approximately 10 times larger piezoelectric stress constants (g_{33} = ~340 mV·m/N) than most other polymers [89, 90]. The classification of ocean energy harvesting methods employing piezoelectric effect applying different parameters is summarized as follows [91]:

Flow induced vibrations can be harvested via vortex-induced vibrations when a piezoelectric membrane is placed behind a bluff body, it will interact with the shed vortices and will start oscillating. This will create bending stresses in the piezoelectric material, which lead to voltage generation. Another way is through self-excited vibrations (SEV) where flexible bodies placed in a uniform steady flow attain self-excited vibrations when the relative speed of the flow exceeds a certain critical speed value for a given body characteristic length. SEV also occur if the characteristic length of the body is greater than a critical length for a given flow speed. If piezoelectric patches are installed in such conditions (known as fluttering conditions), they can be utilized for energy harvesting applications [92]. An example of this kind of ocean energy piezoelectric harvester is shown in Figure 2.7 (b).

Wave motion can be harvested by three methods, of which **heaving and pitching bodies** constitute one of the most common and promising techniques in wave energy extraction. Murray and Rastegar [93] proposed a two-stage energy harvesting process, introduced by Rastegar et al. [94] for a heaving buoy. The energy available in the low-frequency buoy motion is transformed into potential energy in the first stage and then transferred to another system with much higher natural frequency in the second stage as shown in Figure 2.7 (c). The second method of energy harvesting from wave motion consists of **bodies fixed to the ocean bottom**. Piezoelectric polymer PVDF is used in a design based on a cantilever beam mounted on the shallow seabed. The simulated RMS of the generated electric power by the device can be on the order of mW or W depending on the mechanical system and the surrounded conditions [95, 96] (Figure 2.7 (d)).

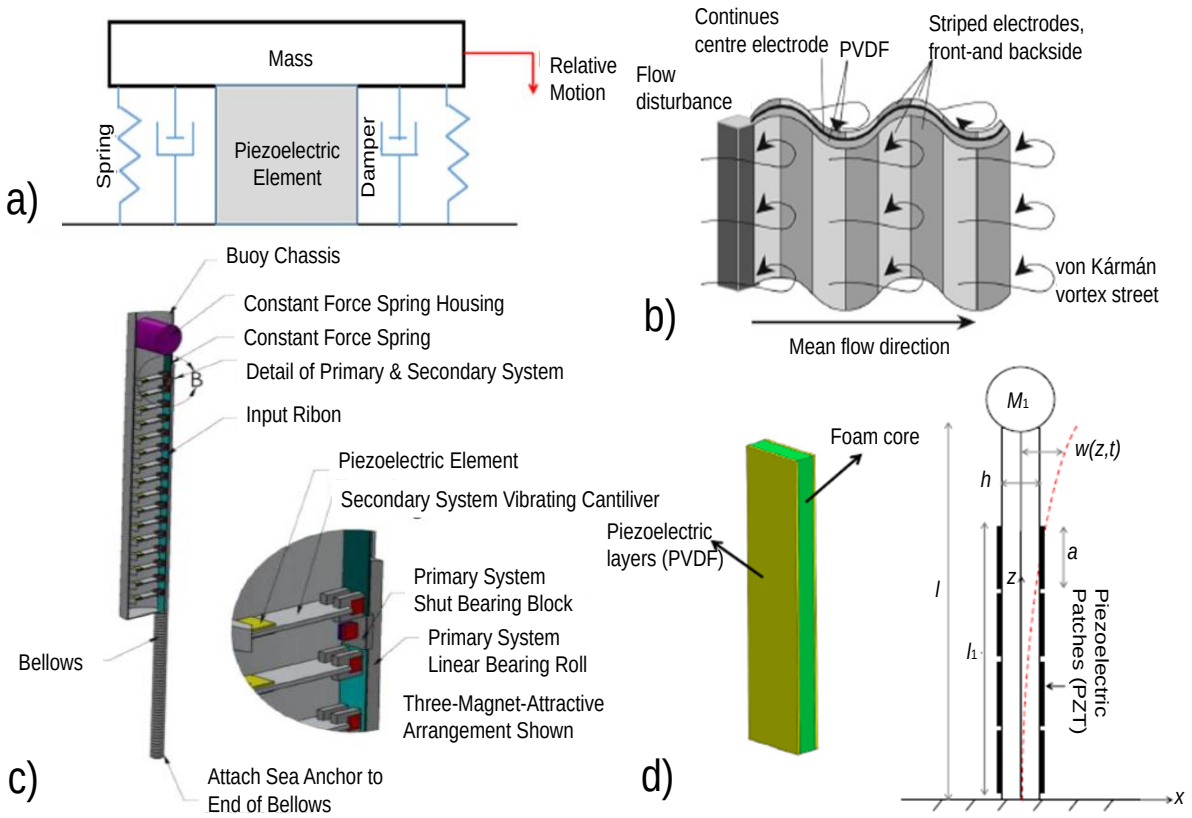

Figure 2.7 (a) Modelling of a piezoelectric power generator [87], (b) Piezoelectric flag. Reproduced with permission from IEEE [97], (c) Heaving based harvester [93] and (d) Design of piezoelectric beam bodies fixed for the ocean bottom. Reproduced with permission from Elsevier [95, 96].

The third method employs **flexible membranes on the ocean surface or placed in shallow water**, in a piezoelectric energy harvesting device based on flow-induced vibrations. A flow source is connected to a flow channel with a flexible diaphragm on top. The flow source generates an oscillating liquid pressure in the channel, which drives the diaphragm to oscillate. If a piezoe lectric film is attached to the diaphragm, the strain will cause the electrical charge to accumulate on the electrodes, with a resulting voltage difference across the sheet [98] (Figure 2.8 (a)).

Wave impact energy harvested utilizing the sloshing of waves on tank walls and ocean structures has been a subject of study for many years. Piezoelectric sheets can be fixed on the walls of large fluid tanks in motion or on offshore structures such as oil platforms. Athanassoulis and Mamis [99] studied a piezoelectric sheet's ability to extract electrical energy directly from the impingement of incident waves on vertical cliffs (Figure 2.8 (b)). The two main advantages offered by such piezoelectric harvesters are the extraction of useful energy and the damping of internal sloshing loads.

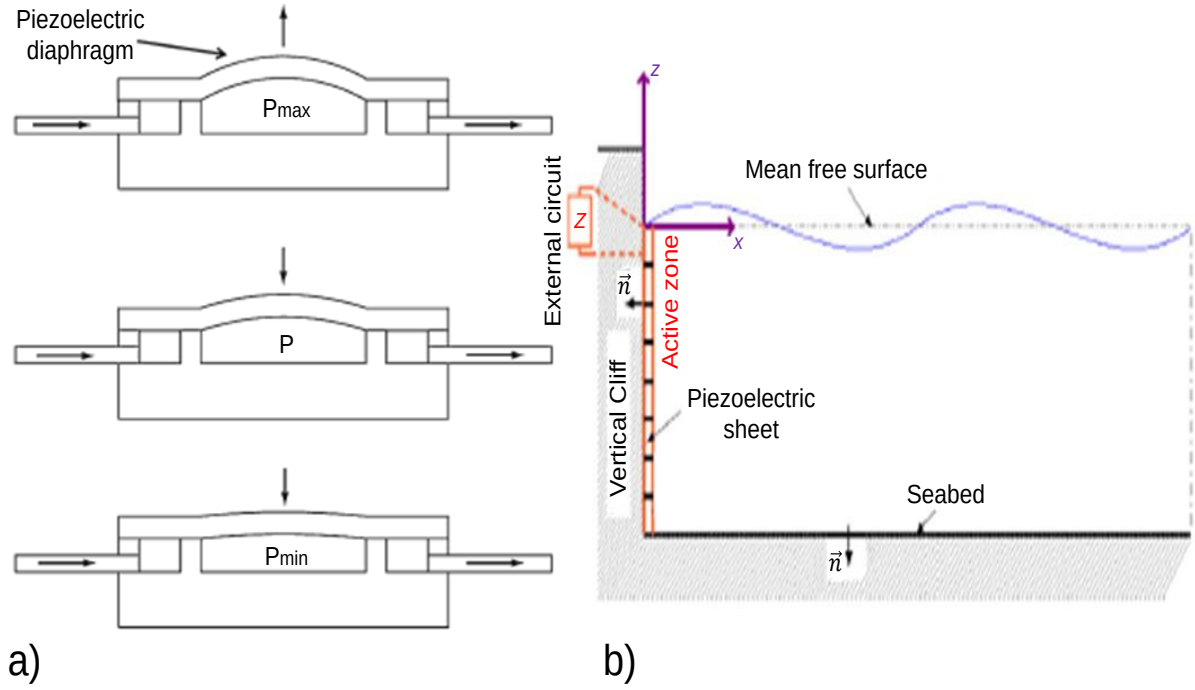

Figure 2.8 (a) The piezoelectric flexible membrane in operation. Adapted with permission from IOP science [98] and (b) hydrodynamic piezoelectric system [99].

Optimization for piezoelectric-based harvesting comprises of a coupled system of three elements. The first element is the dynamic response of the harvesting structure, which is a mature field. The second element is the electrical circuit that is necessary to condition the voltage and charge that is generated, this is an area where there has been active development [100-103]. The final element is the coupled electro-mechanics of the system, which represents the key step in energy harvesting and poses a challenging multi-physics problem to the optimization community. The most common configurations studies are cantilevered beam and plates. Researchers consistently agree that consideration of the electromechanical coupling of the harvester is important [87], elastic stiffness, piezoelectric and dielectric parameters [104].

2.8 Technical barriers for ocean wave energy harvesters

The develop ocean wave energy harvesters, three main technical barriers must be overcome. First, robustness and long-term survivability are paramount and historically, many ocean wave technologies have failed due to over-complex designs, which were vulnerable to saltwater corrosion and mechanical failures. To solve this problem, a simple design is required that is statically sealed.

The second barrier to address is the requirement for a compact size that most ocean wave energy harvesting devices do not meet as they are intended for large-scale power generation. These designs are too large for the requirements of the ocean sensing systems. To solve this problem, a

design that is compact and easily deployable either as a stand-alone unit or as an add-on unit to an existing system is required.

The final barrier is the need for an efficient energy coupling that conventional ocean energy harvesting technologies have adequately addressed this problem by using direct coupling mechanisms. Which allows transmitting the whole power generated in the energy harvesting materials caused by external mechanical forces, because now there is no energy loss in the motion of the device (for example, frictional contact and friction force does not limit the output performance of the device). However, they were accomplished either by using an open system or through dynamic motion seals, and both approaches have lifetime issues in the sea. To solve this problem, the challenge is to design a system that is statically sealed but capable of efficient energy coupling in a broad range of wave conditions.

2.9 Applications for ocean wave energy harvesters

Energy generated from waves is most often used in desalination plants, power plants and water pumps. Energy output is determined by wave height, wave speed, wavelength, and water density. To date, there are only a handful of experimental wave generator plants in operation around the world. Possible applications are described below:

- **Defence and security** to enable ocean security cordons for surface and subsurface vessel tracking, increase mission range and endurance for Unmanned Underwater Vehicles (UUV) by recharging batteries and data transfer, and on-station sensing to detect and track submarines to achieve and maintain undersea dominance.
- **Oil & Gas** to environmental monitoring for engineering and development, monitoring and control of low power equipment both subsea and topside, real-time data analysis of installed machinery/equipment performance, and for innovative inspection, fault diagnosis solutions and structural monitoring.
- **Ocean observing** to enable the integration of larger payloads encompassing more implantable sensors, enable denser real-time data to be collected, process and transmit to any shore station of interest and to reduce operational and life-cycle cost.
- **Aquaculture solutions** for the development of environmentally friendly alternatives to the use of diesel power due to significant power demands of modern offshore fish-farming, feed systems, underwater cameras, sensors and lights, all have power requirements currently met by diesel generators.
- **Utility power** for the development of wave power system to meet the needs of domestic energy supply due to offshore wave power, which can meet up to 5% of global electricity demand.

- **Remote maritime communities** for sustainable power supply as a key issue for remote communities, which typically rely on expensive and harmful diesel generator sets.
- **Breakwater systems** through new breakwater projects to integrate an element of renewable energy generation. (Breakwaters provide an ideal host structure for wave power generation)
- **Active moorings** for developing systems, which significantly reduces peak loads whilst providing controlled motion response and energy recovery options caused by peak mooring loads, which decrease structural and anchoring cost for offshore installations.

2.10 Comparison of triboelectric and piezoelectric ocean wave energy harvesting techniques and their potential for self-powered systems

Table 2.4 Comparison of triboelectric, piezoelectric, electromagnetic and hybrid ocean wave energy harvesting techniques, power density, applications, challenges and recommendations.

Ocean wave energy	Harvesting method	Power order	Power density	Applications	Challenges	Recommendations
Flow induced vibrations	Vortex induced vibrations and Self excited vibrations (Piezoelectric) [92, 97]	mW to W	15 W/m^2	Powering of moving underwater electronic devices such as UUV's and robots	Low hydrodynamic efficiency	Passive control system and use of multiple devices
Wave motion	Heaving and pitching bodies (Piezoelectric) [93, 94]	mW	5 W/m^2	Powering of buoys, powering of sensors used for ocean surveillance, salinity measurements, etc.	Large gap between low wave frequency and high natural frequency of PZT	Transformation of low-frequency vibrations through two stage systems, use of field forces rather than impact forces in two stage systems
	Bodies fixed to ocean bottom (Piezoelectric) [95, 96]	mW to W	13 W/m^2	Electricity collection and transmission to nearby offshore platforms, seismic activity monitoring	Mechanical design and material selection	Compromise between electromechanical coupling and required flexibility and strength
	Flexible membranes on ocean surface (Piezoelectric) [98]	µW to mW	200 W/m^2	Wave dampers around wind turbines and offshore structures, power transmission to nearby ocean structures and floating harbours	Very large devices needed (order of km^2), accommodation of waves with multiple frequencies and directions	Use of multiple piezoelectric elements, external extraction circuits designed effectively to avoid cancelation effects in the general voltage

Wave impact	Sloshing on flexible sheets (Piezoelectric) [99]	µW	Not available	Power transmission to ocean structures, wave load dampers on bodies such as cliffs, offshore structures and ships	Required flexibility not present in currently available piezoelectric materials, low efficiency	Fabrication of new piezoelectric materials with higher degree of flexibility
	Overtopping breakwater, Oscillating water column and piston-type (EMG) [47-52]	kW	6.37 kW/m^2	Integration in breakwater structures and coast protection for large scale applications	Find a suitable breakwater location, low wave reflection effect and structural strength and economic viability	New integration concepts of wave energy and breakwater structure needs to be developed
Shallow wave mechanical kinetic motion	Triboelectric effect (Single unit) [19-27, 29-40]	mW	9.62 W/m^2	Power transmission for commercial applications, ocean structures, offshore structures and ships	Short circuit electrodes due ocean waves, harsh marine environment, large scales, maximum power transfer, ocean waves irregularly (power output will be irregular)	Packaged, anticorrosive, resistant to heat and radiation and chemical inert packaging materials, improvement of the structural design, Network of TENGs required, Power management module, Power from PMM stored in the form of batteries
	Triboelectric effect (Network) [19-21, 26-29]	mW to MW	1.15 W/m^2			
	Hybrid coupling triboelectric and electromagnetic effects [39, 40]	µW to mW	0.055 W/m^2			

2.11 Chapter summary

In summary, the literature review of the potential for ocean wave energy harvesting, the comparison of the triboelectric nanogenerators with robust breaking water wave energy harvesting devices integrated with breakwater structures that utilize electromagnetic generators for large-scale applications and against other mechanical energy harvesting techniques for small scale applications was described in this chapter. Furthermore, the current state of the art in the development, and detailed background of the proposed technology of triboelectric nanogenerators which has been mainly focused on harvesting the random motions of the shallow ocean water waves energy but that has a great potential to harvest the mechanical energies generated by breaking ocean water wave impacts and the oscillatory compressed air bubbles flows at the structural water-interfaces, was discussed in this chapter. Additionally, an explanation of materials for triboelectrification, state of the art of piezoelectric generators for ocean energy harvesting, technical barriers, potential applications and comparison for ocean wave energy harvesters (triboelectric vs piezoelectric, electromagnetic and hybrid generators), was mentioned.

Chapter 3 Modelling and numerical simulation of breaking water wave impact energy harvesting generators

3.1 Introduction

In order to obtain a more quantitative understanding of the working mechanism and to analyze the output performance of the triboelectric nanogenerators for mechanical energy harvesting. Focused on harvesting the breaking water wave energy, numerical studies based on the finite element method (FEM) are helpful. COMSOL Multiphysics software package provides a set of physics interfaces for different areas of application such as structural analysis, electrostatics, electromechanics, electrical circuit, and so on. From a methodology point of view, FEM simulations are complementary to experiments in the whole device design process, shortening the design cycle and reducing overall cost.

The procedure for simulation using COMSOL can be divided into seven steps:

1. Set up the model environment.
2. Built geometry, coordinates systems and create definitions (using parameters, variables and so on).
3. Set the subdomain material properties to the model geometry.
4. Define physics (parameters) by setting all the physical boundary conditions and constraints. This is a key step in the simulation process, where appropriate boundary conditions must be specified using self-consistent analytical methods.
5. Create mesh and check that the mesh is good for the problem being solved.
6. Solve the equations numerically using FEM solver running studies specific to different types of physics and analysis.
7. Postprocess the results by creating plots.

The modelling and numerical simulation of triboelectric nanogenerators in the configuration of dielectric-metal contact-separation mode (DMCS-TENG) and hybrid nanogenerators coupling triboelectric-piezoelectric effects in terms of the estimated range of oscillating frequencies generated by the breaking water wave impact cumulative forces (Figure 1.1 (a-d) and Figure 1.2) is reported in this chapter.

Firstly, it was developed a FEM for a DMCS-TENG, to understand its electromechanical characteristics. Secondly, a FEM was developed for the hybrid devices, to understand the coupling

between piezoelectric-triboelectric effects, study the load resistance matching and parameter optimization in order to find higher electric output performance.

3.2 FEM modelling and simulation of triboelectric nanogenerators for breaking water wave impact energy harvesting

Practical applications require huge improvement of the output performance of TENG, and hence rational design and optimization of both materials and structures are important research topics. Although the performance of TENG is promising, this knowledge can help in choosing the appropriate TENG structure and materials, avoid designs which will harm the output performance, and choose suitable system-level topologies for integrated energy harvesting systems [66]. Furthermore, in this study, it is developing a FEM for the DMCS-TENG to understand its electromechanical characteristics.

3.2.1 Voltage-Charge-Distance *(V-Q-x)* relationship for triboelectric nanogenerators

Triboelectric nanogenerators are well known for their characteristic capacitive nature. Such devices are comprising with tribo-pairs that are two triboelectric materials facing each other and two insulated electrodes connected through an external circuit. When a mechanical force is applied to the TENG, both triboelectric materials move (x) contacting each other producing contact electrification transferring charges (σ) on their surfaces having opposite static charges. Further, transfer charges (Q) flow from one electrode ($-Q$) to the other electrode ($Q+$) balancing the electric potential generated between them, caused for the movement of the triboelectric-pairs.

The electric potential difference is generated by two factors. The contribution of the transferred charges $-Q/C(x)$ assuming that the TENG configuration is a capacitor, and triboelectric charges are not produced as the first factor where the capacitance between the two electrodes is C. Additionally, the generated voltage $V_{OC}(x)$ related with the displacement (x) due to the contribution of the polarized triboelectric charges as the second factor. Consequently, the total voltage difference between the pair of electrodes is [64]:

$$V = -\frac{1}{C(x)}Q + Voc(x) \tag{3.1}$$

The general equation of any TENG is the conjunction between *V-Q-x* (3.1) [64]. An electric potential difference is generated due to the triboelectric charges among the two electrodes, which flow electrons from one electrode to another through an external circuit, screening their electric

potential [65]. The transferred charges completely screen the produced electric potential from the opposite triboelectric charges if the TENG is at short-circuit conditions (SC) [105]:

$$0 = -\frac{1}{C(x)}Qsc(x) + Voc(x) \tag{3.2}$$

As follows, the fundamental dependence between Q_{SC}, C, and V_{OC} can be given by [105]:

$$Qsc(x) = C(x)Voc(x) \tag{3.3}$$

Furthermore, illustrating the combination of the two components on the right side of equation 3.1 as a first-order circuit model (Figure 3.1). First, a capacitor (C) is illustrated as being the capacitance term between the two electrodes. Second, an ideal voltage source (V_{OC}), represents the open-circuit voltage term produced for the polarized triboelectric-charges during the separation of the triboelectric layers. Such, a circuit model is represented as depicted in Figure 3.1 [106]. Moreover, due to the high intrinsic impedance of a TENG close to infinity due to the great insulation of the two electrodes. As a result, the resistance is not included in the first-order circuit model.

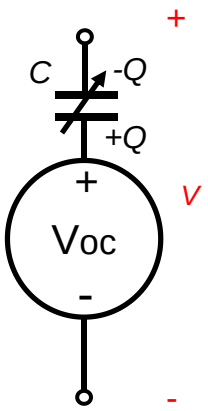

Figure 3.1 First order lumped-parameter equivalent circuit model of triboelectric nanogenerators.

The theoretical models with the *V-Q-x* conjunction for a contact-separation mode triboelectric nanogenerator comprising a parallel dielectric-dielectric and conductor-dielectric structures illustrated in Figure 3.2 (a) and Figure 3.2 (b) can be derived based on electrodynamics. Implementing Gauss theorem [107], the electric field strength E_1, E_2 and E_{air} at each area are given by equations 3.4, 3.5 and 3.6. Where d_{D1} and d_{D2} are the thickness of the dielectric layers, ε_{r1} and ε_{r2} are the relative dielectric constants, S is the area size of the electrodes that through the modelling are considered to be infinitely larger than the increase gap distance ($d_{D1} + d_{D2} + x$). As a result, the charges are evenly dispersed on the inner surfaces of the two electrodes. The electric

field has a positive value in direction to the electrode 2, in the inner area of the dielectric layers and the air gap (ε_0 permittivity of vacuum) [65, 66].

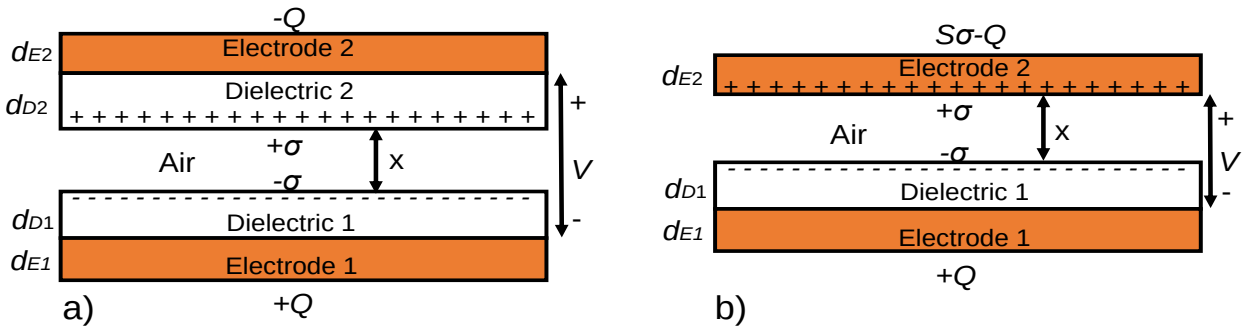

Figure 3.2 Theoretical models for (a) dielectric-to-dielectric contact separation mode TENG and (b) conductor-to-dielectric contact separation mode TENG.

Inside dielectric 1:

$$E_1 = -\frac{Q}{S\varepsilon_0\varepsilon_{r1}} \tag{3.4}$$

Inside the air gap:

$$E_{air} = \frac{-\frac{Q}{S} + \sigma(t)}{\varepsilon_0} \tag{3.5}$$

Inside dielectric 2:

$$E_2 = -\frac{Q}{S\varepsilon_0\varepsilon_{r2}} \tag{3.6}$$

The voltage between the two electrodes can be given by:

$$V = E_1 d_{D1} + E_2 d_{D2} + E_{air} x \tag{3.7}$$

The *V-Q-x* conjunction for dielectric-to-dielectric contact-separation mode TENG (Figure 3.2 (a)) is represented as [65]:

$$V = -\frac{Q}{S\varepsilon_0}\left(\frac{d_{D1}}{\varepsilon_{r1}} + \frac{d_{D2}}{\varepsilon_{r2}} + x(t)\right) + \frac{\sigma x(t)}{\varepsilon_0} \tag{3.8}$$

Furthermore, for the conductor-to-dielectric structure (Figure 3.2 (b)) electrode 2 plays two roles, both as a triboelectric layer and as an electrode. Therefore, the total charges in electrode 2 have to parts, one is the triboelectric charges ($S\sigma$) and the other is the transferred charges between the two electrodes ($-Q$). Thus, the total charges in electrode 2 are ($S\sigma$-Q). The *V*-*Q*-*x* conjunction is represented by [65, 66]:

$$V = E_1 d_{D1} + E_{air} x = -\frac{Q}{S\varepsilon_0}\left(\frac{d_{D1}}{\varepsilon_{r1}} + x(t)\right) + \frac{\sigma x(t)}{\varepsilon_0} \tag{3.9}$$

If the effective dielectric thickness is defined constant d_{D0} the *V*-*Q*-*x* conjunction in equations (3.8) and (3.9) can be unified as follows:

$$V = -\frac{Q}{S\varepsilon_0}\left(d_{D0} + x(t)\right) + \frac{\sigma x(t)}{\varepsilon_0} \tag{3.10}$$

The output V_{OC}, Q_{SC} and *C* of the contact-separation TENG can be derived based on electrodynamics, as follows:

$$V_{OC} = \frac{\sigma x(t)}{\varepsilon_0} \tag{3.11}$$

$$Q_{SC} = \frac{S\sigma x(t)}{d_{D0} + x(t)} \tag{3.12}$$

$$C = \frac{\varepsilon_0 S}{d_{D0} + x(t)} \tag{3.13}$$

The simulation of TENG energy harvesting systems generally comprises two parts, electrostatics simulation and load circuit simulation [106].

Focusing on the calculation of the electrical output power values of the TENG-based systems through load circuit simulation, it is necessary to calculate the numerical conjunction of $V_{OC}(x)$ and

C(x). The governing differential equation of the TENG system can be derived using Kirchhoff's law when the load is very simple and completely resistive can be given by [106]:

$$R_T\frac{dQ}{dt} = -\frac{1}{C(x)}Q + Voc(x) = -\frac{1}{C}Q + V_{OC} \tag{3.14}$$

Such a differential equation can only be derived for few cases using simple load circuits as illustrated in Figure 3.3. Which can be solved by numerical integration and for particular TENG systems and motion conditions. Solving the differential equation set is almost an impossible task with a complex load circuit. Due to that reason, the utilization of simulation programs with integrated circuit analysis like SPICE or COMSOL can be used to simulate the TENG systems [106].

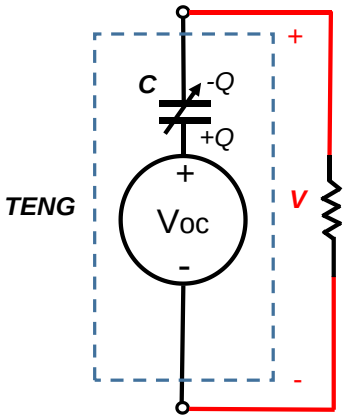

Figure 3.3 Equivalent circuit model of the whole TENG system loaded by a load resistor [65, 66].

3.2.2 Maximum surface charge density calculation for triboelectric nanogenerators considering the ion injection method

A contact-separation process that drives contact electrification is an effect that causes charge transfer between two materials [79, 108]. Such effect is used for mechanical energy harvesting through triboelectric nanogenerators where electric charges generated at the contact act as a source for electrostatic induction drive electricity using various mechanical configurations.

To perform well in those structures, a high density of triboelectric charges must be transferred at the contact [65, 66]. Therefore, controlling triboelectric charge density during the process of contact electrification is critical. The operation mechanism of TENG is based on the conjunction of the triboelectrification and the electrostatic induction. Thus, both the output voltage and the output current of the TENG are equivalent to the surface triboelectric charge density, so that the output power has a dependence on the charge density. Therefore, a key approach for the

improvement of TENG output performance from the materials aspect is to increase the triboelectric charge density through material optimization and surface functionalization.

The ionized-air-injection for the introduction of the surface charges is achieved by an air ionization gun, which can produce ions of both polarities through triggering the discharge of air inside the gun. The polarity of the ions injected through the gun can be manually controlled, which can make the materials surface negative charged or positively charged. Such a method is used to increase the output performance of TENG, which is an efficient approach to reach a maximum surface charge density (MSCD) on the triboelectric materials.

The MSCD for the contact separation mode TENG can be calculated from the theoretical analysis by comparing the threshold voltage for the air breakdown ($V_{a\text{-}b}$) and the actual voltage drop (V_{gap}) across the air gap. Accordingly, when x starts to increase from 0 during the releasing half cycle of the TENG, the $V_{a\text{-}b}$ at any $x > 0$ needs to remain bigger than V_{gap} to avoid breakdown of air.

$$V_{a-b} - V_{gap} > 0 = \frac{A(Px)}{\ln(Px) + B} - \frac{d_D \sigma_0 x}{\varepsilon_0 (d_D + x\varepsilon_r)} > 0 \tag{3.15}$$

From this, the MSCD (σ_{max}) can be calculated by the structure of the TENG where the influence of the dielectric layer thickness (d_D) affects the σ_{max} parameter as follows [109]:

$$\sigma_{max} = \left[\frac{AP\varepsilon_0 (d_D + x\varepsilon_r)}{d_D (\ln (Px + B)}\right] min \tag{3.16}$$

Where P is the gas pressure for the air standard atmospheric pressure of 101 kPa (1 atm) the usual condition of a TENG. A and B are the constants determined by the gas pressure, A = 2.87x10^5 V/(atm·m), and B = 12.6. ε_r is the relative permittivity of the dielectric layer, and ε_0 is the vacuum permittivity.

3.3 Triboelectric nanogenerators FEM results and analysis

The FEM simulations were performed coupling electromechanics and electrical circuit interfaces (Figure 3.4 (a)) for a dielectric-metal contact-separation mode TENG (DMCS-TENG), composed of two triboelectric layers, Polyimide and Aluminum (Al) layers (Figure 3.4), studied under the breaking water wave impact forces generated as shown in Figure 1.1 (a-d) and Figure 1.2 was performed using COMSOL Multiphysics, which help to understand its mechanical and electrical characteristics.

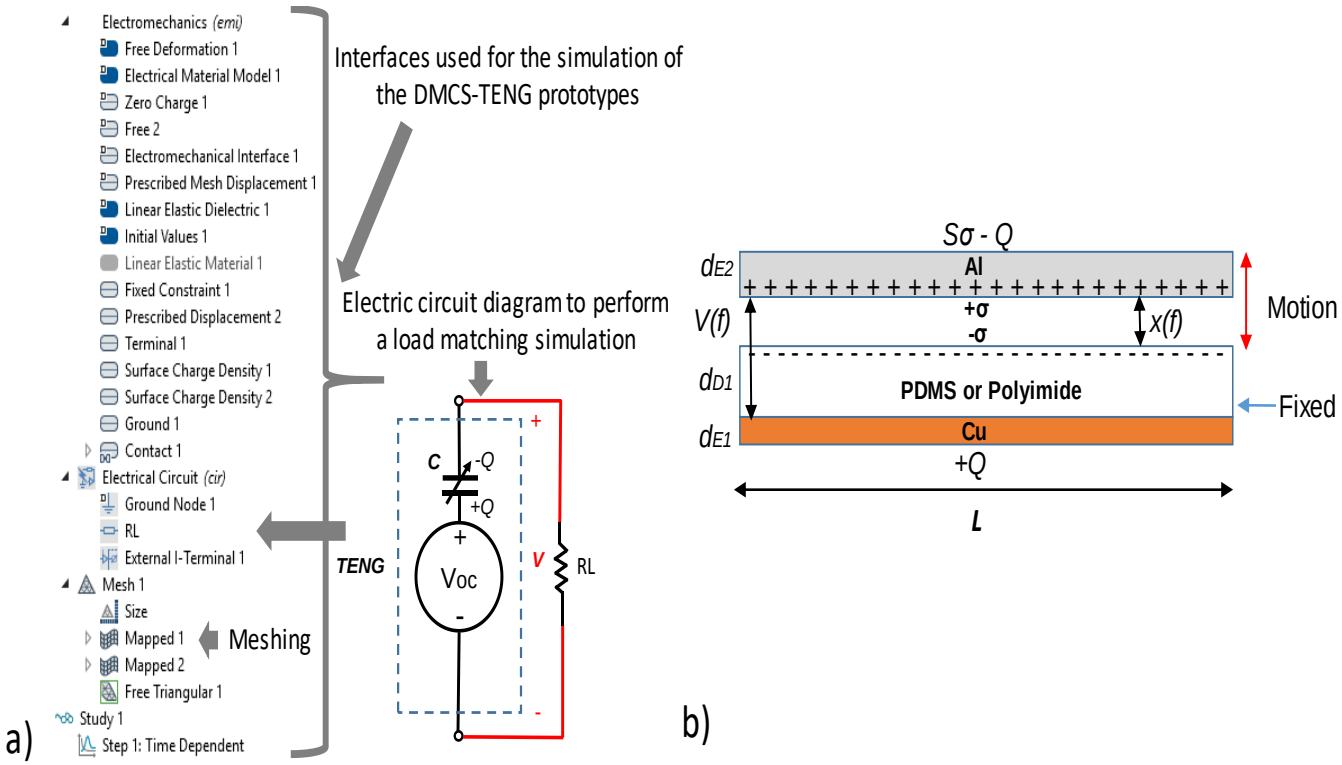

Figure 3.4 (a) FEM simulation model builder of the DMCS-TENG by coupling electromechanics and electrical circuit interfaces. (b) Two-dimensional sketch of the DMCS-TENG prototype.

Considering the aforementioned *V-Q-x* relationship proposed for the operation and modelling of the DMCS-TENG when it is connected with a resistive load (3.14). Where *Voc* is the voltage generated between two DMCS-TENG contacts, *Q* is the amount of charge between the two electrodes, and *x* is the distance between the DMCS-TENG triboelectric layers that varies with the mechanical energy phase of motion at a time, *t*. According to the model, the instantaneous power output performance by the DMCS-TENG was calculated from the generated output current (*I*) and voltage in the influence of the load resistance during the simulation. Which depends and changes according to the constant surface charge density (σ) value from the properties of the dielectric materials calculated according to the maximum surface charge density (3.16) considering the ion injection method by the structure of the DMCS-TENG.

These are based on the DMCS-TENG structure as shown in Figure 3.4. Two structures comprising different dielectric layers, namely polydimethylsiloxane (PDMS, thickness d_{D1} = 125 µm, ε_{r1} = 2.5) and polyimide (Kapton, thickness d_{D1} = 50.8 µm, ε_{r1} = 3.4), were attached to a copper (Cu, thickness d_{E1} = 100 µm) lower electrode 1. An aluminium (Al, thickness d_{E2} = 100 µm) layer was used as the second triboelectric material, the top electrode 2 (grounded). The top layer was fixed in both extreme sides and is the point at which the periodic motion (six cycles (t = 0.12 s)) was applied with the oscillatory frequencies of 30, 80, 150, 200, 219 and 250 Hz and an amplitude of 1 mm.

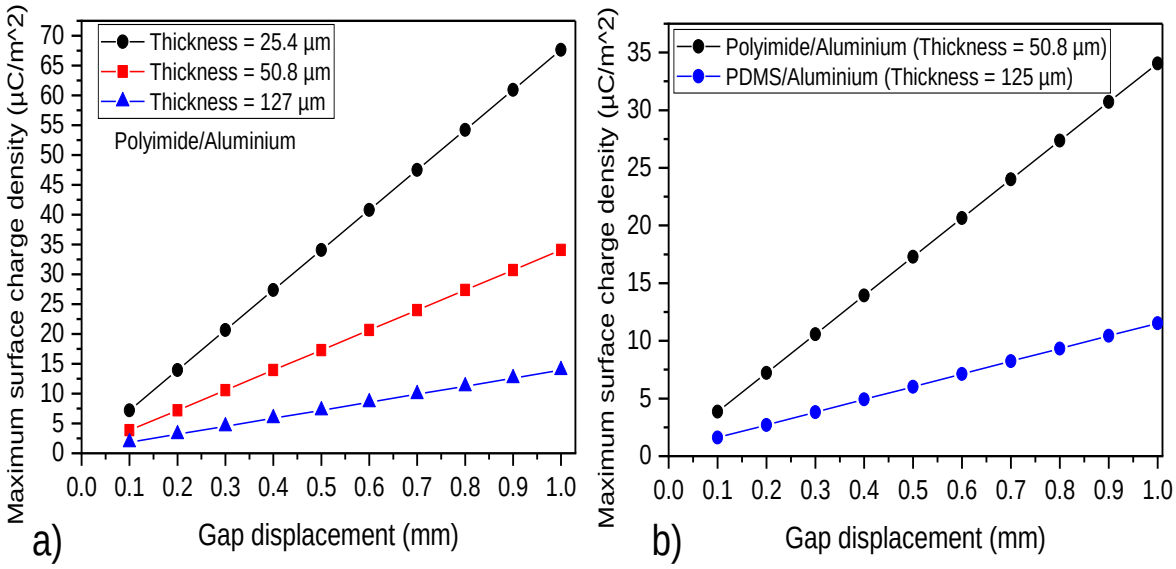

Figure 3.5 Theoretical relationship between maximum surface charge density (σ_{max}) using the ion injection method and the thickness (d_{D1}) at different gap distance (x) (a) between the polyimide dielectric layer with different thicknesses, and (b) polyimide vs PDMS layers of different thicknesses at different gap distance.

From equation (3.16), we consider a scenario where the maximum gap x separation is 1 mm and the time duration is 30 seconds. It was calculated the maximum value that can be reached for the maximum surface charge density of the aforementioned dielectric layers with gap separation between 0.1 mm to 1 mm. As shown in Figure 3.5 (a) and Figure 3.5 (b), the theoretically estimated σ_{max} tends to increase linearly with the maximum gap distance due to the approximately constant denominator value in the calculations using equation (3.16) and the parameters described in Table 3.1. Through numerically plotting the value of the σ_{max} vs d_{D1} with displacement variation x according to equation (3.16), it shows that the σ_{max} increases at smaller film thickness with a comparison of a polyimide dielectric layer with different thicknesses (127 µm, 50.8 µm and 25.4 µm) (Figure 3.5 (a)) and polyimide vs PDMS layers of different thicknesses at different gap distances (Figure 3.5 (b)). The two triboelectric-charge surfaces were assigned to the model with the calculated value $\sigma_{PDMS} = \sigma_{max,PDMS} = \pm 11.53$ µC/m^2 and $\sigma_{max,Polyimide} = \pm 34.06$ µC/m^2. The reduction of d_{D1} from the range of tens of microns will increase the σ_{max} value and the power output of the DMCS-TENG can be enhanced.

A series of simulations were performed to analyze the output performance of the entire system, with different length structures (L = 2.5 cm, 5 cm and 8 cm) over the oscillatory frequency range mentioned earlier, so that the optimal design can be found as well as the optimum resistance to reach the higher output power of the proposed DMCS-TENG. The simulation also provides the output voltage (V), current (I) and the output power. A 2D model configuration is adopted to simplify the calculation and reduce the computational time (detailed parameters are listed in Table 3.1).

Table 3.1 Parameters utilized in the FEM calculation for the dielectric-metal contact-separation TENG, through different frequencies and load resistances.

Parameter	Value
R_load (R_L)	1 to 100 MΩ
Frequencies (f)	30, 80 150, 200, 219, and 252 Hz
Time (t)	1 s
Waveform	6*pi*f
Input	wv1(t)
Time dependant (Simulation time)	range(0,0.006,0.72)s
Surface charge density ($\sigma_{max,\ Polymide}$)	±34.063 µC/m^2
Surface charge density ($\sigma_{max,\ PDMS}$)	±11.53 µC/m^2
Dielectric layer (Polyimide, PDMS, d_{D1}):	
Thickness	50.8 µm, 125 µm
Length (L)	2.5, 5 and 8 cm
Dielectric constant (ε_{r1})	3.4, 2.5
Copper electrode (d_{E1})	100 µm
Aluminium electrode (d_{E2})	100 µm
Maximum separation distance (x)	0 mm
Gas pressure for air at standard atmospheric pressure	101 kPa (1 atm)
Constants determined by the pressure of the gas (A and B)	$2.87x10^5$ V/(atm m), 12.6
Vacuum permittivity (ε_0)	$8.854x10^{-12}$ Fm^{-1}

The highest calculated output performance for both samples was obtained with the DMCS-TENG structure of L = 8 cm at the oscillation frequency of 150 Hz as shown in the three regions of operation [66] of the proposed devices composed with PDMS-Al and polyimide-Al layers as depicted in Figures 3.6 ((a), (c) and (e)) and Figure 3.6 ((b), (d) and (f)). The three working areas of the devices during the simulation at different frequencies were obtained by coupling electrostatic and electrical circuit interfaces in the model, connecting the energy harvesters to different load resistances as illustrated in Figure 3.3 and Figure 3.4 (a).

As a result, using low load resistance values from 0.1 to 1000 Ω shows that the simulated DMCS-TENG system is close to charged transfer in short-circuit state showing a brief drop in the instantaneous output power value as illustrated in the region I in the Figures 3.6 (a-f). Besides, with higher load resistance values between 50 MΩ to 100 MΩ, the instantaneous output voltage saturates at Voc showing that the system electrical output performance is close to open-circuit condition in region III (Figures 3.6 (a-f)). Furthermore, the maximum instantaneous output power of the DMCS-TENG system is generated in region II with a 10 MΩ load resistance as depicted in Figures 3.6 (a-f). In this region II, the instantaneous output current drops dramatically and the instantaneous output voltage increases at a reverse tendency. The DMCS-TENG with polyimide-Al (L = 8 cm) reached a higher maximum instantaneous output power of 3.66 mW with a voltage and current of 191.26 V and 19.12 µA, respectively with a 10 MΩ load shown in region II of Figure 3.6

(b). In comparison, the maximum instantaneous output power of the DMCS-TENG with PDMS-Al (L = 8 cm) was 416.47 μW in region II as depicted in Figure 3.6 (a), with an output voltage and current of 64.53 V and 6.45 μA, respectively.

DMCS-TENG in the original state before the contact of the triboelectric layers do not experience charge transfer, and thus no electrical potential occurs across the electrodes (Figure 3.7 (a)). By applying a force to the upper metal layer on the dielectric, each layer will be brought into surface contact, resulting in electron transfer from the material in the positive side of the triboelectric series to the one in the negative side in the series [86]. Accordingly, electrons will be injected from the Al to the polyimide/PDMS surface, leaving the positive charges on the Al layer. Such a process will continue in the first hundreds of cycles until the accumulated charges reach saturation and equilibrium, and the negative charges will be preserved on the dielectric surface due to the nature of the insulator [110].

Once the pressing force is released, the Al layer of the DMCS-TENG will quickly rebound back due to the elasticity of the film and a gap is formed again between the two layers. From the numerical simulation results, it can be seen that the electric field generated by separate surface charges will give rise to a much higher potential on the Al layer side than the bottom electrode (Figure 3.7 (b)). Such potential difference will drive the flow of positive charges from Al layer to the bottom electrode through the external load until the potential difference is fully offset by the transferred charges, rendering the bottom electrode with a surface charge density of $+Q$, while the charges on the Al is with a sum of two parts. One part is due to the transferred charges between electrode 1 and electrode 2 ($-Q$) and the other part is due to the triboelectric charges at the surface area ($S\sigma$). Thus, the total charges on electrode 2 are $S\sigma - Q$. Subsequently, when the two layers in the DMCS-TENG are in contact again, charge redistribution will result in a positive potential on the bottom electrode, which will drive all the transferred charges $+Q$ to flow back to the Al layer. The complete electricity generation cycle is achieved, and the device will go back to the equilibrium state.

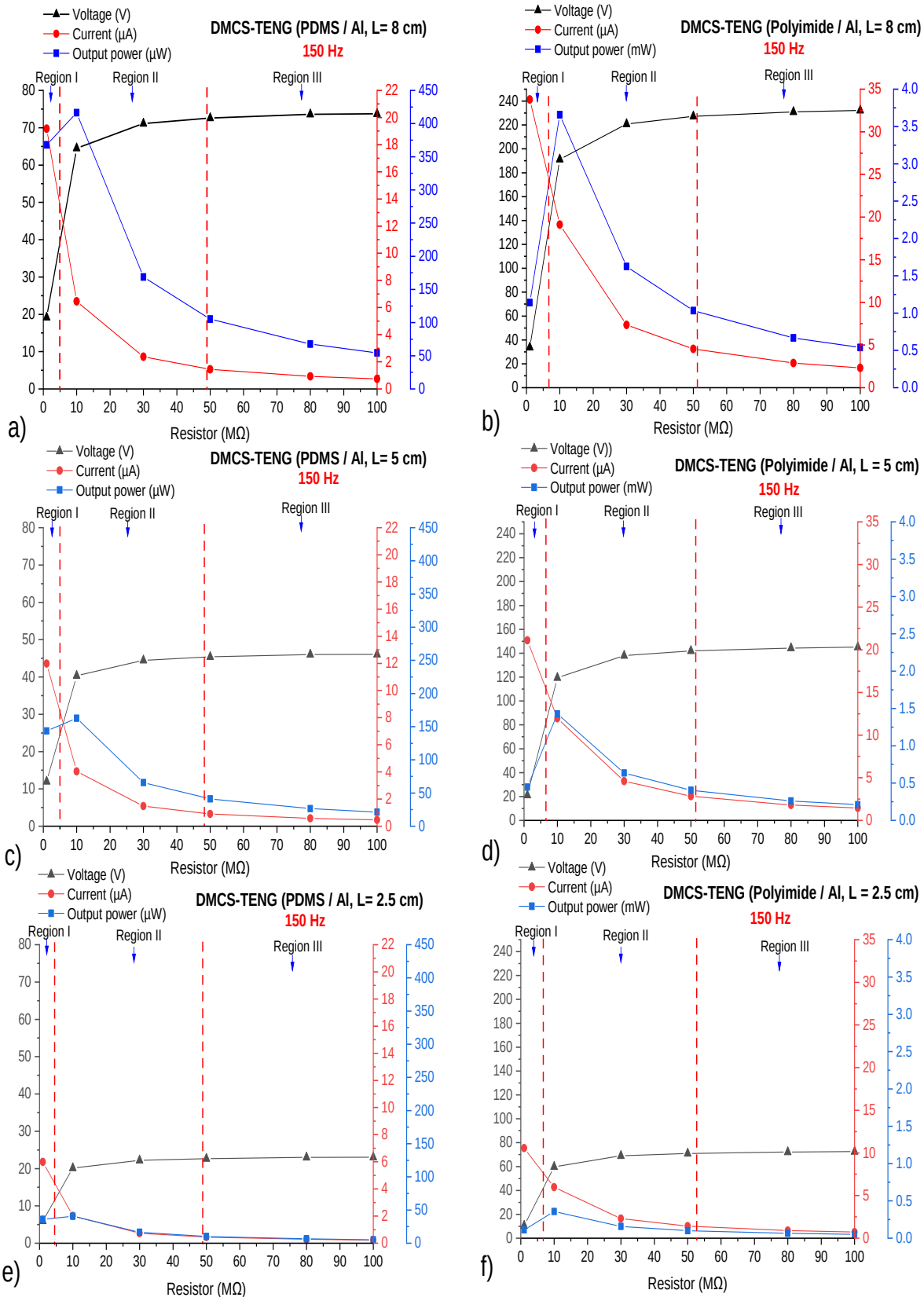

Figure 3.6 The influence of the load resistance divided into three working regions on the magnitude of the peak output voltage (*V*), peak output current (*I*) and maximum output power performance of the DMCS-TENG prototypes with a structure of L = 8 cm composed with (a) PDMS-Al and (b) Polyimide-Al layers at the oscillation frequency of 150 Hz. Structure of L = 5 cm with (c) PDMS-Al and (d) Polyimide-Al layers and (e-f) structure of L = 2.5 cm.

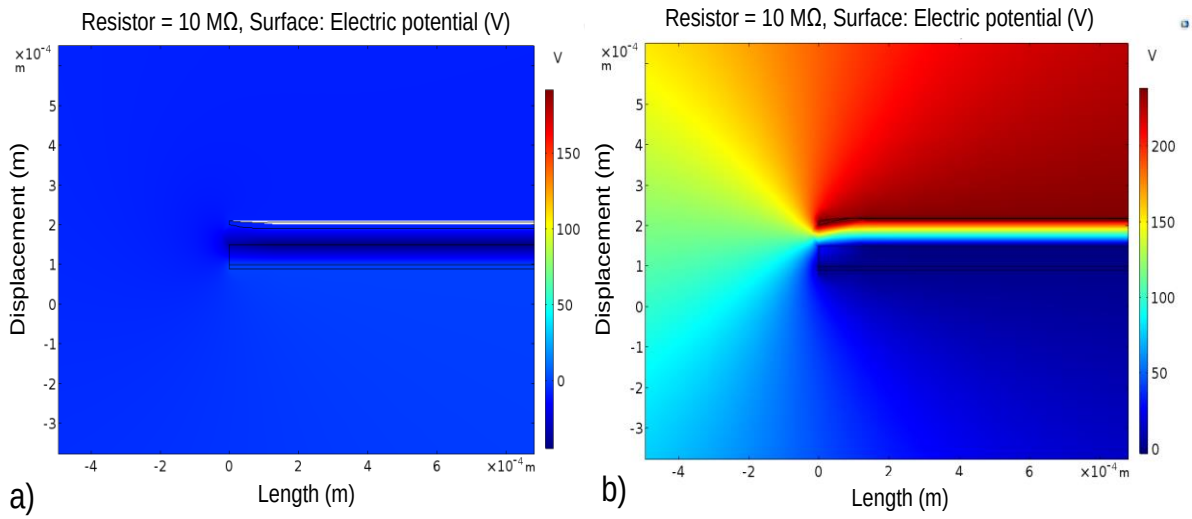

Figure 3.7 DMCS-TENG under oscillatory frequency and deformation. (a) Two-dimensional shape showing the two triboelectric layers in contact, (b) Al layer released, which will raise a much higher potential.

The maximum output power of both energy harvesters is at 150 Hz, followed by 30 Hz under the load resistor of 10 MΩ between 3.7 mW to 369 µW, which tends to fluctuate as the oscillating frequency of operation cycle increases. The DMCS-TENG with the polyimide-Al layers showed an increase by a factor of 8.40 compared with the modelled devices using PDMS-Al layers. Such a difference in the output power of the two simulated DMCS-TENG prototypes across the oscillation frequency range (30 to 252 Hz) with different length sizes is shown in Figure 3.8 (a-c). Which is related to the higher surface charge density at the device with polyimide-Al due to the thinner dielectric layer. Additionally, the reduction in the length (L = 5 cm and 2.5 cm) structure of the DMCS-TENG devices decreases the output power by a factor of 2.5 and 10.2, which generates maximum output power values at 150 Hz from 1.42 mW to 162 µW (Figure 3.8 (b)), and 357 µW to 40.6 µW (Figure 3.8 (c)), respectively. Consequently, as the structure with the L = 8 cm generated the higher output performance for the simulated DMCS-TENG (Figure 3.8 (a)), it was chosen to fabricate such energy harvester for the practical experiments.

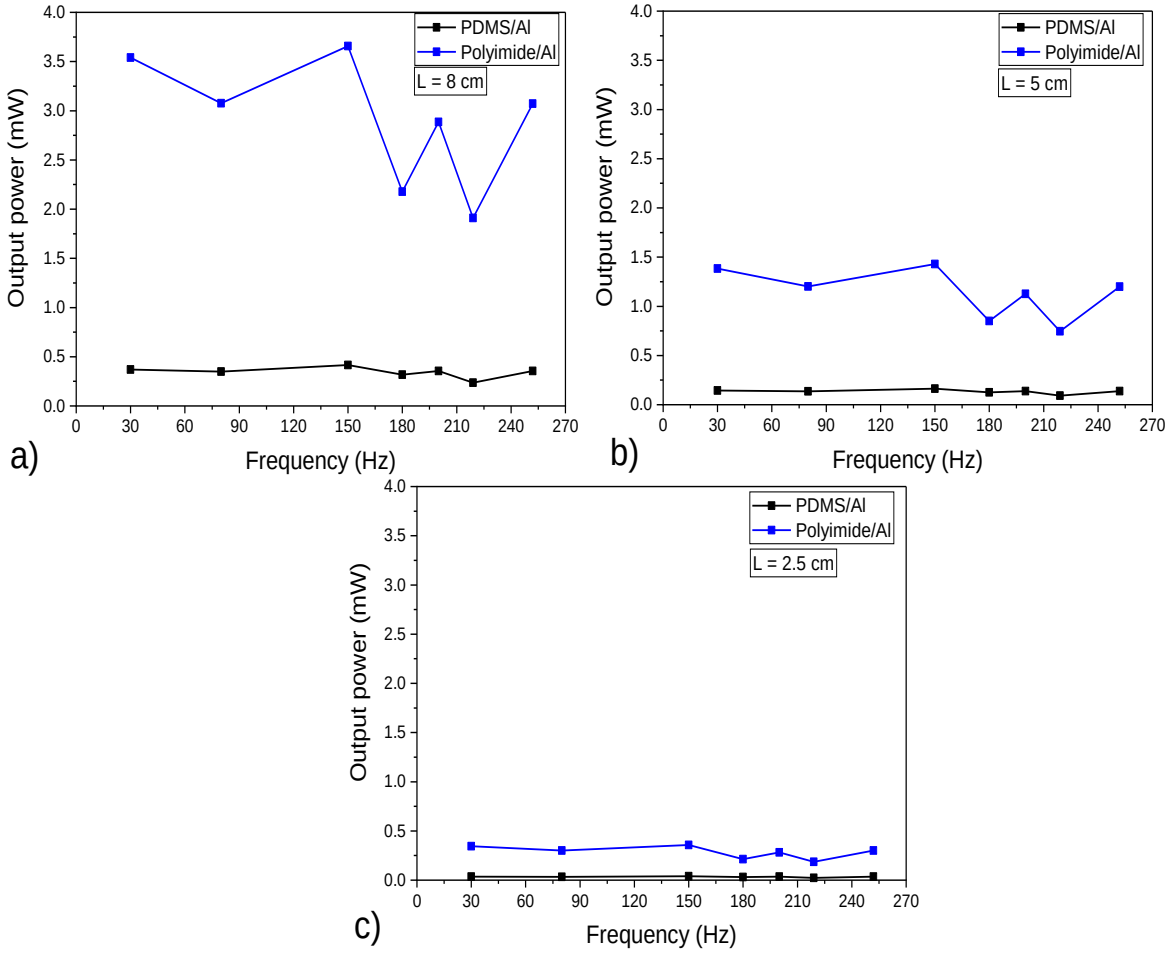

Figure 3.8 Maximum instantaneous output power of simulated DMCS-TENG prototypes with (a) L = 8 cm, (b) L = 5 cm, and (c) L = 2.5 cm as a function of the main oscillatory frequencies of 30, 80, 150, 180, 200, 219 and 252 Hz with an amplitude of 1 mm (t = 0.12s).

3.4 FEM and simulation of hybrid triboelectric-piezoelectric generators for water wave impact energy harvesting

A FEM was developed for the hybrid energy harvesters to understand the output performance, load resistance matching of simultaneous coupling between triboelectric and piezoelectric effects simulated at water wave impact conditions at low frequencies (0.7 Hz to 3 Hz). It was considered the "*V-Q-x* relationship" (3.14) proposed for modelling the operating principles of a TENG (triboelectric effect) at it was presented in detail at the previous point for the model of the DMCS-TENG structure. When it is connected with an external resistive load (R_T), the maximum output power of the TENG system can be derived using Kirchoff's law (3.14). According to this model, the output power performance by the DMCS-TENG depends on the output current (I). The voltage (V) is influenced by the load resistance, and the surface charge density σ depends on the properties of the materials in contact. The piezoelectric nanogenerator has a smaller output voltage but larger

output current, which is caused by the relatively low equivalent resistance. The equivalent external resistance of a piezoelectric nanogenerator (R_P), when the output power reaches its maximum value can be expressed as [111]:

$$R_P = \frac{d_P}{bL\varepsilon_P f} \tag{3.17}$$

where d_P, b, L and ε_P are the thickness, width, length and permittivity of the piezoelectric material and f is the frequency of the external mechanical energy.

3.5 Hybrid triboelectric-piezoelectric generators FEM results and analysis

The FEM simulations were performed by coupling solid mechanics, electrostatics and electrical circuit interfaces as illustrated in Figure 3.9 (a) to model the output current and voltage to calculate the output power generated by the hybrid nanogenerators connected to resistive loads (varying from 0.001 to 100 MΩ) under a horizontal applied periodic motion at low oscillating frequencies of 0.7, 1.2, 1.8, 2.5 and 3 Hz. This applying a waveform, input, and a boundary load on the hybrid device as illustrated and described in Figure 3.9 (c) and Table 3.2. The model is based on the hybrid prototype structure as shown in Figure 3.9 (b-c), with different lengths of (L = 4 cm. 6 cm and 8 cm), so that the best design can be found. The device structure includes a PVDF piezoelectric layer (d_P = 40 µm) with a piezoelectric polarization ($x1$) of 150 µC/m^2 that is connected to two silver electrodes (d_{E2}, d_{E3} = 10 µm) E2 (grounded) and E3. A copper E1 (d_{E1} = 10 µm) with a polyimide dielectric layer (d_{D1} = 50.8 µm) acts as the triboelectric part. The two tribo-charge surfaces were assigned with the theoretical maximum surface charge density (3.16) [109] σ_{max} = ±34.063 µC/m^2, respectively (Table 3.2).

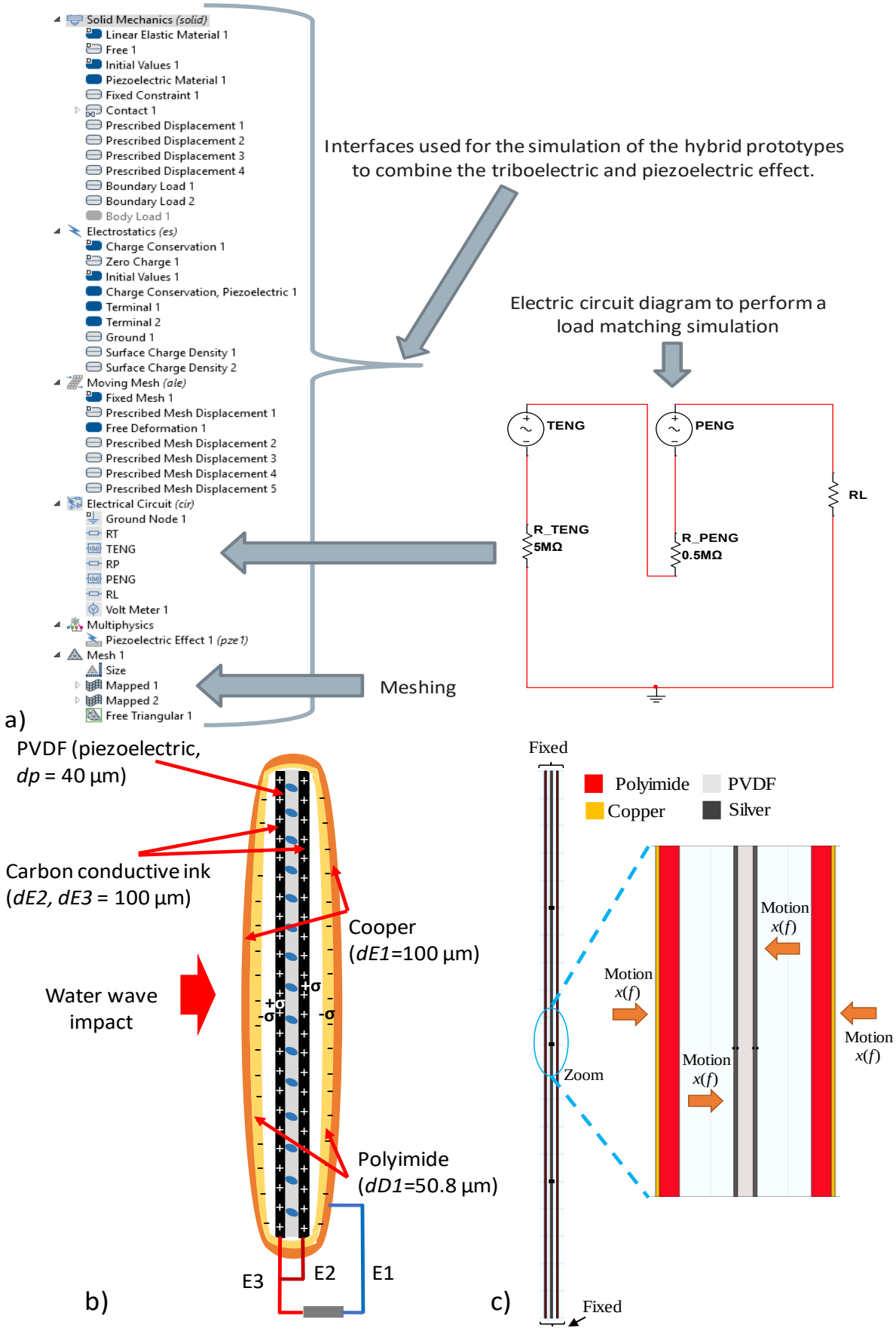

Figure 3.9 (a) FEM simulation model builder of the hybrid nanogenerator by coupling solid mechanics, electrostatics and electrical circuit interfaces. (b) Two-dimensional schematic of the

hybrid nanogenerator (coupling triboelectric-piezoelectric effects). (c) Two-dimensional schematic of the simulated hybrid nanogenerator and direction of the applied horizontal periodic motions to the modelled structure in COMSOL Multiphysics.

Table 3.2 Parameters used in the FEM

Parameter	Value
R_load (R_L)	0.001 to 100 MΩ
R_TENG (R_T)	10 MΩ
R_PENG (R_P)	0.5 MΩ
Frequencies (f)	0.7, 1.2, 1.8, 2.5, and 3 Hz
Time (t)	1 s
Waveform	6*pi*f
Input	wv1(t)
Boundary load	solid.rho*g_const
Surface charge density (σ_{max})	±34.063 µC/m^2
Piezoelectric polarization ($x1$)	150 µC/m^2
Time dependant (Simulation time)	range(0,0.006,0.72)s
Dielectric layer (Polyimide):	
Thickness (d_{D1})	50.8 µm
Length (L)	4, 6 and 8 cm
Dielectric constant (ε1)	3.4
Piezoelectric layer (PVDF):	
Thickness (d_P)	40 µm
Length (L)	4, 6 and 8 cm
Copper electrodes:	
Thickness (d_{E1})	10 µm
Length (L)	4, 6 and 8 cm
Silver electrodes:	
Thickness (d_{E2}, d_{E3})	10 µm
Length (L)	4, 6 and 8 cm
Gap	150 µm

A series of simulations were performed in order to analyse the output performance of the entire system at the frequency range aforementioned. First, an analysis of the load resistance influence in the output performance and electric potential of the triboelectric and piezoelectric part was performed independently as illustrated in Figure 3.10 (a) and Figure 3.10 (b). The results show the highest output power performance with the structures of L = 8 cm at the oscillation of 3 Hz. The triboelectric nanogenerator and piezoelectric nanogenerator reached the maximum output power of 21.88 mW and 19.56 mW with a 10 MΩ and 0.5 MΩ loads, respectively (Figure 3.10 (d) and Figure 3.10 (e)). These calculated from the generated voltage of 467.81 V and current of 44.78 µA by the TENG (Figure 3.10 (d)), and voltage of 98.91 V and current of 197.83 µA by the piezoelectric nanogenerator (PENG) (Figure 3.10 (e)).

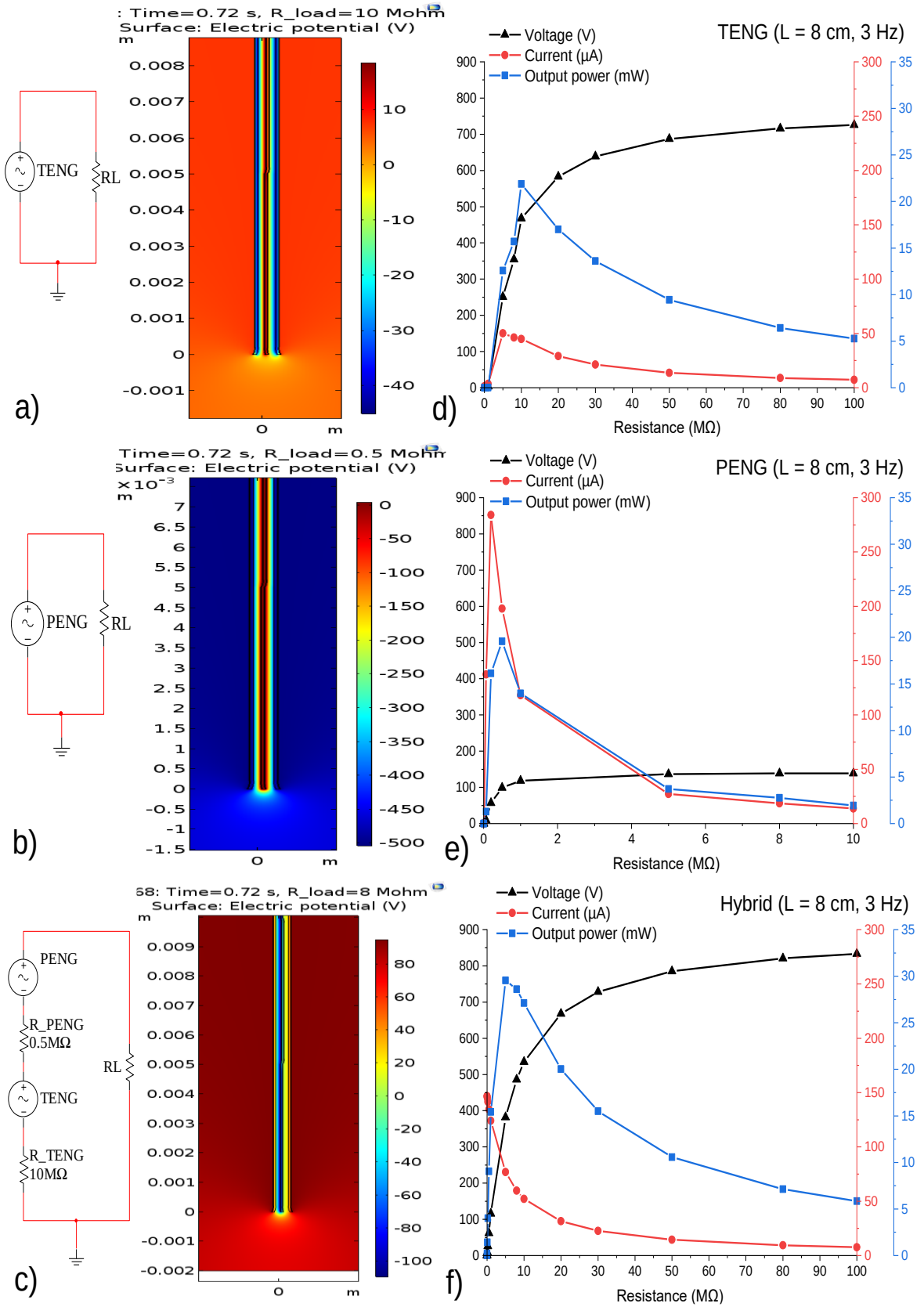

Figure 3.10 Electric potential model and simulated electric circuit diagram of (a) TENG, (b) PENG, and (c) simultaneous coupling of triboelectric-piezoelectric effects (hybrid nanogenerator). Simulation of the influence of the load resistance in the output voltage, current and power of (d) TENG, (e) PENG and (f) Hybrid prototype.

Therefore, the coupling of both effects was performed using the electric circuit diagram shown in Figure 3.10 (c), to perform a quantitative load matching analysis of the hybrid device output performance, and electric potential. The output power of the hybrid prototype shows an enhancement by a factor of 1.36 and 1.56 compared with the simulated triboelectric nanogenerators and piezoelectric nanogenerators tested in similar conditions respectively (Figure 3.10 (f)). The generated output voltage of 381.89 V and output current of 76.87 μA, which corresponds to the maximum output power of 29.54 mW, with a 5 MΩ load as shown in Figure 3.10 (f), and Figure 3.10 (c) illustrates the electric potential generated by the hybrid prototype.

Additionally, the increase in the length (L = 8 cm) and oscillating frequency (0.7 Hz to 3 Hz) of the hybrid devices promote an increase in the output performance from 26.15 mW to 29.94 mW by a factor of 1.34 (L = 4 cm) and 1.06 (L = 6 cm), respectively. Consequently, the optimum load resistance reduces as response [66], so for the hybrid structures L = 4 cm and L = 6 cm the optimum resistances were 10 MΩ and 8 MΩ (Figure 3.11 (a)), with maximum output power that increases from 19.30 mW to 22.27 mW, and from 24.20 mW to 28.22 mW, respectively. Figure 3.11 (b-d) shows the influence of the change in the length of the hybrid nanogenerator structure at different oscillating frequencies (0.7 Hz to 3 Hz), reflected in the optimum load resistance. The increase in the length (L = 8 cm) and oscillating frequency (0.7 Hz to 3 Hz) of the hybrid devices promote an increase in the output power with the optimum load resistance of 5 MΩ (Figure 3.11 (d)) compared with the structures with L = 4 cm and L = 6 cm, respectively. Consequently, the optimum load resistance reduces as a response [66], so for the hybrid structures L = 4 cm and L = 6 cm the optimum resistances were 10 MΩ and 8 MΩ, with a maximum output power of 22.27 mW (Figure 3.11 (b)), and 28.22 mW (Figure 3.11 (c)), respectively.

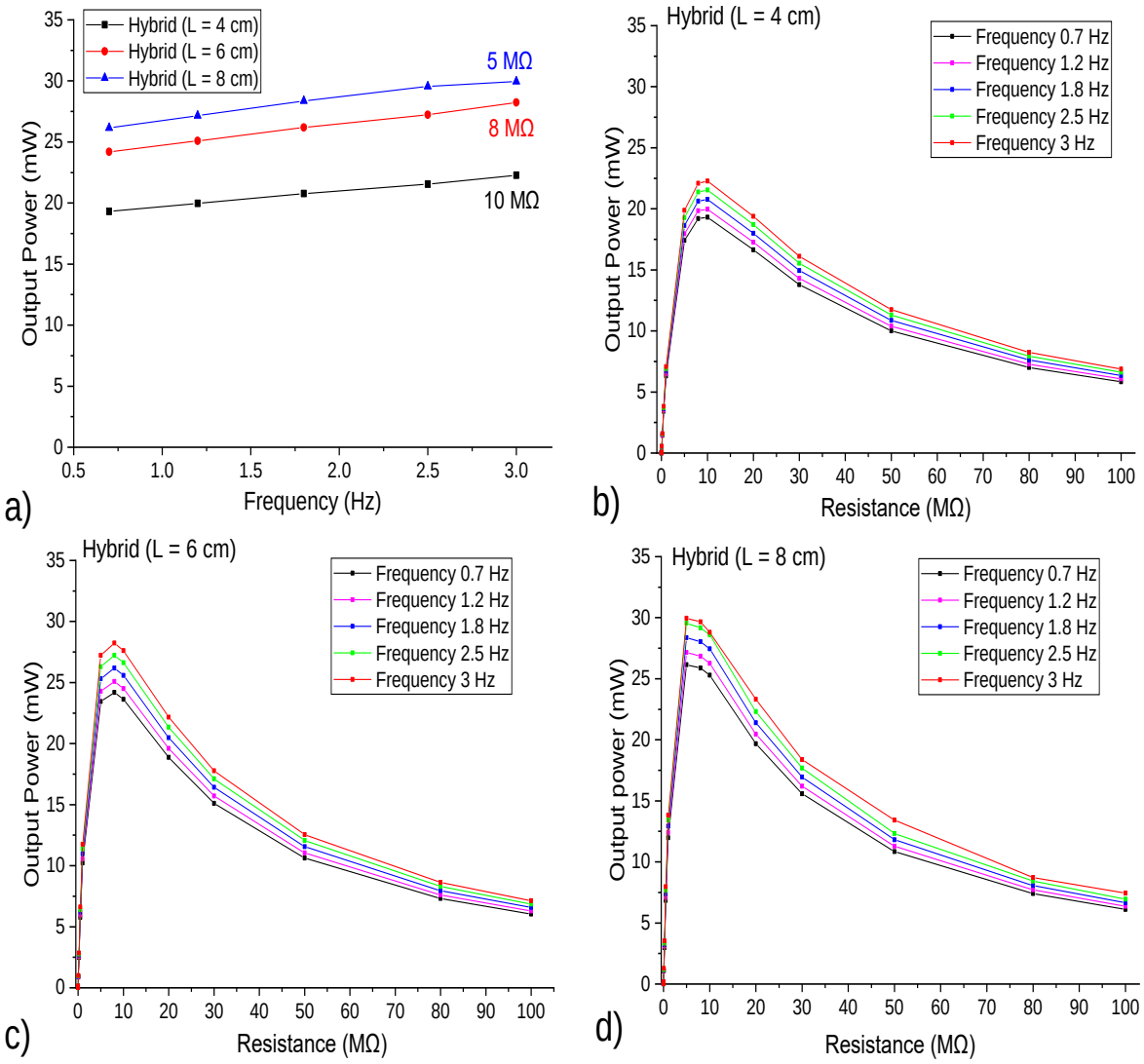

Figure 3.11 (a) Output power of the simulated hybrid devices with different lengths (3 cm, 6 cm and 8 cm) under different frequencies (0.7 Hz to 3 Hz) that highlights the optimum load resistance for every structure. Simulation of the influence of the load resistance in the output power performance of the hybrid nanogenerator prototype at different frequencies (0.7 Hz to 3 Hz) with different length structures (b) L = 4 cm, (c) L = 6 cm and (d) L = 8 cm).

Although the structure of 8 cm is the best to obtain higher output performance for the hybrid device, the structure with the length of 4 cm and to have an active area of 16 cm^2 was selected to fabricate the hybrid nanogenerator, with the purpose of obtain a stable output performance operation. This when the hybrid device and the grid of 4 hybrid devices were attached into the operation area (13 cm x 34 cm) in the water wave impact generator tank (52 cm x 34 cm x 18 cm), which it is explained in detail in Chapter 5.

3.6 Chapter summary

In summary, the modelling and numerical simulation of triboelectric nanogenerators and hybrid nanogenerators for breaking ocean wave impact energy harvesting in order to obtain a more quantitative understanding of the working mechanism and output performance analysis of the proposed energy harvesting technique. It includes a description and explanation of the theoretical background for the triboelectric nanogenerators. The model and FEM simulation parameters settled to perform and obtain the output performance of the entire system of TENG and hybrid nanogenerator techniques were described in detail in this chapter. Furthermore, the output performance obtained results based on the output voltage, current and power through the FEM simulations of the TENG using a dielectric-metal structure for breaking water wave impact energy harvesting under the application of broad oscillatory frequency range between 30 Hz to 252 Hz, were analyzed in this chapter. Additionally, the simultaneous coupling of triboelectric-piezoelectric effects was analyzed under low oscillating frequencies between 0.7 Hz to 3 Hz applied to a hybrid nanogenerator structure. It was found an output voltage, current and power improvement by a factor of 1.36 and 1.56 compared with simulated TENG and PENG tested in similar conditions respectively. Through the numerical simulations employing a structural, electrostatics, electromechanics, solid-mechanics and electrical circuit interfaces, it was found the optimum resistor and parameters to reach the higher output power according to the proposed DMCS-TENG and hybrid nanogenerators structures and studying the three working regions of the proposed energy harvesters.

Chapter 4 Dielectric-metal triboelectric nanogenerators (DMCS-TENG) prototypes for water wave impact energy harvesting

4.1 Introduction

Exploiting the potential advantages of TENG as broadband behaviour, lightweight, high energy density and ease of fabrication utilizing low-cost, readily available materials [18] and with the promising application of such energy harvesters for self-powering sensors [112, 113]. In order to demonstrate the feasibility of the triboelectric nanogenerators as a practical and potential power source to harvest the energy from breaking water wave impact, employing solid-solid materials in contact. Dielectric-metal contact separation mode (DMCS-TENG) prototypes were fabricated and tested. The triboelectric effect is generated as a result of regular, non-uniform contact between a dielectric layer which gains electrons, a negative triboelectric material and a conductive layer that loses electrons, a positive triboelectric material, where the output performance changes in proportion to the mechanical energy applied by pressure oscillation. Firstly, in order to study and to find the most promising triboelectric material combinations based on their output power generation to enhance the DMCS-TENG performance for mechanical energy harvesting, arc-shaped dielectric-metal single electrode triboelectric nanogenerators (DMSE-TENG) were fabricated. The output performance characterization using contact electrification between different dielectric-metal combinations was performed through an impact test. Secondly, by complementing the finite element model (FEM) simulation work described in chapter 3, the output performance of the fabricated DMCS-TENG using the best triboelectric material combination was evaluated at the broad frequency range from 30 Hz to 252 Hz, replicating the oscillatory frequencies generated due to breaking wave impact at coastal defence structures. Finally, the proposed energy harvester that shows the highest output performance was tested in a breaking water wave generator tank, to analyse its performance in realistic conditions.

4.2 Triboelectric material selection using DMSE-TENG

4.2.1 Fabrication and characterization of arc-shaped dielectric-metal single electrode triboelectric nanogenerators (DMSE-TENG) for triboelectric material optimization

In order to maximize the DMCS-TENG performance for mechanical energy harvesting from the oscillatory frequencies generated by breaking wave impact, arc-shaped dielectric-metal single electrode triboelectric nanogenerators (DMSE-TENG) were fabricated using different material combinations. The arc-shaped DMSE-TENG, as illustrated in Figure 4.1 (a) and Figure 4.1 (b), were fabricated using a simple, low-cost process. The device prototypes have an active triboelectric area of 5 cm x 5 cm, and an acrylic sheet was selected as a substrate material. The conductor layer (either aluminium, copper or silver) was attached to the acrylic with a thin adhesive layer, at room temperature. The conductor layer is used as a triboelectric material, and an electrode connected to an external load of 5 MΩ for electrical characterization. Likewise, the dielectric layer (polyimide, PDMS, polytetrafluoroethylene, i.e. PTFE, Teflon FEP etc.) was fixed with thin adhesive on a clear acetate film (d_D = 100 µm). The dielectric layer was attached with an arc-shaped form to the metal electrode using Kapton tape (1cm width) at room temperature. The maximum gap between the arc-shaped dielectric layer and the metal layer was 5 mm. The materials used for the arc-shaped DMSE-TENG prototypes fabrication are shown in Table 4.1 (Literature).

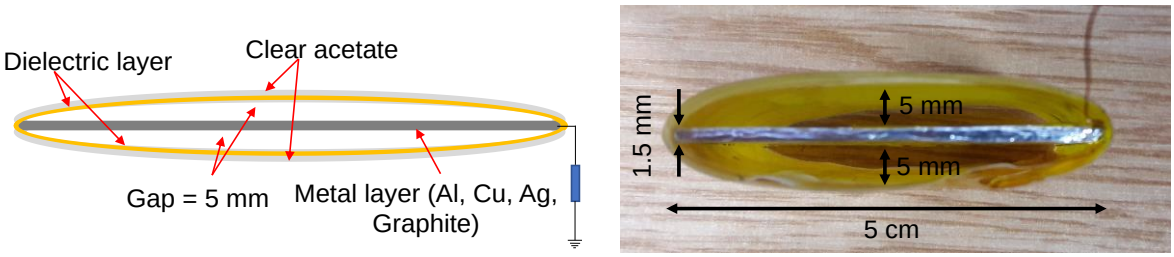

Figure 4.1 (a) Two-dimensional schematic of the arc-shaped DMSE-TENG. (b) Cross-sectional digital photo of the arc-shaped DMSE-TENG.

The output power performance characterization of the arc-shaped DMSE-TENG prototypes was evaluated from the generated output voltage and current, measured with an impact test set-up to study and find the optimum triboelectric material combination to reach the highest output performance. This system uses a 40 mm ball bearing (mass = 261.04 grams) attached to a magnetic switchable base, which is fastened to a RVFM laboratory stand set at the height of 30 cm. The device prototype was held at the base of the laboratory stand and the applied force to it was measured using a force sensor (Interlink electronics FSR406 1.5" diameter force sensing resistor) as shown in Figure 4.2. The output voltage measurements of the arc-shaped DMSE-TENG were obtained with a

digital oscilloscope Tektronix TDS 2014C, the output current measurements were performed using an Agilent Technologies N6705B power analyser (10 measurements performed on each sample).

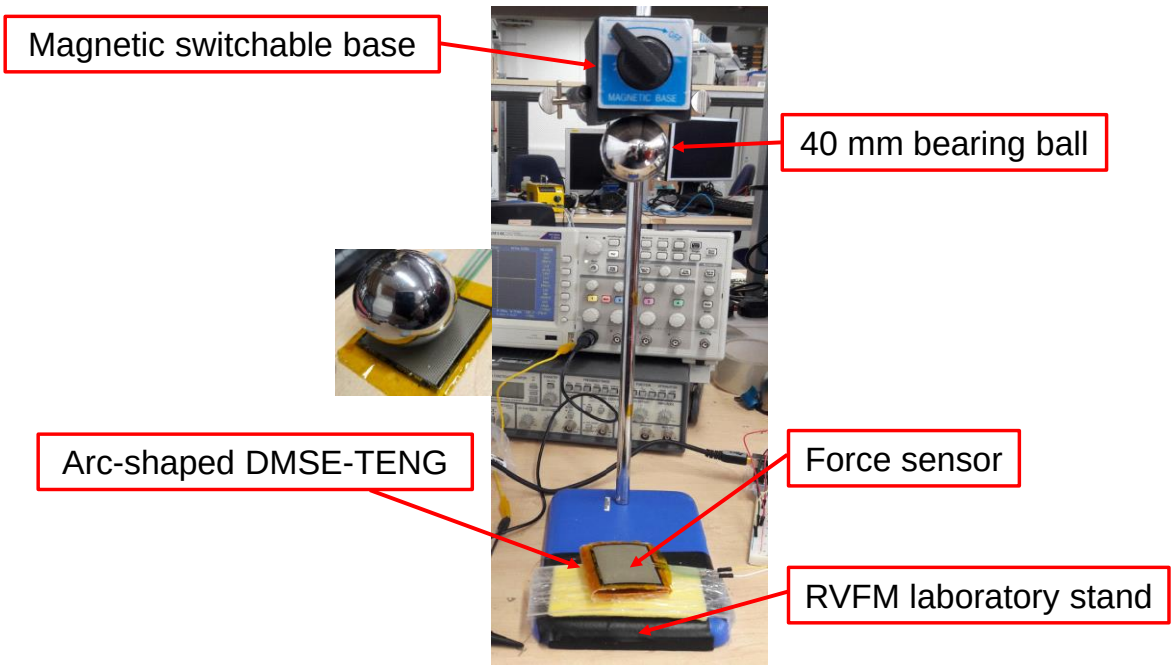

Figure 4.2 Experimental set-up of impact test using a 40 mm ball bearing on the arc-shaped DMSE-TENG prototypes (connected to a 5 MΩ load resistor) with different triboelectric material combinations.

4.2.2 Experimental results and analysis of electrical characterization of the DMSE-TENG prototypes for triboelectric material optimization under impact test

The output performance measurements of the arc-shaped DMSE-TENG prototypes through the impact test, which applies a force impulse of 12 N. The instantaneous output voltage and current of the top five DMSE-TENG prototypes that showed the highest performance using dielectric-metal contact electrification under the impact of a 40 mm ball bearing for 0.7 seconds are shown in Figure 4.3 (a) and Figure 4.3 (b). Such instantaneous values were between 106 V to 11.40 V and 40.59 µA to 4.27 µA, respectively. Consequently, considering the effective values of the output voltage and current, the results show that the maximum output power was 6.28 µW corresponding to an output voltage (V_{RMS}) of 5.22 V and current (I_{RMS}) of 1.20 µA using a triboelectric material combination of PDMS-silver conductive cloth tape as depicted in Figure 4.4.

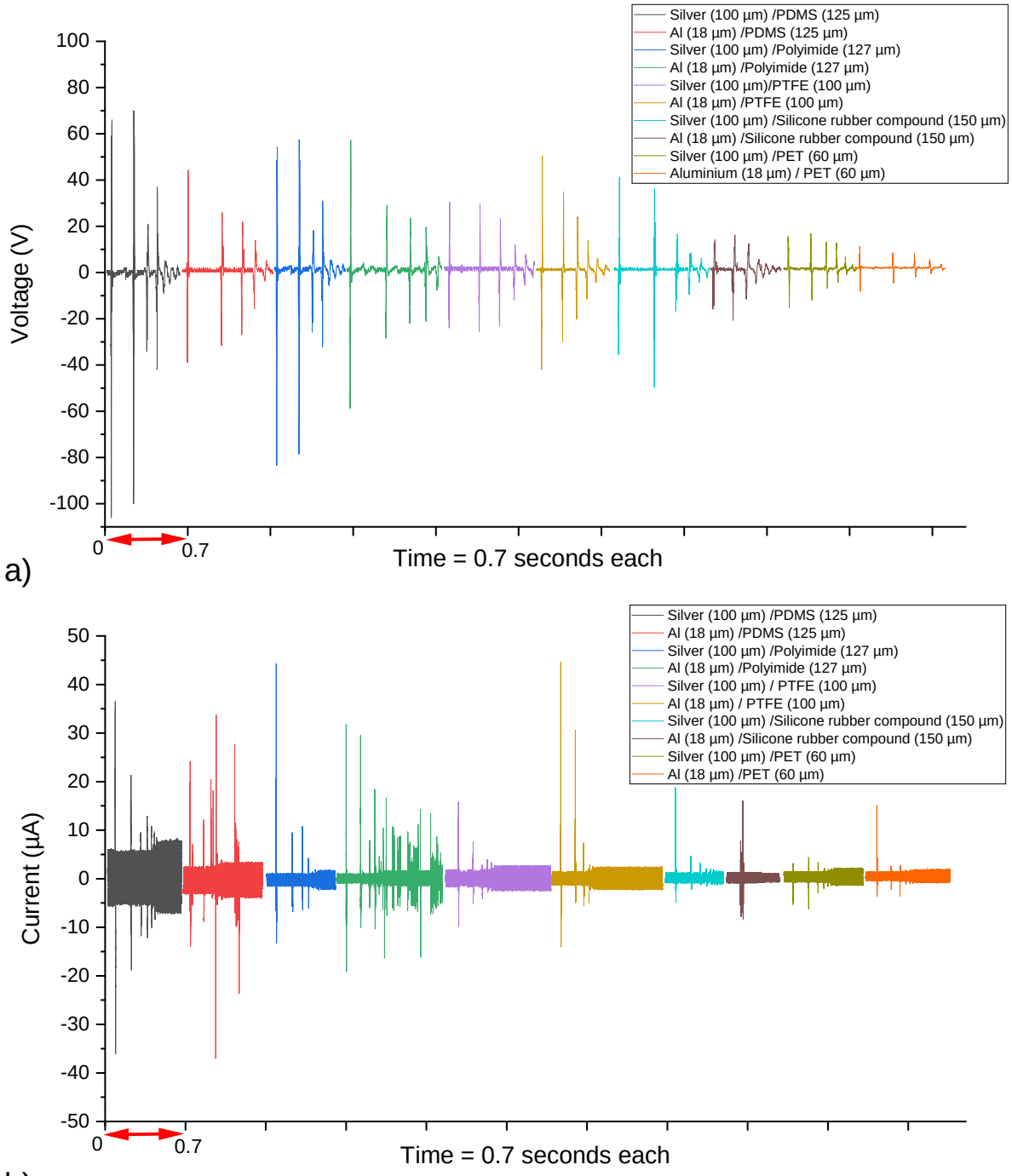

Figure 4.3 Instantaneous output (a) voltage and (b) current of the top-five arc-shaped DMSE-TENG prototypes (connected to a 5 MΩ load resistor) using dielectric-metal contact electrification under the impact of a 40 mm ball bearing for 0.7 seconds.

The highest instantaneous output voltage occurs when the dielectric layer is in contact with the conductor layer. The movement of the top dielectric layer due to the impact of the ball bearing changes the local electrical field distribution created between both layers due to the surface charge transfer, so that there is electron exchange between the bottom electrode, the external load and the ground to maintain the potential change of the electrode. The first impact of the ball bearing generates the highest voltage peak, which is related to the impact force that helps to increase the

contact area between both layers. The instantaneous voltage and current decreases due to the bouncing behaviour of the ball bearing after impact with the sample as shown in Figure 4.3 (a) and Figure 4.3 (b). Among all the arc-shaped DMSE-TENG prototypes the top five highest output power performance was dominated by structures with silver conductive cloth tape in contact with polyimide, PDMS, silicone rubber and PET except PTFE, where the highest performance was in contact with aluminium. The dynamic operation of the DMSE-TENG prototype is as follows:

The kinetic $E_{kinetic}$ and elastic $E_{elastic}$ energy equations (4.1) and (4.2) describe the energy applied to the arc-shaped dielectric-metal single electrode triboelectric nanogenerators (DMSE-TENG) (Figure 4.1) system. Where $E_{kinetic}$ is the energy carried by the moveable arc-shaped dielectric layer that plays the role of contact material for triboelectricity. $E_{elastic}$ is the energy stored in the dielectric layer acting as a spring for separation after contact.

$$E_{kinetic} = \frac{1}{2}mv^2 = 0.34mJ \tag{4.1}$$

$$E_{elastic} = \frac{1}{2}kx^2N = 0.015\ mJ \tag{4.2}$$

The average velocity (v = 1.5 m/s) of the dielectric layer when the contact is made due to the ball bearing impact was estimated with the equation $v = x/t$, where, x is the displacement of the ball bearing when it contacts the dielectric layer (x = 0.3 m) and t is the average time measured when it contacts the dielectric layer (t = 0.2 s). The spring constant (k = 0.59 N/m) was estimated based on the mass of the moveable dielectric layer (m_{PDMS} = 0.303125 g) according to Hooke's law $k = F/x$, where x is the displacement of the dielectric layer that is equal to the spacing between the two contacting surfaces (x = 5 mm). N is the number of springs considered for the arch-shaped DMSE-TENG (N = 2).

Furthermore, to calculate the energy conversion efficiency (η) that is defined as the ratio between the electric energy ($E_{electric}$) delivered to the load resistor of 10 MΩ and the mechanical energy possessed by the DMSE-TENG produced in a single period of contact (t = 0.2 s). The electric energy released by the DMSE-TENG was calculated by:

$$E_{electric} = \int_{t_1}^{t_2} RI^2\,dt = 0.033\,mJ \tag{4.3}$$

Where I is the instantaneous current, and R is the load resistance. The I_{RMS} and instantaneous output current I during the impact tests (Figure 4.2) was measured using an Agilent Technologies N6705B power analyser connecting the DMSE-TENG to an external load resistance of 5 MΩ. Consequently, the η was calculated as [114]:

$$\eta = \frac{E_{electric}}{E_{mechanical}}x100\% = \frac{E_{electric}}{E_{kinetic} + E_{elastic}}x100\%$$

$$\eta = \frac{0.033\ mJ}{0.015\ mJ + 0.34\ mJ} x100\% = 9.33\% \quad (4.4)$$

The above result shows the overall efficiency of the DMSE-TENG that showed the highest output power performance using the triboelectric material combination of PDMS-silver conductive cloth tape.

The output performance comparison of arc-shaped DMSE-TENG devices fabricated with silver conductive cloth tape versus the ones fabricated using aluminium foil and their standard deviation analysis calculated for each prototype (10 measurements performed on each sample) are shown in Figure 4.4. The effective values of output voltage (V_{RMS}), current (I_{RMS}) and power were from 1.22 V to 5.96 V, 0.49 µA to 1.20 µA, and 0.668 µW to 6.284 µW, respectively. Such values showed that the highest performance of the proposed triboelectric energy harvesting devices can be achieved by using silver conductive cloth tape in contact with the dielectric layers of PDMS and polyimide. Furthermore, the polyimide or PTFE-silver conductive cloth tape or aluminium foil combinations can reach similar output power performance, ranging from 3.8 µW to 5.3 µW.

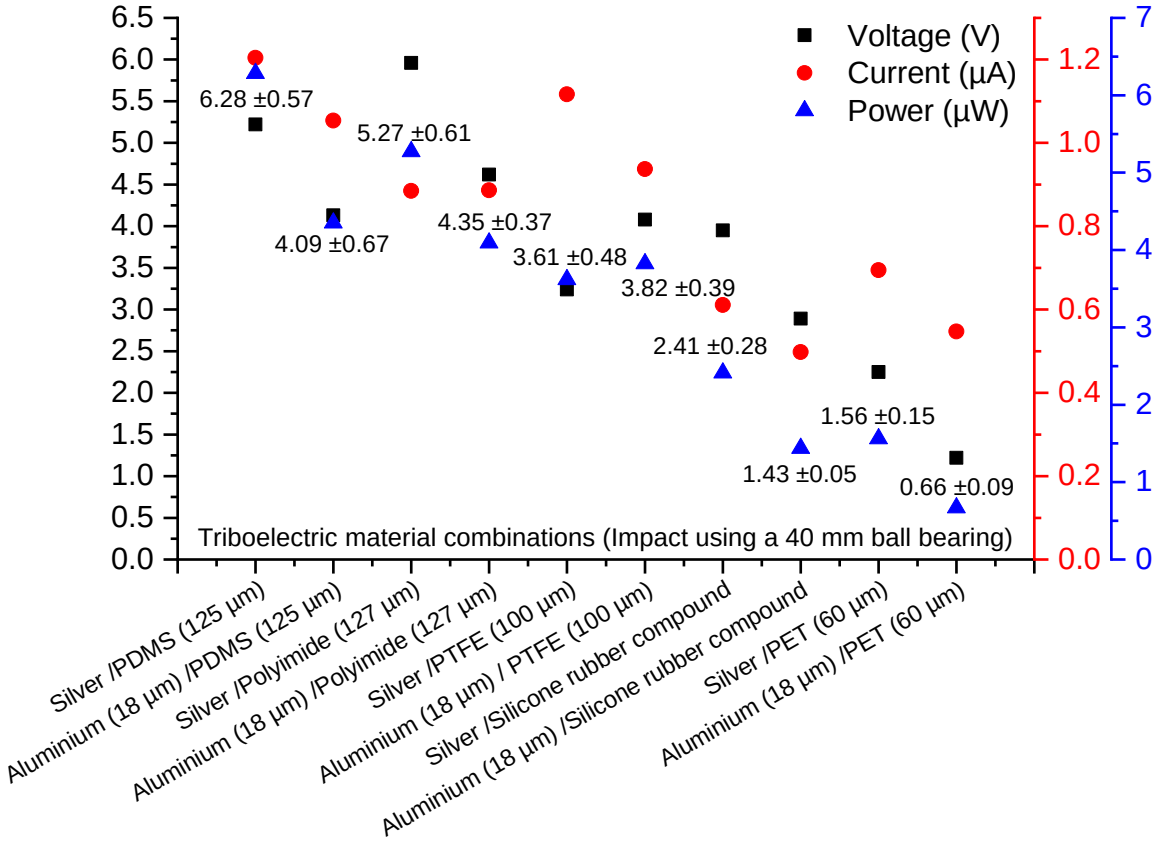

Figure 4.4 Comparison of the output voltage (V_{RMS}), current (I_{RMS}) and power effective values of the top five arc-shaped DMSE-TENG fabricated prototypes (connected to a 5 MΩ load resistor) with silver conductive cloth tape and aluminium foil, under impact test through a 40 mm ball bearing.

The ranking of the triboelectric materials used for the arc-shaped DMSE-TENG prototypes, arranged according to the output performance is shown in Table 4.1 (Tested). The most positive material of the conductors according to the measurements, was shown to be the silver conductive cloth tape and the most negative material was PDMS. This means that the charge transferred using this material combination will be the highest from the selection of triboelectric materials. Each conductor material on Table 4.1 (Tested) was highlighted with a specific colour in order to identify the higher output performance when they are in contact with the insulators highlighted with the same colour. The dominance of the silver tape among the chosen triboelectric materials, with the aim of reaching higher electrical output performance in the proposed energy harvesting prototypes, is clearly seen. Although the silver conductive cloth is the best positive material, aluminium foil was chosen for the fabrication of the DMCS-TENG as a low-cost option with excellent performance.

Table 4.1 Comparison of the rankings of positive and negative triboelectric materials in terms of ease of losing or gaining electrons with data from the literature [14] versus our impact test characterization data.

Triboelectric materials combinations (40 mm ball bearing)			
		Literature	Tested
Conductors	Positive	Aluminum (18 µm)	Conductive cloth tape (Silver)
		Copper (100 µm)	Aluminum (18 µm)
		Conductive cloth tape (Silver) (100 µm)	Copper (100 µm)
Insulators	Negative	Paper	Paper
		Polylactic acid (PLLA) (Polyester)	Polytetrafloroethylene (Teflon) PTFE tape (90 µm)
		Cellulose tape (63.5 µm)	Polylactic acid (PLLA) (Polyester)
		carton paper	Cellulose tape (63.5 µm)
		Polypropylene (PP) (46 µm)	Polytetrafloroethylene (Teflon) PTFE tape (100 µm)
		Polyethylene foam (2 mm)	carton paper
		Polyvinyl chloride (PVC) (100 µm)	Polypropylene (PP) (46 µm)
		Polystyrene (1 mm)	Polyethylene foam (2 mm)
		Polyethylene terephthalate (Polyester) (PET) (60 µm)	Polyvinyl chloride (PVC) (100 µm)
		Polydimethylsiloxane (Silicone rubber compound)	Polystyrene (1 mm)
		Polyimide (127 µm, Kapton, 50.8 µm, 25.4 µm)	Polyethylene terephthalate (Polyester) (PET) (60 µm)
		Polydimethylsiloxane (PDMS) (125 µm)	Polydimethylsiloxane (Silicone rubber compound)
		Polytetrafloroethylene (Teflon) PTFE tape (90 µm)	Polytetrafloroethylene (Teflon FEP, PTFE) (25 µm, 100 µm, 300 µm, 1 mm)
		Polytetrafloroethylene (Teflon) PTFE tape (100 µm)	Polyimide (Kapton) (127 µm, 50.8 µm, 25.4 µm)
		Polytetrafloroethylene (Teflon FEP, PTFE) (25 µm, 100 µm, 300 µm, 1 mm)	Polydimethylsiloxane (PDMS) (125 µm)

4.3 DMCS-TENG electrical characterization under different oscillating frequencies and using breaking water wave generator tank

4.3.1 Fabrication and characterization of DMCS-TENG energy harvester prototypes

For preliminary triboelectric material characterization using the impact tests, five DMCS-TENG prototypes of similar configuration to those used in the COMSOL model (Figure 3.4) were fabricated using the most promising triboelectric material combinations that showed the highest output power (Figure 4.5). The DMCS- TENG prototypes have an active triboelectric area of 8 cm x 8 cm. Two types of aluminium foil were evaluated, one flat aluminium foil with d_{E2} = 18 µm and a honeycomb-patterned aluminium foil with d_{E2} = 16 µm, individual hexagon area = 31.83 mm^2 (Figure 4.5). The aluminium foil was fixed with a thin adhesive layer on the acrylic substrates at room temperature, acting as both the triboelectric material and the electrode 2 that is grounded. The dielectric layers (PDMS (d_{D1} = 125 µm), silicone rubber (d_{D1} = 150 µm), FEP (d_{D1} = 25 µm), polyimide (d_{D1} = 127 µm) and PET (d_{D1} = 60 µm)) were fixed with conductive acrylic adhesive (d_A = 25 µm) at room temperature on a copper layer (d_{E1} = 100 µm) connected to an external load of 10 MΩ for electrical characterization. The honeycomb-patterned aluminium foil was selected to improve the contact electrification due to its surface morphology. Surface patterning is potentially a low-cost option to enhance the output performance of the DMCS-TENG prototypes [68, 115, 116].

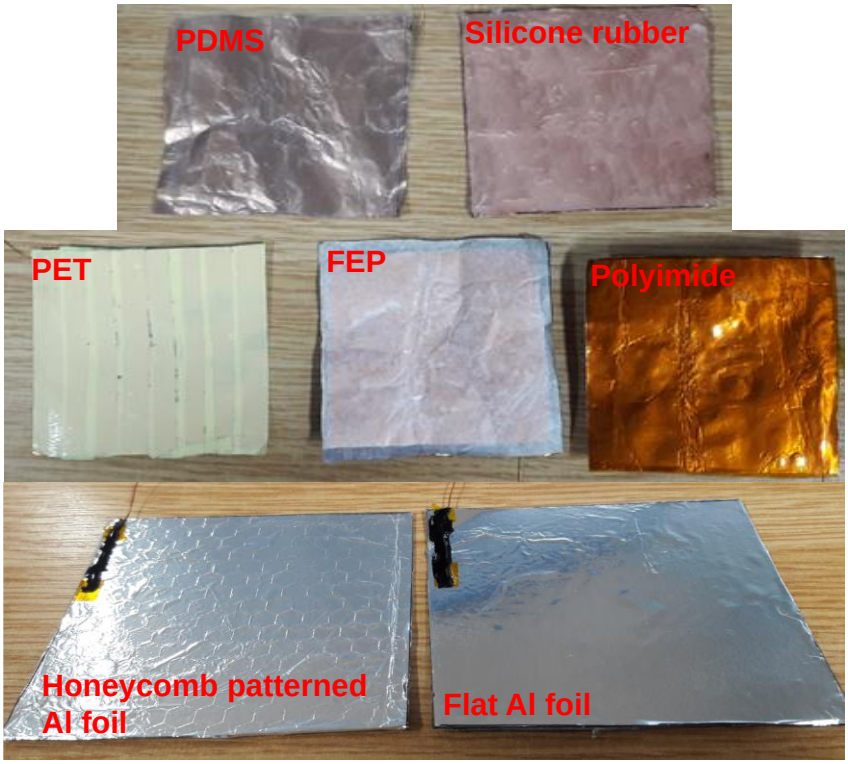

Figure 4.5 Selected triboelectric materials for the DMCS-TENG fabrication, electrical characterization and the study of the effect of surface morphology.

The output performance response of the fabricated DMCS-TENG devices focused in the frequencies of interest 30, 80, 150, 200, 219 and 252 Hz was characterized using a Pasco Scientific SF-9324 mechanical shaker table connected to a TG550 function generator to replicate the conditions of the mechanical energy generated by the oscillating frequencies caused by breaking water wave impacts. The function generator output was configured as a sine wave and the frequency swept from 25 to 300 Hz with an increasing step of 5 Hz for 55 seconds. The driving amplitude was set at 20 V peak-to-peak. The Al electrode was placed facing the surface of the dielectric layer and bound together on each side at the middle with Kapton tape (1 cm width) at room temperature (Figure 4.6 (a)). Finally, each of the DMCS-TENG prototypes was mounted as depicted in Figure 4.6 (b). The gap of the DMCS-TENG varies with the mechanical oscillation producing the triboelectric effect when the dielectric layer is in non-uniform contact with the aluminium film. The average acceleration, velocity and displacement generated by the mechanical shaker on the proposed energy harvester prototypes were measured with a PDV-100 Portable Digital Vibrometer (Figure 4.6 (c)). All the measurements were performed with controlled and standardized conditions to produce repetitive results (10 measurements performed on each sample).

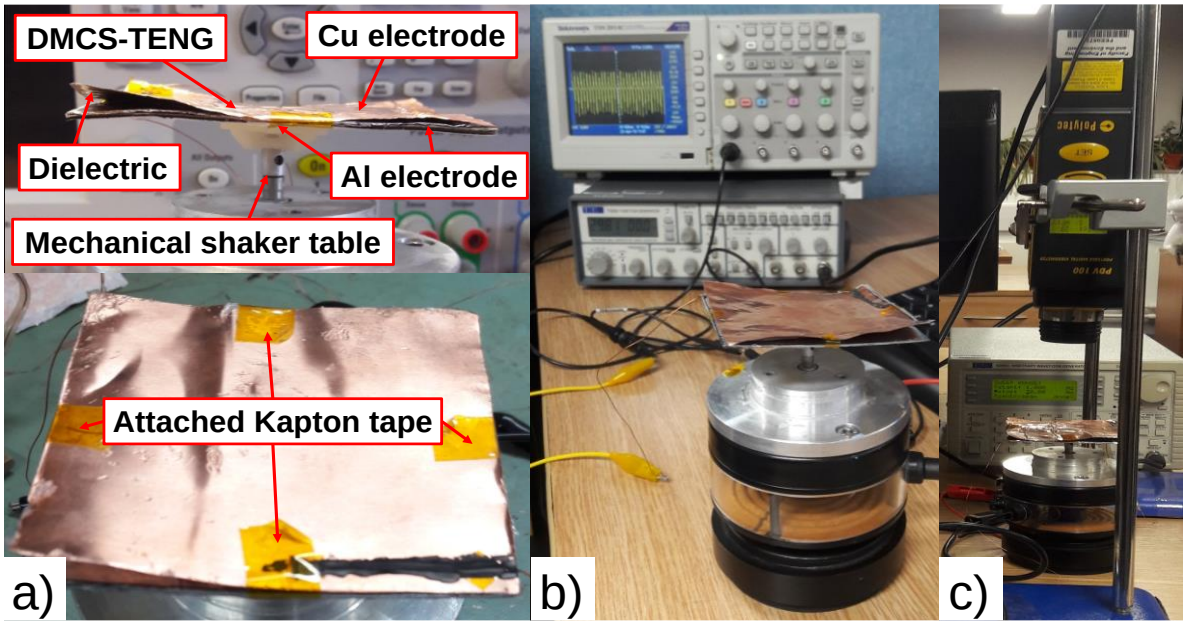

Figure 4.6 (a) Fabricated DMCS-TENG, (b) DMCS-TENG mounted on the mechanical shaker table for the output performance measurements at different frequencies of oscillation. (c) The average measurements of acceleration, velocity, and displacement of the top dielectric layer when contacts the conductor layer of the energy harvester measured with a PDV-100 Portable Digital Vibrometer.

The energy harvester prototype which shows the higher output power performance through the aforementioned experiment was characterized in water conditions using a wave generator tank, to simulate the real conditions of the mechanical energy generated by water wave impacts. A hybrid stepper motor (RS Pro 535-0502) attached with an acrylic layer of 20 cm x 20 cm (t = 8 mm) is used

to generate the breaking water waves into the water wave tank mounted on the left side of the tank. The DMCS-TENG prototype was insulated with a polyethylene plastic pack, to protect it from the contact with water. Such device was placed at the wall on the right side of the tank facing the impact of the water wave as shown in Figure 4.7 where the water wave breaks with an amplitude of 10.5 cm and frequency of 1.20 Hz. The output power generated by the DMCS-TENG prototypes was calculated through the output voltage, and output current measurements performed using a digital oscilloscope Tektronix TDS 2014C and an Agilent Technologies N6705B Power analyser (10 measurements performed on the sample).

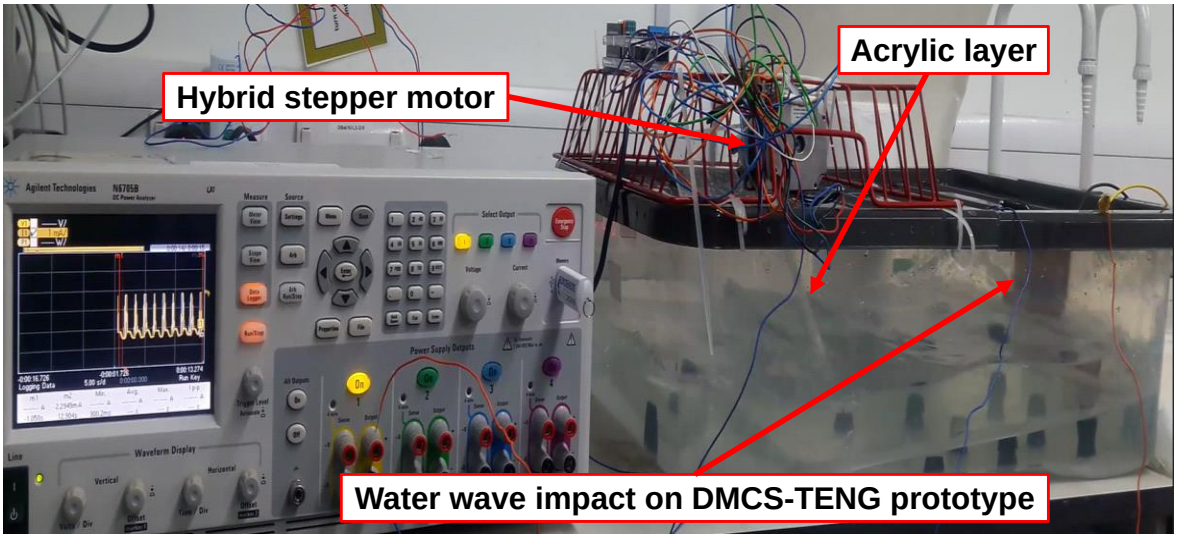

Figure 4.7 Insulated DMCS-TENG prototype placed on the water wave generator tank for its output performance measurements.

4.3.2 The dynamic operation, experimental results and analysis of the electrical characterization of the DMCS-TENG energy harvester prototypes

The analytical model to calculate the maximum open-circuit voltage at the resonant frequency of the DMCS-TENG prototype through the motion of the oscillatory system can be described at the device level as a damped system subjected to a harmonically varying force provided by the mechanical shaker table. The relative displacement of the top plate is a function of the vibration frequency, which is given by [117, 118]:

$$X_t = \frac{F_0 \sin(2\pi f t - \emptyset)}{k\sqrt{(1-\left(\frac{f_0}{f}\right)^2)^2+(\frac{2f_0\zeta}{f})^2}} \quad (4.5)$$

Where f is the vibration frequency, F_0 is the external force amplitude, which is $F_0 = m_0 a$, a is the acceleration of the shaker system. ϕ is the phase angle and ζ is the damping coefficient of the DMCS-TENG system. In the vibration process, due to the non-uniform contact between the

dielectric-metal layer, generates the open-circuit voltage V_{oc} for an electric potential difference between the two electrodes as follows:

$$V_{oc} = \frac{\sigma x}{\varepsilon_0} \tag{4.6}$$

Where σ is the triboelectric charge density, ε_0 is the vacuum permittivity and x is the distance variation between the layers in contact. For a system in vibration, the layer separation is relative to the displacement of the top layer (dielectric layer). As a result, substituting equation (4.5) into equation (4.6), the open circuit is given by:

$$V_{oc} = \left(\frac{\sigma}{\varepsilon_0}\right)\left(\frac{(m_0 a)(\sin(2\pi f t - \emptyset))}{k\sqrt{\left(1-\left(\frac{f_0}{f}\right)^2\right)^2 + \left(\frac{2f_0\zeta}{f}\right)^2}}\right) \tag{4.7}$$

Based on equation (4.7), the open-circuit voltage of the DMCS-TENG can be determined by parameters such as time t, vibration frequency f and phase angle $\emptyset$. However, the maximum open-circuit voltage V_{ocmax} is only a function of vibration frequency, which can be expressed by:

$$V_{ocmax} = \left(\frac{\sigma}{\varepsilon_0}\right)\left(\frac{m_0 a}{k\sqrt{\left(1-\left(\frac{f_0}{f}\right)^2\right)^2 + \left(\frac{2f_0\zeta}{f}\right)^2}}\right) \tag{4.8}$$

Consequently, the V_{ocmax} at resonant frequency ($f = f_0$) can be expressed as [117, 118]:

$$V_{ocmax} = \left(\frac{\sigma}{\varepsilon_0}\right)\left(\frac{m_0 a}{2k\zeta}\right) \tag{4.9}$$

where m_0 is the mass of the top plate, k is the stiffness coefficient of each spring, and a is the acceleration of the mechanical shaker table and the damping coefficient ζ of the DMCS-TENG system that is 0.30 calculated by $\zeta = \frac{2m_0 ln2}{T_{\frac{1}{2}}}$ [6]. Where $T_{1/2} = t_1 - t_2 = 0.009s$, is the time of the open-circuit voltage generated by the DMCS-TENG in one cycle of external vibration as shown in Figure 4.8.

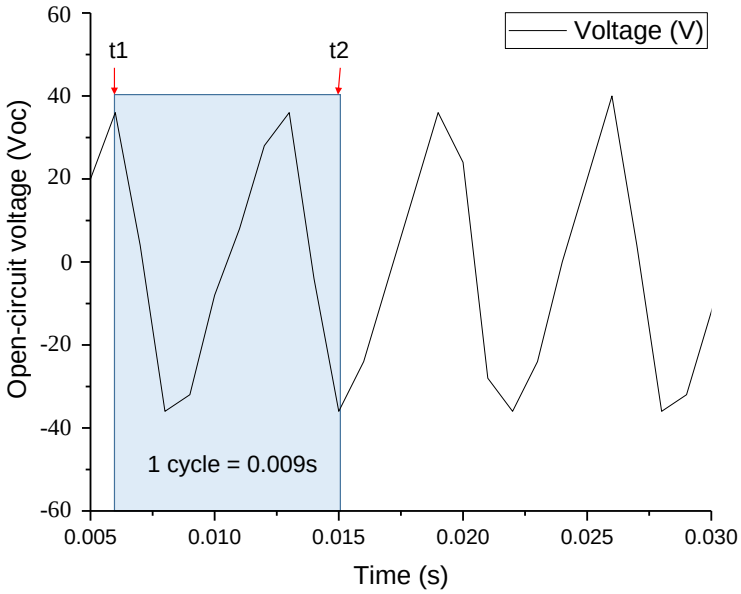

Figure 4.8 Open-circuit voltage generated by the DMCS-TENG in one cycle of external vibration at 150 Hz. The open-circuit voltage sinewave looks distorted for the range of data points acquired during its measurement through the Agilent Technologies N6705B power analyser.

The DMCS-TENG prototypes respond to the mechanical energies applied through resonant oscillatory frequencies. Where the aluminium foil is in constant non-uniform contact with the dielectric film and attracts electrons away from the copper electrode to flow through the external resistance load as shown in Figure 4.9 (a-f) for all the measurements at each frequency over 30 s. It has been observed that the maximum peak-to-peak output performance was measured for the DMCS-TENG prototypes using the honeycomb-patterned foil in contact with polyimide (Figure 4.9 (a-f)). This can be compared with the instantaneous output voltage, current and transferred charges measured using flat Al foil – polyimide illustrated in Figure 4.9 (a-f).

Among all the DMCS-TENG prototypes employing the top five triboelectric material combinations (Table 4.1 (tested)) in contact with flat Al foil and honeycomb-patterned Al foil, the following results were found. The output power performance comparison between 30 to 252 Hz with an acceleration between 319.62 to 559.29 mm/s^2 of amplitude showed an improvement factor of 2.3 for the DMCS-TENG devices fabricated using the patterned aluminium foil, relative to those fabricated using flat foil (Figure 4.11 (a)). Such enhancement of the measured values shows the effectiveness of the honeycomb-patterned aluminium foil to improve the electrical contact and surface charge density between the selected triboelectric layers. The maximum generated output voltage (V_{RMS}) was 12.50 V, with output current (I_{RMS}) of 62.27 µA, and transferred charges of 260 nC, which corresponds to the output power and power density of 781.31 µW and 12.16 µW/cm^2, respectively. This was reached using polyimide in contact with the honeycomb-patterned Al foil at the frequency of 150 Hz and an average acceleration of 559.29 mm/s^2. This is followed by the DMCS-TENG devices using PDMS and FEP with the output voltage (V_{RMS}) from 11.10 V to 4 V, current (I_{RMS}) from 22.16 µA to

63.62 µA, transferred charges between 85.27 nC to 82.44 nC, output power from 244.41 µW to 256.43 µW and power density from 3.84 µW/cm^2 to 3.98 µW/cm^2, in contact with the patterned Al foil (Figure 4.11 (a)). Additionally, the lower output performance was measured with the devices with silicone rubber and PET materials with output voltage (V_{RMS}), current (I_{RMS}), transferred charges, power and power density values from 6.20 V to 3.83 V, 0.66 µA to 1.32 µA, 1.36 nC to 1.68 nC, 4.09 µW to 5.04 µW and 0.063 µW/cm^2 to 0.078 µW/cm^2, respectively (Figure 4.11 (b)).

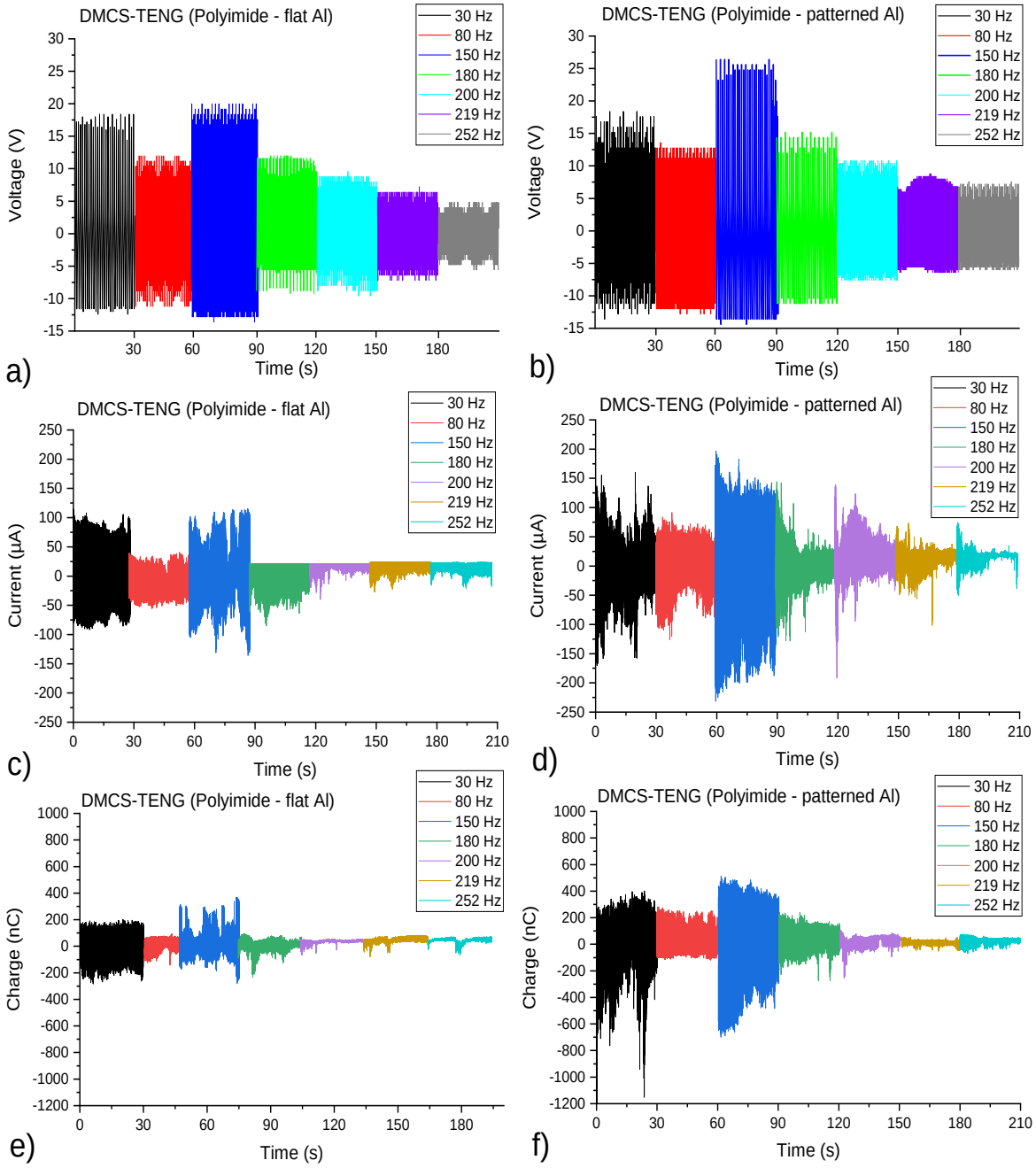

Figure 4.9 DMCS-TENG with polyimide-flat Al and polyimide-honeycomb patterned Al instantaneous (a-b) voltage-time, (c-d) current-time and (e-f) transferred charge-time response through simulated resonant frequencies of 30 Hz, 80 Hz, 150 Hz, 180 Hz, 200 Hz, 219 Hz and 252 Hz.

The total energy conversion efficiency (ECE) η of the DMCS-TENG self-resetting system with Polyimide-honeycomb patterned aluminium foil was defined as the ratio between the input mechanical energy and the generated electrical energy $E_{electric}$ that is delivered to the load resistance of 10 MΩ by the DMCS-TENG. The efficiency is determined by (4.4) [114]:

$$\eta = \frac{E_{electric}}{E_{mechanical}} x100\% = \frac{E_{electric}}{E_{kinetic} + E_{elastic}} x100\% \quad (4.4)$$

The $E_{electric}$ generated by the DMCS-TENG shows an energy output between 0.40 of 13.02 μJ during a time of 60 s. The kinetic $E_{kinetic}$ and elastic $E_{elastic}$ energy applied to the DMCS-TENG by the mechanical shaker ($E_{mechanical} = E_{kinetic} + E_{elastic}$) was calculated by equation (4.1) and (4.2). The measured values for the dynamics of the DMCS-TENG were between 319.62 to 559.29 mm/s^2 for the average acceleration *a*, 163.95 to 286.30 mm/s for the average velocity *v* and between 0.10 to 0.26 mm for the average displacement *x* of the top dielectric layer, measured with a PDV-100 Portable Digital Vibrometer as shown and highlighted in Figure 4.10 (a-d) at the frequencies of interest (30 Hz to 252 Hz). Considering as spring the bending of the top layer, and as constraints the attached kapton tape used to bound four sides of the conductor layer with the dielectric layer that generates the self-resetting system (Depicted in Figure 4.6 (a)). The bending stiffness ($k = \frac{F}{x} = 4$ to 6.14 N/m) was estimated based in the mass ($m_{Polyimide} = 2\ grams$) and average displacement *x* of the moveable top dielectric layer. *N* is the number of springs considered for the DMCS-TENG (*N* = 1), *F* is the force used by the mechanical shaker to move the DMCS-TENG prototypes ($F = ma$, $m_{Polyimide} = 2\ grams$).

$$E_{kinetic} = \frac{1}{2} mv^2 = 26.87\ to\ 81.96\ \mu J \quad (4.1)$$

$$E_{elastic} = \frac{1}{2} kx^2 N = 0.13\ to\ 0.58\ \mu J \quad (4.2)$$

The energy applied ($E_{mechanical}$) to the DMCS-TENG by the mechanical shaker table was calculated to be between 26.91 μJ to 82.11 μJ, which indicates an efficiency between 1.51 % to 15.85 % for the main frequencies of interest between 30 Hz to 252 Hz. The highest efficiency was calculated at 150 Hz and average acceleration of 559.29 mm/s^2, followed by 30 Hz with an acceleration of 549.14 mm/s^2 as shown in Figure 4.11 (a) according to the experimental measurements.

$$\eta = \frac{E_{electric}}{E_{mechanical}} x100\% = \frac{E_{electric}}{E_{kinetic} + E_{elastic}} x100\% = 1.51\ to\ 15.85\% \quad (4.4)$$

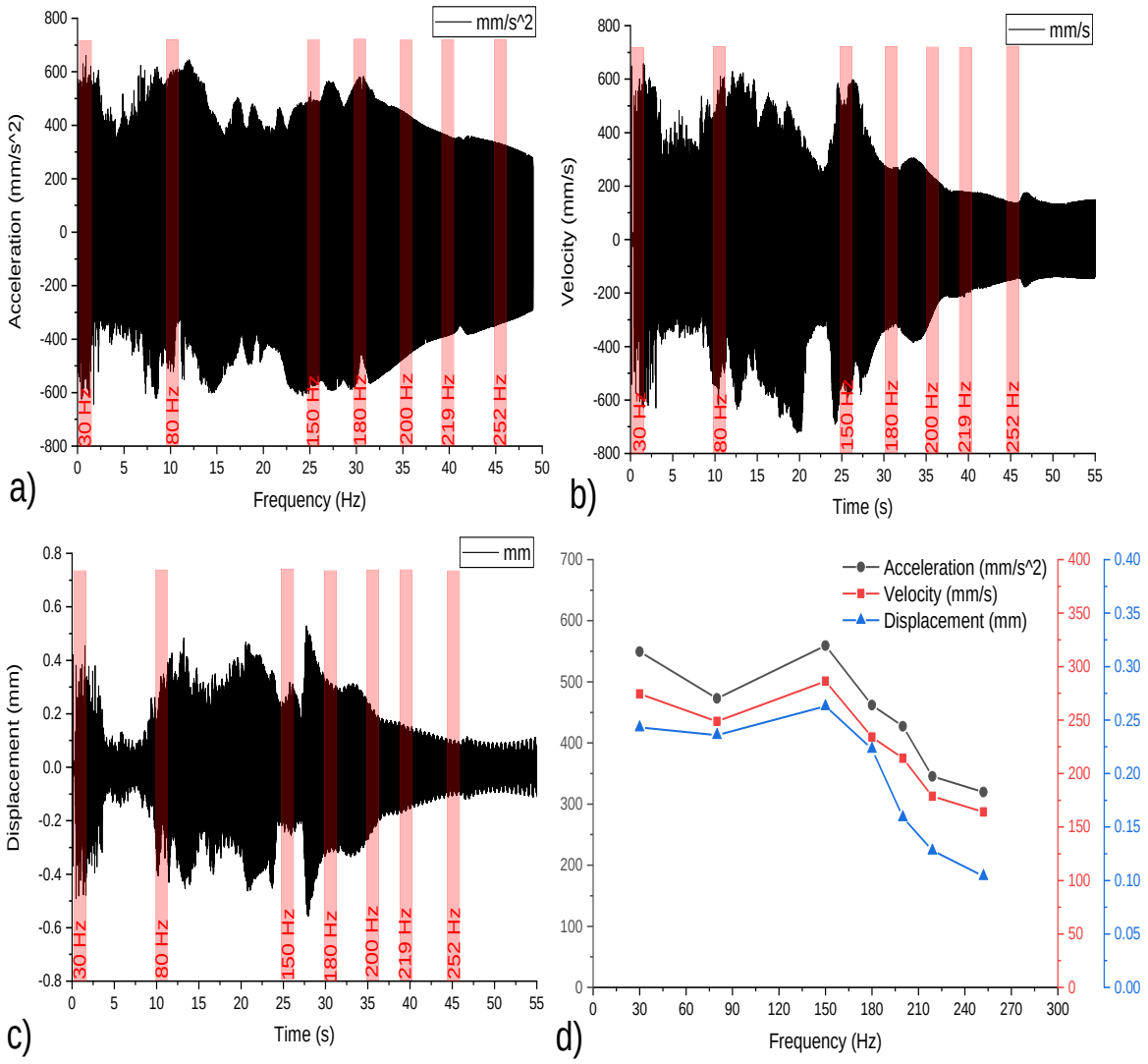

Figure 4.10 (a) Acceleration, (b) velocity and (c) displacement of the top dielectric layer when in contacts the conductor layer of the DMCS-TENG prototype during the vibration frequency swept from 25 to 300 Hz with an increasing step of 5 Hz for 55 seconds. (d) Average acceleration, velocity and displacement of the top dielectric layer measured with a PDV Portable Digital Vibrometer.

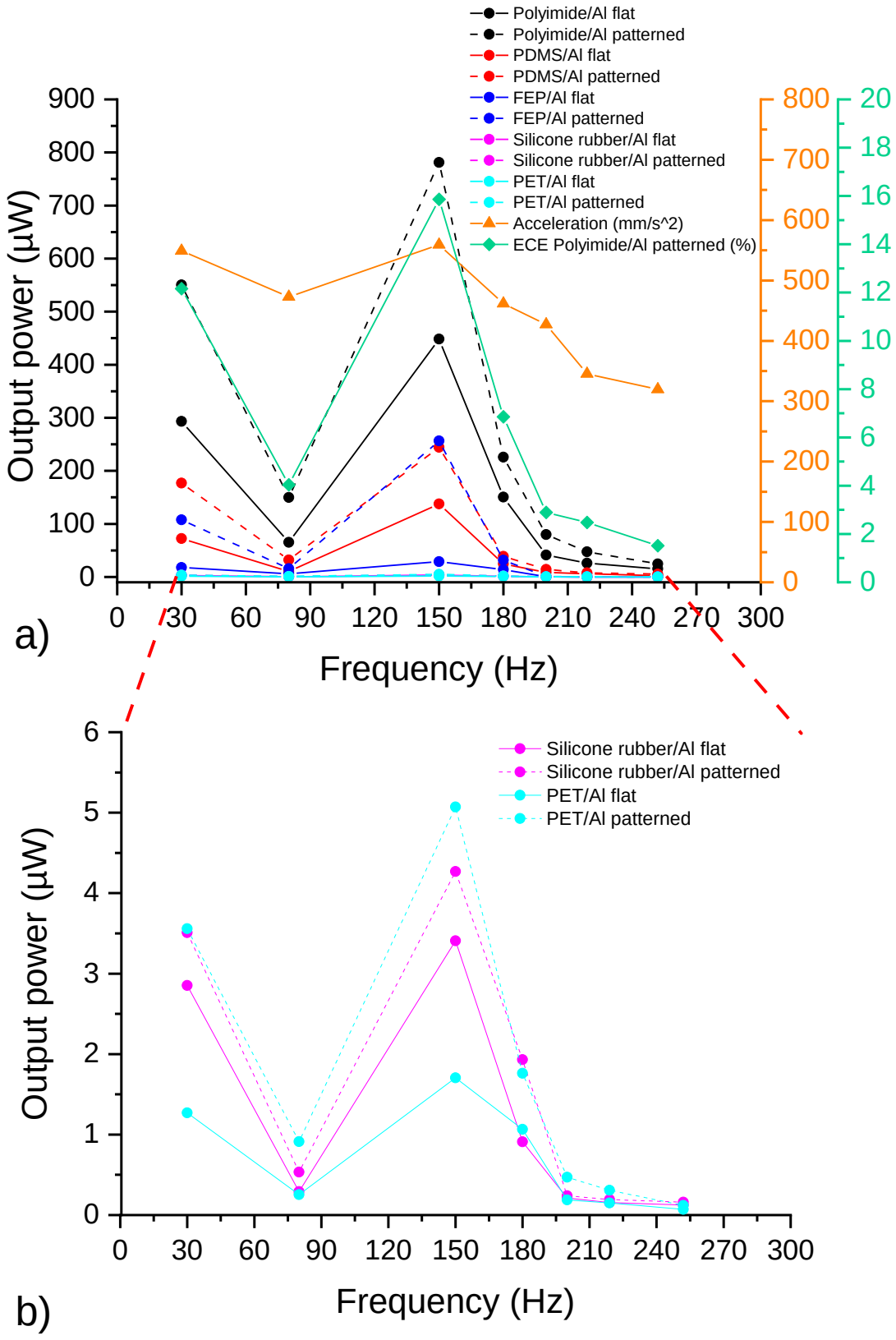

Figure 4.11 (a) DMCS-TENG output power, ECE % and average acceleration measured at the main compressed air bubble frequencies generated during wave impact with polyimide (Kapton), PDMS, FEP, silicone rubber, PET – flat Al foil/honeycomb-patterned Al foil. (b) Zoom of the output power generated for the DMCS-TENG devices with silicone rubber and PET.

It was observed, however, that at 80 Hz with an acceleration of 472.78 mm/s^2 and frequencies greater than 180 Hz with an acceleration between 319.62 to 461.77 mm/s^2, the output power performance response and efficiency of the devices were lower as shown in Figure 4.11 (a). The variation in the output power performance and efficiency (Figure 4.11 (a)) shows that the proposed devices can effectively respond to a broad range of input oscillating frequencies showing different resonant peaks from 25 Hz to 300 Hz (Figure 4.10 (a-d)), because of the non-uniform contact between the dielectric-conductor layer. This shows that the DMCS-TENG has a considerably wide working bandwidth and that can probably reach higher output performance and efficiency within the frequency sweep a part of the frequencies of interest, with the oscillatory frequencies that show higher acceleration, velocity, and displacement of the top dielectric layer depicted in Figure 4.10 (a-c). This means that the device has the potential to produce a higher output power at the moment when the water wave impacts the water-structure interfaces between 30 Hz and 50 Hz, and after the wave collapses, where the air bubbles are formed between 150 Hz and 200 Hz as illustrated in Figure 1.1 (a-d) [12, 13]. The maximum output performance measured experimentally is related to the calculated response obtained by the FEM simulation at 150 Hz for the proposed energy harvester prototypes, under similar conditions of operation as described in Chapter 3. Followed by a similar trend in the output performance at the frequencies of 30 Hz and 80 Hz between the computational simulation and the experimental results in the energy harvesters as illustrated in Figure 3.8 (a-c) and Figure 4.11 (a-b).

Additionally, the difference in the output performance between the simulated DMCS-TENG and the real prototypes arises because the FEM simulations were solved by assuming the maximum surface charge density between layers in contact under ideal conditions. This leads to higher output power values between 3.66 mW to 416.47 µW. Compared with the measured output power values of the built and tested devices between 781.31 µW to 244.41 µW in non-ideal conditions.

Moreover, to demonstrate the capability of the DMCS-TENG prototypes as direct power source, 62 Kingbright L-7104PWC-A 3 mm white LEDs (1200 mcd) were utilized as operating load connected to the device with the triboelectric material combination of polyimide-honeycomb patterned Al foil. The peak AC output current of the DMCS-TENG without rectification was capable of instantaneously and continuously lighting up 62 serially connected white LEDs when the device was under 150 Hz mechanical oscillation and average acceleration of 559.29 mm/s^2 (Figure 4.12 (a)). The measured average power consumption by the LEDs was around 13.48 mW for this demonstration.

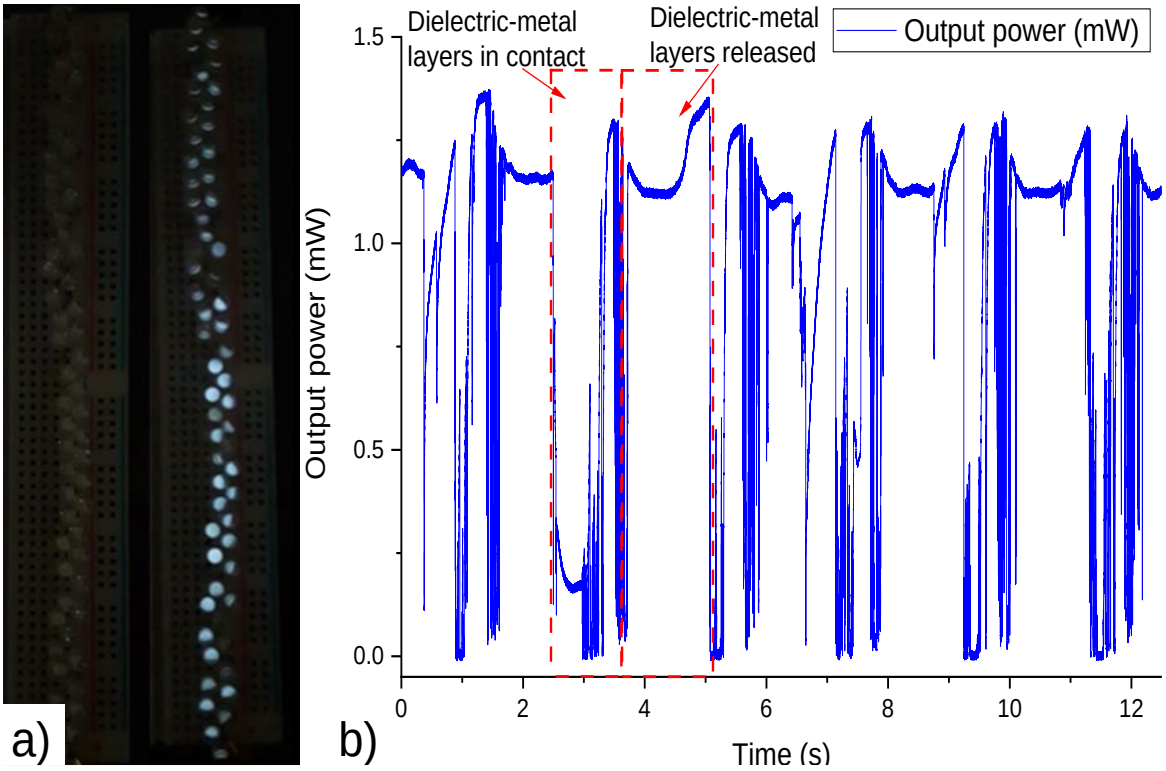

Figure 4.12 (a) Power up of 62 serially-connected white LEDs instantaneously and continuously with the DMCS-TENG prototype (polyimide-honeycomb patterned Al foil). Measured average instantaneous power consumption by the LEDs was around 13.48 mW. (b) Output power generated by the DMCS-TENG prototype (polyimide-honeycomb patterned Al foil), when the dielectric-metal layers are in contact and released exposed to water wave impact with an amplitude of 10.5 cm and frequency of 1.2 Hz.

Finally, the generated output power by the aforementioned energy harvester, when the dielectric-metal layers are in contact and released under the breaking water wave impact generated in the tank, is shown in Figure 4.12 (b). This device with its area of 64 cm^2 generated an instantaneous output power, power density of 1.08 mW, 169.22 mW/m^2, respectively. Consequently, extrapolating the potential of the DMCS-TENG for breaking water wave impact energy harvesting in large scale [26], the output power generated for one energy harvester and the frequency of impact (1.2 Hz) were considered. Assuming that the DMCS-TENG prototypes are tiled (electrically connected) and there is no loss in their output power performance during the scalability covering a water-structure interface with an area of 18 m^2 that receives wave sizes among 0.3 m to 4 m [119]. It is expected to generate output power and energy of 3.05 W and 2.53 J, placing 2,812 of the DMCS-TENG prototypes over the water-structure interface.

The total energy (potential energy and kinetic energy) of a wave can be calculated by [120]:

$$E_{waterwave} = \frac{1}{2}\rho g A_{waterwave}{}^2 \qquad (4.10)$$

Where g is the acceleration of gravity (g = 9.8 m/s^2), ρ is the density of water (ρ = 1000 kg/m^3) and $A_{waterwave}$ is the wave amplitude ($A_{waterwave}$ = 10.5 cm, frequency = 1.2 Hz). The input energy $E_{waterwave}$, produced by the water wave impact in the tank (Figure 4.7), was found to be approximately 49 J. Accordingly, the DMCS-TENG devices have an efficiency of 5.16 %, calculated by:

$$\eta = \frac{E_{electric}}{E_{waterwave}} x100\% = 5.16\% \quad (4.11)$$

As a result of the power levels achieved by the devices, it is feasible to propose that such energy harvesters can be potentially used to energize wireless nodes for coastal sensing applications.

4.4 Chapter summary

The developed work through this chapter has shown that the triboelectric effect using solid-solid triboelectrification can be used to realize an innovative type of energy harvester for breaking ocean wave impact forces. Firstly, by comparing the findings of the literature, PTFE is the most electronegative material which is widely used in TENG fabrication [68, 82]. Therefore, in this work through an impact test, it was found the ideal dielectric-conductor triboelectric material combinations for the fabrication of the DMCS-TENG prototypes. The results showed that silver conductive cloth tape is the material that attains maximum positive charge, and PDMS as the material that attains maximum negative charge. For the same load conditions (5 MΩ), it was found that the best output performance was obtained by using dielectric layers with thicknesses between 100 to 125 µm. Additionally, the highest output power is obtained when using polyimide as the negative material in contact with the honeycomb-patterned Al foil by employing a mechanical shaker for the DMCS-TENG devices output performance characterization. Such results indicate that the experiments set-up change the mechanical force conditions [121, 122] of the contact electrification performance between the dielectric-conductor, which was reflected in the output power performance of the proposed TENG devices. A different most negative material was found compared with the one shown in the literature being polytetrafluoroethylene (PTFE) when the contact is made between dielectric-metal materials [68, 82]. Such results suggest that the previously published triboelectric series [68, 82] may not give the obvious material pair for the best energy harvesting performance under all circumstances, due to the inaccurate qualitative ranking without numerical data and difference in the mechanical properties of the materials (elasticity, hardness, stiffness and thickness). Consequently, for cross-comparison, a standardized method must be created to quantify and normalize the triboelectric series (triboelectrification) [123]

focused on a wide range of dielectric-metal materials using thickness normalized values and standard experimental set-up conditions (atmospheric pressure, temperature, humidity, etc.).
Secondly, it was observed that the proposed devices' output power and ECE efficiency changes with the main oscillation frequencies between 30 Hz to 252 Hz with an amplitude average acceleration between 319.62 to 559.29 mm/s^2. Which was achieved through the fabrication and electrical characterization of the DMCS-TENG with the optimum design found employing the numerical simulation explained in Chapter 3 and under the effect of the wave impact oscillating frequencies. Such variation shows that the proposed devices can effectively respond to a broad range of input oscillating frequencies showing different resonant peaks at the aforementioned frequencies. The maximum output performance was reached using the optimum triboelectric material combination of polyimide – Al foil. Therefore, an enhancement in the output power performance by a factor of 2.3 was achieved using a honeycomb-patterned aluminium foil as a low-cost option to enhance the output performance of the DMCS-TENG prototypes. Such improvement in the output performance is due to the surface pattern of the Al foil, which increases the effective contact area between the materials that increase the triboelectric charges generated during the friction.
Finally, through the integration of the selected DMCS-TENG prototype into the breaking water wave generator tank an output power density of 169.22 mW/m^2 using an area of 64 cm^2 was generated. It is predicted that over an area of 18 m^2 with wave sizes of 0.3 m to 4 m, an output power of around 3.05 W is possible. This offers an alternative approach for generating electrical power for coastal sensing applications that require self-powering. Further investigation is presented in the following chapters, employing a hybrid nanogenerator and the study of liquid-solid interfaces as an alternative to harvest the breaking water wave impact energy and to enhance the electrical output performance.

Chapter 5 Hybrid nanogenerator for breaking water wave impact energy harvesting

5.1 Introduction

At present, wave energy conversion is mainly focused on the extraction of large-scale wave impact energy harvesting through the utilization of electromagnetic generators for the generation of electricity [47]. The EMG comprising turbines, metal coils, bulky and heavy magnets, which are very expensive and technically complicated to fabricate [53]. Consequently, different challenges should be addressed like the proposal of an alternative integration concept of wave energy harvesters and breakwater structures for breaking water wave impact energy harvesting. Due to that reason, as hybrid devices combined with TENG-electromagnetic generators (EMG) [39, 40] have been developed focusing in harvesting the irregular motions at low frequencies between 0.5 Hz to 5 Hz, generated by the shallow ocean wave energy.

Furthermore, it was demonstrated the harvesting of breaking water waves impact forces in a broadband frequency range from 30 Hz to 252 Hz using dielectric-metal contact separation mode triboelectric nanogenerators (DMCS-TENG) with solid materials in contact in the previous chapter [124, 125]. However, further investigation is required to explore suitable designs of TENG with engineering challenges to improve the output power and energy conversion efficiency harvesting the breaking ocean wave impact for self-powered applications. Through this chapter, it is developing research of an alternative approach, stable, easy, simple to fabricate, and lightweight hybrid nanogenerator to promote the output current to improve the low output power of DMCS-TENG harvesting the impact of the water waves as previously studied [124, 125]. Focused at low-frequency impact among 0.7 Hz to 3 Hz, by integrating a polyvinylidene fluoride (PVDF) piezoelectric layer [55, 126] with suitable chosen triboelectric material pairs [82, 83, 116, 125].

Firstly, the simultaneous operation of triboelectric-piezoelectric effects [127-129] in comparison with piezoelectric nanogenerator (PENG), DMCS-TENG and arc-shaped DMSE-TENG under breaking water wave impact was studied. The hybrid nanogenerator energy harvesters utilize dielectric-to-conductor triboelectric contact, and flexible piezoelectric material with an active area of 4 cm x 4 cm. Secondly, complementing the FEM simulation coupling triboelectric-piezoelectric effects to form a hybrid nanogenerator developed in Chapter 3, the generated output voltage, output current, transferred charges and output power by the proposed hybrid devices were characterized in water conditions using a breaking water wave generator tank, which simulates the conditions of

the mechanical energy generated by water wave impacts on the shoreline at low frequencies mentioned above. Thirdly, the electric output performance of the hybrid prototypes was compared with triboelectric nanogenerators and piezoelectric nanogenerators tested in similar conditions [125]. Additionally, a load resistance matching experiment was performed with the objective being to obtain maximum output power performance from the hybrid prototypes.

Finally, the ability to charge a variety of capacitors with a single hybrid device and a grid of four hybrid devices connected in parallel [26, 53, 130] was characterized and their potential to drive small electronic devices was tested.

5.2 Working mechanism of electricity generation, fabrication and characterization of hybrid nanogenerators energy harvester prototypes

The hybrid prototypes composed with a three-electrode configuration with an active area of 4 cm x 4 cm depicted in Figure 5.1 (a) and Figure 5.1 (e), were fabricated using a simple and low-cost process. Two carbon conductive ink electrodes (E2 and E3) were manually printed on both sides of a flexible PVDF piezoelectric layer (PIEZOTECH, d_P = 40 µm) at room temperature (Figure 5.1 (b) and Figure 5.1 (f)). Therefore, by using suitable triboelectric materials [82, 83, 116, 125], a dielectric polyimide (d_{D1} = 50.8 µm) was manually fixed with conductive glue at room temperature on a copper layer (d_{E1} = 100 µm) which acts as E1. Additionally, the E1 layer was manually insulated on the other side using Kapton polyimide heat and chemical resistant tape at room temperature. Then, the E1 layer was placed facing the polyimide dielectric layer over the piezoelectric layer and bonded using Kapton tape at room temperature to form the arc-shaped dielectric-to-conductor structure with a gap of 5 mm on both sides (Figure 5.1 (a)).

Additionally, the arc-shaped dielectric-metal contact separation mode TENG (arc-shaped DMCS-TENG) that have an active area of 4 cm x 4 cm (Figure 5.1 (c)) and Figure 5.1 (g)), and an acrylic sheet was selected as a substrate material. An aluminium conductor layer (d_{E2} = 18 µm) was attached to the acrylic with a thin adhesive layer, at room temperature. Acting as both the triboelectric material and the electrode that is grounded. The polyimide dielectric layer (d_{D1} = 50.8 µm) was fixed with an arc-shaped form using conductive acrylic adhesive at room temperature on a copper layer (d_{E1} = 100 µm) that is used as the second electrode connected to an external load for electrical characterization. Additionally, the copper layer was manually insulated on the other side using Kapton. The maximum gap between the arc-shaped dielectric layer and the conductor layer is 5 mm. Therefore, the DMCS-TENG with self-restoring structure was fabricated following the process described in Chapter 4 (4.3.1) [124, 125] using the dielectric-metal contact between polyimide and aluminium (Figure 5.1 (d)) and Figure 5.1 (h)).

The three-electrode structure of the hybrid nanogenerator prototypes, which utilizes an arc-shaped dielectric-to-conductor triboelectric contact and a flexible piezoelectric material with an active area of 4 cm x 4 cm (Figure 5.1 (a)) and Figure 5.1 (e)). The energy applied to the hybrid nanogenerator system is translated into two coupled effects. The triboelectric effect is affected by $E_{kinetic}$ (5.1), which is the energy carried by the moveable arc-shaped dielectric layer that plays the role of contact material for triboelectricity, and $E_{elastic}$ (5.2) which is the energy stored in the dielectric layer acting as a spring for separation after contact.

$$E_{kinetic} = \frac{1}{2}mv^2 \tag{5.1}$$

$$E_{elastic} = \frac{1}{2}k_T x^2 N \tag{5.2}$$

where, v is the average velocity of the dielectric layer when the contact is made, caused by the water wave impact, m is the mass of the moveable arc-shaped layer. K_T is the spring constant due to a flexural stiffness, x is the displacement of the arc-shaped layer that is equal to the spacing between the two contacting surfaces (x = 5 mm), and N is the number of springs considered for the arc-shaped structure of the hybrid nanogenerator (N = 2).

Additionally, the piezoelectric effect is affected by the mechanical energy of the water wave impact which stresses the piezo-layer a distance x_P, and that can be approximately calculated by the work done, W due to pressing/pulling as shown in (5.3)[131].

$$W = F\Delta L \cong \sigma_P A_c \frac{2{x_P}^2}{L_0} \tag{5.3}$$

The piezo-film is stressed by tension $F = \sigma A_c$, where σ_P is tensile stresses, and A_c is the cross-sectional area of the piezoelectric layer. Considering the piezo-layer as an elastic medium, the spring constant k_P due to the stiffness in stretching that is given by $k_P = EA_c/L_0$, where E is the Young's modulus. The length change of the piezoelectric material ΔL, can be approximated as $\Delta L \cong \frac{2{x_P}^2}{L_0}$, defining $L \cong L_0$ [131].

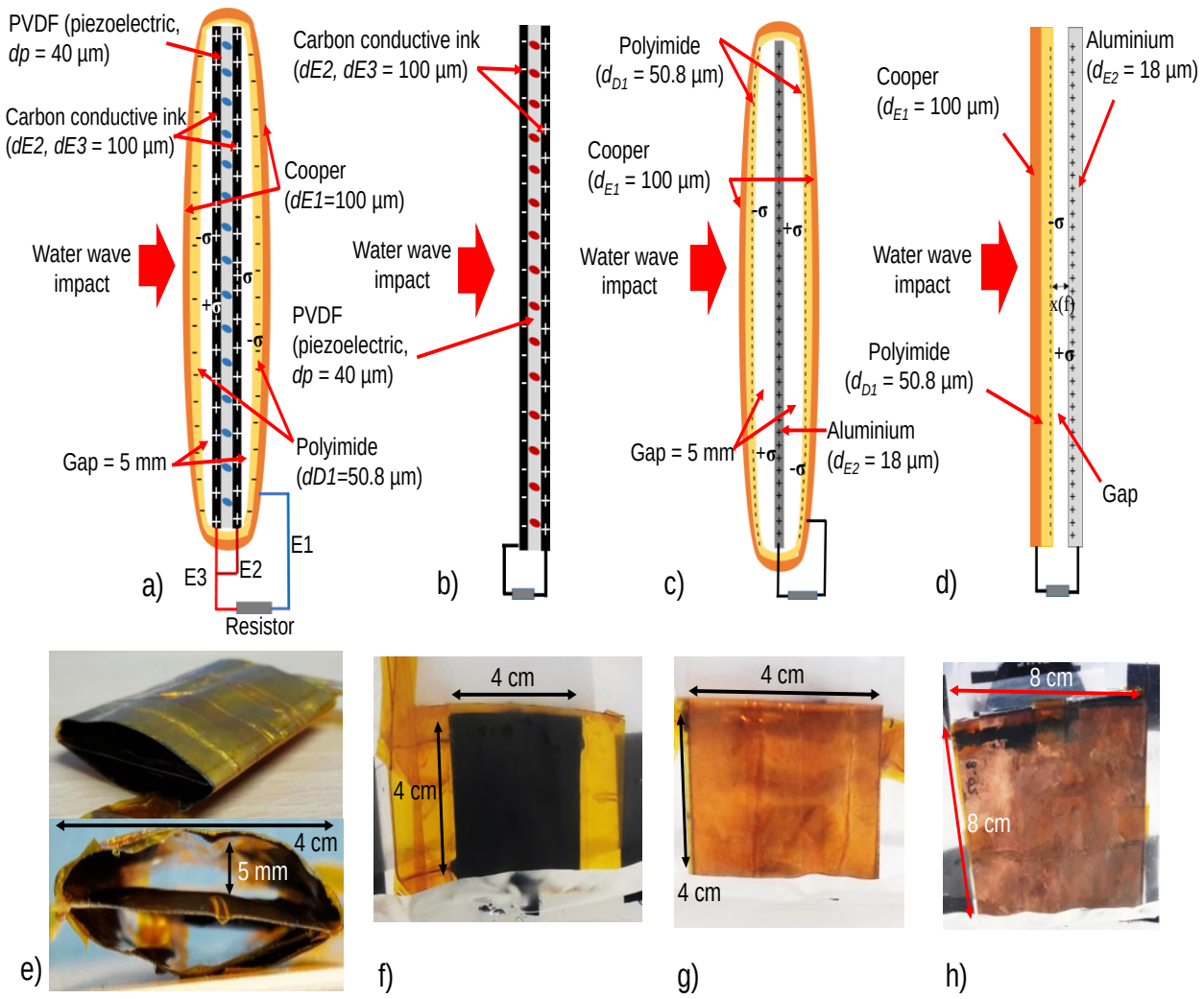

Figure 5.1 Two-dimensional schematic of the (a) Hybrid nanogenerator, (b) PENG with charge distribution when it is under an external force. (c) The arc-shaped DMCS-TENG, and (d) the DMCS-TENG self-resetting system. (e) Digital photo and a cross-sectional digital photo of the hybrid nanogenerator. Digital photo of the (f) PENG, (g) arc-shaped DMCS-TENG and (h) DMCS-TENG self-resetting system.

The operation of the PENG (Figure 5.1 (b)) and the two-electrode structures of the arc-shaped TENG (Figure 5.1 (c)) and DMCS-TENG with self-restoring structure (Figure 5.1 (d)) used to compare the output performance of the hybrid nanogenerator under breaking wave impact is as follows:

The operation of the PENG under breaking wave impact is illustrated in Figure 5.2 (a-e). First, the impact of the water wave produces tensile stress on the piezoelectric layer that changes the polarization as the charges flow from E1 to E2, when the PENG is contacted and pressed (Figure 5.2 (b)). Second, as the water wave breaks down and moves off the PENG device, no polarization exists so E1 and E2 remain electrically neutral as the device it is in the “contacted and released” state (Figure 5.2 (c)). Third, the piezoelectric material recovers to its original shape, with a change in piezoelectric potential, driving the charges to flow in the opposite direction. Therefore, there are

charges with opposite signs in E1 and E2, respectively (Figure 5.2 (d)). Finally, the PENG reaches equilibrium once again (Figure 5.2 (e)). Thus, one operational cycle of the PENG is achieved.

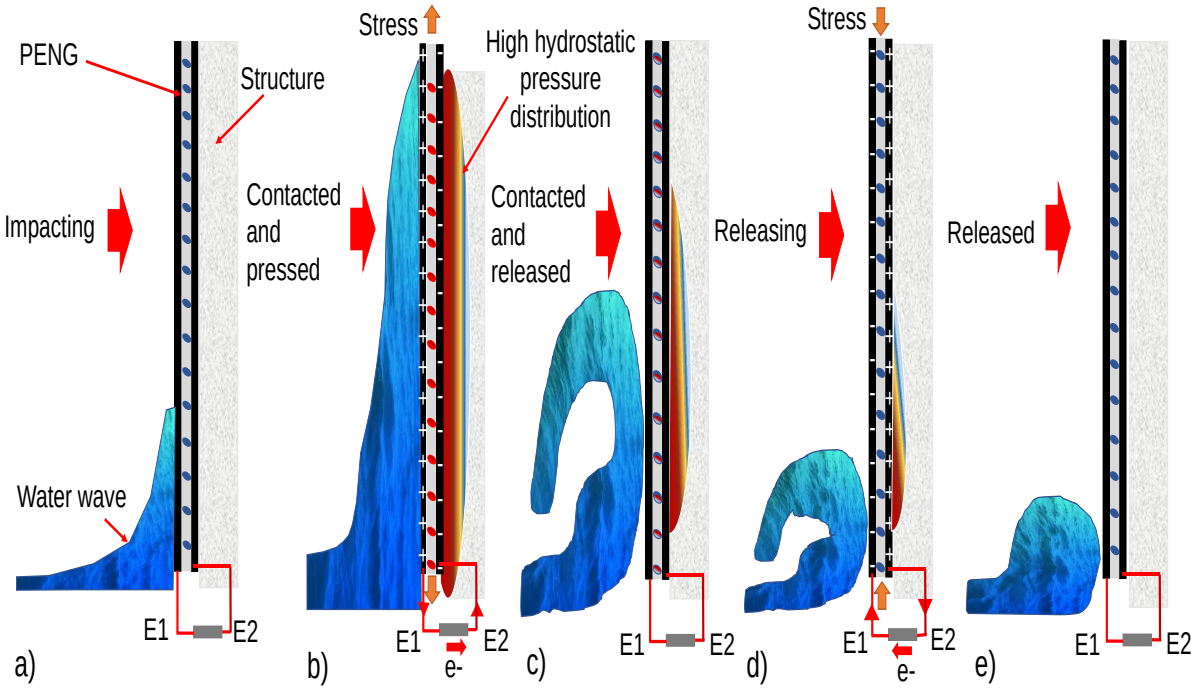

Figure 5.2 (a-e) Working mechanism of the piezoelectric nanogenerator under water wave impact.

Therefore, for the TENG devices, before the water wave impacts the TENG device, there are accumulated negative charges in the dielectric layer, and positive accumulated charges in the surface of the aluminium (Al) layer electrode 2 (E2). Such process will continue in the first cycles until the accumulated charges reach saturation, and the negative charges will be preserved on the dielectric surface due to the nature of the insulator layer [110] (Figure 5.3 (a)) and Figure 5.4 (a)). First, the impact of the water wave produces forward triboelectric effect as the gap between the contact-layers decreases (Figure 5.3 (b)) and Figure 5.4 (b)). Positive charges flow to E2 leaving E1 with negative charges, when the device is contacted and pressed (Figure 5.3 (b)) and Figure 5.4 (b)). Second, as the water wave breaks down and moves off the TENG device, no polarization exists so E1 and E2 remain electrically neutral as the device it is in the "contacted and released" state (Figure 5.3 (c) and Figure 5.4 (c)). Third, once the hydrostatic pressure is released, the dielectric layer rebound back due to the elasticity of the film and the gap increases that hence changes the electric field between the contacted dielectric-conductor materials. Positive charges flow through the external load to E1 leaving E2 with negative charges until the potential difference is fully offset by the transferred charges, rendering the E1 with a surface charge density of +Q, while the charges on E2 is with a sum of two parts. One part is due to the transferred charges between E1 and E2 (-Q) and the other part is due to the triboelectric charges at the surface of contact (Sσ). Thus, the total charges on E2 are Sσ – Q, as the structure of the TENG is releasing (Figure 5.3 (d) and Figure 5.4 (d)).

Finally, the TENG is fully released, and reaches equilibrium once again (Figure 5.3 (e) and Figure 5.4 (e)). Thus, one operational cycle of the TENG energy harvester is achieved. Once the following water wave impacts the TENG prototype, a periodic output will be obtained (Figure 5.3 (a-e) and Figure 5.4 (a-e)).

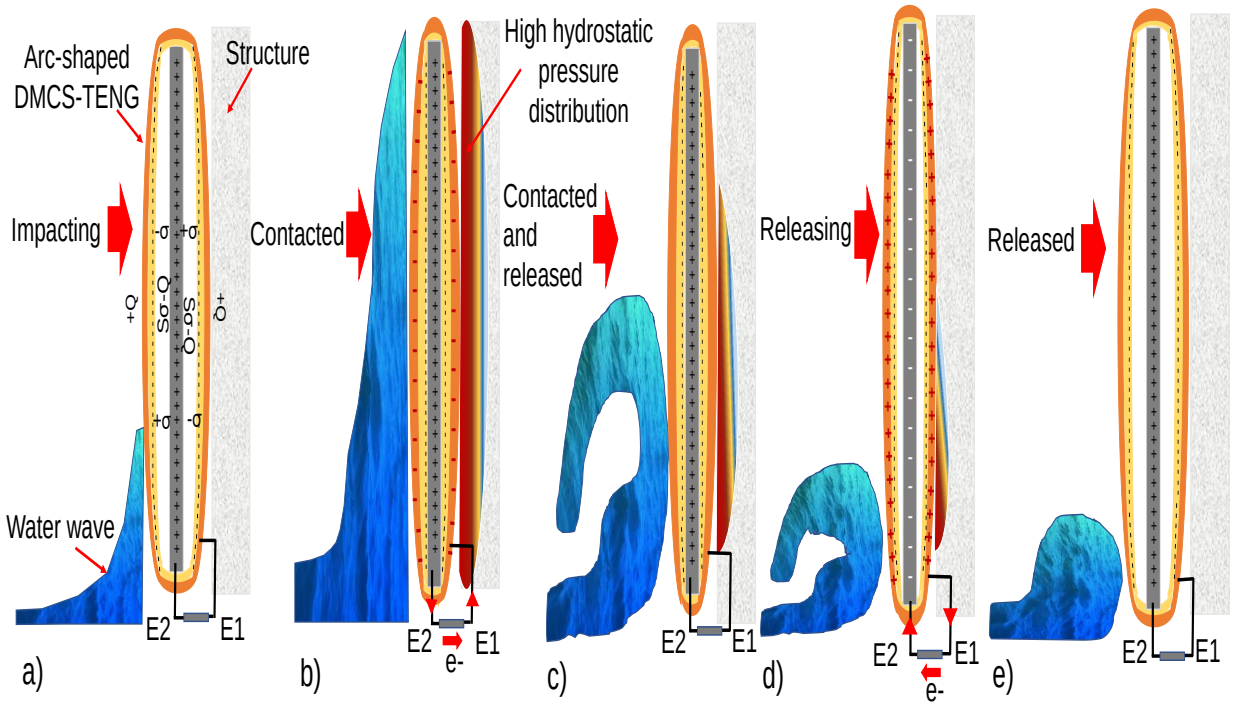

Figure 5.3 (a-e) Working mechanism of the Arc-shaped TENG at water wave impact conditions.

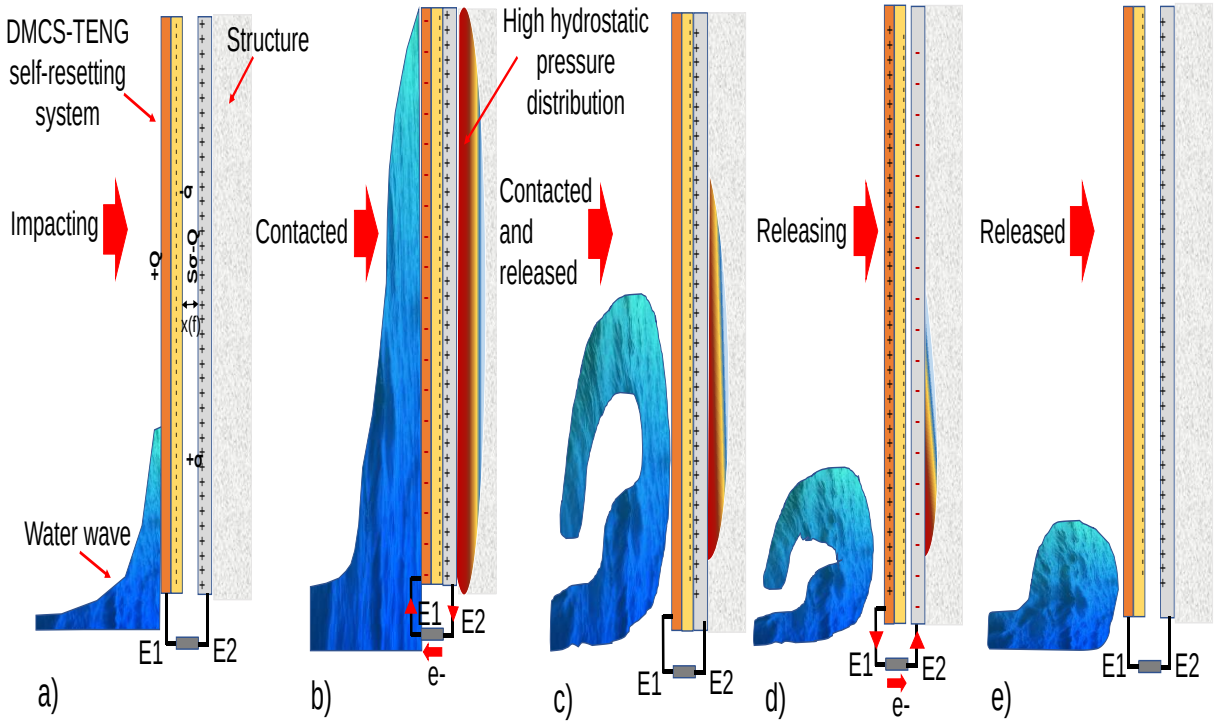

Figure 5.4 (a-e) Working mechanism of the DMCS-TENG at water wave impact conditions.

The simultaneous operation of triboelectric-piezoelectric effects at water wave impact conditions is depicted in Figure 5.5 (a-e). Before the water wave impacts the hybrid nanogenerator, there are accumulated negative charges in the dielectric layer, and positive accumulated charges in electrode 2 (E2) and electrode 3 (E3) caused by dielectric-to-conductor triboelectrification after few cycles of movement (Figure 5.5 (a) and Figure 5.5 (f)). First, the impact of the water wave produces forward triboelectric effect as the gap between contact-layers decreases, and a piezoelectric effect as the charges flow due to tensile stress on the piezoelectric layer (Figure 5.5 (b) and Figure 5.5 (g)). The piezoelectric polarization influences the charge distribution on electrode 1 (E1), and E3 since they are connected. Positive charges flow to E3 leaving E1 with negative charges, when the device is contacted and pressed (Figure 5.5 (b) and Figure 5.5 (g)). Second, as the water wave breaks down and moves off the hybrid device, no polarization exists so E1 and E3 remain electrically neutral as the device it is in the "contacted and released" state (Figure 5.5 (c) and Figure 5.5 (h)). Third, the gap increases and hence this changes the electric field between the contacted dielectric-conductor materials. The piezoelectric material recovers to its original shape, with a change in piezoelectric potential and electric field, driving the charges in the load to flow in an opposite direction. Therefore, there are charges with opposite signs in E1 and E3, respectively (Figure 5.5 (d) and Figure 5.5 (i)) as the structure of the hybrid prototype is releasing. Finally, the hybrid nanogenerator is fully released, and reaches equilibrium once again (Figure 5.5 (e)). Thus, one operational cycle of the hybrid prototype is achieved. Once the following water wave impacts the hybrid prototype, a periodic output will be obtained (Figure 5.5 (a-e)).

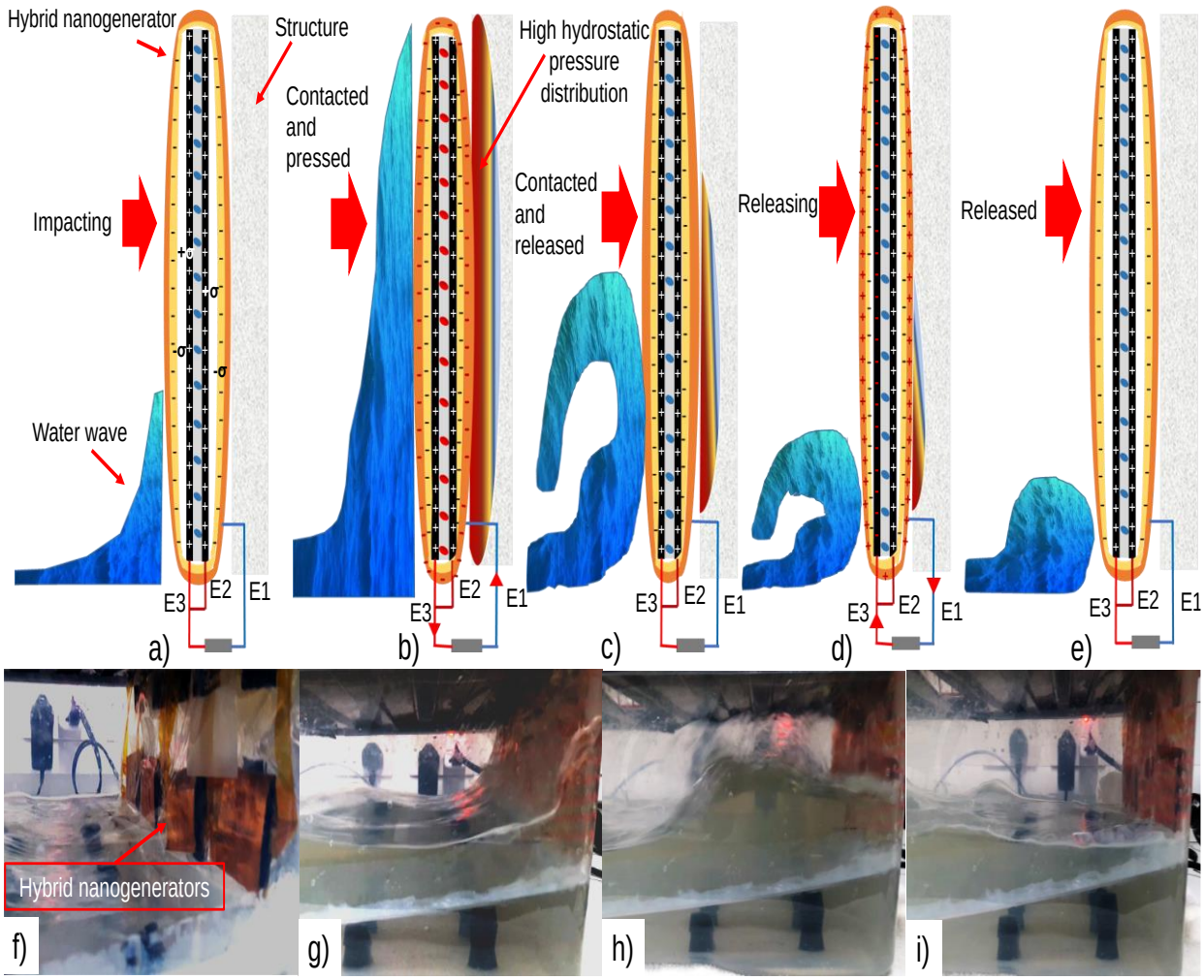

Figure 5.5 (a-e) The working mechanism of the hybrid nanogenerator with a simultaneous operation and electricity generation of triboelectric-piezoelectric effects at water wave impact conditions. Digital photos of the grid of hybrid nanogenerators in the breaking wave impact generator tank (f) before receiving water wave impact, (g) contacted and pressed, (h) contacted and released, and (i) releasing.

The electrodes of the fabricated hybrid prototype were connected to two full-wave bridge rectifiers to perform the electrical characterization, as depicted in Figure 5.6 (a). E1 and E3 were connected to each rectifier as a supply from the hybrid device in a simultaneous operation using the triboelectric effect and piezoelectric effect, respectively. E2 was connected in both rectifiers that is used as the second triboelectric material (grounded) and the second electrode (grounded) of the piezoelectric layer.

Their output voltage, output current, transferred charges and output power performance was compared with triboelectric nanogenerators [125] and piezoelectric nanogenerators (Figure 5.1 (b-d)) which were characterized in similar water conditions. The energy harvesters were insulated with polyethylene packaging, to protect them from the contact with water. Such devices were placed at the wall on the right side of the tank (with Velcro heavy-duty stick-on tape) facing the impact of the

water wave as shown in Figure 5.6 (b), where the water wave breaks with an amplitude of 10 to 12 cm and frequencies of 0.7 Hz to 3 Hz. The generation of the breaking water waves on the tank at previously mentioned frequencies with different amplitudes, it was controlled by a programmed ARDUINO UNO REV 3 and ARDUINO MOTOR SHIELD REV 3 which controls the back and forth movement of a hybrid stepper motor (RS Pro 535-0502) attached with an acrylic layer attached with an acrylic panel of 20 cm x 20 cm (thickness = 8 mm) (Figure 5.6 (b)). The breaking water wave impact frequency operation was verified by recording the time (s) (t = 1.42, 0.82, 0.56, 0.41 and 0.34 s) of every impact into the operation area (13 cm x 34 cm) in the water wave generator tank (52 cm x 34 cm x 18 cm).

Using the following equation (5.4) for the verification:

$$f = \frac{1}{t} \tag{5.4}$$

The amplitude of the impact of the water wave over the operation area was carefully measured with a self-adhesive tape measure.

A practical load resistance matching analysis varying between 100 Ω to 100 MΩ to reach a maximum output power performance with the hybrid nanogenerators was performed.

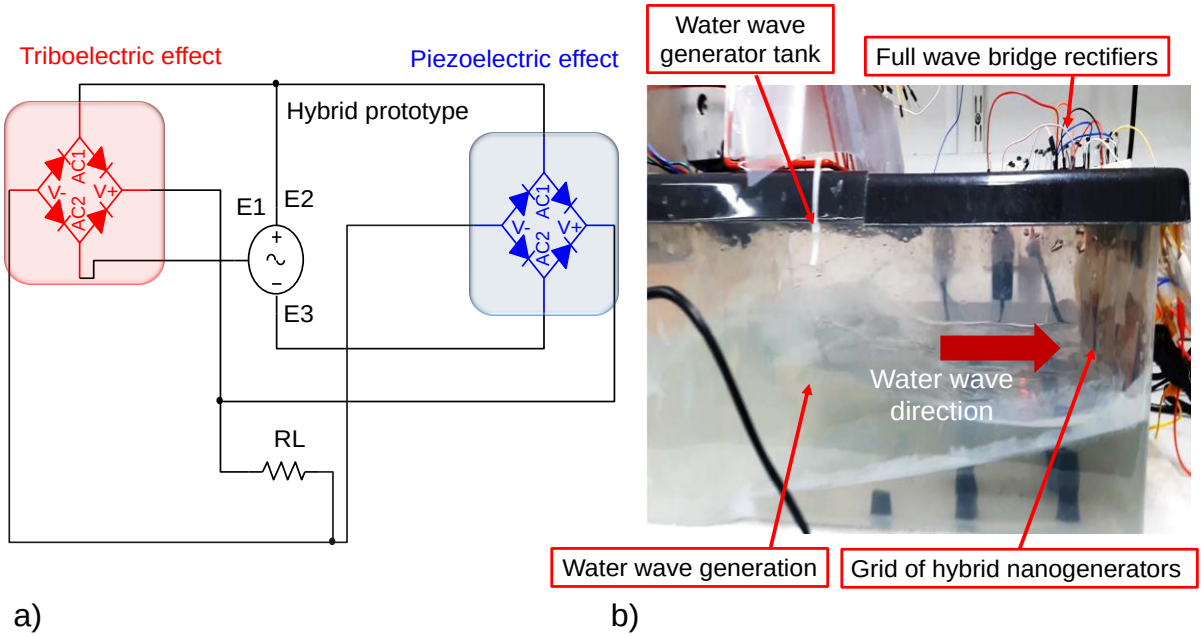

Figure 5.6 (a) Circuit diagram of the hybrid nanogenerators for the load matching and capacitor charging experiments. (b) Grid of hybrid nanogenerators placed in the water wave generator tank for its output performance measurements.

Consequently, the ability to charge a variety of capacitors between 2.2 to 100 µF for a period of 80 seconds with a single hybrid device, a piezoelectric device, triboelectric devices and a grid of four

hybrid devices connected in parallel to increase their output performance was tested. Furthermore, a durability test was performed to the hybrid devices at water wave impact conditions during different periods between 30 min to 180 min and number cycles of operation. Moreover, the potential of the grid of hybrid devices to charge and discharge capacitors was tested for a longer period. The output power generated of the energy harvesters was derived using the rectified output current and rectified output voltage measurements performed using an Agilent Technologies N6705B power analyser. The transferred charges were measured with an electrometer Keithley 6514, and the charging performance of the hybrid devices was measured with a digital oscilloscope Tektronix TDS 2014C, respectively (10 measurements performed on each sample).

5.3 Experimental results, analysis of electrical characterization and battery-less application of the hybrid nanogenerators through breaking water wave impact test

The rectified output current, voltage and charges transferred of the hybrid, TENG and PENG prototypes increases linearly, as the frequency (0.7 Hz – 3 Hz) and amplitude (10 cm – 12 cm) of breaking wave impact rise (Figure 5.7 (a-l)). The maximum output current, voltage and transferred charges generated for the hybrid nanogenerator increases from 35.7 µA to 140.93 µA, 68.23 V to 229.31 V, and 102.12 nC to 399.29 nC, (Figure 5.7 (a-c)) respectively. Thus, the maximum output power performance increases from 6.79 mW to 16.94 mW. The power performance of the hybrid prototypes shows an enhancement by a factor of 2.24, 4.80 and 3.21 compared with the arc-shaped TENG, DMCS-TENG and the piezoelectric nanogenerator (Figure 5.8 (a)). Such output current, voltage and charge transferred increases linearly from 6.28 µA to 76.52 µA, 34.02 V to 107.89 V, and 17.73 nC to 292.90 nC (Figure 5.7 (d-l)). Accordingly, the maximum output power performance of those energy harvesters was between 0.87 mW to 11.42 mW (Figure 5.8 (a)), tested in similar conditions of the mechanical energy generated by water wave impacts, and connected to a 1 MΩ load resistance, respectively. Furthermore, the enhancement was verified with the charging performance of the energy harvesters charging a capacitor of 2.2 µF for 80 seconds, where the hybrid nanogenerators reached a maximum voltage of 5.4 V as shown in Figure 5.8 (b). Where the arc-shaped TENG, PENG and DMCS-TENG reached a maximum voltage of 4.5 V, 3.68 V and 3.16 V, respectively (Figure 5.8 (b)).

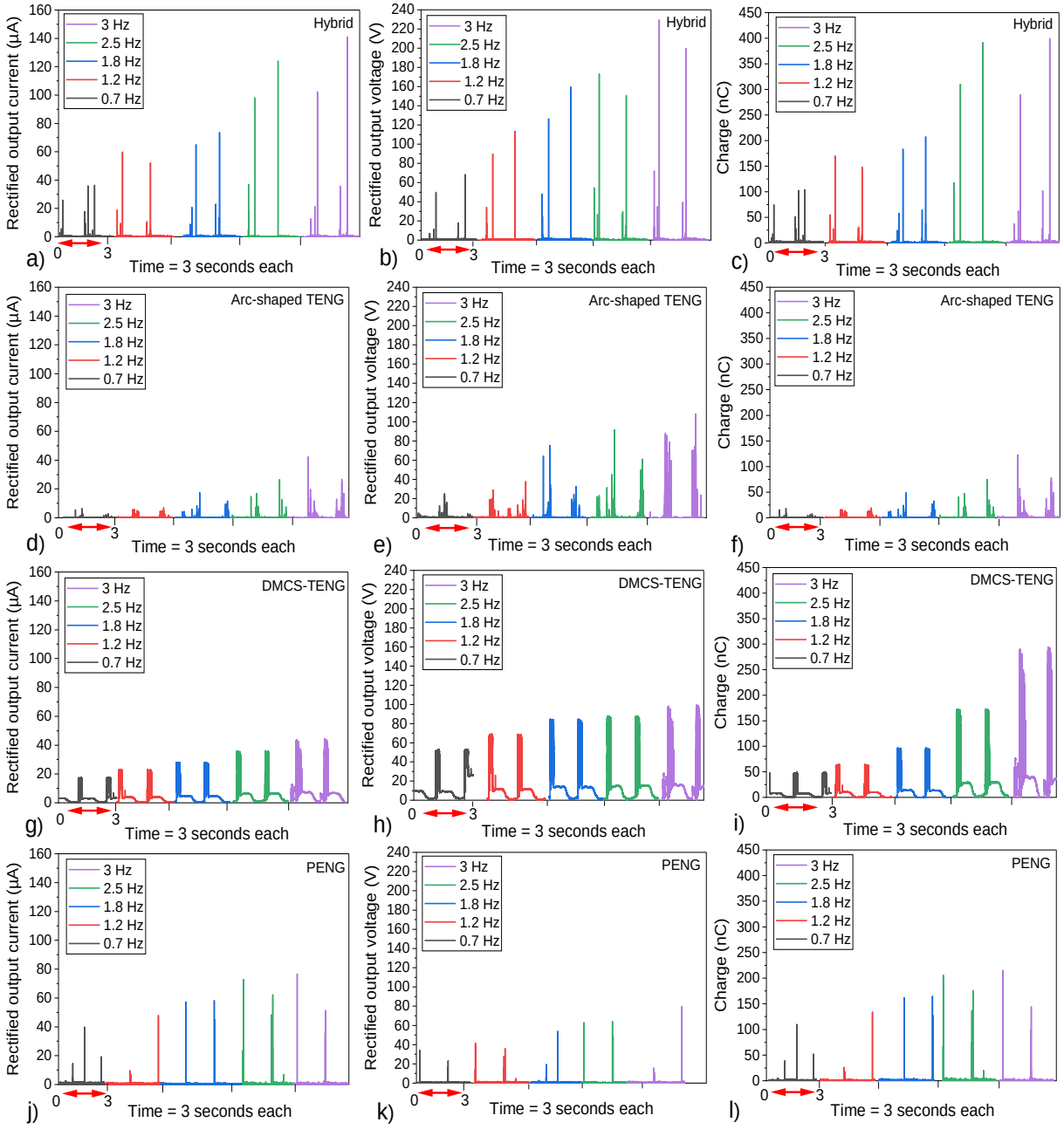

Figure 5.7 (a) Average rectified instantaneous output current, (b) output voltage and (c) transferred charges of hybrid nanogenerator. In comparison with (d-f) arc-shaped TENG, (g-i) DMCS-TENG, and (j-l) PENG average rectified instantaneous output current, output voltage, and transferred charges connected to a 1 MΩ load resistor tested in a water wave impact generator tank under different frequencies of impact between 0.7 Hz to 3 Hz (Data acquired during approximately 3 seconds for each sample).

Furthermore, the maximum average output power and power density of 15.92 mW and 0.99 mW/cm^2, respectively were generated with a load resistance of 8 MΩ through the load resistance matching practical experiment (Figure 5.8 (c)) performed under bre aking water wave impact at 1.2

Hz. This is compared with the maximum generated output power from 19.30 mW to 22.27 mW with a load resistance of 10 MΩ reached through the simulated model of the hybrid prototypes (L= 4 cm) (Figure 3.11 (a-b)). Such output performance and load resistance matching difference results from assuming the maximum surface charge density between the triboelectric materials in contact, and piezoelectric polarization under ideal conditions.

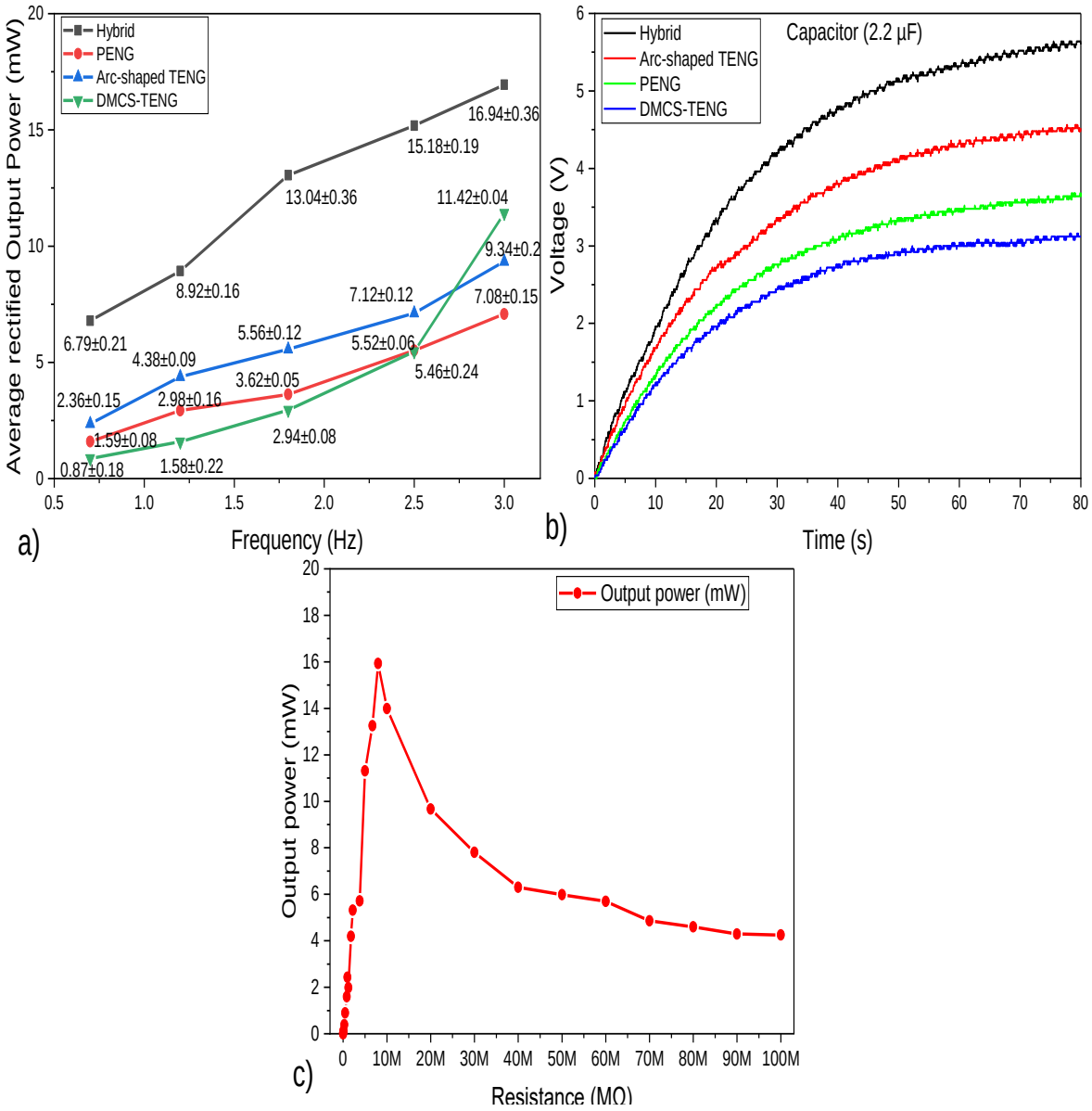

Figure 5.8 (a) Rectified average instantaneous output power and its standard deviation analysis calculated (10 measurements performed for each sample) of Hybrid device compared with TENG and PENG devices connected to a 1 MΩ resistor at water wave impact conditions (0.7 Hz to 3 Hz). (b) Charging performance of a single hybrid device, arc-shaped TENG, PENG, and DMCS TENG connected to a 2.2 µF capacitor. (c) Load resistance matching analysis to reach the highest output power performance of the hybrid device tested in the water generator tank.

Additionally, the maximum voltage reached by the grid of hybrid devices was 12.87 V, compared with a single unit that reached a maximum value of 5.4 V charging a capacitor of 2.2 µF for 80 seconds as depicted in Figure 5.9 (a), and Figure 5.9 (b). The grid of hybrid devices connected in parallel with a total active area of 256 cm^2 resulted in an enhancement factor of 2.43 in the output power (Figure 5.9 (f)) and output performance enhancement in charging different capacitors compared with a single hybrid nanogenerator. Such a grid of four energy harvesters generated a maximum average instantaneous output current, voltage and charge transferred, which rises steadily under the different frequencies (0.7 Hz to 3 Hz) from 89.05 µA to 314.13 µA, 185 V to 631 V, and 346.38 nC to 1095.62 nC, (Figure 5.9 (c-e)) respectively. As a result, the maximum generated output power and power density were between 10.70 mW to 46.58 mW, and 0.042 mW/m^2 to 0.18 mW/m^2 with a load resistance of 1 MΩ, respectively as depicted in Figure 5.9 (f). Furthermore, to calculate the average energy conversion efficiency (ECE) η of the grid of hybrid device system, defined as the ratio between the electric energy ($E_{electric}$) delivered to the load resistor of 1 MΩ and the mechanical energy ($E_{waterwave}$) applied by the water wave impact over a period (t) of 30 seconds with the different frequencies. The $E_{electric}$ released by the grid of hybrid nanogenerators was calculated by:

$$E_{electric} = \int_{t1}^{t2} RI^2 dt = 16.10\ J \tag{5.5}$$

where I is the average instantaneous current and R is the load resistance. The total average energy (potential energy and kinetic energy) produced by the water wave generator tank was calculated as [120]:

$$E_{waterwave} = \frac{1}{2}\rho g {A_{waterwave}}^2 = 59.36\ J \tag{5.6}$$

where g is the acceleration of gravity (g = 9.8 m/s^2), ρ is the density of water (ρ = 1000 kg/m^3), and $A_{waterwave}$ is the wave amplitude (between 10 cm to 12 cm, frequencies = 0.7 Hz to 3 Hz). Consequently, the overall η of the grid of hybrid devices was 27.12% calculated by [114]:

$$\eta = \frac{E_{electric}}{E_{waterwave}} x100\% = 27.12\% \tag{5.7}$$

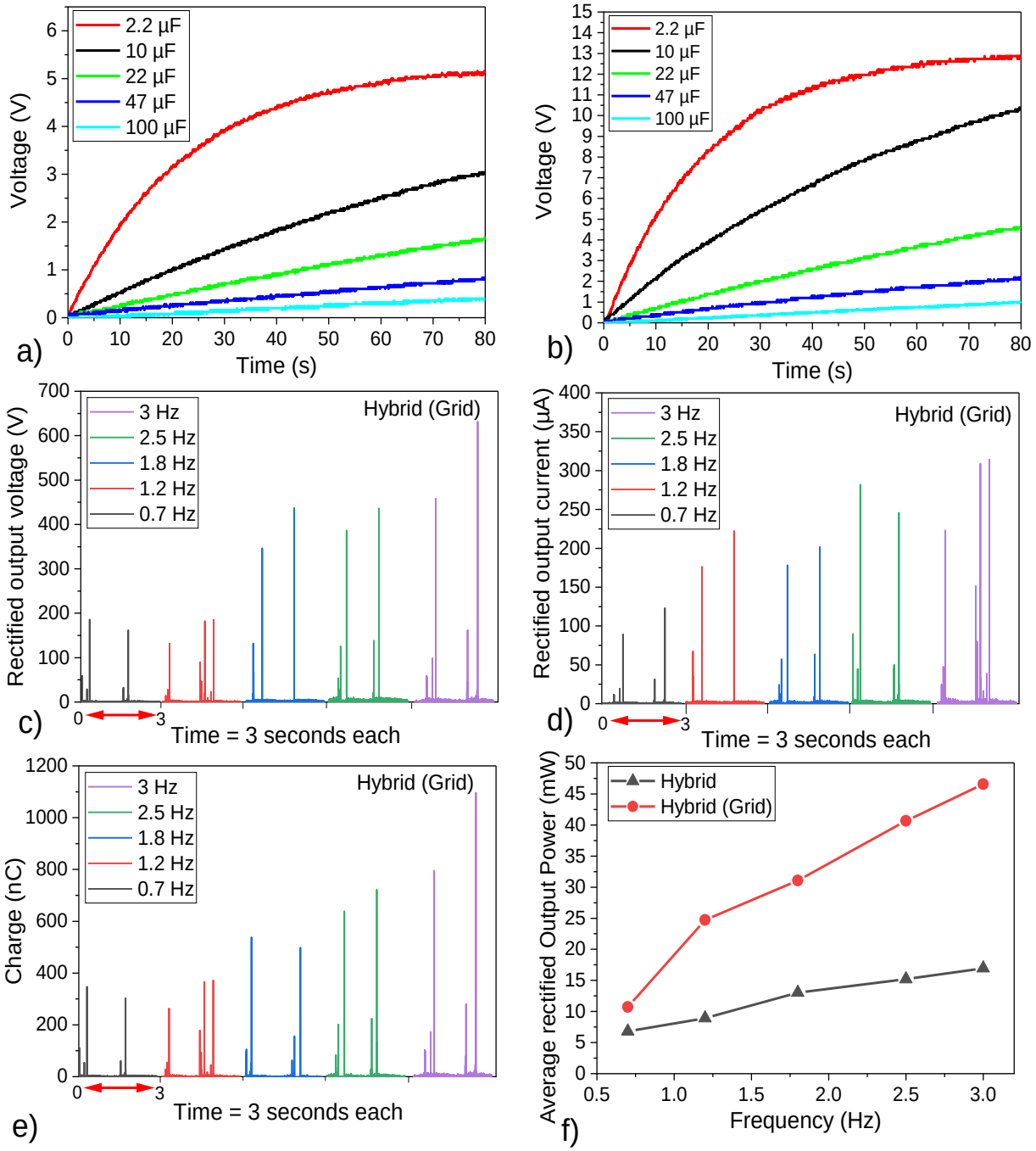

Figure 5.9 (a) Charging performance of a single hybrid device, and (b) a grid of 4 hybrid devices connected in parallel to different capacitors (2.2 µF – 100 µF). (c) Rectified instantaneous output current, (d) output voltage, (e) transferred charges (Data acquired during approximately 3 seconds for each sample), and (f) output power of a grid of hybrid devices compared with a single hybrid device unit connected to a 1 MΩ load resistor.

Moreover, due to the improvement of the water wave impact energy harvesting, and good performance storing energy in different capacitors using the grid of hybrid nanogenerators, an application was demonstrated. The grid of hybrid nanogenerators was used to power a one way wireless 433 MHz transmitter (Seeed 113990010) and sent a signal to the receiver to turn on 4

Kingbright L-7104PWC-A 3 mm white LEDs (1200 mcd), with a transmission distance from 2 m to 8 m as shown in Figure 5.10 (a) and Figure 5.10 (b). This was achieved after charging a capacitor of 47 µF between 312 seconds to 857 seconds, the voltage reached was within 2.95 V to 8.51 V and the switch was open to power up the transmitter as depicted in Figure 5.10 (c). Furthermore, as the transmission distance increases, more energy was required with a longer charging time required for the capacitor. The energy stored in the capacitor for the grid of hybrid devices, and the power generated for the capacitor during the discharging process for powering the wireless transmitter were between 204.51 µJ to 1.54 mJ, and 340.85 µW to 2.57 mW, respectively (Figure 5.10 (d)). Besides, it was demonstrated that the grid of hybrid energy harvesters shows the capacity to drive small electronic devices by the achieved output power levels.

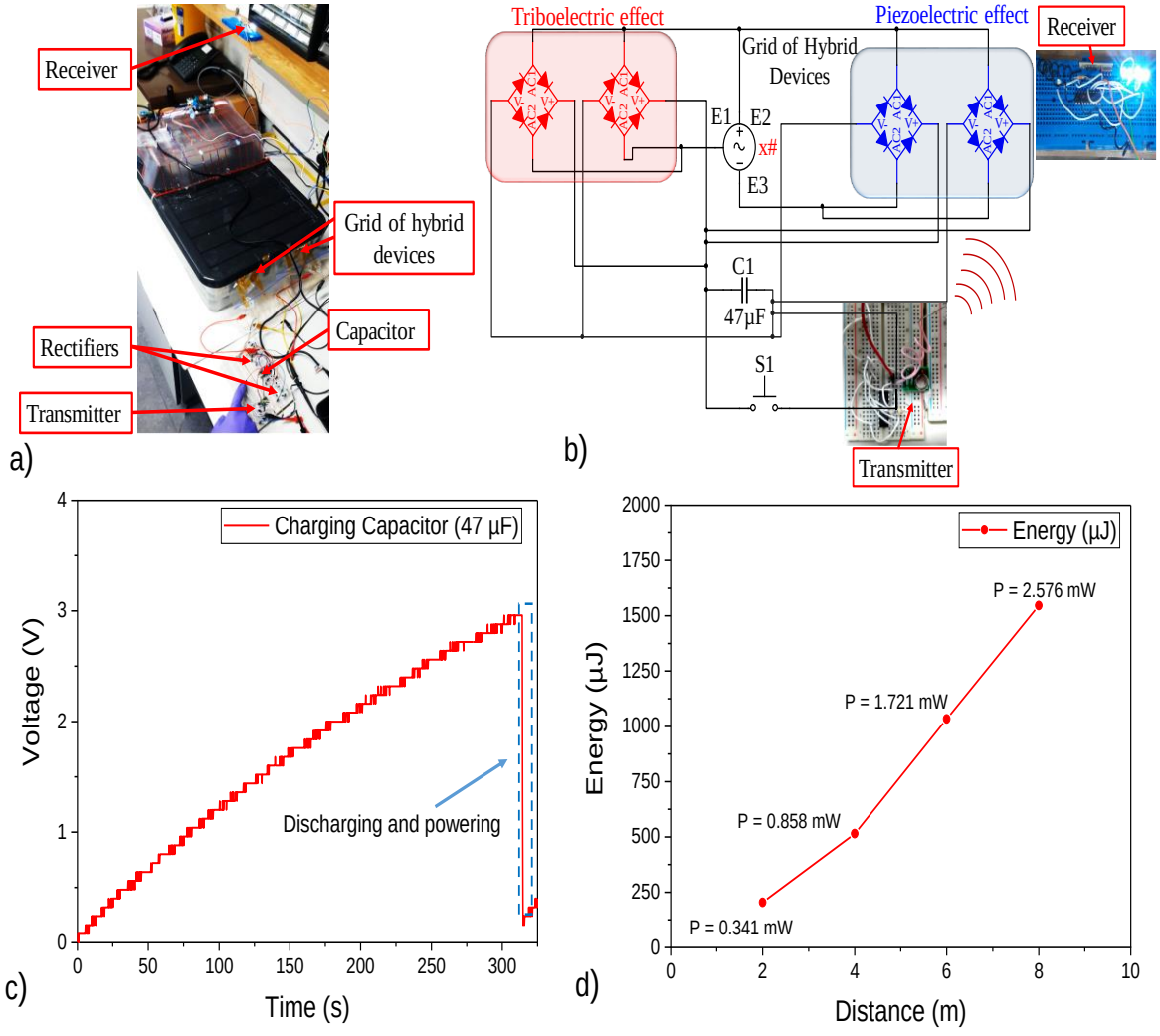

Figure 5.10 (a) Set-up for powering the wireless transmitter with the grid of hybrid nanogenerators under the water wave impact. (b) Electrical circuit diagram of the hybrid nanogenerators to charge the capacitor of 47 µF for powering the wireless transmitter. (c) Capacitor charging and discharging process for powering the wireless transmitter under the water wave impact with a frequency of 1.2 Hz. (d) Energy stored in the capacitor of 47 µF for the grid of hybrid devices, and the power

generated for the capacitor during the discharging process for powering the wireless transmitter to send a signal to a receiver with a transmission distance from 2 m to 8 m.

A durability test was applied to the hybrid nanogenerator under breaking water wave impact with a frequency of 1.2 Hz and amplitude of 10.5 cm during different periods 30, 60, 90, 120, 150, and 180 min. Based on the measurement of the rectified output current and number of cycles of operation of the hybrid energy harvester. The results show that the hybrid device maximum average output current is stable during 60 min and 4336 cycles of operation under the impact of water waves as shown in Figure 5.11. Subsequently, the hybrid nanogenerator performance decreases linearly as the operation time increases from 60 min to 180 min with a decrease by a factor of 2.34 (Figure 5.11). The average maximum instantaneous current decreased from 57.45 µA to 24.48 µA as the cycle of operation increases from 4336 to 19512, respectively. Although under the first 4000 cycles of operation, the hybrid device performance was stable, further investigation is required with engineering challenges to improve the energy conversion efficiency and device durability to withstand the harsh environmental conditions of the ocean.

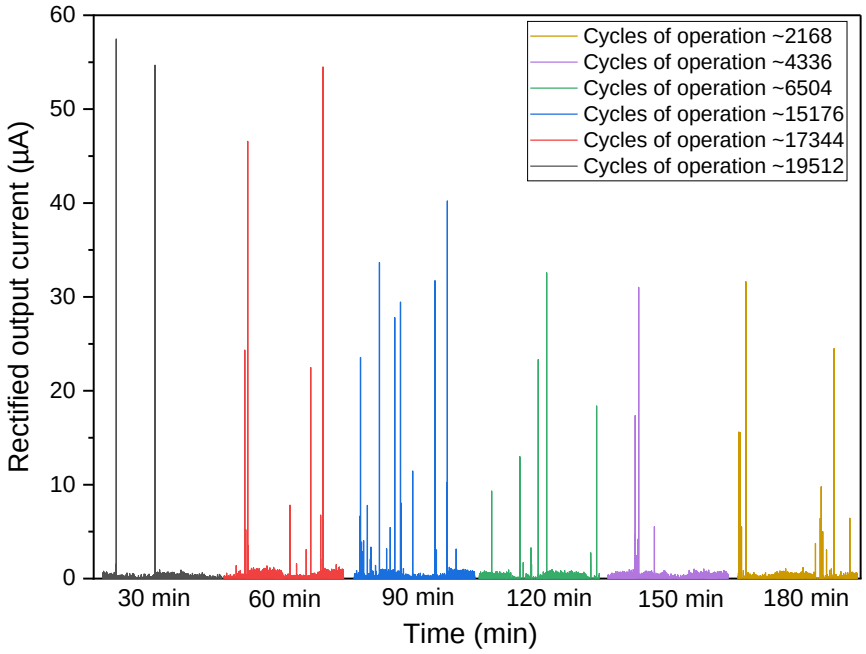

Figure 5.11 Maximum average instantaneous output current generated by the hybrid nanogenerator during different periods (30 min to 180 min) and cycles of operation (2168 to 19512) at water wave impact conditions.

Finally, extrapolating the potential to scale up [26] the capability of a grid of these hybrid energy harvesters by constructing large water-hybrid nanogenerators-structure interfaces (Figure 5.12) with an area of 18 m^2 that receives wave sizes among 0.3 m to 4 m [119]. It was considered the enhancement factor of the grid of the hybrid devices in comparison with a single unit, the output power generated for the grid and the frequency of impact of the water wave of 1.2 Hz. If the

interface is integrated with 11,250 hybrid devices connected in parallel, it is estimated to generate an average output power, and energy of 21.61 W, and 23.70 kJ. Considering a water wave impact over the proposed interface with a maximum amplitude of 4 m, it is calculated to generate total energy of 78.4 kJ using (5.6). Using (5.7), it is calculated that the large-scale hybrid nanogenerators could have an energy conversion efficiency of 30.22 %, harvesting the impact energy of water waves in large scale.

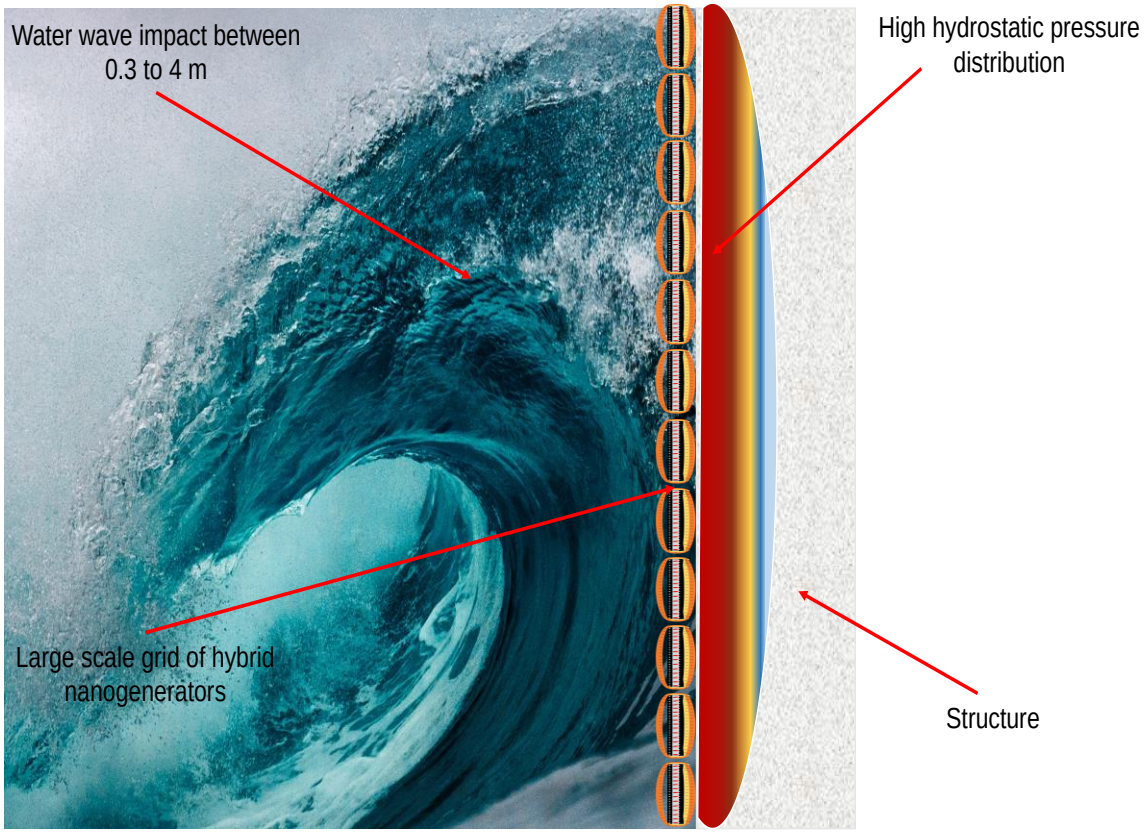

Figure 5.12 Two-dimensional schematic illustration of the configuration of the proposed large water-hybrid nanogenerators-structure interfaces to escalate the energy harvesting of water wave impact (Ocean water wave adapted from [132]).

5.4 Chapter summary

In this study developed through this chapter, the improvement in the output performance of prototype devices for water wave, impact force energy harvesting was achieved by simultaneously coupling triboelectric-piezoelectric effects, and also by the attribution of an electrically parallel connection of a grid of such devices. Developed by comparing their output performance with triboelectric nanogenerators (DMCS-TENG with self-resetting structure and arc-shaped DMCS-TENG) and piezoelectric nanogenerators (PENG) tested under similar conditions. The results show an enhancement by a factor of 2.24, 4.80 and 3.21 with the hybrid energy harvesters with the integration of the piezoelectric layer that works as triboelectric material and generates the

piezoelectric effect under stress when contacted-pressed and released states. Which promotes the output performance of the triboelectric nanogenerator under the impact of the water wave at low frequencies (0.7 Hz to 3 Hz). This was verified by measuring the output current, voltage, charge transferred, output power, and examining the ability to charge a selection of capacitors with a grid of four hybrid devices connected in parallel and tested under simulated wave conditions at low frequencies. As a result, the output performance response of the hybrid devices increases linearly, as the frequency between 0.7 Hz to 3 Hz and amplitude between 10 cm to 12 cm of breaking wave impact rises. Moreover, the grid of hybrid nanogenerators has the potential to drive low-power electronic devices. This was demonstrated by using the stored energy in a capacitor charged over different periods. The devices were capable of powering a wireless transmitter and sending a signal to a receiver at varying distances. Finally, the high output power obtained shows that the integrated grid of devices offers a promising innovative approach for the production of high-performance energy harvesting mechanisms focused on harvesting water wave impact energy at low frequencies. These are capable of energizing self-powered marine sensing systems for environmental monitoring requiring an average power consumption in the range from 1 mW to 100 mW [133, 134]. Further, it is estimated that with the construction of large water-hybrid nanogenerator-structure interfaces for the generation of electricity on a larger scale, harvesting the impact of the water waves for powering networks of self-powered sensing systems for smart fish farms having an average power consumption from 100 W to 1 kW [135].

Chapter 6 Water-dielectric single electrode triboelectric nanogenerators (WDSE-TENG) for water wave impact energy harvesting

6.1 Introduction

The potential to harvest breaking water wave impact has been studied in the previous chapters by the utilization of dielectric-metal contact separation mode triboelectric nanogenerators (DMCS-TENG) [124, 125] and dielectric-conductor contact-separation mode hybrid nanogenerators [136] employing contact electrification with solid-solid materials in contact at a wide frequency range between 0.7 Hz to 252 Hz. Consequently, as triboelectricity exists when liquids are flowing or in contact with solid insulated materials [18, 35, 122, 123, 137-143], which creates an electric double layer (EDL) in two steps called the Wang model [123, 140]. Electron exchange between liquid-solid interface due to contact electrification as the first step that makes atoms on the solid surface to be ions. The interaction between the solid-liquid interface ions as the second step, resulting in a gradient distribution of cations and anions near the interface [123, 140]. Practically, electron exchange and ion adsorption occur simultaneously and coexist in the liquid-solid interaction [140, 142]. Specially, the contact electrification between hydrophobic surfaces and liquid solutions is more likely to be dominated by electron transfer and the contact electrification between hydrophilic surfaces and liquid solutions is likely dominated by ion transfer [141]. The research work develops through this chapter is aimed at an extended experimental study, analysis and optimization to exploit the liquid-solid contact electrification characteristic between different materials in contact for harvesting the breaking wave impact energy, under low frequencies from 0.7 Hz to 3 Hz. Such energy can be potentially harvested, exploited and improved using a well-adjusted, light-handed and facile to produce a grid of water-dielectric single electrode mode triboelectric nanogenerators (WDSE-TENG). Such energy harvester converts the external mechanical energy into electricity by a combination of the triboelectric effect and electrostatic induction, based on contact electrification between water and selected hydrophobic dielectric polymer layers due to their high negativity in the triboelectric series [83, 86]. Such as polydimethylsiloxane (PDMS, with silicon, oxygen bonds), polytetrafluoroethylene (PTFE, with carbon-fluoride bonds), silicone rubber compound (acetoxy, elastomer, with silicon-oxygen bonds), fluorinated ethylene propylene (FEP, with carbon-fluoride bonds) and polyimide (Kapton, with two acyl groups (C=O), bonded to nitrogen).

First, to explore the opportunity to use water as one type of triboelectric material choice for TENG, single-electrode and split-electrode TENG prototypes were fabricated and characterized based on their generated output voltage, output current, transferred charge and output power to study and analyse the contact electrification between water and the aforementioned dielectric polymer films. Tap water, deionized water (DI) and sodium chloride (NaCl) with a concentration of 0.6 M, which is similar to that in seawater, were compared when in contact with the hydrophobic polymer films. This was achieved in a wave tank that generates breaking water wave impacts at frequencies and amplitudes between 0.7 Hz to 3 Hz and 10 cm to 12 cm, respectively. The aim was to find the optimum dielectric material to reach the highest output power harvesting the water wave impact. Second, a load resistance matching experiment was performed with the objective being to obtain maximum output power from the WDSE-TENG with a suitable selection of solid materials that gives the highest performance from the proposed prototypes.

Third, the produced output performance and ability to charge a variety of capacitors with a single, and also a grid of five, WDSE-TENG prototypes in a multi-unit parallel connection [26, 53, 130] to increase the current output were characterized in seawater under breaking water wave impact at the aforementioned frequencies. Finally, the potential of the grid of WDSE-TENG to drive small electronic devices and its integration with a power management control circuit (PMCC) was tested to solve the challenge that this system and many self-powered systems based on TENG have, in that they are not able to work continuously. Besides, the potential scalability for the WDSE-TENG utilization at big-scales was estimated.

6.2 Fabrication, working mechanism through water-dielectric interfaces for electricity generation and characterization of WDSE-TENG energy harvester prototypes

The fabricated WDSE-TENG prototypes have a triboelectric active area of 7 cm × 4 cm and three different configurations, as depicted in Figure 6.1, using hydrophobic dielectric layers with high negativity in the triboelectric series [83]. For the first sample of a WDSE-TENG, a dielectric layer was bonded onto a copper electrode (thickness (d_E) = 100 µm) with conductive acrylic glue (Electrical resistance through glue = 0.003 ohm, and d_A = 25 µm). The other exposed side of the copper layer was insulated with black PTFE tape to protect it from the water to prevent a short circuit (Figure 6.1 (a)). With this device configuration, the contact electrification occurs at the face of the dielectric layer in contact with water. A number of different dielectric layers were tested, namely PTFE (d_D = 100 µm), FEP (d_D = 25 µm), Silicone rubber compound (d_D = 150 µm), Kapton (d_D = 127 µm), and PDMS (d_D = 125 µm). For the second configuration, a Cu layer (d_E = 100 µm) was completely insulated within silicone rubber layers on both sides to protect it from the water (Figure 6.1 (b))

and with the aim to increase the contact area to produce contact electrification on both faces of the device when water contacts it. Additionally, using the second configuration, a copper layer was insulated on one side with a layer of PDMS and the other side with a layer of PTFE using conductive acrylic adhesive to test the combination of two different materials in contact electrification with water at the same time. For the electrical characterization, the electrode of each sample was connected to an external load of 1 MΩ.

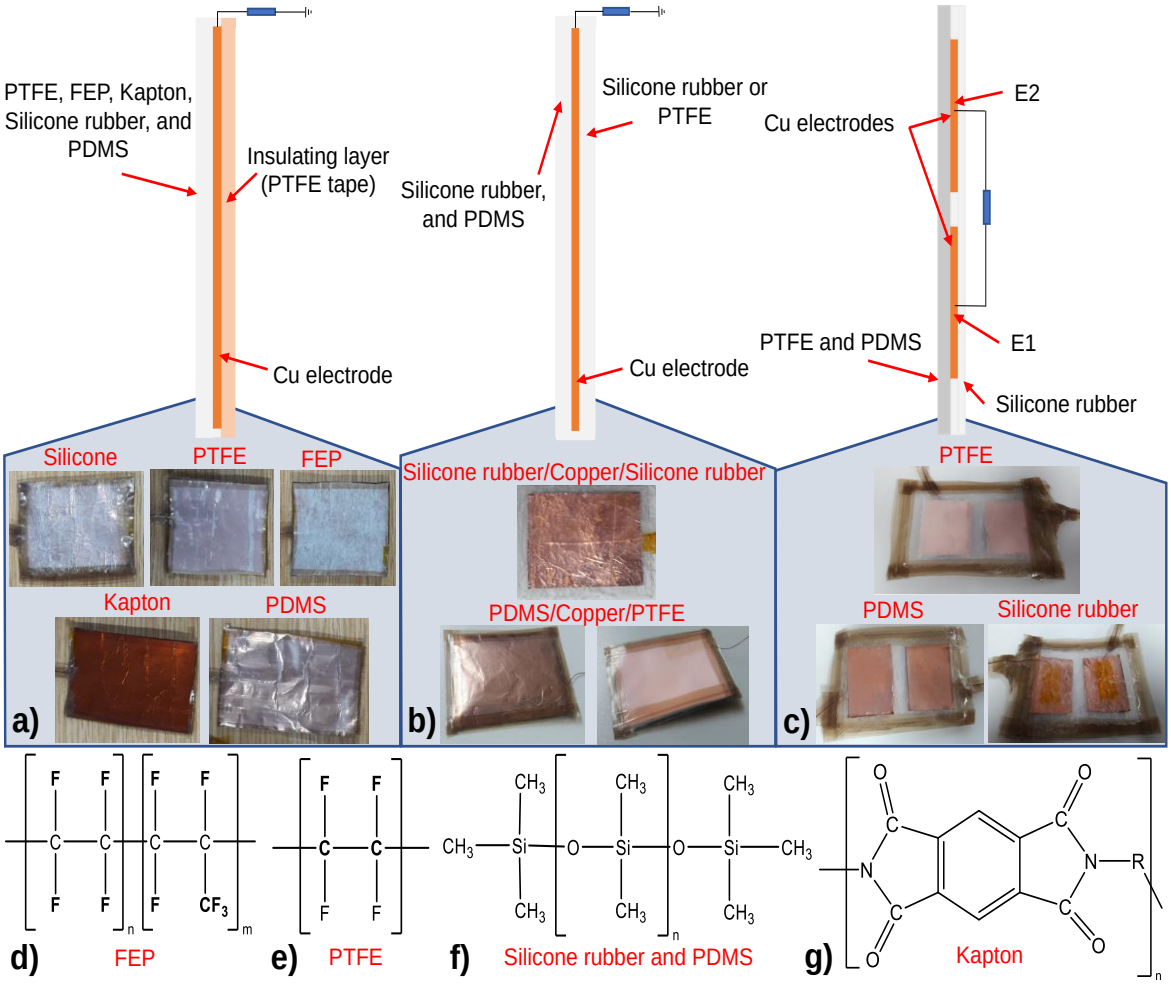

Figure 6.1 Two-dimensional schematic and digital images of the three configurations of fabricated WDSE-TENG prototypes (a) WDSE-TENG with one dielectric layer, (b) full device covered with two dielectric layers, and (c) split electrode-two dielectric layers. Molecular structure of d) FEP, e) PTFE, f) Silicone rubber (Acetoxy, elastomer) and PDMS and g) Kapton.

The third configuration comprised two copper layers (split electrode) with an active area of 2.5 cm × 3 cm per layer, and a separation distance of 8 mm, which were bonded with conductive acrylic adhesive on a dielectric layer of either PTFE (d_D = 100 µm) or PDMS (d_D = 125 µm). The other face of the device was insulated with a layer of silicone rubber to protect it from short-circuit in contact with water (Figure 6.1 (c)). The contact electrification is produced on both faces of the device when it contacts the water and the two electrodes (E1 and E2) were connected to an external load of 1

MΩ for electrical characterization. The objective of implementing a split electrode design is to increase the overall charge transfer relative to a WDSE-TENG.

Figure 6.2 (a-g) and Figure 6.3 (a-g) illustrates the working mechanism of the WDSE-TENG with one-dielectric layer and two dielectric layers configuration due to contact electrification and ion interaction between the breaking water wave and the hydrophobic dielectric layers. Before the dielectric layers make contact with water (Figure 6.2 (a) and Figure 6.3 (a)), no charge transfer and ion adsorption occur. When the water wave starts to make partially contact against the dielectric layers (Figure 6.2 (b) and Figure 6.3 (b)), the electron exchange and ionization of the surface groups on the dielectric layers will cause the dielectric layer to be negatively charged [144] and create a positively charged EDL on the contact surface of the water wave to maintain electrical neutrality [123, 140-142, 145, 146] (Figure 6.2 (c) and Figure 6.3 (c)). As the water wave breaks down and moves off the dielectric layers, the positive charges in the EDL can be carried away with the water and the negative charges can remain on the surface of the dielectric layers. The negative electric potential difference between the electrode and the load resistor to ground attains equilibrium as electrons flow to the ground (Figure 6.2 (d) and Figure 6.3 (d)) due to the triboelectric charges on the dielectric layers, which can be retained for hours or even days [147]. When another water wave is partially impacting/contacting the negatively charged dielectric layers in a short period (~0.0008 s) of the impact motion process (Figure 6.6 (a)), the negative charges will attract counter ions from the water to form another positively charge EDL, and establishes a positive electric potential difference. Therefore, electrons will flow from ground and load resistor to the electrode (Figure 6.2 (e) and Figure 6.3 (e)) that produces an instantaneous current peak until a new equilibrium is reached (~0.29s, Figure 6.2 (f), Figure 6.3 (f) and Figure 6.6 (a)). When the water wave breaks down (~0.0103 s) and leaves the dielectric layers, a negative electric potential difference will be established between the electrode and load resistor to the ground and another new equilibrium is achieved (Figure 6.2 (g), Figure 6.3 (g) and Figure 6.6 (a)). Once the following water wave contacts with the dielectric layers of the WDSE-TENG (Figure 6.2 (a-g) and Figure 6.3 (a-g)), power generation cycle repeats itself.

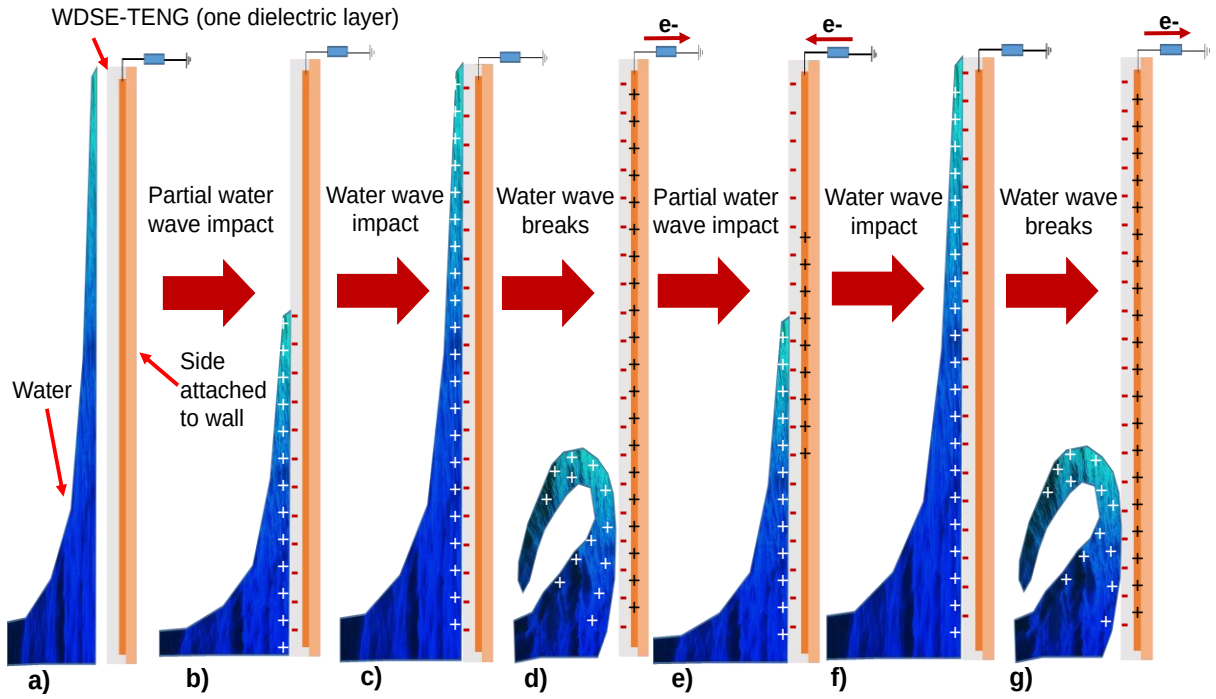

Figure 6.2 (a-g). Working mechanism of the WDSE-TENG with one-dielectric layer by the contact electrification of dielectric layers with breaking water wave impact.

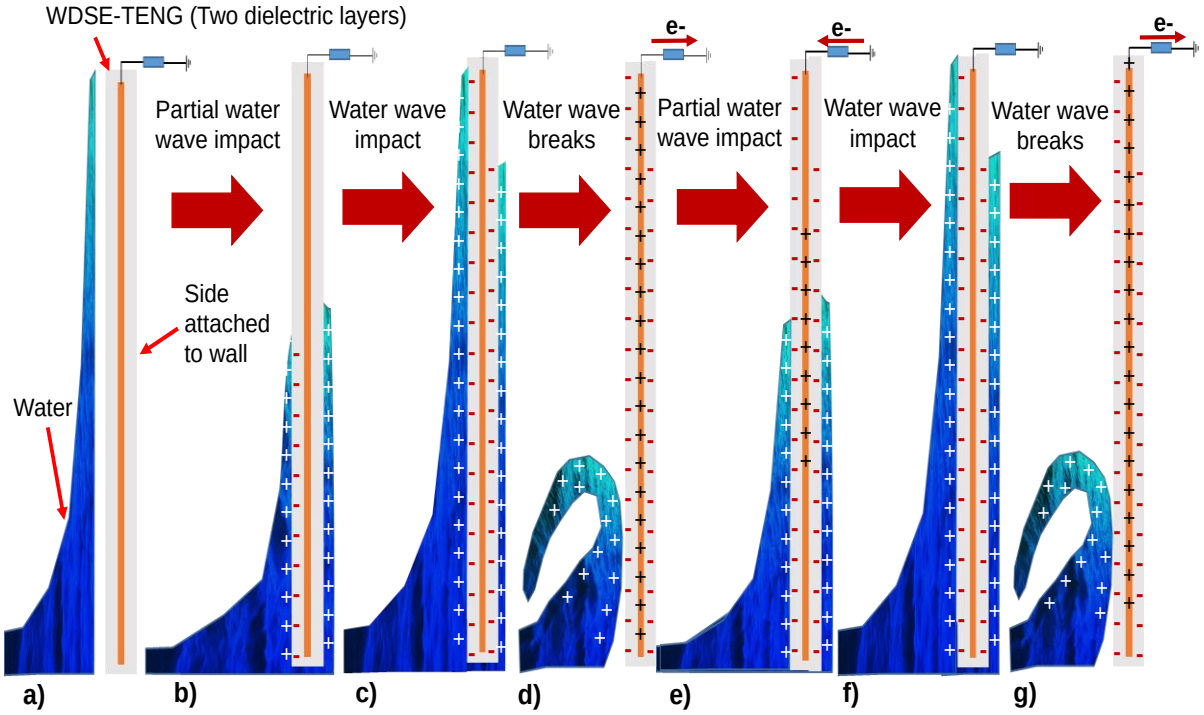

Figure 6.3 (a-g). Working mechanism of the WDSE-TENG with two-dielectric layers by the contact electrification of dielectric layers with breaking water wave impact.

Additionally, the working mechanism of the WDSE-TENG with split-electrode and two-dielectric layers configuration is depicted in Figure 6.4 (a-g). No charge transfer and ion adsorption take place before the contact electrification between the dielectric layers and water (Figure 6.4 (a)).

Subsequently, the water wave starts its contact over the WDSE-TENG, and this results in electrical neutrality with a negative charge on the dielectric layer surface, which also creates a positively charged EDL on the water (Figure 6.4 (b)). This generates an unbalanced electric potential difference between E1 and E2 that drives the movement of electrons from E2, through the load resistance to E1 as the water wave is partially impacting the WDSE-TENG energy harvester (Figure 6.4 (b)). This process produces an instantaneous negative current (Figure 6.4 (b)). Therefore, once the water wave fully impacts the device dielectric layers, induced electrons move back from E1 to E2, through the load resistance as the electric potential distribution changes toward equilibrium which produces an instantaneous positive current (Figure 6.4 (c)). As the water wave breaks down and moves off the dielectric layers, the positive charges in the EDL can be carried away with the water and the negative charges can remain on the surface of the dielectric layers (Figure 6.4 (d)). Once the following water wave starts impacting with the dielectric layers of the split-electrode WDSE-TENG with two-dielectric layers (Figure 6.4 (e)), another cycle of operation is completed (Figure 6.4 (f-g)). The water wave after the impact with the dielectric layers of the WDSE-TENG prototypes should not leave residual water on the dielectric hydrophobic layers surface, in an ideal situation to generate the maximum electrical output.

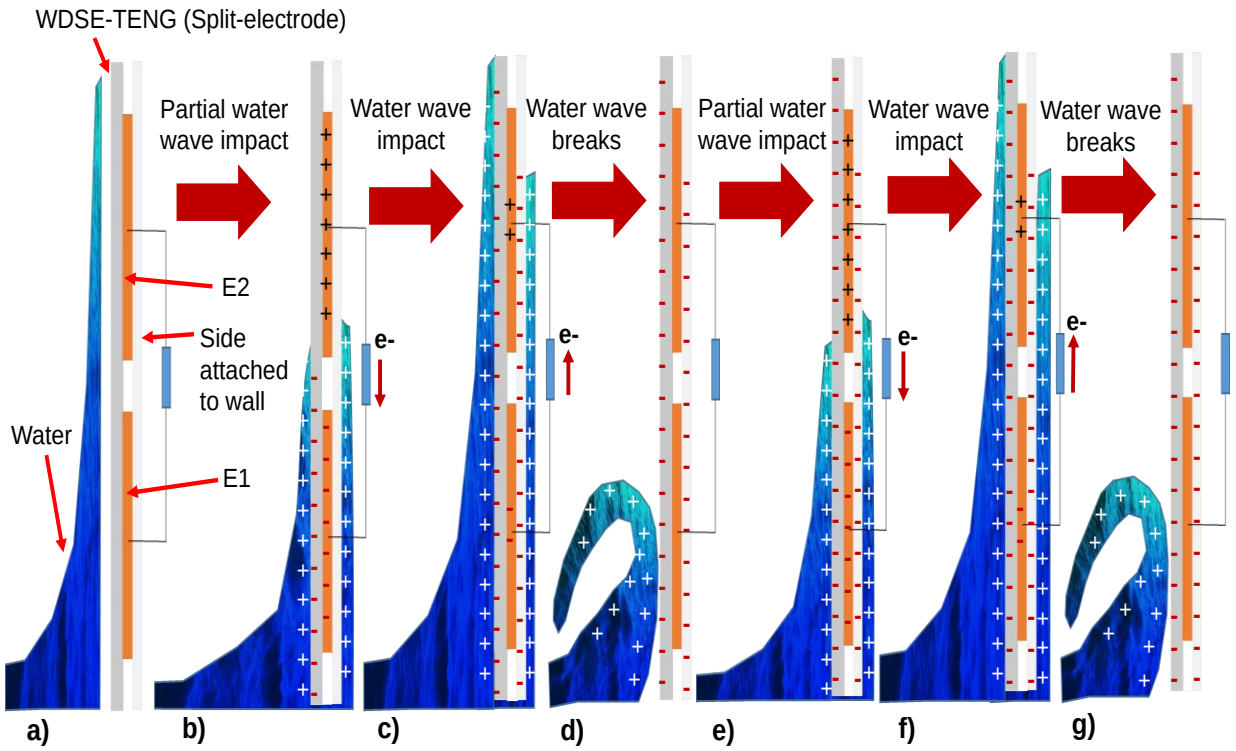

Figure 6.4 Working mechanism of the split-electrode WDSE-TENG with two-dielectric layers by the contact electrification of dielectric layers from breaking water wave impact.

The WDSE-TENG output voltage, output current, charge transfer and output power of the prototypes were characterized in a breaking water wave generator tank in order to replicate the conditions of the mechanical energy generated by ocean wave impact. A hybrid stepper motor (RS Pro 535-0502) attached with an acrylic panel of 20 cm × 20 cm (t = 8 mm) is used to generate the wave motion in the water tank at different frequencies. The water wave breaks with frequencies from 0.7 Hz to 3 Hz and amplitudes between 10 cm and 12 cm as described at point 5.2. The WDSE-TENG devices were attached at the wall on the right side of the tank with Velcro heavy-duty stick-on tape in order to fix them where the water wave breaks against the dielectric triboelectric layer, which generates interchange of triboelectric charges between both surfaces as shown in Figure 6.5 (a) and Figure 6.5 (c-d). DI water, tap water and 0.6 M NaCl solution (artificial seawater) were used in contact with the WDSE-TENG devices. Therefore, a practical load resistance matching analysis with load resistances varying between 100 Ω to 100 MΩ connected to the energy harvester prototype was performed to obtain the maximum output power as depicted in Figure 6.5 (b).

Additionally, the rectified output performance and the ability to charge a variety of capacitors varying from 4.7 μF to 470 μF for 85 seconds with a single device (Figure 6.5 (a)), and a grid of five WDSE-TENG devices connected in parallel were tested as illustrated in Figure 6.5 (c) and Figure 6.10 (a). Every WDSE-TENG device was connected to a full-wave bridge rectifier (using BAS 40 diodes) for the electrical characterization of the grid of such devices. Furthermore, a durability test was performed to the WDSE-TENG energy harvester under breaking water wave impact through different periods from 30 min to 210 min and a number of cycles of operation. Moreover, the grid of energy harvesters was used to drive electronic devices including an HC-SR04 ultrasonic ranger by storing and discharging electrical energy using capacitors. Finally, a PMMC unit was developed using the grid of WDSE-TENG as a source and this improved its energy extraction to have a direct wave impact-to-electrical conversion.

All the WDSE-TENG prototypes and connection wires were insulated to avoid short circuit conditions when the devices are in contact with water. The output voltage and current measurements of the WDSE-TENG energy harvesters were performed using an Agilent Technologies N6705B Power analyzer (10 measurements performed for each sample). The output power was calculated from these measurements. Furthermore, the transferred charges were calculated by integrating the output current peaks generated during the impact of the water waves over the devices, and the charge of different capacitors (4.7 µF to 470 µF) by the energy harvesters were obtained with a Tektronix TDS 2014C digital oscilloscope (10 measurements performed for each sample).

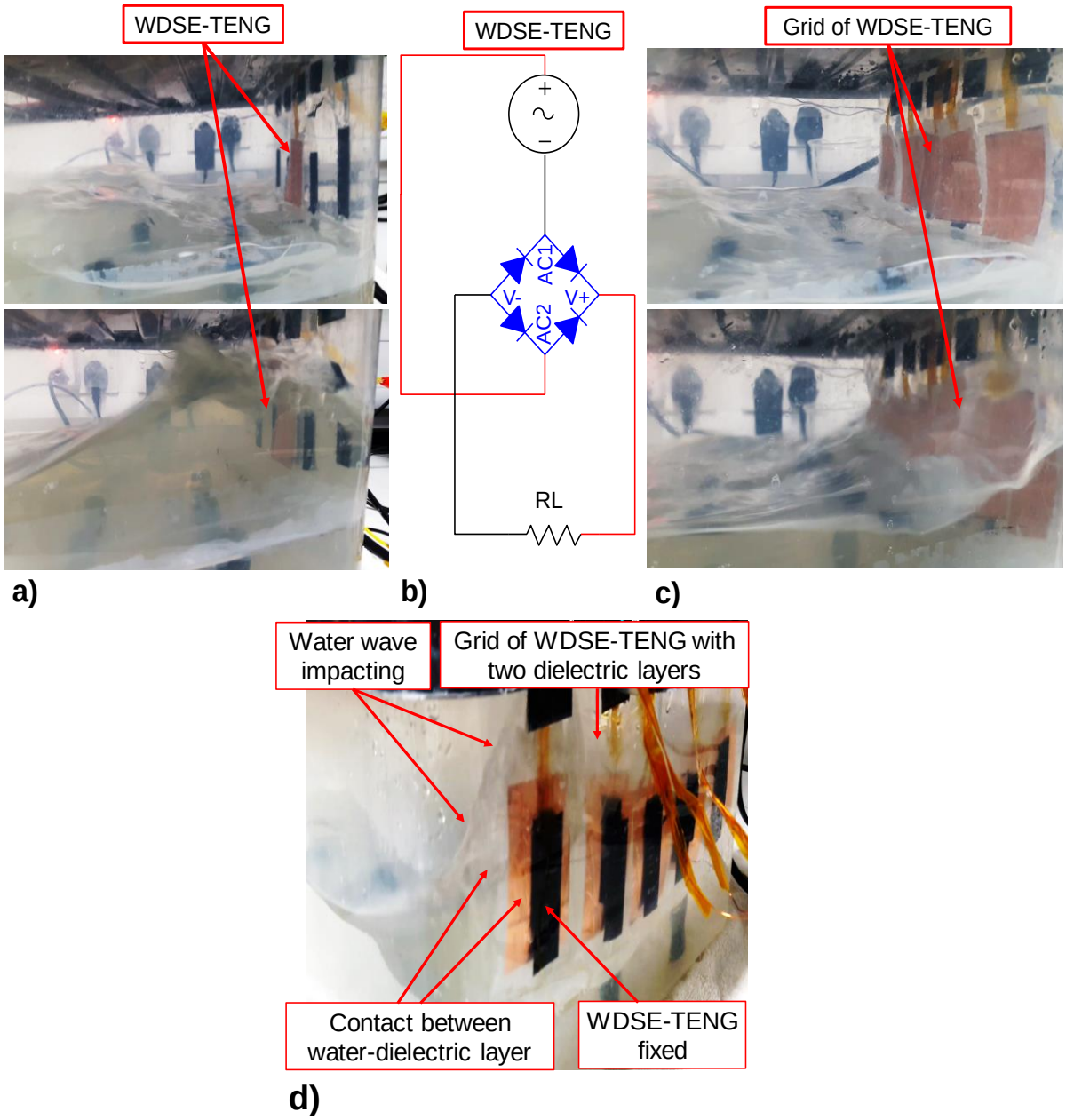

Figure 6.5 (a) Digital image of the single WDSE-TENG attached and under breaking water wave impact in the water wave impact generator tank. (b) Circuit diagram of the WDSE-TENG for the load matching and charging of different capacitors. (c) Digital image of the grid of five WDSE-TENG devices attached and under breaking water wave impact in the water wave impact generator tank. (d) Digital image of the back view of the grid of five WDSE-TENG devices under breaking water wave impact that illustrates the contact of the water wave in both of their faces.

6.3 Experimental results and analysis of the electrical characterization of the WDSE-TENG energy harvester prototypes through water wave impact test

6.3.1 Water-dielectric triboelectric materials selection and optimization

The output current peaks illustrated in Figure 6.6 (a-b) are the instantaneous peaks generated during the working mechanism of the WDSE-TENG in two cycles of operation at breaking water wave conditions produced in a short period named water wave partially impacting/contacting (0.0008 s), fully contacted (0.2928 s), water wave breaks down (0.0103 s) and non-contacted (0.4634 s) as described in Figure 6.3 (e-g). Figure 6.6 (b) illustrates in detail the comparison of the average instantaneous output current generated for the WDSE-TENG energy harvesters with different configurations and materials in contact with tap water. The average instantaneous output current generated of the WDSE-TENG with one dielectric layer of FEP and the WDSE-TENG with two dielectric layers of silicone rubber in contact with tap water is illustrated in detail in Figure 6.6 (b).

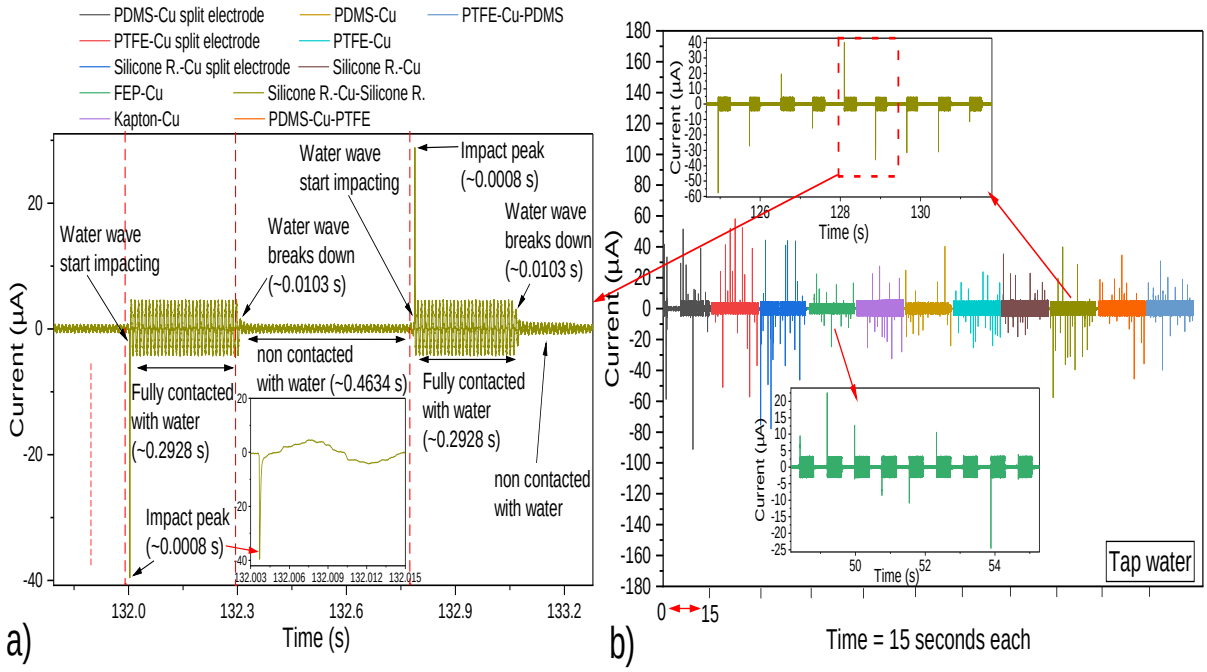

Figure 6.6 (a) Instantaneous output current generation of the WDSE-TENG in two cycles of operation at breaking water wave impact conditions (with a frequency and amplitude of 1.2 Hz and 10.5 cm). (b) The average instantaneous output current of the WDSE-TENG with different configurations and materials in contact with tap water (Data acquired during 15 seconds for each sample).

Consequently, the comparison of the three configurations for the WDSE-TENG energy harvester prototypes according to their electrical output performance measurements in contact with DI water, tap water and seawater with a frequency and amplitude of impact of 1.2 Hz and 10.5 cm is shown in Figure 6.7 (a-i). In contact with DI water, the devices had a maximum output voltage (V_{RMS}), output current (I_{RMS}) and transferred charges ranging from 3.06 V to 7.36 V, 1.87 µA to 5.06 µA and 5.41 nC to 13.70 nC (Figure 6.7 (a-c)), respectively. As a result, a maximum output power between 5.71 µW to 22.42 µW was calculated (Figure 6.8). In contact with tap water, the maximum output power was between 2.88 µW to 19.72 µW and this was calculated from the measured V_{RMS} (1.47 V to 5.76 V) and I_{RMS} (1.04 µA to 4.80 µA), along with transferred charges of 4.98 nC to 9.93 nC (Figure 6.7 (d-f)). The output performance using tap water was reduced by a factor of 1.46 compared with the DI water (Figure 6.8).

The WDSE-TENG with one dielectric layer using FEP (d_D = 25 µm) in contact with tap water and DI water produced the highest output performance (Figure 6.8). The prototype with two dielectric layers of silicone rubber produced the next highest output performance, likely due to the large contact area (V_{RMS}, I_{RMS} and power of 5.76 V to 6.21 V, 2.74 µA to 3.04 µA and 15.83 µW to 18.77 µW, respectively). However, the output performance decreased for the WDSE-TENG with split-electrode with two dielectric layers due to the reduced active area of 2.5 cm × 3 cm. Furthermore, the configuration of the WDSE-TENG with two distinct dielectric layers of PDMS and PTFE have shown relatively poor output power performance from 3.30 µW to 6.14 µW (Figure 6.8).

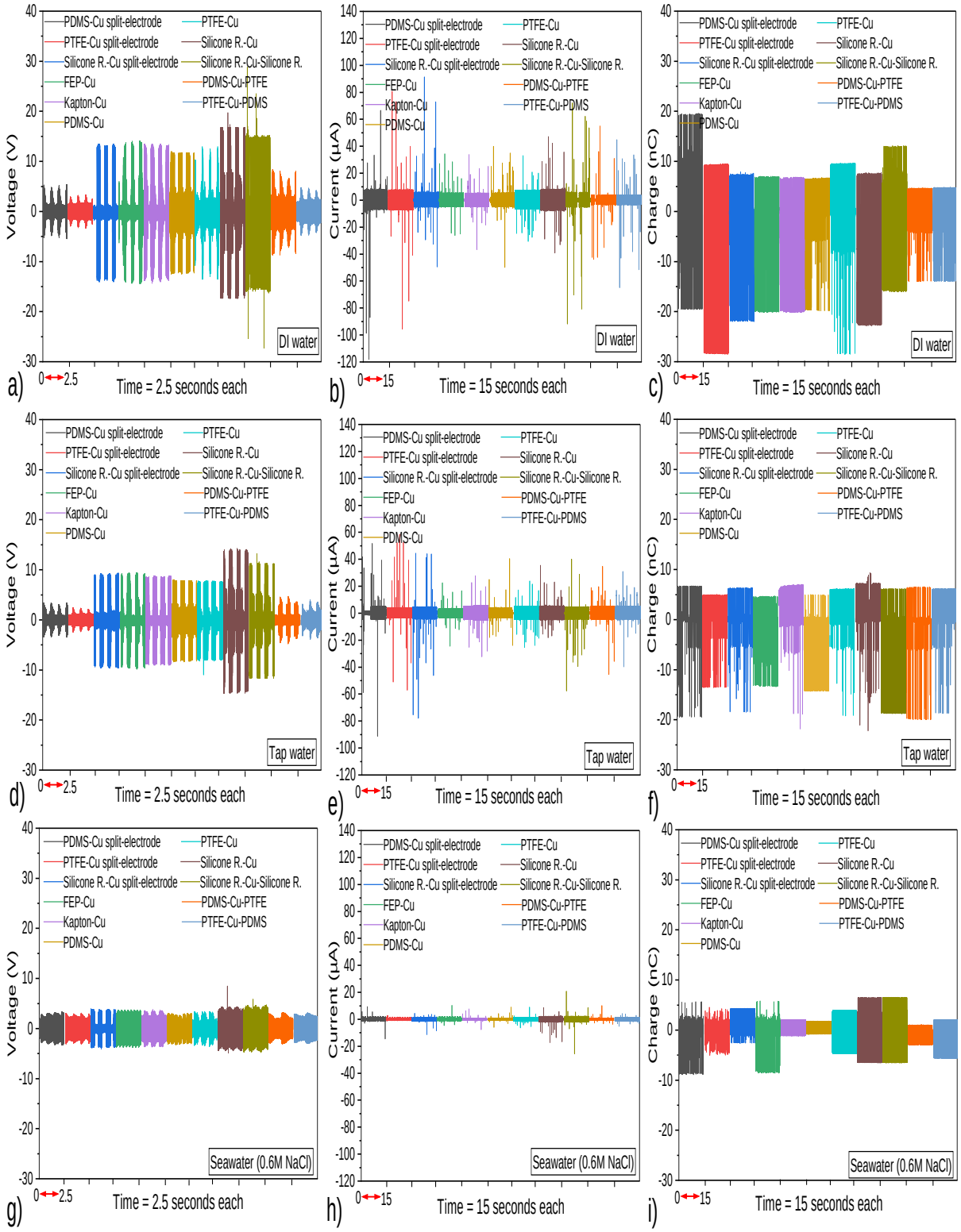

Figure 6.7 The average instantaneous output voltage (Data acquired during 2.5 s for each sample), output current and transferred charge (Data acquired during 15 seconds for each sample) of the WDSE-TENG with different configurations and materials in contact with (a-c) DI water, (d-f) tap water and (g-i) artificial seawater.

Moreover, the output power for the water-dielectric energy harvesters was reduced by a factor of 4.20 and 2.86 when they were in contact with seawater compared with the DI and tap water,

respectively (Figure 6.8). The maximum output voltage, current, transferred charge and output power values were 3.75 V, 2.37 µA, 4.63 nC and 8.89 µW with the two dielectric layer configuration using silicone rubber compound (d_D = 150 µm) with a Cu electrode as depicted in Figure 6.7 (g-i) and Figure 6.8. For the one dielectric layer configuration using silicone rubber, a maximum output power of 4.76 µW (Figure 6.8) was obtained, with corresponding output voltage, current and transferred charge values of 4.93 V, 0.96 µA and 3.98 nC, respectively. The reduction in the performance of the WDSE-TENG energy harvesters indicated that they are affected by the electrolytes in water. This is due to the fact that dielectric materials cannot be completely elude the adhesion of water droplets after it is separated from the water wave impact. Once there are electrolytes in water, more positive charges including dissolved ions will remain on the dielectric films, resulting in the partial screening of the tribo-charges on the films [83, 144, 148-151]. In the near future, this issue could be solved by the creation of superhydrophobic dielectric layers or by changing the dielectric film with a specific functional group to counter the ions with opposite charges that remain on the contacted surfaces [149] during water wave impact.

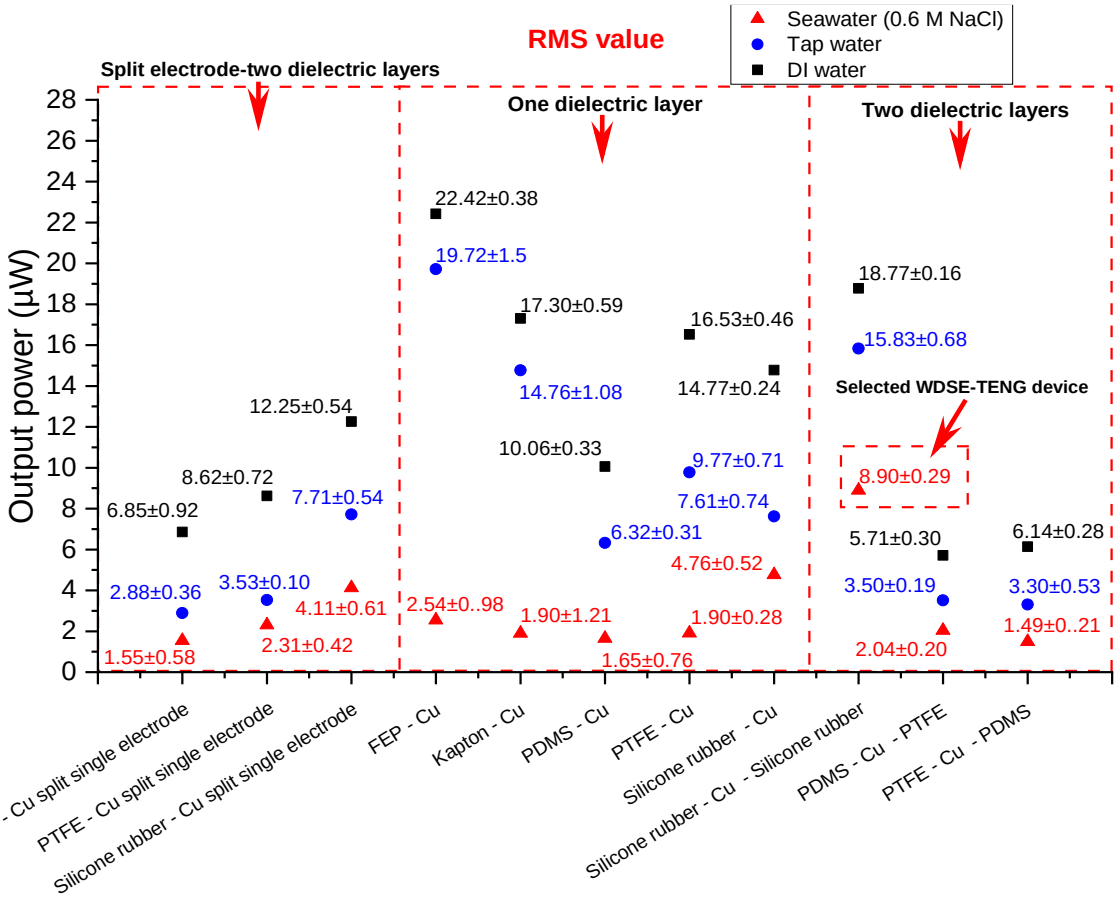

Figure 6.8 Comparison of the output power calculated for each of the three WDSE-TENG prototypes when exposed to 10.5 cm amplitude waves at 1.2 Hz (with 1 MΩ load).

The results show that the reduction in the performance of the WDSE-TENG can be compensated by increasing the contact area of the devices operating with seawater to obtain a better output

performance (Figure 6.8). Consequently, as the WDSE-TENG energy harvesters must be working in seawater conditions under breaking water wave impact, the selected devices for further characterization were the ones composed with two dielectric layers composed of silicone rubber (Figure 6.8). The selected devices generated the highest power performance of 8.90 µW under seawater conditions due to the effective contact area of 46 cm^2 (Figure 6.1 (b)), compared with the other energy harvesters with active areas of 28 cm^2 and 27.2 cm^2 (Figure 6.1 (a) and Figure 6.1 (c)). The performance of the triboelectric liquid-solid interfaces used for the WDSE-TENG energy harvesters, arranged according to the output performance under breaking water wave impact is summarized in Table 6.1 (a-b). The most negative material in contact with DI water and tap water was FEP (Table 6.1 (a)). On the contrary, the most negative dielectric material with the seawater-dielectric interface interaction was silicone rubber compound (Figure 6.8 and Table 6.1 (b)), which means that the charge transferred using this water-dielectric interface is the highest from the selected triboelectric materials, with the objective being to reach the highest electric output performance in the proposed WDSE-TENG energy harvesters in seawater conditions. Nevertheless, the WDSE-TENG devices comprising FEP, PTFE, Polyimide and PDMS layers in contact with seawater show weak electron transfer effect, which means that ion adsorption effect dominates the contact electrification with those polymers [122, 143].

Table 6.1 Comparison of the level of positive and negative triboelectric water-dielectric interfaces in terms of ease of losing or gaining electrons through breaking water wave impact comprising (a) DI water and tap water and (b) seawater.

Triboelectric liquid-solid interfaces combination			
Arranged according to the best dielectric layers in contact with DI water and tap water			
Liquid	Positive ↑	DI water Tap water Seawater (0.6M NaCl)	**a)**
Solid	Negative ↓	Polydimethylsiloxane (PDMS) (125 µm) Silicone rubber compound (Acetoxy Elastomer) (150 µm) Polytetrafloroethylene (PTFE) (100 µm) Polyimide (127 µm) Fluorinated ethylene propylene (FEP) (24 µm)	
Arranged according to the best dielectric layers in contact with seawater			
Liquid	Positive ↑	DI water Tap water Seawater (0.6M NaCl)	**b)**
Solid	Negative ↓	Polydimethylsiloxane (PDMS) (125 µm) Polyimide (127 µm) Polytetrafloroethylene (PTFE) (100 µm) Fluorinated ethylene propylene (FEP) (24 µm) Silicone rubber compound (Acetoxy Elastomer) (150 µm)	

6.3.2 Single/Grid WDSE-TENG output performance electrical characterization under different breaking water wave impact frequencies and potential battery-less applications

The WDSE-TENG with two-dielectric layers comprising silicone rubber compound exhibit maximum output power and power density of 9.65 mW and 0.21 mW/cm^2, respectively. These values were obtained with a load resistance of 3.8 MΩ, selected from a load resistance matching characterization under breaking water wave impact at 3 Hz with an amplitude of 12 cm (Figure 6.10 (g)). Further, the grid/single WDSE-TENG tested in seawater through different breaking water wave impact frequencies (0.7 Hz-3 Hz) and amplitudes (10 cm- 12 cm) show a linear increase in their electric output performance focused on the transferred charges, an enhancement factor of 4.06 and 3.25 was calculated with the single WDSE-TENG and grid of five WDSE-TENG devices as illustrated in Table 6.2. Further, the overall electric output performance enhancement factors of the single and grid of WDSE-TENG are of 3.29 and 2.54 as the frequency of impact increases as illustrated in Figure 6.10 (a-f). Such increase is attributed and proportional to the total mechanical energy of the breaking water wave impact (6.2) consisting of potential and kinetic energy that contacts on the WDSE-TENG devices. Which rises from 50.76 J to 73.10 J that produces an increase in the friction between the liquid-solid interface [122, 152-154] (Figure 6.3 (e)) increasing the electron exchange and ion adsorption that occurs simultaneously [123, 140-142] as the frequency and amplitude of impact rises (Figure 6.9 (a-b)).

Table 6.2 Estimation of the electric output performance enhancement factor of the single WDSE-TENG and grid of five WDSE-TENG energy harvesters focused on the transferred charges (Q) at breaking water wave impact conditions with a frequency from 0.7 to 3 Hz with amplitudes of 10 cm to 12 cm.

Breaking water wave impact		Single WDSE-TENG	Grid of five WDSE-TENG
Frequency (Hz)	Amplitude (cm)	Transferred charges (Q)	Transferred charges (Q)
0.7	10	41.54	144.9
1.2	10.5	68.67	237.07
1.8	11	87.31	302.81
2.5	11.5	138.24	421.95
3	12	169.04	471.34
Enhancement factor		4.069330766	3.252864044

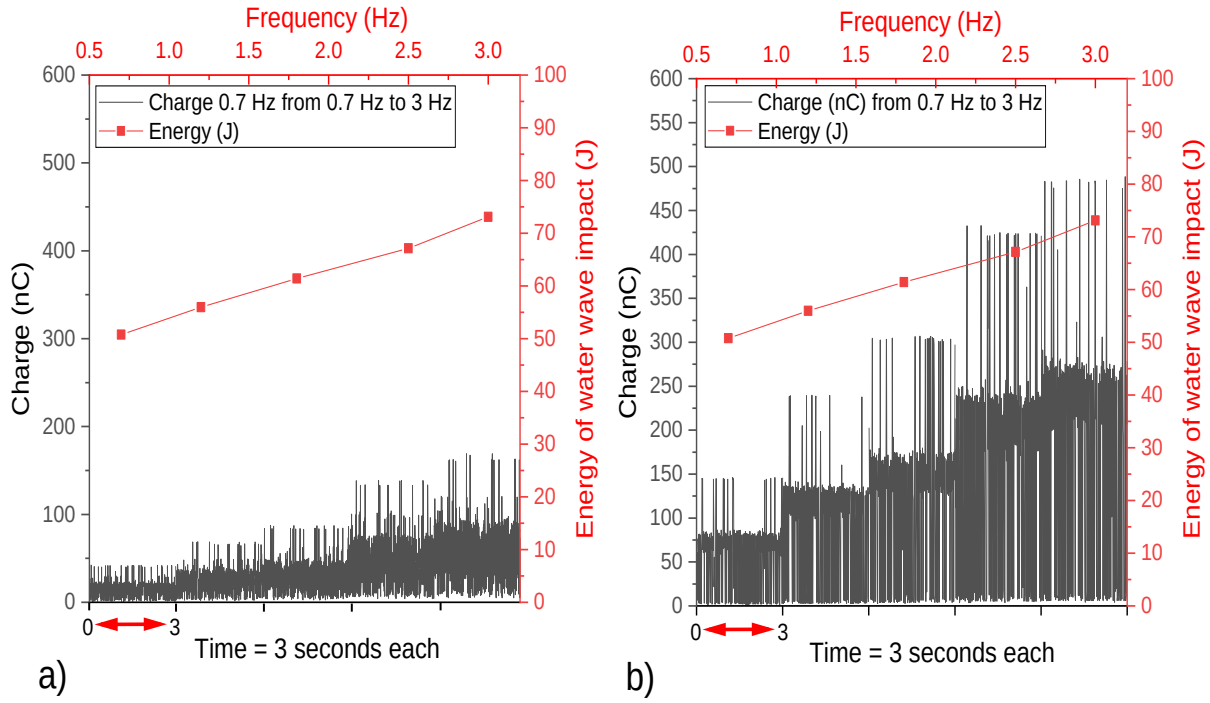

Figure 6.9 Transferred charges of (a) a single WDSE-TENG and (b) grid of five WDSE-TENG devices through different breaking water wave frequencies (0.7 Hz to 3 Hz) in proportion to the total mechanical energy of the breaking water wave impact consisting of potential and kinetic energy that contacts on the WDSE-TENG (Data acquired during 3 seconds for each sample).

The maximum rectified output power of the single WDSE-TENG device increases from 1.21 mW to 9.76 mW (Figure 6.10 (a-b)), with corresponding maximum instantaneous output voltage, current and transferred charge values of 56.84 V to 130 V, 21.31 µA to 74.67 µA and 41.79 nC to 169 nC, respectively (Figure 6.10 (a-c)).

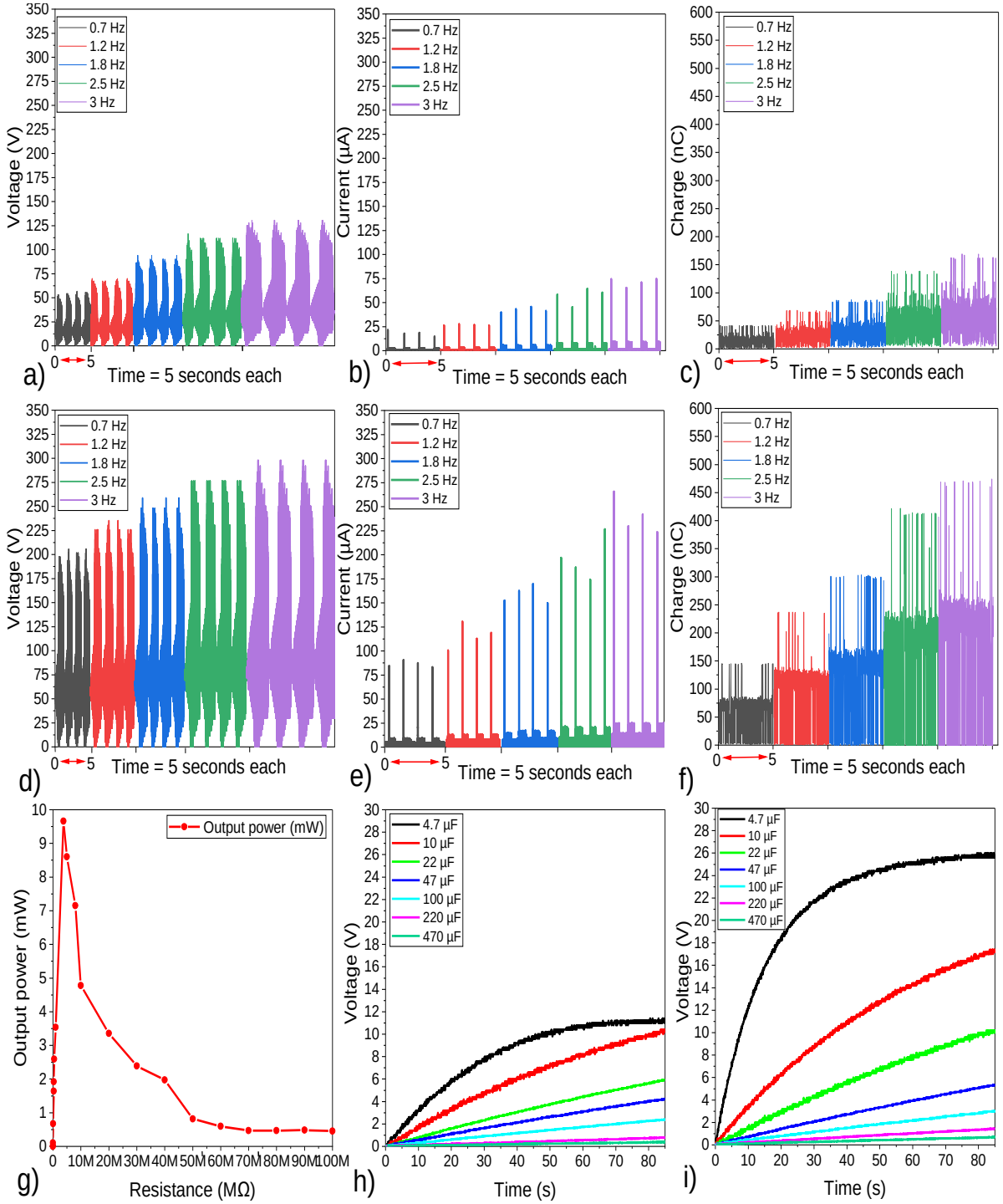

Figure 6.10 (a) The Instantaneous output voltage, (b) current and (c) transferred charges of a single WDSE-TENG with two-dielectric layers of silicone rubber compound. (d) Instantaneous output voltage, (e) current and (f) transferred charges of the grid of five WDSE-TENG devices through different breaking wave impact frequencies (0.7 Hz to 3 Hz) with a load resistance of 3.8 MΩ (Data acquired during 5 seconds for each sample). (g) Load resistance matching analysis to obtain the highest output power performance with the WDSE-TENG devices. (h) Charging performance of a single WDSE-TENG energy harvester, and (i) a grid of five WDSE-TENG energy harvesters connected in parallel to different capacitors (4.7 μF to 470 μF) tested in the water generator tank.

In comparison, the grid of five energy harvesters connected in parallel, with a total active area of 230 cm^2, showed an overall enhancement by a factor of 6.14 in the average rectified instantaneous output performance with an increasing output voltage, current and transferred charges from 205.63 V to 298 V, 90.52 µA to 265.78 µA and 144.9 nC to 469.70 nC, respectively (Figure 6.10 (d-f)). Consequently, the grid of energy harvesters generated a maximum output power and power density of 18.61 mW to 79.18 mW (Figure 6.11 (a-b)) and 0.081 mW/cm^2 to 0.344 mW/cm^2 (3.8 MΩ load). Furthermore, the output performance enhancement was verified by charging different capacitors from 4.7 µF to 470 µF. The maximum voltage reached by the single unit of WDSE-TENG was 11.18 V, compared with the grid of WDSE-TENG devices that reached a maximum value of 25.73 V, when charging a capacitor of 4.7 µF for 85 seconds as illustrated in Figure 6.10 (h) and Figure 6.10 (i).

Additionally, the average energy conversion efficiency (ECE) η of one WDSE-TENG energy harvester and a grid of WDSE-TENG composed of five devices was calculated. The ECE is defined as the ratio between the electric energy ($E_{electric}$) delivered to the load resistor of 3.8 MΩ and the mechanical energy ($E_{waterwave}$) applied by the breaking water wave impact on the single/grid of WDSE-TENG devices. A time period of 15 seconds was considered when calculating $E_{electric}$ for different frequencies (0.7 Hz- 3 Hz) and amplitudes (10 cm- 12 cm). The $E_{electric}$ released for the single and grid WDSE-TENG energy harvesters were from 0.6 J to 4.84 J and 9.23 J to 39.28 J, respectively as shown in Figure 6.11 (a-b). These values were estimated using the following equation:

$$E_{electric} = \int_{t1}^{t2} RI^2 dt \tag{6.1}$$

where I is the average instantaneous current generated by the devices and R is the load resistance. The total mechanical energy of the water waves was between 50.76 J to 73.10 J consisting of potential energy and kinetic energy [120]:

$$E_{waterwave} = \frac{1}{2}\rho g {A_{waterwave}}^2 \tag{6.2}$$

Where g is the acceleration of gravity, ρ is the density of seawater (1036 kg/m^3) [155], and $A_{waterwave}$ is the wave amplitude from 10 cm to 12 cm. Consequently, the overall η of the single/grid of WDSE-TENG energy harvesters rise linearly between 1.18 % to 6.62 % and 18.19 % and 53.74 % as depicted in Figure 6.11 (a-b), calculated by [114]:

$$\eta = \frac{E_{electric}}{E_{waterwave}} x100\% \tag{6.3}$$

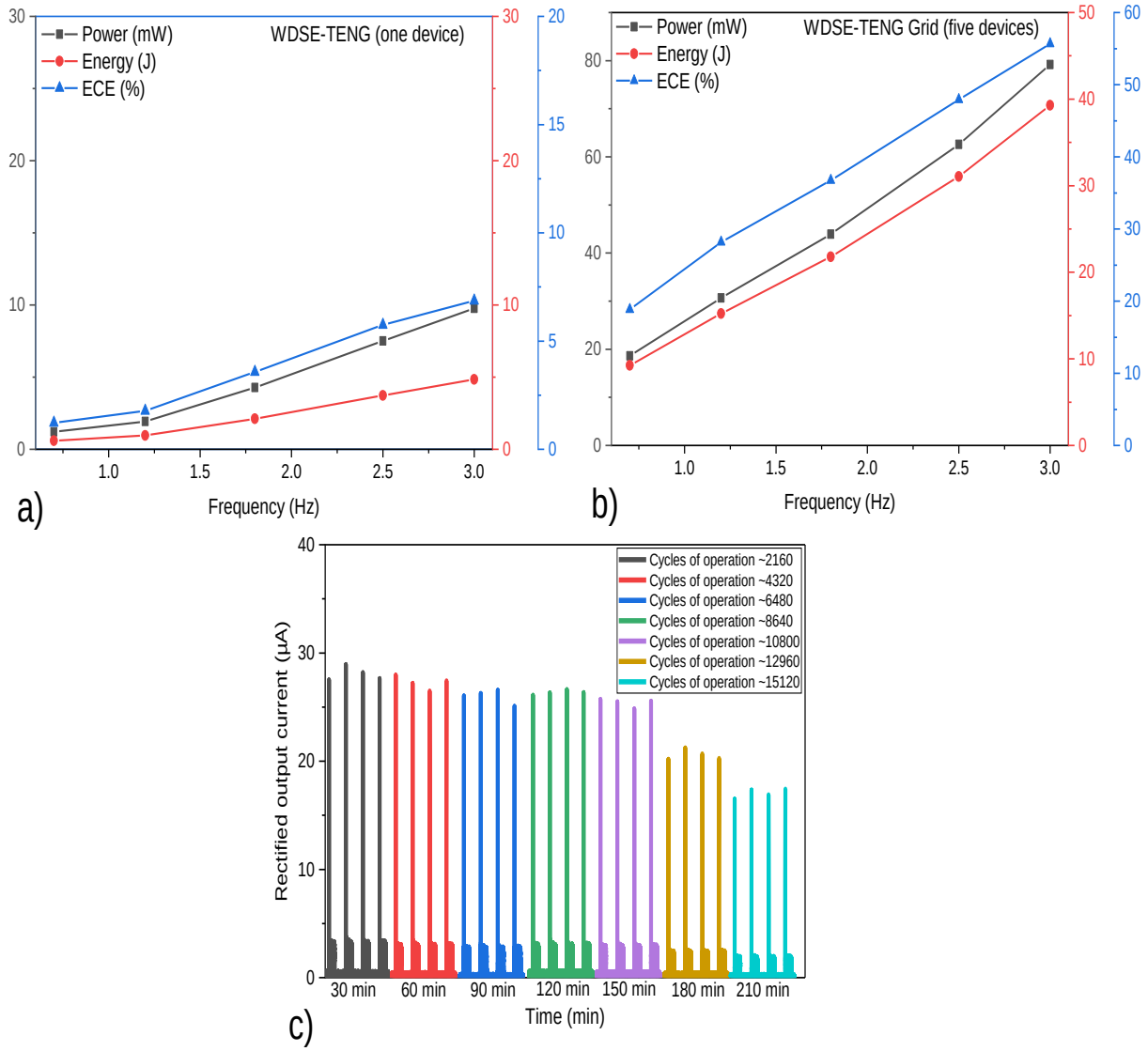

Figure 6.11 (a) Average instantaneous output power, energy and energy conversion efficiency of a single WDSE-TENG with two-dielectric layers of silicone rubber compound over 15 seconds. (b) Average instantaneous output power, energy and energy conversion efficiency of the grid of five WDSE-TENG devices through different breaking wave impact frequencies (0.7 Hz to 3 Hz) and amplitudes (10 cm to 12 cm) with a load resistance of 3.8 MΩ, for 15 seconds. (c) Maximum average instantaneous output current generated by the WDSE-TENG during different periods and cycles of operation from 30 min to 210 min and 2160 cycles to 15120 cycles under breaking water wave impact.

Moreover, analyzing to extrapolate the potential to scale up [26] the energy harvesting of breaking water wave on an area of 18 m^2, where the water wave breaks with amplitudes between 0.3 m to 4 m [119] using a grid of WDSE-TENG. Considering the output power of a single WDSE-TENG and the frequency of water wave impact. This could be possible with the fabrication of big water-dielectric triboelectric-structure interfaces composed with 7,200 energy harvesters connected in

parallel, which could have the potential to generate an average output power, and energy of 30.63 W and 15.20 kJ, respectively. Consequently, estimating the breaking of a water wave with an amplitude of 4 m that generates the energy of 78.4 kJ (6.2) impacting over the big proposed interface. The big-scale grid of WDSE-TENG could have an ECE of 19.38% (6.3), collecting breaking water wave impacts in big-scale with different amplitudes in the aforementioned area. Besides, a durability test was performed on the WDSE-TENG device composed of two silicone rubber dielectric layers under breaking water wave impact with a frequency and amplitude of 1.2 Hz and 10.5 cm, over different periods of 30, 60, 90, 120, 150 180 and 210 min. Based on the number of cycles of operation and the rectified output current of the WDSE-TENG energy harvester. The results show that the energy harvester maximum average output current is stable over 150 min and ~10800 cycles of operation under the impact of water waves as illustrated in Figure 6.11 (c). Subsequently, the performance decreases linearly as the operation time increases from 150 min to 180 min and 210 min with a decrease by a factor of 1.27 and 1.55, respectively (Figure 6.11 (c)). The average maximum instantaneous current decreased from 27.14 µA (60 to 150 min) to 21.21 µA and 17.41 µA (180 to 210 min) as the cycle of operation increases from 12960 to 15120, respectively. Although under 10800 cycles of operation, the WDSE-TENG performance was stable, further investigation is required to improve the energy conversion efficiency and device durability to withstand the harsh environmental conditions of the ocean and liquid environments.

Besides, due to the improvement of the breaking water wave energy harvesting through the implementation of the grid of WDSE-TENG devices charging different capacitors (Figure 6.12 (a)), some applications were demonstrated. First, the grid of WDSE-TENG energy harvesters was used to power a one way wireless 433 MHz transmitter (Seeed Studio RF link kit part no. 113990010) to send a signal to the receiver to turn on a therma-hygrometer with a transmission distance from 2 m to 8 m as shown in Figure 6.12 (b-c). This was achieved after charging a 47 µF capacitor between 129 to 370 seconds, resulting in a voltage of 3.19 V to 9.81 V across the capacitor, and then using the stored electrical energy to power up the transmitter. To transmit at longer distances, more energy can be stored by charging suitable capacitors for a longer time. The energy stored in the capacitor for the grid of WDSE-TENG devices, and the power generated for the capacitor during the discharging process for powering the wireless transmitter were between 193.56 µJ to 2.24 mJ, and 322 µW to 3.73 mW, respectively (Figure 6.13 (a) and Figure 6.13 (c)).

Furthermore, an ultrasonic range sensor (HC-SR04) for detection of objects was powered by charging a 470 µF capacitor for 570 seconds (Figure 6.12 (d) and Figure 6.13 (b)) using the grid of energy harvesters. The range sensor was able to track the movement of a plastic sheet located at a distance of 30 cm over a short period (~1 s) as illustrated in Figure 6.12 (d). The energy stored in the capacitor for the grid of energy harvesters and the power supplied by the capacitor to power up the ultrasonic ranger sensor were 5.96 mJ and 5.18 mW, respectively. This demonstration

confirmed that the grid of energy harvesters using a liquid-solid interface was able to drive typical electronic devices found in wireless sensor systems.

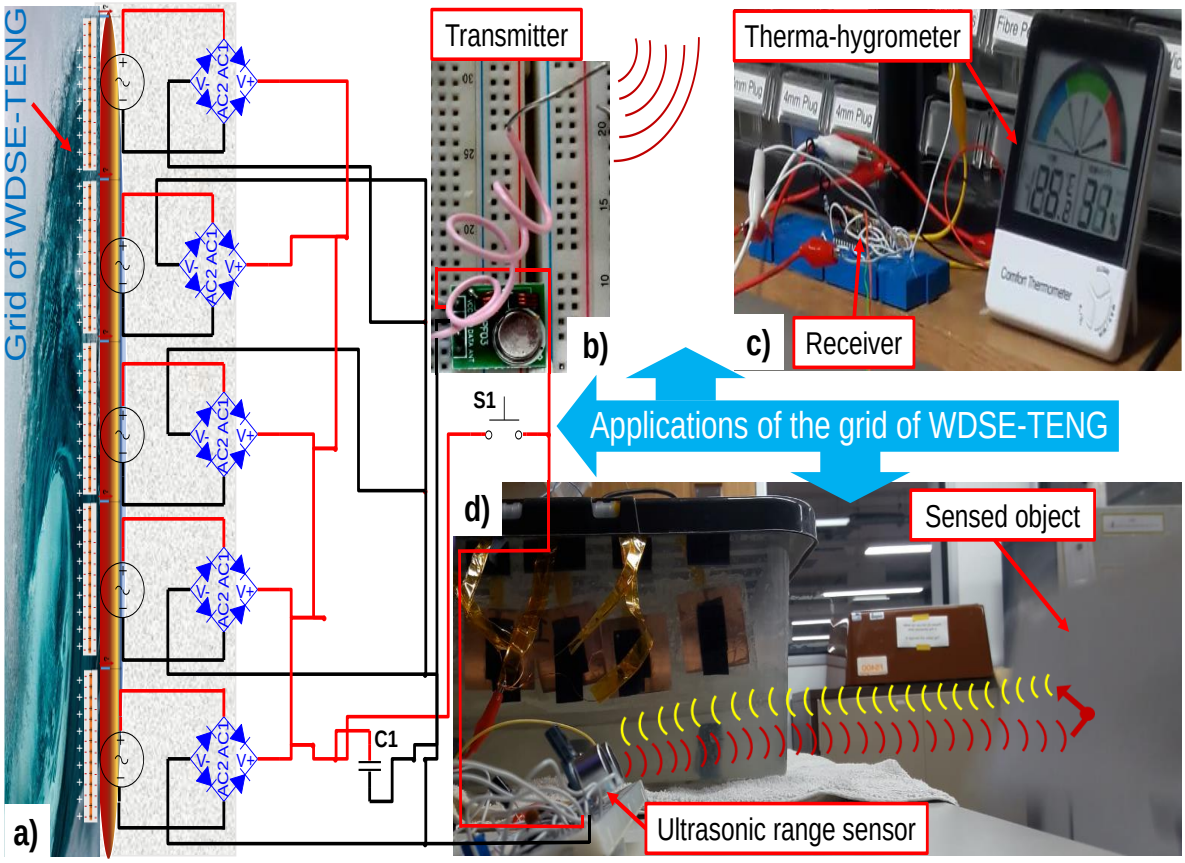

Figure 6.12 (a) Electrical circuit diagram of the grid of WDSE-TENG energy harvesters under breaking water wave impact to charge the 47 µF and 470 µF capacitors to power-up (b) the wireless transmitter to turn (c) a Therma-hygrometer and (d) an ultrasonic ranger sensor (Ocean water wave adapted from Refs. [132]).

Finally, the most critical problem to develop a direct integration between a triboelectric energy harvester (very high impedance) and a storage unit (very low impedance) is the impedance mismatch causing low charging efficiency [156]. To improve the energy transfer, a system with a pre-storage capacitor (Ct) was used to store the energy from the grid of WDSE-TENG and to maintain the optimal voltage across the diode rectifier bridge in order to optimize energy extraction. This was achieved using a flyback converter circuit that gives more design flexibility [157]. Therefore, an LT8303 micropower high-voltage insolated flyback converter was integrated to the grid of WDSE-TENG to form a power management control circuit (PMCC) [157] as shown in Figure 6.13 (d-e). The objective of the PMCC is to maintain the voltage constant across the diode rectifier when the temporary capacitor (4.7 µF) reaches approximately 5 V after 12.8 seconds (Figure 6.13 (f)). This is achieved by transferring one part of the energy stored in Ct to the storage capacitor (Cs, 100 µF) through the flyback converter (Figure 6.13 (f)). Harvesting the breaking water wave impact for 200 seconds, the storage capacitor reached a maximum voltage of 2.64 V with a

stored energy of 16.37 µJ, as shown in Figure 6.13 (f). This power conversion principle enables the utilization of multiple WDSE-TENG connected in parallel using one coupled inductor and only one PMCC (Figure 6.13 (d-e)). This system is able to improve the output power of the water-dielectric energy harvesters with the potential to power up electronic devices such as autonomous wireless sensor nodes for detecting fish and measuring water levels at smart fish farms.

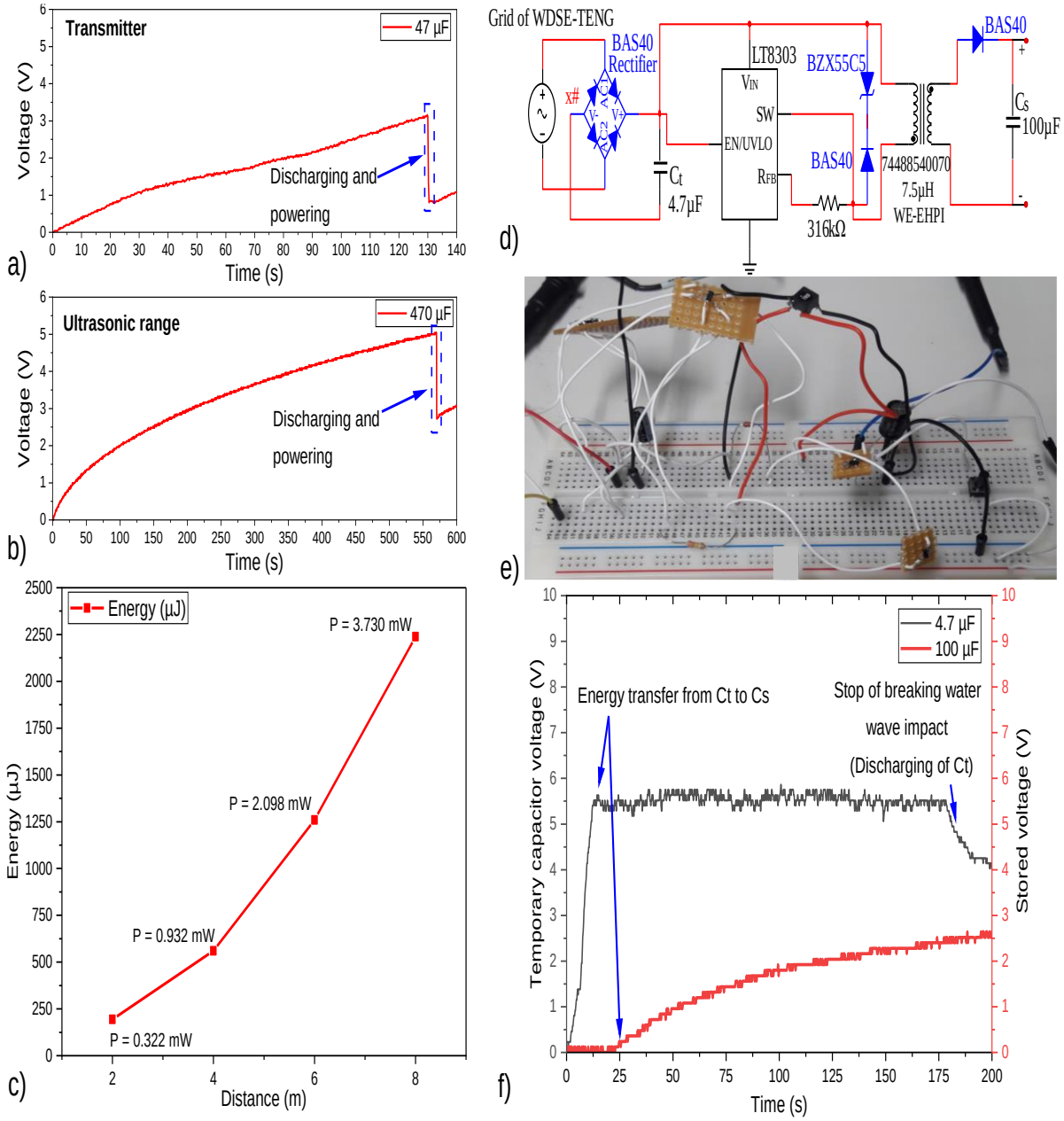

Figure 6.13 Capacitor charging and discharging process for powering the (a) wireless transmitter to power-up the therma-hygrometer, and (b) ultrasonic range sensor under the breaking water wave impact with a frequency of 1.2 Hz. (c) Energy stored in the 47 µF capacitor for the grid of WDSE-TENG devices, and the power supplied by the capacitor during the discharging process for powering the wireless transmitter to turn on a therma-hygrometer. (d) Integration of the grid of WDSE-TENG with an LT8303 micropower high-voltage insolated flyback converter to form a power management

control circuit (PMCC). (e) Digital image of the PMCC circuit with the grid of WDSE-TENG. (f) Energy transfer from Ct to Cs from harvesting the breaking water wave impact for 200 seconds.

6.4 Chapter summary

In summary, the research work developed through this chapter has demonstrated the potential of WDSE-TENG devices as an innovative and alternative approach for harvesting mechanical energy from breaking wave impact forces at the structure-water interfaces using water as a triboelectric material.

Firstly, by comparing WDSE-TENG composed of different device configurations and five hydrophobic dielectric materials in contact with DI water, tap water and seawater, the ideal energy harvester configuration and the liquid-solid interface was found in order to enhance the output performance of the proposed energy harvesters. The performance of the DI/tap water-FEP WDSE-TENG were the most promising. On the other hand, a reduction in the performance of the WDSE-TENG with seawater-dielectric interfaces was observed, but it was demonstrated that this can be compensated by increasing the contact area of the devices to enhance the output performance. Consequently, the WDSE-TENG energy harvester comprising two-hydrophobic silicone rubber compounds showed the highest electrical output working in seawater conditions under breaking water wave impact. Secondly, it was demonstrated that an improvement in the power output by a factor of 6.14 for the seawater-dielectric energy harvesters was possible. This was achieved using a parallel connection of a grid of five WDSE-TENG devices with a coverage area of 230 cm^2 compared to a single WDSE-TENG device. The ability to charge different capacitors was demonstrated, and the output voltage, current, transferred charges, output power and ECE values respond with linear increase as the water wave impact energy rises, increasing the liquid-solid interface friction, electron exchange and ion adsorption [122, 140-142, 152-154] as the frequency varies from 0.7 Hz to 3 Hz, with amplitudes between 10 cm to 12 cm.

Thirdly, the grid of WDSE-TENG devices has the potential to drive low-power electronic devices with stored energy levels between 2.24 mJ and 5.96 mJ, and they generate power in the range 3.73 mW to 5.18 mW, which is sufficient to power an ultrasonic range sensor, and also to power a wireless transmitter. Finally, the integration of the grid of WDSE-TENG devices with a PMCC allows the device to achieve power levels from 1 mW to 100 mW [133, 134] for powering electronic devices continuously using a TENG. Further investigation is required to explore the integration of superhydrophobic materials to withstand the seawater conditions utilizing the WDSE-TENG energy harvesters that have a stable electrical output under 10800 cycles of operation during 150 min, measured through a durability test. The integration of the grid of WDSE-TENG offers an innovative approach that is able to work in liquid environments.

Chapter 7 Conclusion and future work

7.1 Conclusion

Different energy harvesters were designed, modelled, fabricated, characterized, used and integrated as a source to power up small electronic devices exploiting the potential to harvest breaking water wave impact energy at a wide frequency range from lower frequencies between 0.7 Hz to 3 Hz and high frequencies between 30 Hz to 252 Hz. This was achieved through an alternative approach, stable, easy, simple to fabricate and lightweight triboelectric nanogenerators and hybrid nanogenerators using contact electrification between solid-solid and liquid-solid interfaces.

Firstly, studying the triboelectric effect using solid-solid triboelectrification between dielectric-conductor materials, it was found the ideal triboelectric material combination for the fabrication of the DMCS-TENG devices. The results show that the experimental set-up changes the mechanical force conditions [121, 122] of the contact electrification performance between the tested materials combinations based on the electric output performance. The results show that the triboelectrification between silver-PDMS exchanges more charges using an impact test and by utilizing dielectric layers with a thickness from 100 µm to 125 µm. On the contrary, it was found that the contact electrification between polyimide-honeycomb patterned Al foil exchanges the most charges based on the generated output power of the DMCS-TENG devices through an oscillatory test with a mechanical shaker in a broad frequency range. Consequently, a distinct most negative material was found compared with the one shown in the literature focused on the contact-electrification between dielectric-metal materials [68, 82]. These findings suggest that the previously published triboelectric series [68, 82] may not give the obvious material pair for the best energy harvesting performance under all circumstances, due to the inaccurate qualitative ranking without numerical data and difference in the mechanical properties of the materials (elasticity, hardness, stiffness and thickness). Consequently, for cross-comparison, a standardized method must be created to quantify and normalize the triboelectric series [123] focused on a wide range of dielectric-metal materials using thickness normalized values and standard experimental set-up conditions (atmospheric pressure, temperature, humidity, etc.).

Furthermore, through the FEM modelling, fabrication, electric characterization and testing of the DMCS-TENG energy harvesters. It was found that these devices can effectively respond to a broad range of input oscillatory frequencies from 30 Hz to 252 Hz showing different resonant peaks along with that range. Additionally, an enhancement in the output power by a factor of 2.3 of the DMCS-TENG devices was achieved by incorporating a honeycomb-patterned Al to the DMCS-TENG devices

as a low-cost option to improve their electrical output performance. Such improvement in the output performance is due to the increase of effective contact area between the dielectric-metal materials, increasing the triboelectric charge generation during the friction caused by the surface pattern of the aluminium foil.

Secondly, through the simultaneous integration of triboelectric and piezoelectric effects based on solid-solid contact triboelectrification and piezoelectricity. The improvement in the output performance of fabricated hybrid nanogenerators for water wave, impact force energy harvesting was achieved, tested under simulated breaking water wave conditions at low frequencies and amplitudes between 0.7 Hz to 3 Hz and 10 cm to 12 cm, respectively. These hybrid energy harvesters show a linear enhancement in the electric output performance by a factor of 2.24, 4.80 and 3.21 in comparison with arc-shaped DMCS-TENG, DMCS-TENG self-resetting system and piezoelectric nanogenerator (PENG) tested in similar conditions. Moreover, by the attribution of an electrically parallel connection to build a grid of four hybrid nanogenerators, improved the output power by a factor of 2.43 in comparison with a single hybrid energy harvester.

Thirdly, it was demonstrated the potential to utilize DI water, tap water and seawater as a triboelectric active material in contact with hydrophobic dielectric materials as an alternative approach for harvesting the mechanical energy from the breaking water waves impact forces at the aforementioned low frequencies. Through the fabricated WDSE-TENG comprising different configurations and by studying the contact electrification between liquid-solid materials combinations. The results showed a maximum and similar output performance with the DI/tap water-FEP interface compared to the WDSE-TENG. On the other hand, a reduction factor of 4.20 and 2.86 in the performance of the WDSE-TENG with seawater-dielectric interfaces was observed, compared with the devices comprising DI/tap water-hydrophobic dielectric interfaces. Further, it was demonstrated that such electric output reduction can be compensated and enhanced by increasing the contact area of the devices. Consequently, the highest electrical output performance was achieved with a WDSE-TENG device comprising two-hydrophobic silicone rubber compound layers working in seawater conditions under breaking water wave impact. Additionally, such power output was linearly improved by a factor of 6.14 through a grid of five seawater-dielectric energy harvesters connected in parallel compared to a single WDSE-TENG device.

Fourthly, the capacity of the grid comprising hybrid nanogenerators and the grid of WDSE-TENG with the generated power levels and ECE between 24.63 mW to 30.64 mW and 27.12 % and 28.17%, respectively. It was demonstrated that they are capable to drive low-power electronic devices by using the stored energy in a capacitor and generated power from 193.56 µJ to 2.24 mJ, and 322 µW to 3.73 mW, charged over different periods. The devices were capable of powering a wireless transmitter and sending a signal to a receiver at varying distances to turn on LEDs and a hygrometer for humidity/temperature measurements. Furthermore, the grid of energy harvesters was able to

power up an ultrasonic ranger sensor HC-SR04 for distance measurement or detection of objects in a distance of 30 cm during a short time (~1 s). This was achieved with stored energy and generated power of 5.96 mJ and 5.18 mW, respectively. Besides, a potential solution to solve the challenge that the DMCS-TENG, hybrid and WDSE-TENG energy harvesters systems proposed through this research project and many self-powered systems based in TENG that cannot work continuously. Such a grid of energy harvester was integrated with a PMCC that allows the output power to achieve power consumption levels from 1 mW to 100 mW [133, 134] for electronic devices. Moreover, it is estimated with the construction of large water-nanogenerators-structure interfaces integrated with 11,250 to 2,812 energy harvesters connected in parallel for the generation of electricity on a large scale, harvesting breaking water wave in area of 18 m^2. Which could have the potential to generate average output powers, power densities and ECE from 3.05 W to 30.63 W, 0.169 W/m^2 to 1.7 W/m^2, and 5.16% to 30.22%, respectively, where it is estimated to generate the highest electric output performance employing a large grid of WDSE-TENG energy harvesters. Such results are supported for the research work performed by Jun Chen [26] that proposed a network of triboelectric nanogenerators for harvesting the energy of shallow water waves over an area of 1 km^2 performing a similar extrapolation according to their energy harvesting configuration that estimates to produce an average power of 1.15 MW.

Finally, between the tested and characterized energy harvesters considering the electric output performance for a single unit. The highest power density of 3.8 W/m^2 was generated with the hybrid nanogenerators as illustrated in Figure 7.1, followed by the WDSE-TENG and DMCS-TENG with power densities between 1.7 W/m^2 and 0.695 W/m^2, respectively. Although, the proposed energy harvesters have a stable electrical output under 4320 and 10800 cycles of operation during 60 and 150 min through a durability test. Further investigation is required to explore superhydrophobic materials, more design parameters and more efficient energy coupling to withstand the seawater conditions utilizing the DMCS-TENG, hybrid nanogenerators and WDSE-TENG energy harvesters. The integration of the grid of the proposed energy harvesters offers an innovative approach that is able to work in liquid environments using contact electrification between solid-solid and liquid-solid triboelectric interfaces. This is effectively an energy source that could be implemented for smart self-powered wireless sensing systems at water-structure interfaces for aquaculture applications as fish detection, water level measurement, weather conditions monitoring at smart fish farms. At small and big scales harvesting breaking water wave impact energy in areas between 145 cm^2 and 18 m^2, and the utilization to prevent critical structural damage in coastal defence systems. Such applications having average power consumptions from 1 mW to 100 mW [133, 134] for small scales, and 100 W to 1 kW [135] for large scales, respectively. This research work provides a promising alternative and innovative approach to harvest breaking water wave impact energy at a broad

frequency range between 0.7 to 252 Hz, with the generated power density levels from 0.695 to 3.8 W/m^2, implementing the proposed energy harvesters that show a stable performance. Which contributes and similar power density levels were generated in comparison to the previous energy harvesting studies that are focused on harvesting shallow water wave energy at a low-frequency range from 0.5 to 10 Hz, with generated power densities between 0.05 and 9.62 W/m^2 [19-27, 29-40] as illustrated in Figure 7.1.

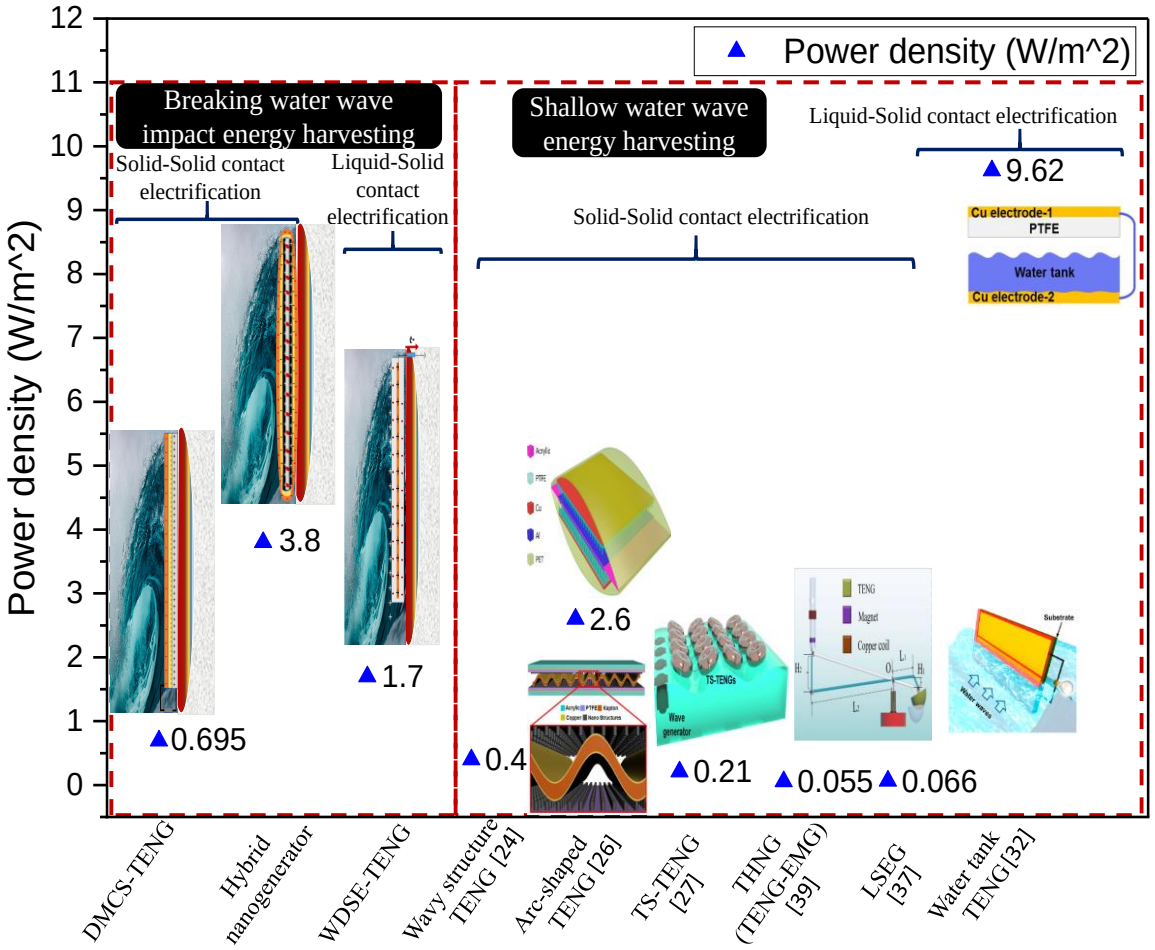

Figure 7.1 Power density generated by the DMCS-TENG [124, 125] (Results can be found in section 4.3.2 and section 5.3), hybrid nanogenerators [136] (section 5.3) with contact electrification between solid-solid materials, and WDSE-TENG [158, 159] (section 6.3.2) with contact electrification between liquid-solid materials for breaking water wave impact energy harvesting. The power density of energy harvesters based in TENG, Hybrid TENG-EMG and liquid-solid-enabled generator (LSEG) for shallow water wave energy harvesting using solid-solid and liquid-solid contact electrification [19-40].

7.2 Future work

Future studies on DMCS-TENG, hybrid nanogenerators, WDSE-TENG should be focused on the improvement of the electrical output performance (focus on reducing the device impedance and improve the output current), ECE, durability, integration with power management control circuits and scalability exploiting the collection of breaking wave impact energy. In order to achieve these challenges, the following points should be addressed:

- A standardized method to quantify and normalize the triboelectric series focused on a wide range of contact electrification between dielectric-metal, dielectric-dielectric and liquid-dielectric materials must be created using thickness normalized values and standard experimental set-up conditions (atmospheric pressure, temperature, humidity, etc.).

- Further investigation is required to enhance the contact electrification and surface triboelectric charge density between the solid-solid and liquid-solid materials in contact. Focus on material surface physical and chemical modification, in order to improve the output performance of the energy harvesters. Creating patterns with different shapes and sizes as wires, pyramids, pores, channels and so on, over the surface of the dielectric-metal layers or the hydrophobic dielectric layers with normalized thicknesses, to enhance the effective contact area of the devices. These patterns can created by using different etching methods as ion etching, chemical etching, nanoparticle deposition, plasma etching, electrochemical anodization, ion injection methods or by using commercial sandpapers with different grit dimensions as a low-cost and practical method.

- In order to increase the durability and efficiency of the energy harvesters to withstand the seawater conditions and to avoid the adhesion of positive charges and free ions to the surface of the hydrophobic layers, which reduces the output power of the WDSE-TENG devices. Studies should be oriented in the creation and integration of superhydrophobic dielectric layers, or by changing the dielectric film with a specific functional group to counter ions with opposite charges that remain on the contacted surfaces during water wave impact. Additionally, to increase the durability of the DMCS-TENG and hybrid nanogenerators, waterproof sealing/packaging should be incorporated in the fabrication process of such devices. For better device robustness to reduce the surface friction, a TENG working in the freestanding-mode could be developed to harvest the breaking water wave impact.

- Characterization of the output performance of the hybrid nanogenerators coupling triboelectric-piezoelectric effect at broad frequencies from 30 Hz to 252 Hz, the comparison

with triboelectric nanogenerators with material surface modification in the triboelectric pairs and different design structures.

- The integration of TENG with other energy harvesting techniques as photovoltaic and electromagnetic should be studied and compared with the potential of the hybrid devices incorporated with the piezoelectric effect. In order to enhance the output current to increase the output power of the devices, harvesting the energy harvesting of the breaking wave impact.

- Further research on the integration of the energy harvesters with a PMCC circuit, in order to enhance the energy extraction of the energy harvesters, to efficiently store the TENG electric energy into an energy storage unit as a battery. Aimed at the impedance matching between the TENG energy harvesters (very high impedance) and the energy storage device (very low impedance). Circuit simulation of the integration between the energy harvesters and the PMCC components to optimize the energy extraction and efficiency of the system. For the potential development of a grid-TENG smart battery-less wireless sensing system for water-structure interfaces in aquaculture (e.g. for fish detection or water level measurement) and weather condition monitoring.

- The electrical output performance and durability of the proposed and studied grids of energy harvesters should be performed under real breaking water wave conditions to test their capability and potential under real harsh environmental conditions.

- Furthermore, scalability in the fabrication process of the triboelectric energy harvesters should be studied. For the fabrication of the proposed large-scale water-Grid of DMCS-TENG/WDSE-TENG-structure interfaces for the harvesting of breaking water wave impact energy at large scale. Which potentially can be fabricated in large scales for mass production and commercial applications due to the extensive choice of materials that can be utilized for the fabrication of the triboelectric nanogenerators.

Appendix A

A contact-separation mode triboelectric nanogenerator for ocean wave impact energy harvesting

Ulises Tronco Jurado[1,2], Suan Hui Pu[1,3], Neil M. White[2]
[1]Faculty of Engineering and the Environment: Mechatronics Research Group, Southampton SO17 1BJ, UK
[2]Faculty of Physical Sciences and Engineering: Electronics, and Computer Science, Southampton SO17 1BJ, UK
[3]University of Southampton Malaysia Campus, Iskandar Puteri 79200, Johor, Malaysia
utj1n15@soton.ac.uk, suanhui.pu@southampton.ac.uk, nmw@ecs.soton.ac.uk

***Abstract*—This paper describes the effect of ocean wave impact compressed air bubbles on the output performance of a dielectric-metal contact separation mode triboelectric nanogenerator (DMCS-TENG). The triboelectric effect is generated by regular, non-uniform contact between a negative polyimide dielectric layer of easy gaining electrons and positive Aluminum foil of easy losing electrons according the triboelectric series, where the electrical performance changes in proportion to the mechanical energy applied by oscillatory frequencies. At the range of operation of 30 Hz to 300 Hz, the open-circuit voltage, short-circuit current, power and output power density of the device can reach to 3.83 V, 80.38 μA, 307.88 μW and 19.24 μW/cm², respectively for a load resistance of 10 MΩ. The proposed work demonstrates that the device can function as an energy harvesting mechanism for ocean wave monitoring applications that require self-powering.**

Keywords—ocean wave impact; compressed air bubbles; triboelectric; oscillatory frequencies; energy harvesting; ocean wave monitoring; self-powering

I. INTRODUCTION

Ocean wave energy has attracted great interest as a source of electrical energy for many years [2]. It can potentially meet 10% of the total worldwide electrical demand [3]. Effective utilization and sustainability of this kind of energy can be exploited due to the effects of climate change, leading to the rapid increase of sea levels and more recurrent flood coastal zones. Specifically, the cumulative loads of wave impact forces at coastal defense structures deliver high magnitude pulse-like forces with a wide frequency range of destructive oscillatory compressed air bubbles at the structure-water interfaces. The fluid-structure interaction has been predicted by means of a compressible fluid simulation during wave impact at porous structures [1, 4-7]. The initial impact produces a first pressure peak, after the wave collapses a plunging breaker is formed and a bubble is entrained, which compresses and dilates in a resonant oscillatory manner yielding a cyclical pressure response as shown in Fig. 1.

The principal oscillating frequencies within the flow are in the range 30 Hz to 300 Hz with a pressure range of 50 to 350 Pa [1, 7]. Such energy can be potentially harvested and exploited using triboelectric nanogenerators (TENG) in the operating

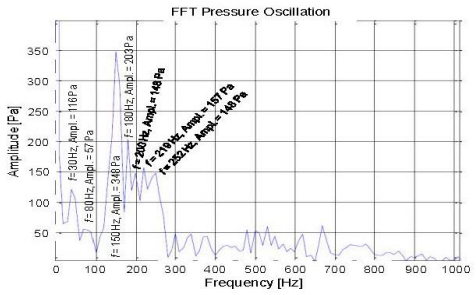

Fig. 1. Pressure signals recorded at face porous structures [1]

principle of contact-separation mode (CS-TENG). CS-TENG converts the external mechanical energy into electricity by a combination of triboelectric effect and electrostatic induction, based on contact electrification between two materials and charge transfer between their electrodes. Their advantages include broadband behavior, lightweight, good energy density and easy fabrication process exploiting low-cost abundant choice materials [8]. TENG can be used as energy harvesters for self-powering sensors [9],[10]. For these reasons, in this study, we fabricated and developed a finite element model (FEM) for a dielectric-metal CS-TENG (DMCS-TENG), composed of two triboelectric layers, Polyimide (PI) and Aluminium (Al) layers.

The output performance of the DMCS-TENG was evaluated in terms of the range of cumulative loads by the air bubbles' resonant oscillatory frequencies due to ocean wave impact forces (Fig. 1) in order to maximize the device performance and parameter optimization. It is expected that the enhanced output performance of the proposed DMCS-TENG will enable future advancement in energy harvesting at porous water interfaces to prevent critical damage and production of clean electricity at coastal defences.

II. THE DMCS-TENG FEM MODEL

Considering the so called "V-Q-x relationship" proposed for the operation and modelling of a TENG when it is connected with a resistive load (R), utilizing Kirchhoff's law, the governing equation of the whole system can be easily given by [11]:

978-1-5090-1012-7/17/$31.00 ©2017 IEEE

$$R\frac{dQ}{dt} = -\frac{1}{C(x)}Q + Voc(x) = -\frac{1}{C}Q + V_{OC} \qquad (1)$$

Where V_{OC} is the voltage generated between two DMCS-TENG contacts, Q is the amount of charge between the two contacts, C is a capacitor due the inherent capacitance between the two electrodes, and x is the distance between the DMCS-TENG triboelectric layers that varies with the mechanical energy and period of motion process (t). According to these models, the power output performance by the DMCS-TENG depends on the output current (I), voltage in the influence of the load resistance and the constant surface charge density σ from the properties of the dielectric materials. The maximum surface charge density σ_{max} (MSCD) for TENG was determined considering the ion injection method by the structure of the DMCS-TENG where the influence of the dielectric layer thickness d affects the σ_{max} parameter [12]:

$$\sigma_{max} = \left[\frac{AP\varepsilon_0(d+x\varepsilon_r)}{d(\ln(Px+B)}\right] min \qquad (2)$$

Where P is the gas pressure for air at standard atmospheric pressure of 101 kPa the usual condition of a TENG, A and B are the constants determined by the pressure of the gas, A = $2.87x10^5$ V/(atm·m), and B = 12.6. ε_r is the relative permittivity of the dielectric layer, and ε_0 is the vacuum permittivity.

The simulations were performed using COMSOL Multiphysics, for resistive loads (from 1 MΩ to 100 MΩ) for ocean wave impact forces generated by the oscillatory frequencies of compressed air bubbles as shown in Fig. 1. These are based on the DMCS-TENG structure shown in Fig. 2. A structure comprising a copper (Cu) electrode (thickness d_{e1} =100 μm) as the lower electrode with Polyimide dielectric (thickness d_{d1} = 25.4 μm) and an Aluminium (Al) layer (thickness d_{e2} = 100 μm) used as both the second triboelectric material and the top electrode (which was grounded) and also the point at which the mechanical energy was applied. The two tribo-charge surfaces were assigned with the calculated value σ = σ_{max} = ±22.06 μC/m², respectively.

A series of simulations were performed in order to analyse the output performance of the entire system, with different length structures (with lengths L = 2.5 cm, 5 cm and 8 cm) over the oscillatory frequency range mentioned earlier, so that the optimal design can be found. The highest calculated output performance was obtained with the DMCS-TEG structure of L = 8 cm at the oscillation frequency of 150 Hz. The maximum current drops dramatically with a value of Isc = 13 μA but the maximum voltage increases at a reverse trend Voc = 122 V, the DMCS-TENG reaches its maximum instantaneous output power = 1.58 mW with a 10 MΩ load shown in Fig. 3 a.

Fig. 3 b shows six cycles of the DMCS-TENG under oscillatory frequency of 150 Hz, where the maximum voltage is proportional to the value of the external resistor. However when R = 10 MΩ, the voltage decreases with time, which means that the charge cannot get saturated due to the limit of the charge

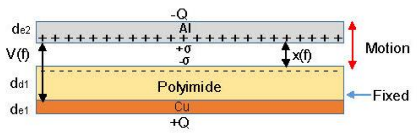

Fig. 2. Two-dimensional sketch of the DMCS-TENG prototype.

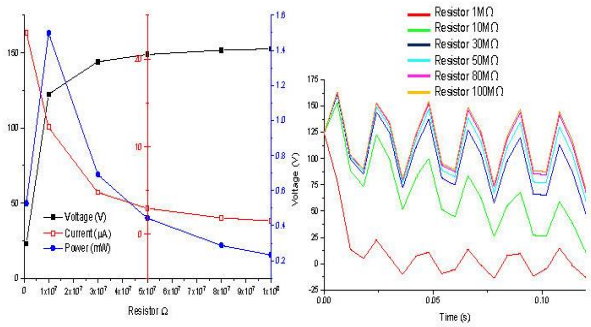

Fig. 3. a) Maximum output performance of the DMCS-TENG influenced by the load resistance b) Real-time voltage-time relationship at different load resistances under oscillation frequency of 150 Hz.

transfer rate by the resistor, resulting in unobstructed charge transfer from electrode 1 to electrode 2.

III. DMCS-TENG Prototype Fabrication and Electrical Characterization Measurements Set-Up

The device prototype was fabricated using a simple and low cost process. The fabricated DMCS-TENG prototype has an active triboelectric area of 8 cm x 8 cm and the dielectric to conductor structure is shown in Fig. 2 as the FEM simulation model results show the highest output performance. An Acrylic was selected as the substrate material, where an Al foil (with t_{e2} = 18 μm) was manually fixed with glue stick on it at room temperature, which is used as both the triboelectric material and the electrode 2 that is grounded. Therefore the dielectric Polyimide (with ε_r = 3.4, and d_{d1} = 25.4 μm) was manually fixed with conductive glue at room temperature on the Cu layer which acts as electrode 1 (t_{e1} = 100 μm) connected to an external load of 10 MΩ for the electrical characterization.

The realized DMCS-TENG output performance was characterized using a Pasco Scientific SF-9324 mechanical shaker table connected to a RIGOL DG1062 function generator, in order to replicate the conditions of the mechanical energy generated by the oscillating compressed air bubbles. The function generator was configured as a sine wave at different frequencies shown in Fig. 1. The driving amplitude was set at 20 V peak-to-peak. The Al electrode was manually placed facing the surface of the Polyimide dielectric layer and bound together on each side at the middle with Kapton Polyimide heat and chemical resistant tape (1 cm width) at room temperature. Finally the DMCS-TENG was mounted as depicted in Fig. 4.

The gap of the DMCS-TENG varies with the oscillatory frequencies variation to generate the triboelectric effect when the Polyimide dielectric layer is in not uniform contact variation

Fig. 4. Fabricated DMCS-TENG mounted on the mechanical vibrator for the output performance measurements.

with the Al film, which generates interchange of triboelectric charges between both surfaces. The output voltage, output current and output power of the DMCS-TENG measurements were performed using an Agilent Technologies N6705B Power analyser.

IV. Experimental Results and Discussion

The output voltage performance responds to the mechanical energies applied through resonant oscillatory frequencies to the device for 30 seconds, where the Al foil is in constant non-uniform contact with the Polyimide dielectric film and attracts electrons in the opposite direction to that of the copper electrode to flow in the 10 MΩ external load as shown in Fig. 5.

It has been observed that the maximum peak-to-peak open circuit voltage varies with the oscillation frequency, in a similar manner to the pressure signals predicted in the porous structures due to the air bubbles resulting from the impact of ocean waves. The maximum generated open circuit voltage (V_{oc}, rms value) was 3.83 V and short circuit current (I_{sc}, rms value) of 80.38 µA, which corresponds to the output power and power density of 307.88 µW and 19.24 µW/cm^2 respectively. The output performance for all measurements at each frequency are shown in detail in TABLE I.

Finally, the highest output performance response generated by the DMCS-TENG was measured at frequencies of 30 Hz and 150 Hz, which means that the device has the potential to respond with higher output voltage, at the moment when the ocean wave impacts the porous structures between 30 Hz and 50 Hz, and after the wave collapses, where the air bubbles are formed between 150 Hz and 200 Hz. The maximum output performance measured experimentally is related to the calculated response through the FEM simulation model at 150 Hz of the proposed prototype under similar conditions of operation.

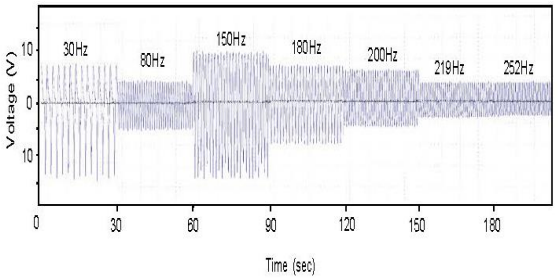

Fig. 5. DMCS-TENG voltage-time response through simulated resonant frequencies of 30 Hz, 80 Hz, 150 Hz, 180 Hz, 200 Hz, 219 Hz and 252 Hz.

V. Conclusions

It has been shown that the triboelectric effect can be used to realize a new type of energy harvester for ocean wave impact forces. This offers an alternative approach for generating electrical power that can be integrated into porous water interfaces, which are used to prevent critical damage in coastal defense systems. Further investigation is required to explore suitable materials and designs to improve the output performance of the device, where engineering challenges, such as efficient energy coupling and robustness to withstand the harsh environmental conditions of the ocean.

TABLE I. Output performance parameters measured through the simulated resonant oscillatory frequencies for the DMCS-TENG.

Frequency	Voltage RMS (V_{RMS})	Current RMS (I_{RMS})	Power
30 Hz	2.91 V	61.32 µA	178.44 µW
80 Hz	437 mV	13.17 µA	5.76 µW
150 Hz	3.83 V	80.38 µA	307.88 µW
180 Hz	2.43 V	48.30 µA	117.37 µW
200 Hz	1.9 V	43.22 µA	88.12 µW
219 Hz	1.13 V	21.62 µA	24.43 µW
252 Hz	1.12 V	19.91 µA	22.30 µW

Acknowledgment

We thank CONACYT for the fellowship awarded to Ulises Tronco Jurado.

References

[1] R. B. Mayon, Z. Sabeur, M. Tan, and K. Djidjeli, "Analysis of fluid flow impact oscillatory pressures with air entrapment at structures," *Coastal Engineering Proceedings,* vol. 1, p. 31, 2017.

[2] N. Elvin and A. Erturk, *Advances in energy harvesting methods*: Springer Science & Business Media, 2013.

[3] C. McGowin, "Ocean Tidal and Wave Energy: Renewable Energy Technical Assessment Guide," *Electric Power Research Institute, Palo Alto, CA, Paper No. TAG-RE,* 2005.

[4] Z. Sabeur, W. Roberts, and A. Cooper, "Development and use of an advanced numerical model using the volume of fluid method for the design of coastal structures," *Numerical Methods for Fluid Dynamics,* vol. 5, pp. 565-573, 1995.

[5] Z. Sabeur, J. Cohen, J. Stephens, and A. Veldman, "Investigation on free-surface flow oscillatory impact pressures with the Volume-of-Fluid method," *Numerical Methods for Fluid Dynamics,* vol. 6, pp. 493-498, 1998.

[6] R. B. M. Z. A. Sabeur, M. Tan, K. Djidjeli, "Analysis of fluid flow impact oscillatory pressures with air entrapment at structures, International Conference on Coastal Engineering (ICCE)," *American Society of Civil Engineers (Accepted for publication),* 2016.

[7] Z. A. S. R.B. Mayon, M. Tan, K. Djidjeli, "Investigation of Wave Impacts on Porous Structures for Coastal Defences, 12th International Conference on Hydrodynamics (ICHD)," *18-23 September 2016, Delft, Netherland,* 2016.

[8] U. Khan and S.-W. Kim, "Triboelectric Nanogenerators for Blue Energy Harvesting," *ACS nano,* vol. 10, pp. 6429-6432, 2016.

[9] Z. L. Wang, L. Lin, J. Chen, S. Niu, and Y. Zi, "Applications in Self-powered Systems and Processes," in *Triboelectric Nanogenerators*, ed: Springer, 2016, pp. 351-398.

[10] Z. L. Wang, L. Lin, J. Chen, S. Niu, and Y. Zi, "Harvesting Large-Scale Blue Energy," in *Triboelectric Nanogenerators*, ed: Springer, 2016, pp. 283-306.

[11] Z. L. Wang, L. Lin, J. Chen, S. Niu, and Y. Zi, "Theoretical Modeling of Triboelectric Nanogenerators," in *Triboelectric Nanogenerators*, ed: Springer, 2016, pp. 155-183.

[12] S. Wang, Y. Xie, S. Niu, L. Lin, C. Liu, Y. S. Zhou, *et al.*, "Maximum Surface Charge Density for Triboelectric Nanogenerators Achieved by Ionized-Air Injection: Methodology and Theoretical Understanding," *Advanced Materials,* vol. 26, pp. 6720-6728, 2014.

proceedings

MDPI

Proceedings

Water-Dielectric Single Electrode Mode Triboelectric Nanogenerators for Ocean Wave Impact Energy Harvesting †

Ulises Tronco Jurado [1,2,*], Suan Hui Pu [1,3] and Neil M. White [2]

1 Mechatronics Research Group, University of Southampton, Southampton SO17 1BJ, UK; suanhui.pu@soton.ac.uk
2 Smart Electronic Materials and Systems Research Group, University of Southampton, Southampton SO17 1BJ, UK; nmw@ecs.soton.ac.uk
3 Mechatronics Research Group, University of Southampton Malaysia Campus, Iskander Puteri 79200, Johor, Malaysia
* Correspondence: utj1n15@soton.ac.uk; Tel.: +44-792-624-1394
† Presented at the Eurosensors 2018 Conference, Graz, Austria, 9–12 September 2018.

Published: 21 December 2018

Abstract: The effect of water wave impacts and breakdown on the output performance of Water-Dielectric Single Electrode Mode Triboelectric Nanogenerators (WDSE-TENG) has been evaluated. When water contacts a TENG consisting of a hydrophobic dielectric layer, the triboelectric effect is generated with a net negative charge on the dielectric material and net positive charge on the water surface. The hydrophobic dielectric materials, which show the highest electrical output performance in contact with water, were FEP, silicone rubber and polyimide. The average output power of each sample for a load resistance of 10 MΩ was found to be in the range 14.69 to 19.12 μW. The results demonstrate that WDSE-TENG devices can work as an alternative energy harvesting mechanism by using water as a triboelectric material.

Keywords: water-dielectric; triboelectricity; energy harvesting; sensing; self-powering

1. Introduction

Ocean wave energy has attracted great interest as a source of electrical energy for many years. Effective utilization and sustainability of this kind of energy can be exploited due to the effects of climate change with the rapid increase of sea levels and more recurrent flooding in coastal zones. Specifically, the cumulative loads of wave impact forces at coastal defence structures deliver high magnitude pulse-like forces with a wide frequency range of destructive oscillatory compressed air bubbles at the structure-water interfaces in the range of 30 to 300 Hz with a pressure range of 50 to 350 Pa predicted through a fluid-structure simulation [1]. Such energy can be potentially harvested and exploited using WDSE-TENG that converts the external mechanical energy into electricity by a combination of triboelectric effect and electrostatic induction, based on contact electrification between water and hydrophobic dielectric polymer films (Polydimethylsiloxane (PDMS), Polytetrafloroethylene (PTFE), silicone rubber, Fluorinated ethylene propylene (FEP) and Polyimide (Kapton)).

Traditionally, TENG are designed to work between solid materials in contact and they work well under dry conditions [2]. However, triboelectricity can exist when liquids are flowing through insulating tubes [3,4]. Therefore, in order to explore the opportunity to use water as one type of triboelectric material choice for TENG, a single electrode and split single electrode TENG prototypes were fabricated and characterized to study and analyze the contact electrification between water and

the aforementioned dielectric polymer films. Which can derive an alternative and novel approach of energy harvesting for ocean wave monitoring applications that require self-powering in liquid environments. Potential applications include sensing at structure-water interfaces, such as those used to prevent critical damage in coastal defence systems.

2. WDSE-TENG Prototypes Fabrication and Electrical Characterization Measurements Set-Up

The fabricated WDSE-TENG prototypes have a triboelectric active area of 7 cm × 4 cm and three different configurations, as depicted in Figure 1, using hydrophobic dielectric layers with high negativity in the triboelectric series [5]. For the first WDSE-TENG a dielectric layer (PTFE (thickness (t = 100 μm), FEP (t = 25 μm), Silicone rubber (t = 150 μm) and PDMS (t = 125 μm)) was manually fixed with conductive glue on a copper layer (t = 100 μm), which acts as electrode. The other exposed side of the copper layer was insulated with black PTFE tape to protect it from the water to prevent a short circuit (Figure 1a). With this device configuration, the contact electrification occurs at the face of the dielectric layer in contact with water. For the second configuration a metal layer (Al (t = 18 μm), Cu (t = 100 μm)) was completely insulated within silicone rubber layers on both sides to protect it from the water (Figure 1b) and with the aim to increase the contact area to produce contact electrification in both faces of the device when the water contacts it. Additionally, using the second configuration, a copper layer was manually insulated on one side with a layer of PDMS and on the other side with a layer of PTFE with conductive acrylic adhesive (t = 25 μm) to test the combination of two different materials in contact electrification with water at the same time. For the electrical characterization, the electrode of each sample was connected to an external load of 10 MΩ.

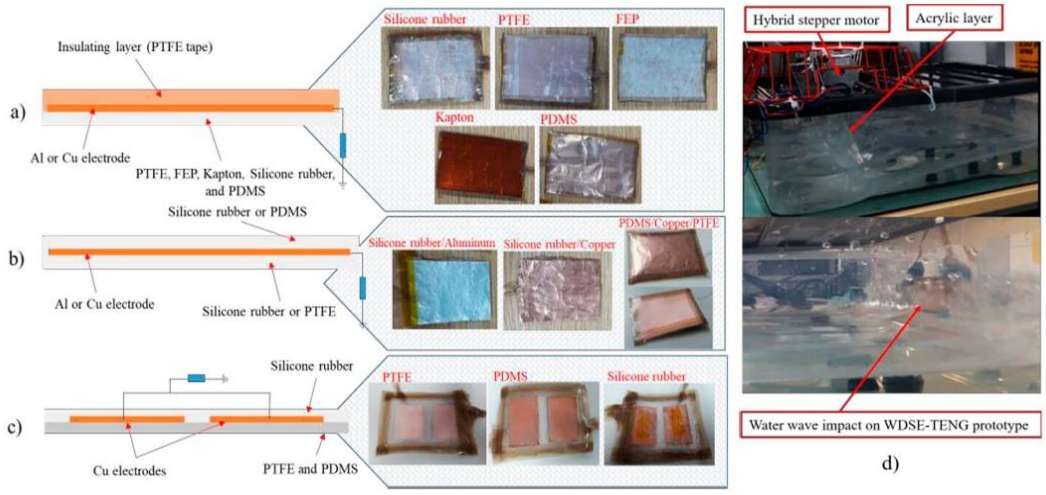

Figure 1. Three configurations of fabricated WDSE-TENG prototypes (**a**) WDSE-TENG with one dielectric layer, (**b**) full device covered with two dielectric layers, and (**c**) split single electrode-two dielectric layers in contact with water. (**d**) WDSE-TENG prototypes placed on the water wave generator tank for their output performance measurements on water conditions.

The third configuration comprised two copper layers (split electrode) with an active area of 2.5 cm × 3 cm and a separation distance of 8 mm, which were manually fixed with conductive acrylic adhesive on a dielectric layer (PTFE (t = 100 μm), PDMS (t = 125 μm)). The other face of the device was insulated with a layer of silicone rubber to protect it from short-circuit in contact with water (Figure 1c). The contact electrification will be produced on both faces of the device when it contacts the water with the two electrodes connected to an external load of 10 MΩ for the electrical characterization with the objective to increase the charge transfer between the split electrode compared with the WDSE-TENG. The complete fabrication process was performed at room temperature.

The WDSE-TENG output performance of the prototypes was characterized using a water wave generator tank in order to replicate the conditions of the mechanical energy generated by ocean wave

impact. A hybrid stepper motor (RS Pro 535-0502, RS Components Ltd., Corby, UK) attached with an acrylic layer of 20 cm × 20 cm (t = 8 mm) is used to generate the water waves motion into the water tank at different frequencies mounted on the left side of the tank. The WDSE-TENG devices were placed at the wall on the right side of the tank where the water wave breaks (at a frequency of 1.20 Hz) against the wall facing the impact of the water wave with the dielectric triboelectric layer, which generates interchange of triboelectric charges between both surfaces as shown in Figure 1d. All the WDSE-TENG prototypes and connection wires were insulated to avoid short circuit when the devices get in contact with water. The output voltage measurements were obtained with a digital oscilloscope Tektronix TDS 2014C (Premier Farnell Limited, Leeds, UK). The output current and output power of the DMSE-TENG measurements were performed using an Agilent Technologies N6705B Power analyzer (Premier Farnell Limited, Leeds, UK).

3. Experimental Results and Discussion

Figure 2 illustrates the contact electrification between the water wave and the hydrophobic dielectric layers and also the working mechanism of the WDSE-TENG, which can be explained as a result of contact electrification and electrostatic induction. Before the dielectric layer makes contact with water (Figure 2a), no charge transfer occurs. When the water wave starts to contact against the dielectric layer (Figure 2b), the ionization of the surface groups on the dielectric layer will cause the dielectric layer to be negatively charged [6] and create a positively charged electrical double layer (EDL) on the contact surface of the water wave to maintain electrical neutrality [7,8] (Figure 2c). As the water wave breaks down and moves off the dielectric layer, the positive charges in the EDL can be carried away with the water and the negative charges can remain on the surface of the dielectric layer. The negative electric potential difference between the electrode and load resistor (10 MΩ) to the ground attains equilibrium as electrons flow to ground (Figure 2d). This process produces an instantaneous negative current due to the triboelectric charges on the dielectric layer, which can be retained for a long time. When another water wave makes contact with the negatively charged dielectric layer, the negative charges will attract counter ions from the water to form another positively charge EDL, and establishes a positive electric potential difference. Therefore, electrons will flow from ground and load resistor to the electrode (Figure 2e) until reaching a new equilibrium (Figure 2f). This process produces an instantaneous positive current. When the water wave breaks down and leaves the dielectric layer, a negative electric potential difference will be established between the electrode and load resistor to the ground and another new equilibrium is achieved (Figure 2g). Once the following water wave contacts with the dielectric layer of the WDSE-TENG prototype (Figure 2a–g), a continuous output will be obtained. The water wave after the impact with the dielectric layer of the WDSE-TENG prototype should not leave residual water on the dielectric hydrophobic layer surface, in an ideal situation with the objective to generate the maximum electrical output.

The comparison of the three configurations for the WDSE-TENG energy harvester prototypes according to their electrical output performance measurements is shown in Figure 3a. The average output power (1.5 μW to 20 μW) was calculated from the measured V_{RMS} (1 V to 7.3 V) and I_{RMS} (1 μA to 5 μA) of the proposed devices. The WDSE-TENG with one dielectric layer using FEP (t = 25 μm) in contact with water produced the highest output power of 19.12 μW, which corresponds to a V_{RMS} of 4.11 V and an I_{RMS} of 4.80 μA (Figure 3b). The prototype with two dielectric layers of silicone rubber and aluminum as electrode produced the next highest output power, likely due to the large contact area (V_{RMS}, I_{RMS} and power of 7.31 V, 2.84 μA and 17.24 μW, respectively). However, the output performance decreased for the WDSE-TENG with split single electrode due to the reduced active area of 2.5 cm × 3 cm. Furthermore, the configuration of the WDSE-TENG with two distinct dielectric layers of PDMS and PTFE shown relatively poor output power performance (Figure 3a).

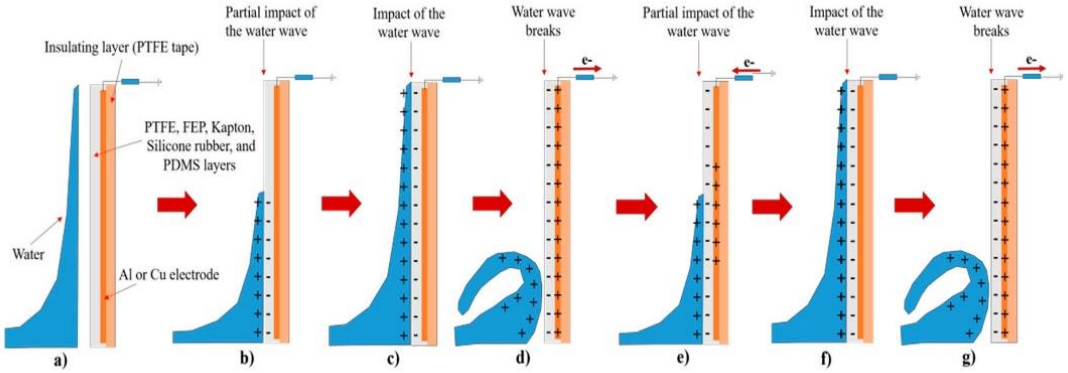

Figure 2. Working mechanism of the WDSE-TENG prototypes by the contact electrification of dielectric layers with water wave impact. (**a**) Before the dielectric layer makes contact with water, no charge transfer occurs. (**b**) The ionization of the surface groups on the dielectric layer will cause the dielectric layer to be negatively charged and (**c**) create a positively charged EDL on the contact surface of the water wave to maintain electrical neutrality. (**d**) The negative electric potential difference attains equilibrium as electrons flow to ground. (**e**) When another water wave contacts the negatively charged dielectric layer, establishes a positive electric potential difference as electrons will flow to the electrode, (**f**) until reaching a new equilibrium. (**g**) When the water wave breaks down and leaves the dielectric layer, another new equilibrium is achieved. (**a**–**g**) Once the following water wave contacts the WDSE-TENG prototype, a continuous output will be obtained.

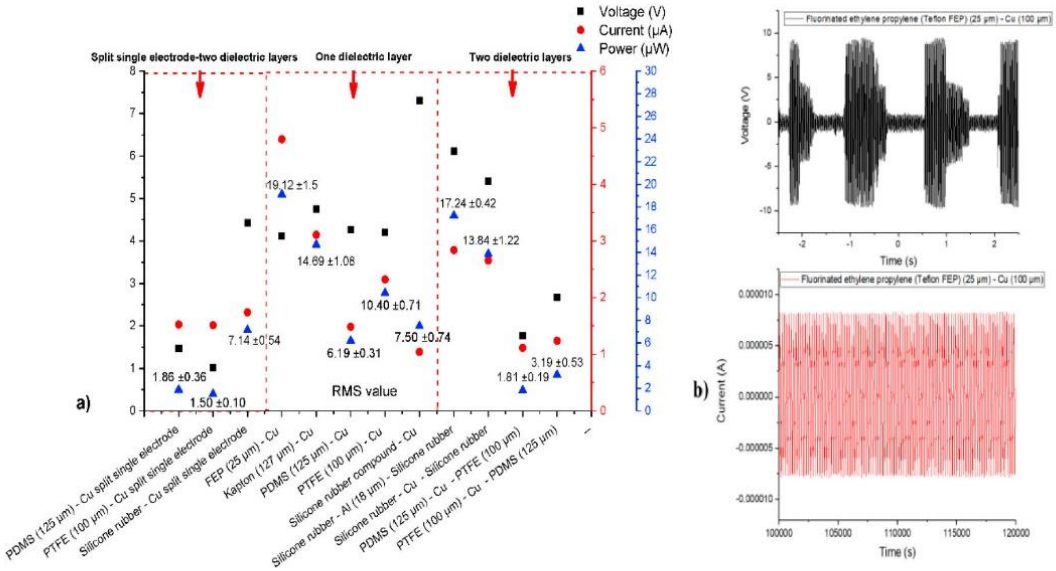

Figure 3. (**a**) Comparison of the output voltage (V_{RMS}), current (I_{RMS}) and average output power of the WDSE-TENG prototypes with three configurations exposed to 1.2 Hz water wave impact. (**b**) Instantaneous output voltage (V) and current (I) of the WDSE-TENG using a FEP dielectric layer.

4. Conclusions

In summary, the output performance measurements have demonstrated the potential of the proposed WDSE-TENG prototypes for harvesting mechanical energy from ocean wave impact forces at the structure-water interfaces using water as a triboelectric active material. These new devices can work in liquid environments and hence can provide an energy source for sensing. Further investigation is required to explore suitable designs and efficient energy coupling to enhance the WDSE-TENG output performance employing the hydrophobic dielectric layers that shows a highest performance in contact with water.

Acknowledgments: We thank CONACYT for the fellowship awarded to Ulises Tronco Jurado.

Conflicts of Interest: The authors declare no conflict of interest.

References

1. Mayon, R.B. Investigation of Wave Impacts on Porous Structures for Coastal Defences. In Proceedings of the 12th International Conference on Hydrodynamics (ICHD), Delft, The Netherland, 18–23 September 2016.
2. Zhu, G.; Lin, Z.H.; Jing, Q.; Bai, P.; Pan, C.; Yang, Y.; Zhou, Y.; Wang, Z.L. Toward large-scale energy harvesting by a nanoparticle-enhanced triboelectric nanogenerator. *Nano Lett.* **2013**, *13*, 847–853.
3. Ravelo, B.; Duval, F.; Kane, S.; Nsom, B. Demonstration of the triboelectricity effect by the flow of liquid water in the insulating pipe. *J. Electrost.* **2011**, *69*, 473–478.
4. Paillat, T.; Touchard, G. Electrical charges and liquids motion. *J. Electrost.* **2009**, *67*, 326–334.
5. Diaz, A.; Felix-Navarro, R. A semi-quantitative tribo-electric series for polymeric materials: the influence of chemical structure and properties. *J. Electrost.* **2004**, *62*, 277–290.
6. Choi, D.; Lee, H.; Kang, I.S.; Lim, G.; Kim, D.S.; Kang, K.H. Spontaneous electrical charging of droplets by conventional pipetting. *Sci. Rep.* **2013**, *3*, 2037.
7. Lyklema, J. *Fundamentals of Interface and Colloid Science: Soft Colloids*; Elsevier: Amsterdam, The Netherlands, 2005; Volume 5.
8. Lin, Z.H.; Cheng, G.; Lee, S.; Pradel, K.C.; Wang, Z.L. Harvesting Water Drop Energy by a Sequential Contact-Electrification and Electrostatic-Induction Process. *Adv. Mater.* **2014**, *26*, 4690–4696.

Dielectric-Metal Triboelectric Nanogenerators for Ocean Wave Impact Self-Powered Applications

Ulises Tronco Jurado, Suan Hui Pu, *Member, IEEE*, and Neil M. White, *Senior Member, IEEE*

***Abstract*—This paper describes the effect of oscillatory frequencies caused by ocean wave impact on the output performance of dielectric-metal contact separation mode triboelectric nanogenerators (DMCS-TENG). The triboelectric effect is generated as a result of regular, non-uniform contact between a dielectric layer which gains electrons (negative triboelectric material) and a conductive layer that loses electrons (positive triboelectric material). Impact testing was used to characterize arc-shaped dielectric-metal single electrode triboelectric nanogenerators (DMSE-TENG) with different triboelectric material combinations based on their output power generation, using a 40-mm ball bearing to apply a 12-N force impulse. It was found that the best dielectric-conductor combination for the DMCS-TENG performance was polyimide and PDMS in contact with the conductor layers of aluminum and silver conductive cloth tape. Therefore, in the range of operation from 30 to 300 Hz with an amplitude acceleration of 319.62 to 559.29 mm/s^2, the maximum generated output power, power density, and total energy conversion efficiency of the device, made with polyimide and honeycomb patterned aluminum foil, can reach up to 778.43 μW, 12.16 μW/cm^2, and 15.85 % respectively, for a load resistance of 10 MΩ. The output power performance of the DMCS-TENG shows an enhancement by a factor of 2.3 with a honeycomb-patterned aluminum foil, by increasing the surface charge density between the layers in contact, relative to flat aluminum foil. Additionally, through the integration of the energy harvester prototype into a water wave generator tank, an output power density of 169.218 mW/m^2 was reached, where it is expected to generate output power energy around 3.05 W, over an area of 18 m^2 with wave sizes among 0.3 to 4 m. This paper demonstrates that the device can function as an energy harvesting mechanism for ocean wave sensing applications that require self-powering.**

***Index Terms*—Ocean wave impact, compressed air bubbles, oscillatory frequencies, triboelectric effect, dielectric-conductor, ocean wave sensing, self-powering.**

I. Introduction

OCEAN wave energy has been attracting a great interest as a source of electrical energy for many years [1]. Effective utilization and sustainability of this kind of energy can be exploited due to the effects of climate change with the rapid increase of sea levels and recurrent flooding of coastal zones. Specifically, the cumulative loads of wave impact forces at coastal defense structures deliver high magnitude pulse-like forces with a wide frequency range of oscillatory compressed air bubbles at structure-water interfaces. The surging flow front impacts the structure, spreads vertically upwards as shown in Fig. 1 (a), and produces the first hydrostatic pressure oscillations peak between 30 to 80 Hz with an amplitude range of 57 to 116 Pa. After the wave collapses a plunging breaker is formed (Fig. 1 (b) and many air bubbles are entrained (Fig. 1 (c)), which compresses and dilates in a high frequency oscillatory manner, impinging upon the coastal protective structure as shown in Fig. 1 (d). This yields a cyclic hydrostatic pressure response between 150 to 252 Hz with an amplitude range of 148 to 348 Pa, predicted through a fluid-structure simulation [2], [3]. Such energy can be potentially harvested and exploited using a dielectric-metal contact separation mode triboelectric nanogenerators (DMCS-TENG) as a new type of energy harvester for ocean wave impacts (Fig. 1 (a)). This aim in the main frequencies 30, 80, 150, 180, 200, 219 and 252 Hz to harvest the major energy [2], [3]. The triboelectric effect is generated by regular non-uniform contact between a dielectric layer that gains electrons (negative triboelectric material) and a conductive layer that loses electrons (positive triboelectric material), where the output performance changes in proportion to the mechanical energy applied by pressure oscillation [4]. TENG can be used as energy harvesters for self-powering sensors [5], [6]. Their advantages include broadband behavior, lightweight, high energy density and ease of fabrication exploiting low-cost, readily available materials [7]. Firstly, in order to study and to find the most promising triboelectric material combinations based on their output power generation to enhance the DMCS-TENG performance for mechanical energy harvesting, arc-shaped dielectric-metal single electrode triboelectric nanogenerators (DMSE-TENG) were fabricated. The output performance characterization using contact electri-

Manuscript received March 13, 2019; accepted April 10, 2019. Date of publication April 18, 2019; date of current version July 17, 2019. A conference paper related with this research project was presented at the IEEE Sensors 2017 Conference, Glasgow, U.K., and was published in its Proceedings. The associate editor coordinating the review of this paper and approving it for publication was Dr. Shanhong Xia. *(Corresponding author: Ulises Tronco Jurado.)*

U. Tronco Jurado is with the Mechatronics Research Group, The University of Southampton, Southampton SO17 1BJ, U.K., and also with the Smart Electronic Materials and Systems Research Group, The University of Southampton, Southampton SO17 1BJ, U.K. (e-mail: utj1n15@soton.ac.uk).

S. H. Pu is with the Nano Research Group, School of Electronics and Computer Science, University of Southampton, Southampton SO17 1BJ, U.K., and also with the School of Engineering, University of Southampton Malaysia Campus, Iskandar Puteri 79200, Malaysia (e-mail: suanhui.pu@soton.ac.uk).

N. M. White is with the Smart Electronic Materials and Systems Research Group, The University of Southampton, Southampton SO17 1BJ, U.K. (e-mail: nmw@ecs.soton.ac.uk).

This paper has supplementary downloadable multimedia material available at http://ieeexplore.ieee.org provided by the authors. The Supplementary Material contains three sections as a support information of the paper titled Dielectric-metal triboelectric nanogenerators for ocean wave impact self-powered applications. The first section describes the dynamic operation analysis of the Dielectric-metal single electrode mode triboelectric nanogenerators (DMSE-TENG). The second section shows the analysis of the maximum surface charge density calculation for the triboelectric materials, and the third section describes the modelling of dynamic operation of the Dielectric-metal contact separation mode triboelectric nanogenerators (DMCS-TENG). This material is 699 KB in size.

Digital Object Identifier 10.1109/JSEN.2019.2912070

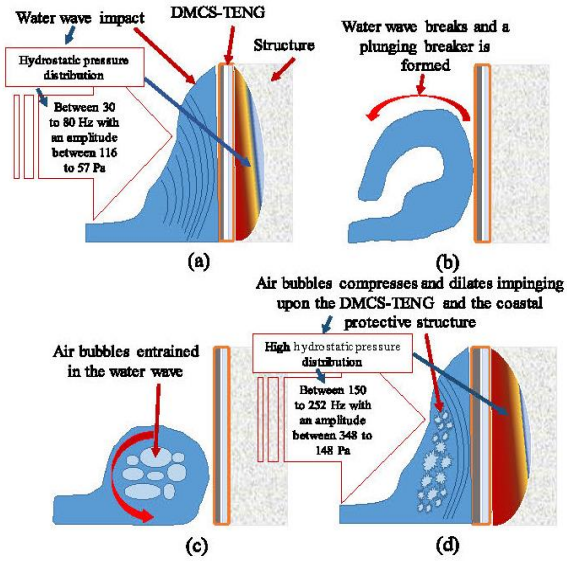

Fig. 1. (a-d) Hydrostatic pressure distribution of the ocean wave impact at the water-structure interface and main frequencies of interest (30, 80, 150, 200, 219 and 252 Hz) [2], [3] for ocean wave energy harvesting generated by (a) the water wave impact and (d) the impact of oscillatory compressed air bubbles flows at the water-structure interface exploited using the DMCS-TENG.

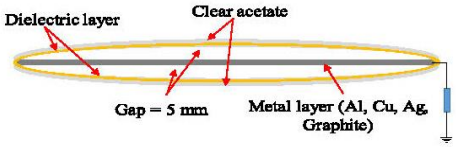

Fig. 2. Two-dimensional schematic of the arc-shaped DMSE-TENG (Prototype 1).

fication between different dielectric-metal combinations was performed through an impact test. Secondly, in this study we have developed a finite element model (FEM) for a DMCS-TENG using COMSOL Multiphysics, to understand its electromechanical characteristics. Thirdly, the output performance of the fabricated DMCS-TENG using the best triboelectric material combination was evaluated at the frequencies mentioned above. Finally, the proposed energy harvester that shows the highest output performance was tested in a water wave generator tank, to analyze its performance in realistic conditions. It is expected that the enhanced output performance of the proposed energy harvesting prototypes will enable future advancement in energy harvesting at structure-water interfaces for ocean wave monitoring applications that require self-powering sensors.

II. Triboelectric Material Selection Using DMSE-TENG

A. DMSE-TENG Fabrication and Electrical Characterization Set-Up

In order to maximize the DMCS-TENG performance for mechanical energy harvesting from the oscillatory frequencies generated by wave impact, arc-shaped dielectric-metal single electrode triboelectric nanogenerators (DMSE-TENG) were fabricated using different material combinations. The arc shaped DMSE-TENG, as illustrated in Fig. 2 (prototype 1),

TABLE I

Comparison of The Rankings of Positive and Negative Triboelectric Materials in Terms of Ease Of Losing or Gaining Electrons With Data From the Literature [14] Versus Our Impact Test Characterization Data

Triboelectric materials combinations (40 mm ball bearing)		
	Literature	Tested
Conductors (Positive)	Aluminum (18 μm)	Conductive cloth tape (Silver)
	Copper (100 μm)	Aluminum (18 μm)
	Conductive cloth tape (Silver)	Copper (100 μm)
Insulators (Negative)	Paper	Paper
	Polylactic acid (PLLA) (Polyester)	Polytetrafluoroethylene (Teflon) PTFE tape (90 μm)
	Cellulose tape (63.5 μm)	Polylactic acid (PLLA) (Polyester)
	carton paper	Cellulose tape (63.5 μm)
	Polypropylene (PP) (46 μm)	Polytetrafluoroethylene (Teflon) PTFE tape (100 μm)
	Polyethylene foam (2 mm)	carton paper
	Polyvinyl chloride (PVC) (100 μm)	Polypropylene (PP) (46 μm)
	Polystyrene (1 mm)	Polyethylene foam (2 mm)
	Polyethylene terephthalate (Polyester) (PET) (60 μm)	Polyvinyl chloride (PVC) (100 μm)
	Polydimethylsiloxane (Silicone rubber compound)	Polystyrene (1 mm)
	Polyimide (127 μm, Kapton, 50.8 μm, 25.4 μm)	Polyethylene terephthalate (Polyester) (PET) (60 μm)
	Polydimethylsiloxane (PDMS) (125 μm)	Polydimethylsiloxane (Silicone rubber compound)
	Polytetrafluoroethylene (Teflon) PTFE tape (90 μm)	Polytetrafluoroethylene (Teflon FEP, PTFE) (25 μm, 100 μm, 300 μm, 1 mm)
	Polytetrafluoroethylene (Teflon) PTFE tape (100 μm)	Polyimide (127 μm, Kapton, 50.8 μm, 25.4 μm)
	Polytetrafluoroethylene (Teflon FEP, PTFE) (25 μm, 100 μm, 300 μm, 1 mm)	Polydimethylsiloxane (PDMS) (125 μm)

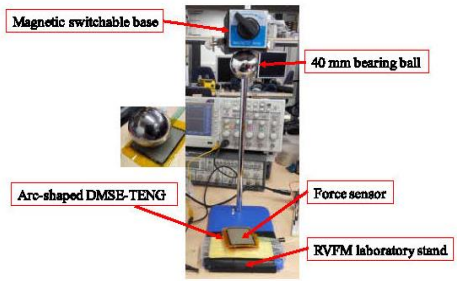

Fig. 3. Experimental set-up of impact test using a 40 mm ball bearing on the arc-shaped DMSE-TENG prototypes (connected to a 10 MΩ load resistor) with different triboelectric materials combinations.

were fabricated using a simple, low-cost process. The device prototypes have an active triboelectric area of 5 cm × 5 cm, and an acrylic sheet was selected as a substrate material. The conductor layer (either aluminum, copper or silver) was attached to the acrylic with a thin adhesive layer, at room temperature. The conductor layer is used as a triboelectric material, and an electrode connected to an external load of 10 MΩ for electrical characterization. Likewise, the dielectric layer (polyimide, PDMS, polytetrafluoroethylene, i.e. PTFE, Teflon FEP etc.) was fixed with thin adhesive on a clear acetate film (thickness = 100 μm). The dielectric layer was attached with an arc-shaped form to the metal electrode using Kapton tape (1cm width) at room temperature. The maximum gap between the arc-shaped dielectric layer and the metal layer was 5 mm. The materials used for the arc-shaped DMSE-TENG prototypes fabrication are shown in Table I (Literature).

The output power performance characterization of the arc-shaped DMSE-TENG prototypes was evaluated from the generated output voltage and current, measured with an impact test set-up in order to study and find the optimum triboelectric material combination to reach the highest output performance. This system uses a 40 mm ball bearing (mass = 261.04 grams) attached to a magnetic switchable base, which is fastened to a

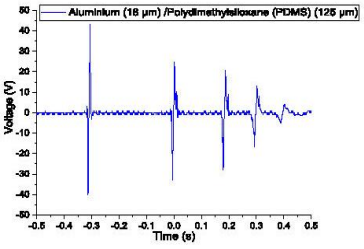

Fig. 4. Instantaneous output voltage of arc-shaped DMSE-TENG prototype (connected to a 10 MΩ load resistor) using PDMS in contact with Aluminum under the impact of a 40 mm ball bearing.

RVFM laboratory stand set at the height of 30 cm. The device prototype was held at the base of the laboratory stand and the applied force to it was measured using a force sensor (Interlink electronics FSR406 1.5" diameter force sensing resistor) as shown in Fig. 3. The output voltage measurements of the arc-shaped DMSE-TENG were obtained with a digital oscilloscope Tektronix TDS 2014C, the output current measurements were performed using an Agilent Technologies N6705B power analyser.

B. Electrical Characterization of the Arc-Shaped DMSE-TENG for the Triboelectric Material Optimization

The output performance measurements of the arc-shaped DMSE-TENG prototypes through the impact test, which applies a force impulse of 12 N. The results show that the maximum output power was 6.28 μW corresponding to an output voltage (V_{RMS}) of 5.22 V and current (I_{RMS}) of 1.20 μA using a triboelectric material combination of PDMS-silver conductive cloth tape. The instantaneous voltage of the sample using PDMS in contact with aluminum under the impact of a 40 mm ball bearing is shown in Fig. 4.

The highest instantaneous output voltage occurs when the dielectric layer is in contact with the conductor layer. The movement of the top dielectric layer due to the impact of the ball bearing, changes the local electrical field distribution created between both layers due the surface charge transfer, so that there is electron exchange between the bottom electrode, external load of 10 MΩ and the ground to maintain the potential change of the electrode. The first impact of the ball bearing generates the highest voltage peak, which is related with the impact force that helps to increase the contact area between both layers. The instantaneous voltage decreases due the bouncing behavior of the ball bearing after impact with the sample as shown in Fig. 4. Among all the arc-shaped DMSE-TENG prototypes the top five highest output power performance was dominated by structures with silver conductive cloth tape in contact with polyimide, PDMS, silicone rubber and PET except PTFE, where the highest performance was in contact with aluminum. The dynamic operation of the DMSE-TENG prototype is shown in the Supplementary Information document.

The output performance comparison of arc-shaped DMSE-TENG devices fabricated with silver conductive

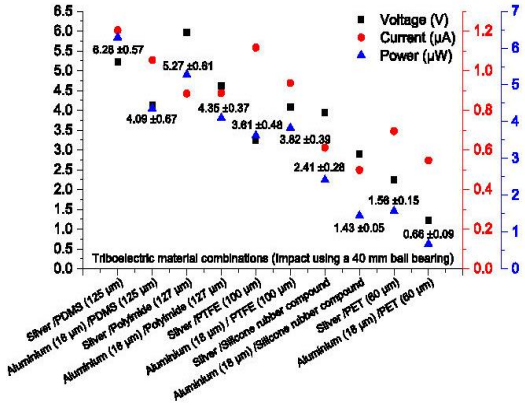

Fig. 5. Comparison of the output voltage (V_{RMS}), current (I_{RMS}) and power effective values of the top five arc-shaped DMSE-TENG fabricated prototypes (connected to a 10 MΩ load resistor) with silver conductive cloth tape and aluminum foil, under impact test through a 40 mm ball bearing.

cloth tape versus the ones fabricated using aluminum foil is shown in Fig. 5. The effective values of output voltage (V_{RMS} of 1.22 V to 5.96 V), current (I_{RMS} of 0.49 μA to 1.20 μA), output power (0.668 μW to 6.284 μW) and its standard deviation analysis calculated for each prototype (10 measurements performed on each sample). Such values showed that the highest performance of the proposed triboelectric energy harvesting devices can be achieved by using silver conductive cloth tape in contact with the dielectric layers of PDMS and polyimide. Furthermore, the polyimide or PTFE-silver conductive cloth tape or aluminum foil combinations can reach similar output power performance, ranging from 3.8 μW to 5.8 μW.

The ranking of the triboelectric materials used for the arc-shaped DMSE-TENG prototypes, arranged according to the output performance is shown in Table I (Tested). The most positive material of the conductors according the measurements, was shown to be the silver conductive cloth tape and the most negative material was PDMS. This means that the charge transferred using this material combination will be the highest from the selection of triboelectric materials. Each conductor material on Table I (Tested) was highlighted with a specific color in order to identify the higher output performance, when they are in contact with the insulators highlighted with the same color. The dominance of the silver tape among the chosen triboelectric materials, with the aim of reaching higher electrical output performance in the proposed energy harvesting prototypes, is clearly seen. Although silver conductive cloth is the best positive material, Al foil was chosen for the fabrication of the DMCS-TENG as a low-cost option with excellent performance.

III. DMCS-TENG FEM Model

Considering the so called "V-Q-x relationship" proposed for the operation and modeling of a TENG when it is connected with a resistive load (R), utilizing Kirchhoff's law, the governing equation of the whole system can be given by [8]:

$$R\frac{dQ}{dt} = -\frac{1}{C(x)}Q + Voc(x) = -\frac{1}{C}Q + V_{OC} \qquad (1)$$

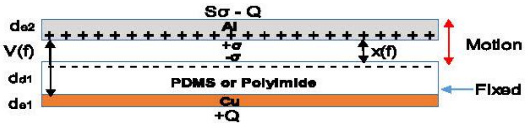

Fig. 6. Two-dimensional schematic of the DMCS-TENG prototype (Prototype 2).

where V_{OC} is the voltage generated between two DMCS-TENG contacts, Q is the amount of charge between the two contacts, C is the capacitance between the two electrodes, and x is the distance between the DMCS-TENG triboelectric layers that varies with the mechanical energy and phase of motion at time, t. According to these models, the power output performance by the DMCS-TENG depends on the output current (I). The voltage (V_{OC}) is influenced by the load resistance, and the surface charge density σ depends on the properties of the dielectric materials. The maximum theoretical surface charge density σ_{max} for contact DMCS-TENG was determined using the ion injection method, by comparing the threshold voltage for the air breakdown (V_{a-b}) and the actual voltage drop (V_{gap}) across the air gap. Thus, when x starts to increase from 0 during the releasing half cycle of the DMCS-TENG, the V_{a-b} at any $x > 0$ needs to remain bigger than V_{gap} in order to avoid breakdown of air.

$$V_{a-b} - V_{gap} > 0 = \frac{A\,(Px)}{\ln\,(Px) + B} - \frac{d\sigma x}{\varepsilon_0\,(d + x\varepsilon_r)} > 0 \qquad (2)$$

where P is the gas pressure for air at standard atmospheric pressure of 101 kPa, A and B are the constants determined by the pressure of the gas, $A = 2.87 \times 10^5$ V/(atm·m), and $B = 12.6.\varepsilon_r$ is the relative permittivity of the dielectric layer, and ε_0 is the vacuum permittivity. From equation (2), σ_{max} can be determined as follows [9]:

$$\sigma_{max} = \left[\frac{AP\varepsilon_0(d + x\varepsilon_r)}{d(\ln(Px + B)}\right] min \qquad (3)$$

The FEM simulations were performed coupling electro-mechanics and electrical circuit interfaces, to model the current, voltage and output power generated by the DMCS-TENG connected to resistive loads (varying from 1 MΩ to 100 MΩ) under the oscillating frequencies estimated of the ocean wave impact forces (Fig. 1). These are based on the DMCS-TENG structure (Prototype 2), as shown in Fig. 6. Two structures comprising different dielectric layers, namely polydimethylsiloxane (PDMS, thickness $d_{d1} = 125\ \mu$m, $\varepsilon_r = 2.5$) and polyimide (Kapton, thickness $d_{d1} = 50.8\ \mu$m, $\varepsilon_r = 3.4$), were attached to a copper (Cu, thickness $d_{e1} = 100\ \mu$m) lower electrode 1. An aluminum (Al, thickness $d_{e2} = 100\ \mu$m) layer was used as the second triboelectric material, the top electrode 2 (grounded). The top layer was fixed in both extreme sides and is the point at which the periodic motion (six cycles (t = 0.12 s)) was applied with the oscillatory frequencies of 30, 80, 150, 200, 219 and 250 Hz and an amplitude of 1 mm.

From equation (3), we consider a scenario where the maximum gap x separation is 1 mm and the time duration is

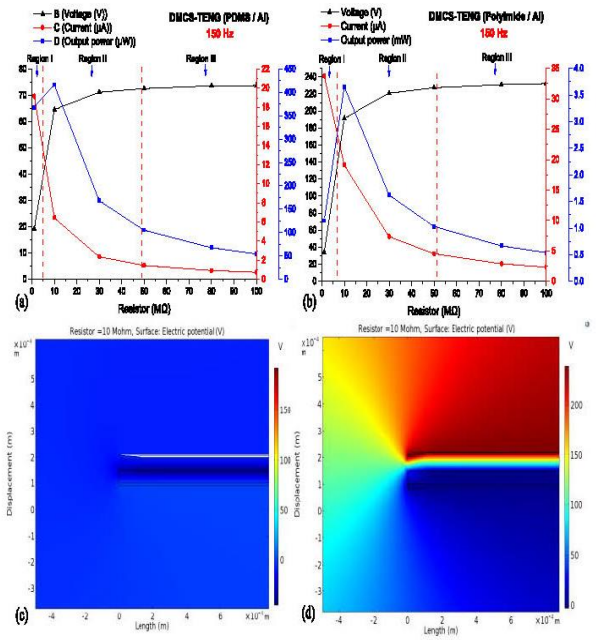

Fig. 7. The influence of the load resistance divided into three working regions on the magnitude of the output voltage (V), current (I) and maximum output power performance of the DMCS-TENG prototype ($L = 8$ cm) with (a) PDMS-Al and (b) Polyimide-Al layers at the oscillation frequency of 150 Hz. DMCS-TENG under oscillatory frequency and deformation. (c) Two dimensional shape showing the two triboelectric layers in contact, (d) Al layer released, which will rise a much higher potential.

30 seconds. The two tribo-charge surfaces were assigned to the model with a calculated value $\sigma_{PDMS} = \sigma_{max,PDMS} = \pm 11.53\ \mu$C/m^{2}and $\sigma_{max,Polyimide} = \pm 34.06\mu$C/m^2(see Supplementary Information document). A series of simulations were performed in order to analyze the output performance of the entire system, with different structure lengths ($L = 2.5$ cm, 5 cm and 8 cm) over the oscillatory frequency range mentioned earlier, so that the best design can be found. The highest calculated output performance for both samples was obtained with the DMCS-TENG structure of $L = 8$ cm at the oscillation frequency of 150 Hz as shown in the three regions of operation [8] of the proposed devices in Fig. 7 (a) and Fig. 7 (b). The DMCS-TENG with polyimide-Al reached a higher maximum instantaneous output power = 3.66 mW with a 10 MΩ load shown in Fig. 7 (b). In comparison, the maximum instantaneous output power of the DMCS-TENG with PDMS-Al was 416.47 μW in region II as depicted in Fig. 7 (a).

DMCS-TENG in the original state before the contact of the triboelectric layers do not experience charge transfer, and thus no electrical potential occurs across the electrodes (Fig. 7 (c)). By applying a force to the upper metal layer on the dielectric, each layer will be brought into surface contact, resulting in electron transfer from a material in the positive side of the triboelectric series to the one in the negative side in the series [10]. Accordingly, electrons will be injected from the Al to the polyimide/PDMS surface, leaving the positive charges on the Al layer. Such a process will continue in the first hundreds of cycles until the accumulated charges reach a saturation and equilibrium, and the negative charges will be

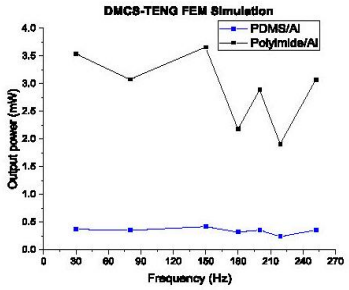

Fig. 8. Maximum instantaneous output power of simulated DMCS-TENG prototypes as a function of the main oscillatory frequencies of 30, 80, 150, 180, 200, 219 and 252 Hz with an amplitude of 1 mm (t = 0.12s).

preserved on the dielectric surface due to the nature of the insulator [11].

Once the pressing force is released, the Al layer of the DMCS-TENG will quickly rebound back due to the elasticity of the film and a gap is formed again between the two layers. From the numerical simulation results, it can be seen that the electric field generated by separate surface charges will give rise to a much higher potential on the Al layer side than the bottom electrode (Fig. 7 (d)). Such potential difference will drive the flow of positive charges from Al layer to the bottom electrode through the external load until the potential difference is fully offset by the transferred charges, rendering the bottom electrode with a surface charge density of $+Q$, while the charges on the Al is with a sum of two parts. One part is due to the transferred charges between electrode 1 and electrode 2 ($-Q$) and the other part is due to the triboelectric charges at the surface area ($S\sigma$). Thus, the total charges on electrode 2 are $S\sigma - Q$. Subsequently, when the two layers in the DMCS-TENG are in contact again, charge redistribution will result in a positive potential on the bottom electrode, which will drive all of the transferred charges $+Q$ to flow back to the Al layer. The complete electricity generation cycle is achieved and the device will go back to the equilibrium state.

The maximum output power of both energy harvesters is at 150 Hz, followed by 30 Hz under the load resistor of 10 MΩ (between 3.7 mW to 230 μW), which tends to decrease and fluctuate as the operation cycle increases. The difference in the output power of the two simulated DMCS-TENG prototypes across the oscillation frequency range (30 to 252 Hz) is shown in Fig. 8. Such difference is related to the higher surface charge density at the device with polyimide-Al due the thinner dielectric layer.

IV. DMCS-TENG Electrical Characterization Under Different Oscillating Frequencies and Using a Water Wave Generator Tank

A. DMCS-TENG Fabrication and Electrical Characterization Set-Up

For preliminary triboelectric material characterization using the impact tests, five DMCS-TENG prototypes of similar configuration to those used in the COMSOL model (Fig. 6) were fabricated using the most promising triboelectric material combinations that showed the highest output power. The DMCS- TENG prototypes have an active triboelectric area

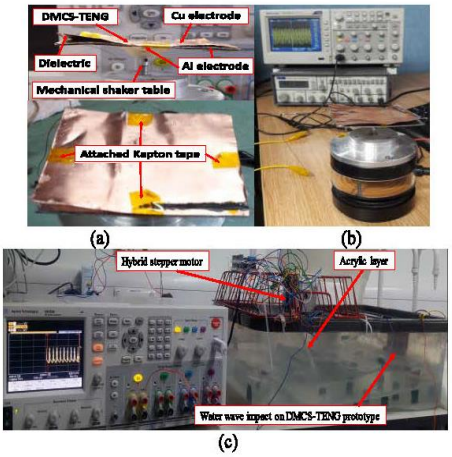

Fig. 9. (a) Fabricated DMCS-TENG, (b) DMCS-TENG mounted on the mechanical shaker table for the output performance measurements at different frequencies of oscillation. (c) Insulated DMCS-TENG prototype placed on the water wave generator tank for its output performance measurements.

of 8 cm × 8 cm. Two types of aluminum foil were evaluated, one flat aluminum foil (with t_{e2} = 18 μm) and a honeycomb patterned aluminum foil (with t_{e2} = 16 μm, individual hexagon area = 31.83 mm^2). The aluminum foil were fixed with a thin adhesive layer on the acrylic substrates at room temperature, acting as both the triboelectric material and the electrode 2 that is grounded. The dielectric layers (PDMS (d_{d1} = 125 μm), silicone rubber (d_{d1} = 150 μm), FEP (d_{d1} = 25 μm), polyimide (d_{d1} = 127 μm) and PET (d_{d1} = 60 μm)) were fixed with conductive acrylic adhesive (thickness = 25 μm) at room temperature on a copper layer (t_{e1} = 100 μm) connected to an external load of 10 MΩ for electrical characterization. The honeycomb patterned aluminum foil was selected to improve the contact electrification due to its surface morphology. Surface patterning is potentially a low-cost option to enhance the output performance of the DMCS-TENG prototypes [12]–[14].

The output performance response of the fabricated DMCS-TENG devices (focused in the frequencies of interest 30, 80, 150, 200, 219 and 252 Hz) was characterized using a Pasco Scientific SF-9324 mechanical shaker table connected to a TG550 function generator in order to replicate the conditions of the mechanical energy generated by the oscillating frequencies caused by ocean wave impacts. The function generator output was configured as a sine wave and the frequency swept from 25 to 300 Hz with an increasing step of 5 Hz for 55 seconds. The driving amplitude was set at 20 V peak-to-peak. The Al electrode was placed facing the surface of the dielectric layer and bound together on each side at the middle with Kapton tape (1 cm width) at room temperature (Fig 9 (a)). Finally, each of the DMCS-TENG prototypes were mounted as depicted in Fig 9 (b). The gap of the DMCS-TENG varies with the mechanical oscillation producing the triboelectric effect when the dielectric layer is in non-uniform contact with the Al film. The average acceleration, velocity and displacement generated by the mechanical shaker on the proposed energy

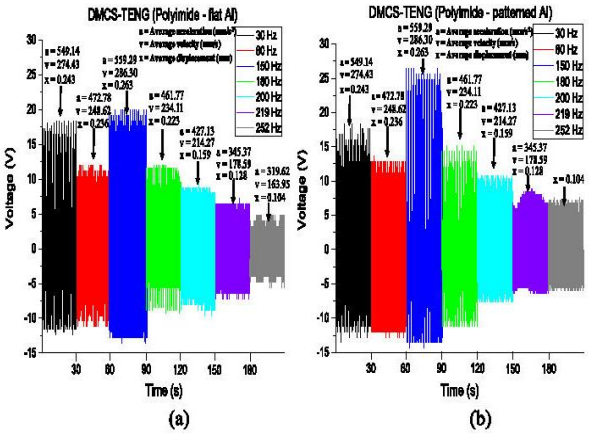

Fig. 10. DMCS-TENG with (a) polyimide-flat Al and (b) polyimide-honeycomb patterned Al voltage-time response through simulated resonant frequencies of 30 Hz, 80 Hz, 150 Hz, 180 Hz, 200 Hz, 219 Hz and 252 Hz. Average acceleration, velocity and displacement inputs measured with a PDV-100 Portable Digital Vibrometer.

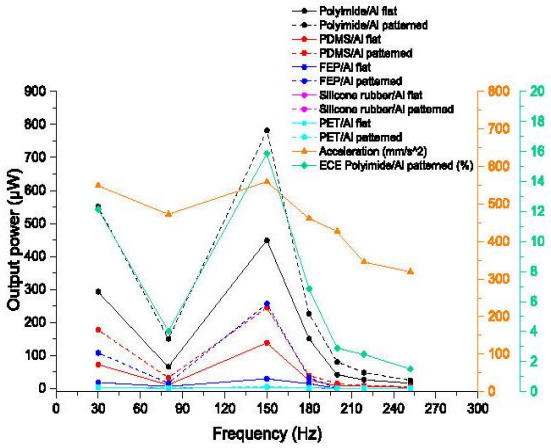

Fig. 11. DMCS-TENG output power, ECE % and average acceleration measured at the main compressed air bubble frequencies generated during wave impact with polyimide (Kapton), PDMS, FEP, silicone rubber, PET – flat Al foil/honeycomb patterned Al foil.

harvester prototypes were measured with a PDV-100 Portable Digital Vibrometer.

The energy harvester prototype which shows the higher output power performance through the aforementioned experiment, was characterized in water conditions using a wave generator tank, in order to simulate the real conditions of the mechanical energy generated by ocean wave impacts. A hybrid stepper motor (RS Pro 535-0502) attached with an acrylic layer of 20 cm × 20 cm (t = 8 mm) is used to generate the water waves motion into the water wave tank mounted on the left side of the tank [15]. The DMCS-TENG prototype was insulated with a Polyethylene plastic pack, in order to protect it from the contact with water. Such device was placed at the wall on the right side of the tank facing the impact of the water wave as shown in Fig. 9(c) where the water wave breaks with an amplitude of 10 cm and frequency of 1.20 Hz. The output power generated by the DMCS-TENG prototypes was calculated through the output voltage, and output current measurements performed using a digital oscilloscope Tektronix TDS 2014C and an Agilent Technologies N6705B Power analyser.

B. DMCS-TENG Dynamic Operation, Experimental Results and Discussion

The analytical model to calculate the maximum open-circuit voltage at the resonant frequency of the DMCS-TENG prototype through the motion of the oscillatory system can be described at device level as a damped system subjected to a harmonically varying force provided by the mechanical shaker table. Consequently, the V_{ocmax} at resonant frequency can be expressed as [16], [17] (see Supplementary Information document):

$$V_{ocmax} = \left(\frac{\sigma}{\varepsilon_0}\right)\left(\frac{m_0 a}{2k\zeta}\right) \tag{4}$$

where m_0 is the mass of the top plate, k is the stiffness coefficient of each spring, ζ is the damping coefficient of the DMCS-TENG system and a is the acceleration of the mechanical shaker table. The DMCS-TENG prototypes respond to the mechanical energies applied through resonant oscillatory frequencies. Where the Al foil is in constant non-uniform contact with the dielectric film and attracts electrons away from the copper electrode to flow through the 10 MΩ external load as shown in Fig 10 (a) and (b) for all the measurements at each frequency over 30 s. It has been observed that the maximum peak-to-peak voltage was measured for the DMCS-TENG prototypes using the honeycomb patterned foil in contact with polyimide (Fig 10 (b)). This can be compared with the output voltage measured using flat Al foil – polyimide (Fig. 10 (a)).

Among all the DMCS-TENG prototypes employing the top five triboelectric material combinations (Table I (tested)) in contact with flat Al foil and honeycomb patterned Al foil, the following results were found. The output power performance comparison between 30 to 252 Hz with an acceleration between 319.62 to 559.29 mm/s^2 of amplitude showed an improvement factor of 2.3 for the DMCS-TENG devices fabricated using the patterned Al foil, relative to those fabricated using flat foil (Fig. 11). Such enhancement of the measured values shows the effectiveness of the honeycomb patterned Al foil to improve the electrical contact and surface charge density between the selected triboelectric layers. The maximum generated output voltage (V_{RMS}) was 12.50 V, with an output current (I_{RMS}) of 62.27 μA, which corresponds to the output power and power density of 778.43 μW and 12.16 μW/cm^2, respectively. This was reached using polyimide in contact with the honeycomb patterned Al foil at the frequency of 150 Hz and average acceleration of 559.29 mm/s^2. This is followed by the DMCS-TENG devices using PDMS and FEP with the output voltage (V_{RMS}) from 11.10 V to 4 V, current (I_{RMS}) from 22.16 μA to 63.62 μA, output power from 246.02 μW to 254.48 μW and power density from 3.84 μW/cm^{2}to 3.98 μW/cm^2, in contact with the patterned Al foil (Fig. 11).

The total energy conversion efficiency (ECE) η of the DMCS-TENG self-resetting system with Polyimide-honeycomb patterned Al foil was defined as the ratio between the input mechanical energy and the generated elec-

trical energy E_{ele} that is delivered to the load resistance of 10 MΩ by the DMCS-TENG. The efficiency is determined by (5) [18]:

$$\eta = \frac{E_{electric}}{E_{mechanical}} x100\% = \frac{E_{electric}}{E_{kinetic} + E_{elastic}} x100\% \quad (5)$$

The E_{ele} generated by the DMCS-TENG shows an energy output between 0.40 of 13.02 μJ during a time of 60 s. The kinetic $E_{kinetic}$ and elastic $E_{elastic}$ energy applied to the DMCS-TENG by the mechanical shaker ($E_{mechanical} = E_{kinetic} + E_{elastic}$) was calculated by equation (6) and (7). The measured values for the dynamics of the DMCS-TENG were between 319.62 to 559.29 mm/s^2 for the average acceleration a, 163.95 to 343.59 mm/s for the average velocity v and between 0.10 to 0.26 mm for the average displacement x of the top dielectric layer. Considering as spring the bending of the top layer, and as constraints the attached kapton tape used to bound four sides of the conductor layer with the dielectric layer that generates the self-resetting system (Depicted in Fig. 9 (a)). The bending stiffness ($k = 4$ to 6.14 N/m) was estimated based in the mass ($m_{Polyimide} = 2g$) and average displacement x of the moveable top dielectric layer. N is the number of springs considered for the DMCS-TENG ($N = 1$) (Supplementary Information).

$$E_{kinetic} = \frac{1}{2} m v^2 = 26.87 \; to \; 81.96 \; \mu J \quad (6)$$

$$E_{elastic} = \frac{1}{2} k x^2 N = 0.13 \; to \; 0.58 \; \mu J \quad (7)$$

The energy applied ($E_{mechanical}$) to the DMCS-TENG by the mechanical shaker table was calculated to be between 26.91 to 82.11 μJ, which indicates an efficiency between 1.51 to 15.85 % for the main frequencies of interest between 30 to 252 Hz. The highest efficiency was calculated at 150 Hz and average acceleration of 559.29 mm/s^2, followed by 30 Hz with an acceleration of 549.14 mm/s^2 as shown in Fig. 11 according to the experimental measurements.

It was observed, however, that at 80 Hz with an acceleration of 472.78 mm/s^2 and at frequencies greater than 180 Hz with acceleration between 319.62 to 461.77 mm/s^2, the output power performance response and efficiency of the devices were lower as shown in Fig. 11. The variation in the output power performance and efficiency (Fig. 11) shows that the proposed devices can effectively respond to a broad range of input oscillating frequencies showing different resonant peaks from 25 to 300 Hz. This means that the device has the potential to produce a higher output power at the moment when the ocean wave impacts the porous structures between 30 Hz and 50 Hz. After the wave collapses, where the air bubbles are formed between 150 Hz and 200 Hz [2], [3]. The maximum output performance measured experimentally is related to the calculated response obtained by the FEM simulation at 150 Hz for the proposed energy harvester prototypes, under similar conditions of operation as described in section III.

Additionally, the difference in the output performance between the simulated DMCS-TENG and the real prototypes arises because the FEM simulations were solved by assuming the maximum surface charge density between layers in contact under ideal conditions. This leads to higher output power values (between 3.66 mW to 416.47 μW). Compared with the measured output power values of the built and tested devices (between 781.31 μW to 244.41 μW) in non-ideal conditions.

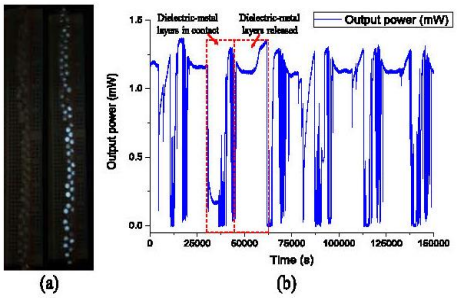

Fig. 12. (a) Power up of 62 serially-connected white LEDs instantaneously and continuously with the DMCS-TENG prototype (polyimide-honeycomb patterned Al foil). Measured average instantaneous power consumption by the LEDs was around 13.48 mW. (b) Output power generated by the DMCS-TENG prototype (polyimide-honeycomb patterned Al foil), when the dielectric-metal layers are in contact and released exposed to water wave impact with an amplitude of 10 cm and frequency of 1.2 Hz.

Moreover, to demonstrate the capability of the DMCS-TENG prototypes as direct power source, 62 Kingbright L-7104PWC-A 3 mm white LEDs (1200 mcd) were utilized as operating load connected to the device with the triboelectric material combination of polyimide-honeycomb patterned Al foil. The peak AC output current of the DMCS-TENG (without rectification) was capable of instantaneously and continuously lighting up 62 serially-connected white LEDs when the device was under 150 Hz mechanical oscillation and average acceleration of 559.29 mm/s^2 (Fig. 12 (a)). The measured average power consumption by the LEDs was around 13.48 mW for this demonstration.

Finally, the generated output power by the aforementioned energy harvester, when the dielectric-metal layers are in contact and released under the water wave impact generated in the tank, is shown in Fig. 12 (b). This device with its area of 64 cm^2 generated an instantaneous output power, power density of 1.08 mW, 169.22 mW/m^2, respectively. Consequently, it is expected to generate output power and energy of 3.05 W and 2.53 J, if 2,812 of the DMCS-TENG prototypes are tiled (electrically connected) over a water-structure interface with an area of 18 m^2 that received wave sizes among 0.3 m to 4 m [19].

The total energy (potential energy and kinetic energy) of a wave can be calculated by [20]:

$$E = \frac{1}{2} \rho g A^2 \quad (8)$$

where g is the acceleration of gravity (g = 9.8 m/s^2), ρ is the density of water (ρ = 1000 kg/m^3) and A is the wave amplitude (A = 10 cm, frequency = 1.2 Hz). The input energy E, produced by the water wave impact in the tank (Fig. 9 (c)), was found to be approximately 49 J. Accordingly, the DMCS-TENG devices have an efficiency of 5.16 %, calculated by:

$$\eta = \frac{E_{electric}}{E_{waterwave}} x100\% = 5.16\% \quad (9)$$

As a result of the power levels achieved by the devices, it is feasible to propose that such energy harvesters can be used to energize wireless nodes for coastal sensing applications.

V. Conclusion

The proposed work has shown that the triboelectric effect can be used to realize an innovative type of energy harvester for ocean wave impact forces. Firstly, by comparing the findings of the literature, PTFE is the most electronegative material which is widely used in TENG fabrication [12], [21]. Therefore, in our work through an impact test, it was found the ideal dielectric-conductor triboelectric material combinations for the fabrication of the DMCS-TENG prototypes. The results showed that silver conductive cloth tape is the material that attains maximum positive charge, and PDMS as the material that attains maximum negative charge. For the same load conditions (10 MΩ), it was found that the best output performance was obtained by using dielectric layers with thicknesses between 100 to 125 μm. Additionally, by employing a mechanical shaker for the DMCS-TENG prototypes output power performance characterization. The results show that excellent output power is obtained when using polyimide as the negative material in contact with the honeycomb patterned Al foil. Such results indicate that the experiments set-up change the contact electrification performance between the dielectric-conductor, which was reflected in the output power performance of the proposed TENG devices. A different most negative material was found compared with the one shown in the literature when the contact is made between dielectric-metal materials [12], [21]. Such results suggest that the previously published triboelectric series [12], [21] may not give the obvious material pair for the best energy harvesting performance under all circumstances, and for cross-comparison, thickness normalized values must be used.

Secondly, through numerical simulation to obtain a quantitative understanding of the working mechanism and analysis of the output performance of the entire system under the effect of the ocean wave impact oscillating frequencies, the optimum design of the DMCS-TENG was found.

Thirdly, it was observed that the proposed devices' output power and ECE efficiency changes with the main oscillation frequencies between 30 Hz to 252 Hz with an amplitude average acceleration between 319.62 to 559.29 mm/s^2. Such variation shows that the proposed devices can effectively respond to a broad range of input oscillating frequencies showing different resonant peaks at the aforementioned frequencies. The maximum output performance was reached using the optimum triboelectric material combination of polyimide – Al foil. Therefore, an enhancement in the output power performance by a factor of 2.3 was achieved using a honeycomb patterned aluminum foil as a low-cost option to enhance the output performance of the DMCS-TENG prototypes. Such improvement in the output performance is due the surface pattern of the Al foil, which increase the effective contact area between the materials that increase the triboelectric charges generated during the friction.

Finally, through the integration of the selected DMCS-TENG prototype into the water wave generator tank an output power density of 169.22 mW/m^2 using an area of 64 cm^2 was generated. It is predicted that over an area of 18 m^2 with wave sizes of 0.3 m to 4 m, an output power of around 3.05 W is possible. This offers an alternative approach for generating electrical power for coastal sensing applications that require self-powering. Further investigation is required to explore suitable designs to improve the output electrical performance of the energy harvesting prototypes, with engineering challenges, such as efficient energy coupling and robustness to withstand the harsh environmental conditions of the ocean.

Acknowledgment

The authors thank CONACYT for the fellowship awarded to Ulises Tronco Jurado.

References

[1] Z. L. Wang, L. Lin, J. Chen, S. Niu, and Y. Zi, "Harvesting large-scale blue energy," in *Triboelectric Nanogenerators*. Geneva, Switzerland: Springer, 2016, pp. 283–306.
[2] R. B. Mayon, Z. Sabeur, M. Tan, and K. Djidjeli, "Analysis of fluid flow impact oscillatory pressures with air entrapment at structures," *Coastal Eng. Proc.*, vol. 1, no. 35, p. 31, 2017.
[3] R. B. Mayon, "Investigation of wave impacts on porous structures for coastal defences," Doctoral Thesis, Univ. Southampton, Southampton, U.K., Tech. Rep. ID:422221, 2017.
[4] U. T. Jurado, S. H. Pu, and N. M. White, "A contact-separation mode triboelectric nanogenerator for ocean wave impact energy harvesting," in *Proc. IEEE SENSORS*, Oct./Nov. 2017, pp. 1–3.
[5] Z. L. Wang, L. Lin, J. Chen, S. Niu, and Y. Zi, "Applications in self-powered systems and processes," in *Triboelectric Nanogenerators*. Cham, Switzerland: Springer, 2016, pp. 351–398.
[6] Z. L. Wang, L. Lin, J. Chen, S. Niu, and Y. Zi, "Harvesting large-scale blue energy," in *Triboelectric Nanogenerators*. Cham, Switzerland: Springer, 2016, pp. 283–306.
[7] U. Khan and S.-W. Kim, "Triboelectric nanogenerators for blue energy harvesting," *ACS Nano*, vol. 10, no. 7, pp. 6429–6432, 2016.
[8] Z. L. Wang, L. Lin, J. Chen, S. Niu, and Y. Zi, "Theoretical modeling of triboelectric nanogenerators," in *Triboelectric Nanogenerators*. Cham, Switzerland: Springer, 2016, pp. 155–183.
[9] S. Wang *et al.*, "Maximum surface charge density for triboelectric nanogenerators achieved by ionized-air injection: Methodology and theoretical understanding," *Adv. Mater.*, vol. 26, no. 39, pp. 6720–6728, 2014.
[10] D. K. Davies, "Charge generation on dielectric surfaces," *J. Phys. D, Appl. Phys.*, vol. 2, no. 11, p. 1533, 1969.
[11] F. Saurenbach, D. Wollmann, B. D. Terris, and A. F. Diaz, "Force microscopy of ion-containing polymer surfaces: Morphology and charge structure," *Langmuir*, vol. 8, no. 4, pp. 1199–1203, 1992.
[12] J. Chen and Z. L. Wang, "Reviving vibration energy harvesting and self-powered sensing by a triboelectric nanogenerator," *Joule*, vol. 1, no. 3, pp. 480–521, 2017.
[13] J. Chen *et al.*, "Automatic mode transition enabled robust triboelectric nanogenerators," *ACS Nano*, vol. 9, no. 12, pp. 12334–12343, 2015.
[14] Y. Yu and X. Wang, "Chemical modification of polymer surfaces for advanced triboelectric nanogenerator development," *Extreme Mech. Lett.*, vol. 9, pp. 514–530, Dec. 2016.
[15] U. T. Jurado, S. H. Pu, and N. M. White, "Water-dielectric single electrode mode triboelectric nanogenerators for ocean wave impact energy harvesting," in *Proc. Eurosensors*, Graz, Austria, 2018, p. 714.
[16] R. V. Dukkipati, *Vibration Analysis*. Oxford, U.K.: Alpha Science, 2004.
[17] J. Chen *et al.*, "Harmonic-resonator-based triboelectric nanogenerator as a sustainable power source and a self-powered active vibration sensor," *Adv. Mater.*, vol. 25, pp. 6094–6099, Nov. 2013.
[18] W. Tang *et al.*, "Liquid-metal electrode for high-performance triboelectric nanogenerator at an instantaneous energy conversion efficiency of 70.6%," *Adv. Funct. Mater.*, vol. 25, no. 24, pp. 3718–3725, 2015.
[19] Oceanweather. *Current Marine Data*. Accessed: Oct. 30, 2018. [Online]. Available: http://www.oceanweather.com/data/index.html
[20] A. Khaligh and O. C. Onar, *Energy Harvesting: Solar, Wind, and Ocean Energy Conversion Systems*. Boca Raton, FL, USA: CRC Press, 2009.
[21] J. Lowell and A. C. Rose-Innes, "Contact electrification," *Adv. Phys.*, vol. 29, no. 6, pp. 947–1023, Jul. 1980.

Nano Energy 72 (2020) 104701

Contents lists available at ScienceDirect

Nano Energy

journal homepage: http://www.elsevier.com/locate/nanoen

Full paper

Grid of hybrid nanogenerators for improving ocean wave impact energy harvesting self-powered applications

Ulises Tronco Jurado [a,b,*], Suan Hui Pu [a,c], Neil M. White [b]

[a] Mechatronics Research Group, University of Southampton, Southampton, SO17 1BJ, UK
[b] Smart Electronic Materials and Systems Research Group, University of Southampton, Southampton, SO17 1BJ, UK
[c] University of Southampton Malaysia, Iskandar Puteri, 79200, Johor, Malaysia

ARTICLE INFO

Keywords:
Coastal wave impact
Dielectric-conductor
Triboelectric-piezoelectric effects
Hybrid nanogenerators
Marine sensing platforms
Water-structure interfaces

ABSTRACT

This paper describes an alternative approach for improving the output power performance for coastal wave impact energy harvesting systems, located at water-structure interfaces. This is achieved by simultaneously coupling the triboelectric and piezoelectric effects, exhibited in some materials. The use of finite element modelling, and experimental electrical characterization, enables the integration of hybrid devices into a breaking water wave generator tank. This provides a mechanism for simulating actual ocean wave conditions at low frequencies (0.7 Hz–3 Hz). Enhancements in the output performance by a factor of 2.24 and 3.21, relative to those obtained from using single triboelectric and piezoelectric nanogenerators, were achieved. This is demonstrated by evaluating the output current, voltage, transferred charge, and charging performance from a grid of up to four hybrid devices connected to capacitors of different capacitance values. Such hybrid devices were capable of powering a one-way wireless transmitter with a generated output power between 340.85 μW and 2.57 mW and sent a signal to a receiver at different distances from 2 m to 8 m. The research shows that such an integrated device can provide a promising mechanism for developing high-performance energy harvesting mechanisms for ocean wave impact to drive self-powered systems having an average power consumption of 1–100 mW. Further, it is estimated that through the construction of large water-hybrid nanogenerator-structure interfaces, output powers of approximately 21.61 W can be generated for powering networks of self-powered sensing systems in smart large-scale applications.

1. Introduction

The energy harvested from the shallow ocean waves has been attracting a great potential as a source of electricity for many years [1]. Specially, different triboelectric nanogenerators (TENG) based on contact electrification of solid-solid and liquid-solid interfaces [2–8], and hybrid devices combined with TENG-electromagnetic generators (EMG) [9,10] have been developed focusing in harvesting the irregular motions at low frequencies between 0.5 Hz and 5 Hz, generated by the shallow ocean wave energy. Therefore, this work focuses on harvesting the breaking wave impact energy at coastal structures that varies between slowly-acting pulsating loads, and more intense impulsive loads [11], which can be effectively exploited as a source of electrical energy. Two different approaches for harvesting coastal wave impact forces have been demonstrated using a dielectric-metal contact separation mode triboelectric nanogenerators (DMCS-TENG) with solid materials in contact at wide frequency range (30 Hz–252 Hz) [12,13], and also water-dielectric contact [14] using water as a triboelectric material at low frequency range (1.2 Hz). However, as further investigation is required to explore suitable designs of TENG with engineering challenges to improve the energy conversion efficiency harvesting the breaking ocean wave impact. This research proposes an alternative approach, stable, ease, simple to fabricate, and lightweight hybrid nanogenerator to promote the output current to improve the low output power of DMCS-TENG harvesting the impact of the water waves as previously studied [12–15]. Focused at low frequency impact among 0.7 Hz–3 Hz, by integrating a polyvinylidene fluoride (PVDF) piezoelectric layer [16,17] with suitable chosen triboelectric material pairs [13,18–20].

Firstly, the simultaneous operation of triboelectric-piezoelectric effects [21–23] under water wave impact was studied. The hybrid nanogenerator energy harvesters utilize dielectric-to-conductor triboelectric

* Corresponding author. Mechatronics Research Group, University of Southampton, Southampton, SO17 1BJ, UK.
E-mail addresses: utj1n15@soton.ac.uk (U.T. Jurado), SuanHui.Pu@soton.ac.uk (S.H. Pu), nmw@ecs.soton.ac.uk (N.M. White).

https://doi.org/10.1016/j.nanoen.2020.104701
Received 28 January 2020; Received in revised form 9 March 2020; Accepted 9 March 2020
Available online 13 March 2020

contact, and a flexible piezoelectric material with an active area of 4 cm × 4 cm. Secondly, a finite element model (FEM) was developed for the hybrid devices using COMSOL Multiphysics, to understand the coupling between both effects, study the load resistance matching and parameter optimization in order to find higher output performance.

Thirdly, the generated output voltage, output current, transferred charges and output power by the proposed hybrid devices were characterized in water conditions using a breaking water wave generator tank, which simulates the conditions of the mechanical energy generated by ocean wave impacts on the shoreline at low frequencies mentioned above. The output performance of the hybrid prototypes was compared with triboelectric nanogenerators and piezoelectric nanogenerators (PENG) tested in similar conditions [13,14]. Additionally, a load resistance matching experiment was performed with the objective being to obtain maximum output power performance from the prototypes.

Finally, the ability to charge a variety of capacitors with a single hybrid device, and a grid of four hybrid devices connected in parallel [24–26] was characterized. An enhancement in the output performance by exploiting the advantage by the combined triboelectric-piezoelectric effects using the proposed grid of energy harvesters was achieved as a result of simultaneous operation of both mechanisms under water wave impact at low frequency range in a single contacted-pressed-release operation. Additionally, it was demonstrated that such grid of energy harvesters has the potential to drive small electronic devices that will enable future advancement for powering a variety of battery-less, self-powered marine sensing platforms for environmental monitoring.

2. Working mechanism of electricity generation using triboelectric-piezoelectric effects under water wave impact

The three-electrode structure of the hybrid nanogenerator prototypes utilizes an arc-shaped dielectric-to-conductor triboelectric contact and a flexible piezoelectric material with an active area of 4 cm × 4 cm (Fig. 1 a, Fig. 1e and 1 f). The energy applied to the hybrid nanogenerator system is translated into two coupled effects. The triboelectric effect is affected by $E_{kinetic}$ (1), which is the energy carried by the moveable arc-shaped dielectric layer that plays the role of contact material for triboelectricity, and $E_{elastic}$ (2) which is the energy stored in the dielectric layer acting as a spring for separation after contact.

$$E_{kinetic} = \frac{1}{2}mv^2 \tag{1}$$

$$E_{elastic} = \frac{1}{2}k_t x^2 N \tag{2}$$

where, v is the average velocity of the dielectric layer when the contact is made, caused by the water wave impact, m is the mass of the moveable arc-shaped layer. k_t is the spring constant due a flexural stiffness, x is the displacement of the arc-shaped layer that is equal to the spacing between the two contacting surfaces ($x = 5$ mm), and N is the number of springs considered for the arc-shaped structure of the hybrid nanogenerator ($N = 2$).

Additionally, the piezoelectric effect is affected by the mechanical energy of the water wave impact which stress the piezo-layer a distance a, and that can be approximately calculated by the work done, W due to pressing/pulling as shown in (3) [27].

$$W = F\Delta L \cong \sigma A_c \frac{2a^2}{L_0} \tag{3}$$

The piezo-film is stressed by tension $F = \sigma A_c$, where σ is tensile stresses, and A_c is the cross-sectional area of the piezoelectric layer. Considering the piezo-layer as an elastic medium, the spring constant k_p due the stiffness in stretching that is given by $k_p = EA_c/L_0$, where E is the Young's modulus. The length change of the piezoelectric material ΔL, can be approximated as $\Delta L \cong \frac{2a^2}{L_0}$, defining $L \cong L_0$ [27].

The operation of the PENG (Fig. 1 b) and the two-electrode structures of the arc-shaped TENG (Fig. 1 c) and DMCS-TENG with self-restoring structure (Fig. 1 d) used to compare the output performance of the hybrid nanogenerator under breaking wave impact is illustrated in the

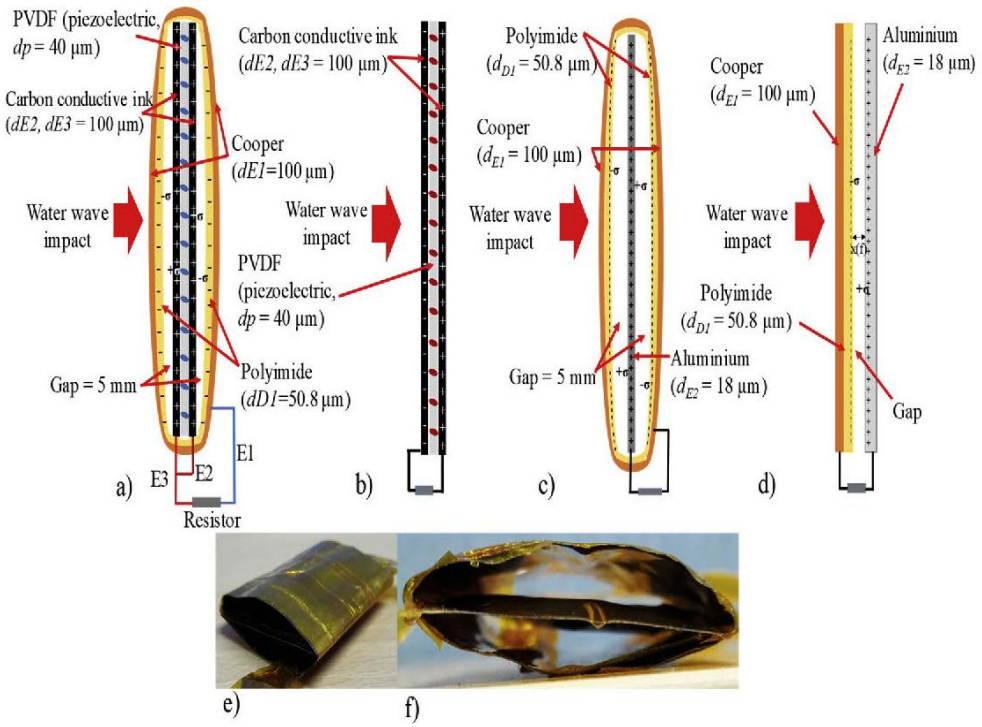

Fig. 1. Two-dimensional schematic of the a) Hybrid nanogenerator, b) PENG with charge distribution when it is under an external force. c) The arc-shaped DMCS-TENG, and d) the DMCS-TENG self-resetting system. e) Digital photo and f) cross sectional digital photo of the hybrid nanogenerator.

Supplementary Information document.

The simultaneous operation of triboelectric-piezoelectric effects under water wave impact is depicted in Fig. 2(a–e). Before the water wave impacts the hybrid nanogenerator, there are accumulated negative charges in the dielectric layer, and positive accumulated charges in electrode 2 (E2) and electrode 3 (E3) caused by dielectric-to-conductor triboelectrification after few cycles of movement (Fig. 2 a and 2 f). First, the impact of the water wave produces forward triboelectric effect as the gap between contact-layers decreases, and a piezoelectric effect as the charges flow due to tensile stress on the piezoelectric layer (Fig. 2 b and 2 g). The piezoelectric polarization influences the charge distribution on electrode 1 (E1), and E3 since they are connected. Positive charges flow to E3 leaving E1 with negative charges, when the device is contacted and pressed (Fig. 2 b and 2 g). Second, as the water wave breaks down and moves off the hybrid device, no polarization exist so E1 and E3 remain electrically neutral as the device it is in the "contacted and released" state (Fig. 2 c and 2 h). Third, the gap increases and hence this changes the electric field between the contacted dielectric-conductor materials. The piezoelectric material recovers to its original shape, with a change in piezoelectric potential and electric field, driving the charges in the load to flow in an opposite direction. Therefore, there are charges with opposite signs in E1 and E3, respectively (Fig. 2 d and 2 i) as the structure of the hybrid prototype is releasing. Finally, the hybrid nanogenerator is fully released, and reaches equilibrium once again (Fig. 2 e). Thus, one operational cycle of the hybrid prototype is achieved. Once the following water wave impacts the hybrid prototype, a periodic output will be obtained (Fig. 2 a-e).

3. Hybrid nanogenerators FEM

An FEM was developed for the hybrid energy harvesters in order to understand the output performance, load resistance matching of simultaneous coupling between triboelectric and piezoelectric effects under water wave impact. We first consider the "*V-Q-x* relationship" [28,29] proposed for modelling the operating principles of a TENG. When it is connected with an external resistive load (R_t), the maximum output power of the whole system can be derived using Kirchoff's law [28,29]:

$$R_t\frac{dQ}{dt} = -\frac{1}{C(x)}Q + V_{OC(x)} = -\frac{1}{C}Q + V_{OC} \tag{4}$$

where *Voc* is the voltage generated between two DMCS-TENG contacts, *Q* is the amount of charge within the two contacts, *C* is the capacitance of the two electrodes, and *x* is the distance between the triboelectric layers that varies with the mechanical energy and phase of motion at time, t. According to this model, the output power performance by the DMCS-TENG depends on the output current (*I*). The voltage (*V*) is influenced by the load resistance, and the surface charge density σ depends on the properties of the materials in contact. The piezoelectric nanogenerator has a smaller output voltage but larger output current, which is caused by the relatively low equivalent resistance. The equivalent external resistance of a piezoelectric nanogenerator (R_p), when the output power reaches its maximum value can be expressed as [30]:

$$R_p = \frac{d_p}{bL\varepsilon_{ij}f} \tag{5}$$

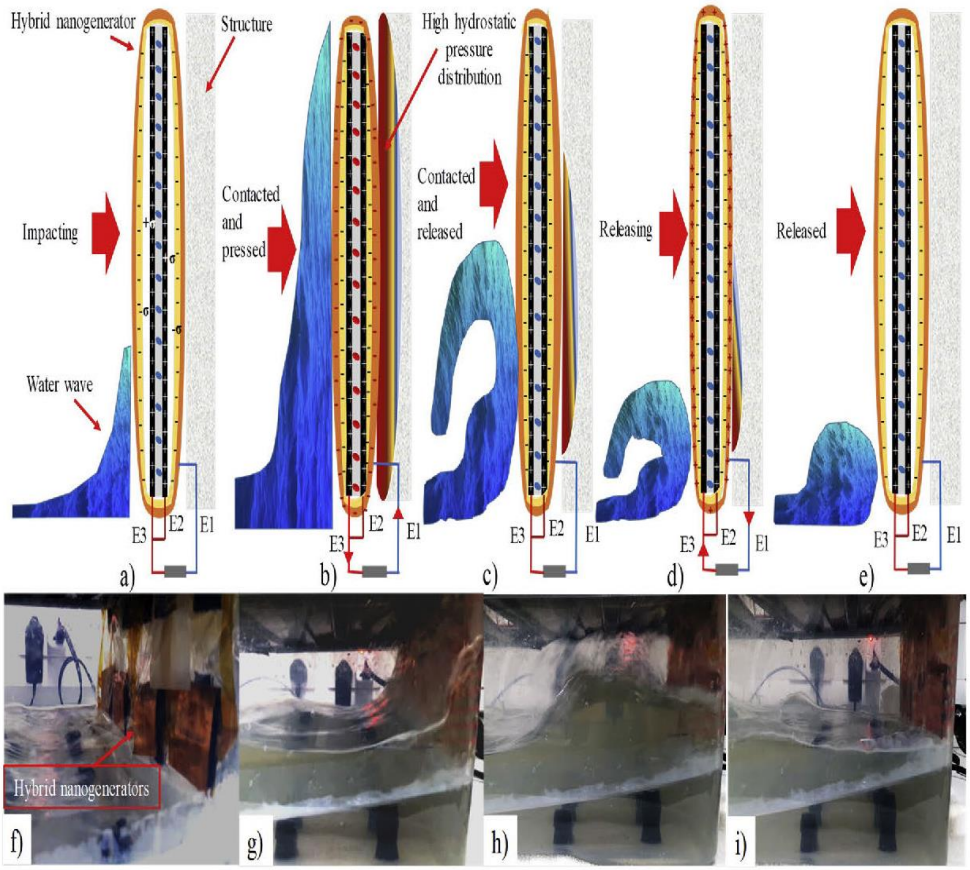

Fig. 2. (a–e) Working mechanism of the hybrid nanogenerator with a simultaneous operation and electricity generation of triboelectric-piezoelectric effects under water wave impact. Digital photos of grid of hybrid nanogenerators in the breaking wave impact generator tank f) before receiving water wave impact, g) contacted and pressed, h) contacted and released, and i) releasing.

where d_p, b, L and ε_p are the thickness, width, length and permittivity of the piezoelectric material and f is the frequency of the external mechanical energy.

The FEM simulations were performed by coupling solid mechanics, electrostatics and electrical circuit interfaces so as to model the output current, voltage and power generated by the hybrid nanogenerators connected to resistive loads (varying from 0.001 to 100 MΩ) under a horizontal applied periodic motion at the oscillating frequencies of 0.7, 1.2, 1.8, 2.5 and 3 Hz. This applying a waveform, input, and a boundary load on the hybrid device as described in Table 1. The model is based on the hybrid prototype structure as shown in Fig. 1 a, with different lengths of (L = 4 cm, 6 cm and 8 cm), so that the best design can be found. The device structure includes a PVDF piezoelectric layer ($d_p = 40$ μm) with a piezoelectric polarization ($x1$) of 150 μC/m^2 that is connected to two silver electrodes (d_{E2}, $d_{E3} = 10$ μm) E2 (grounded) and E3. A copper E1 ($d_{E1} = 10$ μm) with a polyimide dielectric layer ($d_{D1} = 50.8$ μm) acts as the triboelectric part. The two tribo-charge surfaces were assigned with the theoretical maximum surface charge density [13,31] $\sigma_{max} = \pm 34.063$ μC/m^2, respectively (Table 1).

A series of simulations were performed in order to analyse the output performance of the entire system at the frequency range aforementioned. First, an analysis of the load resistance influence in the output performance and electric potential of triboelectric and piezoelectric part was performed independently as illustrated in Fig. 3 a and Fig. 3 b. The results show a highest output power performance with the structures of L = 8 cm at the oscillation of 3 Hz. The triboelectric nanogenerator and piezoelectric nanogenerator reached the maximum output power of 21.88 mW and 19.56 mW with a 10 MΩ and 0.5 MΩ load, respectively (Fig. 3 d).

Therefore, the coupling of both effects was performed using the electric circuit diagram shown in Fig. 3 c, to perform a quantitative load matching analysis of the hybrid device output performance, and electric potential. The output power of the hybrid prototype shows an enhancement by a factor of 1.36 and 1.56 compared with the simulated triboelectric nanogenerators and piezoelectric nanogenerators tested in similar conditions respectively (Fig. 3 d). The maximum generated output voltage 381.89 V and output current of 76.87 μA, which corresponds to the maximum output power of 29.94 mW, with a 5 MΩ load as shown in Fig. 3 d, and Fig. 3 c illustrates the electric potential generated by the hybrid prototype.

Additionally, the increase in the length (L = 8 cm) and oscillating frequency (0.7 Hz–3 Hz) of the hybrid devices promote an increase in the output power by a factor of 1.34 (L = 4 cm) and 1.06 (L = 6 cm), respectively. Consequently, the optimum load resistance reduces as response [28], so for the hybrid structures L = 4 cm and L = 6 cm the optimum resistances were 10 MΩ and 8 MΩ (Fig. 3 e), with a maximum output power of 22.27 mW, and 28.22 mW, respectively (see Supplementary Information document).

Although the structure of 8 cm × 8 cm is the best to obtain higher output performance for the hybrid device, the structure with the active area of 4 cm × 4 cm was selected to fabricate the hybrid nanogenerator, with the purpose of obtain a stable output performance operation. This when the hybrid device and the grid of 4 hybrid devices were attached into the operation area (13 cm × 34 cm) in the water wave impact generator tank (52 cm × 34 cm x 18 cm).

Table 1
Parameters used in the FEM.

Parameter	Value
R_load (R_L)	0.001–100 MΩ
R_TENG (R_t)	10 MΩ
R_PENG (R_p)	0.5 MΩ
Frequencies (f)	0.7, 1.2, 1.8, 2.5, and 3 Hz
Time (t)	1 s
Waveform	6*pi*f
Input	wv1(t)
Boundary load	solid.rho*g_const
Surface charge density (σ_{max})	±34.063 μC/m^2
Piezoelectric polarization (x_1)	150 μC/m^2
Time dependant (Simulation time)	range(0,0.006,0.72)s
Dielectric layer (Polyimide, d_{D1})	Thickness = 50.8 μm Length = 4, 6 and 8 cm
Piezoelectric layer (PVDF, d_p)	Thickness = 40 μm Length = 4, 6 and 8 cm
Copper electrodes (d_{E1})	Thickness = 10 μm Length = 4, 6 and 8 cm
Silver electrodes (d_{E2}, d_{E3})	Thickness = 10 μm Length = 4, 6 and 8 cm
Gap	150 μm

4. Hybrid nanogenerator prototype fabrication and electrical characterization set-up

4.1. Fabrication

The hybrid prototypes composed with a three-electrode configuration with an active area of 4 cm × 4 cm depicted in Fig. 1 a and Fig. 1 e-f, were fabricated using a simple and low-cost process. Two carbon conductive ink electrodes (E2 and E3) were manually printed on both sides of a flexible PVDF piezoelectric layer (PIEZOTECH, $d_p = 40$ μm) at room temperature (Fig. 1 b). Therefore, by using suitable triboelectric materials [13,18–20], a dielectric polyimide ($d_{D1} = 50.8$ μm) was manually fixed with conductive glue at room temperature on a copper layer ($d_{E1} = 100$ μm) which acts as E1. Additionally, the E1 layer was manually insulated on the other side using Kapton polyimide heat and chemical resistant tape at room temperature. Then, the E1 layer was placed facing the polyimide dielectric layer over the piezoelectric layer and bonded using Kapton tape at room temperature to form the arc-shaped dielectric-to-conductor structure with a gap of 5 mm on both sides (Fig. 1 a).

Additionally, the arc-shaped TENG have an active area of 4 cm × 4 cm (Fig. 1 c), and an acrylic sheet was selected as a substrate material. An aluminum conductor layer (thickness = 18 μm) was attached to the acrylic with a thin adhesive layer, at room temperature. Acting as both the triboelectric material and the electrode that is grounded. The polyimide dielectric layer (thickness = 50.8 μm) was fixed with an arc-shaped form using conductive acrylic adhesive at room temperature on a copper layer (thickness = 100 μm) that is used as the second electrode connected to an external load for electrical characterization. Additionally, the copper layer was manually insulated on the other side using Kapton. The maximum gap between the arc-shaped dielectric layer and the conductor layer is 5 mm. Therefore, the DMCS-TENG with self-restoring structure was fabricated following the process described in Ref. [13] using the dielectric-metal contact between polyimide and aluminium (Fig. 1 d).

4.2. Electrical characterization

The electrodes of the fabricated hybrid prototype were connected to two full wave bridge rectifiers in order to perform the electrical characterization, as depicted in Fig. 4 a. E1, and E3 were connected to each rectifier as a supply from the hybrid device in a simultaneous operation using the triboelectric effect and piezoelectric effect, respectively. E2 was connected in both rectifiers that is used as the second triboelectric material (grounded) and second electrode (grounded) of the piezoelectric layer.

Their output voltage, output current, transferred charges and output power performance was compared with triboelectric nanogenerators, and piezoelectric nanogenerators [13] (Fig. 1 b-d) which were characterized in similar water conditions. The energy harvesters were insulated with polyethylene packaging, in order to protect them from the contact with water. Such devices were placed at the wall on the right side of the tank facing the impact of the water wave as shown in Fig. 4 b, where the water wave breaks with an amplitude of ~10–12 cm and

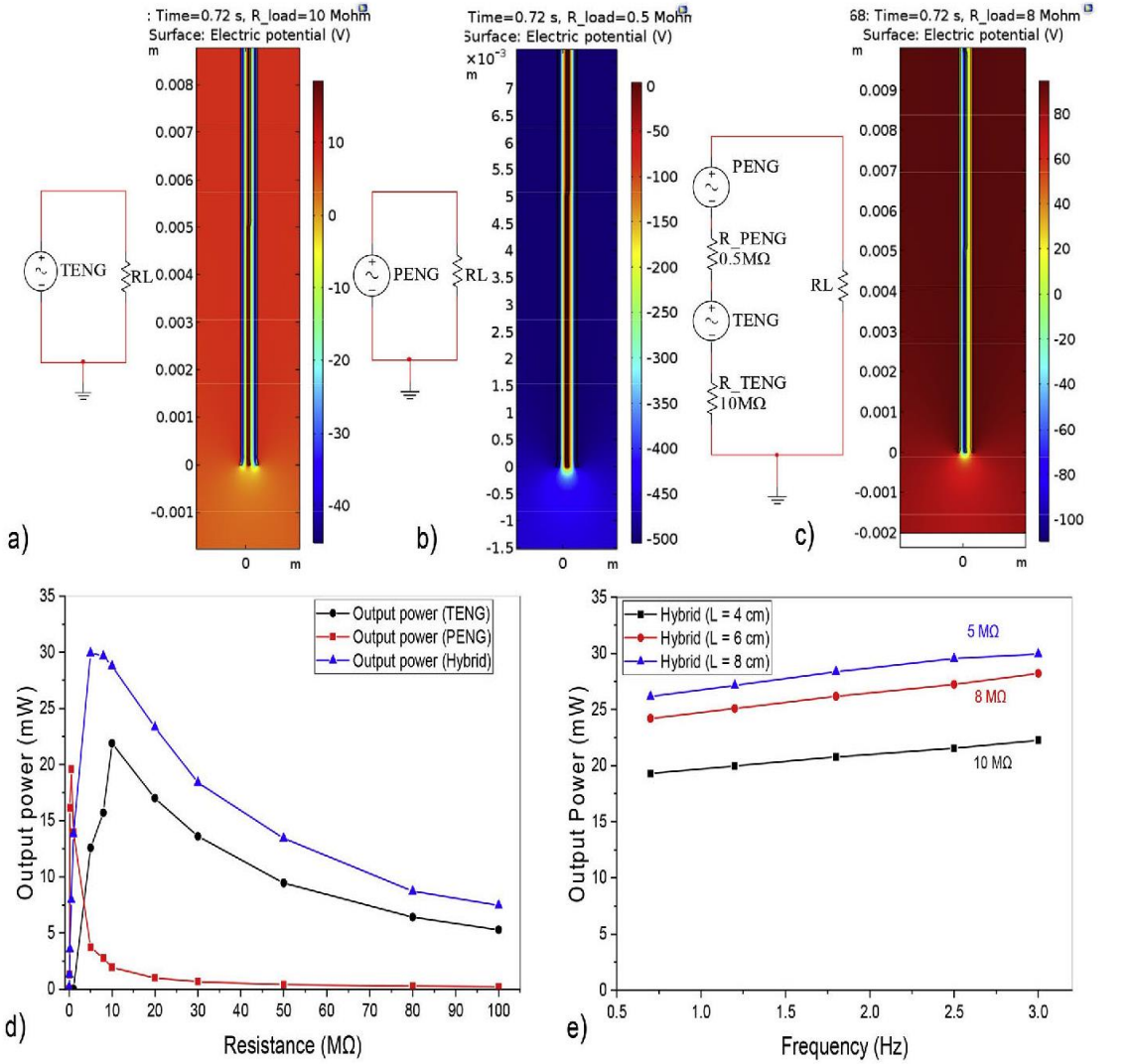

Fig. 3. Electric potential model and simulated electric circuit diagram of a) TENG, b) PENG, and c) simultaneous coupling of triboelectric-piezoelectric effects (hybrid nano generator). d) Simulation of the influence of the load resistance in the output power of TENG, PENG and Hybrid prototype. e) Output power of the simulated hybrid devices with different lengths (3 cm, 6 cm and 8 cm) under different frequencies (0.7 Hz–3 Hz) that highlights the optimum load resistance for every structure.

frequencies of 0.7 Hz–3 Hz [13,14]. A practical load resistance matching analysis (varying between 100 Ω and 100 MΩ) to reach a maximum output power performance with the hybrid nanogenerators was performed.

Consequently, the ability to charge a variety of capacitors (between 2.2 and 100 μF) for a period of 80 s with a single hybrid device, piezoelectric device, triboelectric devices and a grid of four hybrid devices (connected in parallel in order to increase their output performance) was tested. Furthermore, a durability test was performed to the hybrid devices under water wave impact during different periods between 30 min and 180 min and number cycles of operation (see Supplementary Information document). Moreover, the potential of the grid of hybrid devices to charge and discharge capacitors was tested for a longer period. The output power generated of the energy harvesters was derived using the rectified output current and rectified output voltage measurements performed using an Agilent Technologies N6705B power analyser. The transferred charges was measured with an electrometer Keithley 6514 (See Supplementary Information document), and the charging performance of the hybrid devices was measured with a digital oscilloscope Tektronix TDS 2014C, respectively (10 measurements performed on each sample).

5. Experimental results and discussion

The rectified output current, voltage and charge transferred of the hybrid, TENG and PENG prototypes increases linearly, as the frequency (0.7 Hz–3 Hz) and amplitude (10 cm–12 cm) of breaking wave impact rises (Fig. 5 a-l). The maximum output current, voltage and transferred charges generated for the hybrid nanogenerator increases from ~35.7 μA to ~140.93 μA, ~68.23 V–~229.31 V, and ~102.12 nC–~399.29 nC (Fig. 5 a-c), respectively. Thus, the maximum output power performance increases from ~6.79 mW to 16.94 mW. The power performance of the hybrid prototypes shows an enhancement by a factor of 2.24, 4.80 and 3.21 compared with the arc-shaped TENG, DMCS-TENG and the piezoelectric nanogenerator (Fig. 6 a). Such output current, voltage and charge transferred increases linearly from ~6.28 μA to ~76.52 μA, ~34.02 V–~107.89 V, and ~17.73 nC–~292.90 nC (Fig. 5 d-l). Accordingly, the maximum output power performance of those energy harvesters were between ~0.87 mW and ~11.42 mW (Fig. 6 a), tested in similar conditions of the mechanical energy generated by water wave

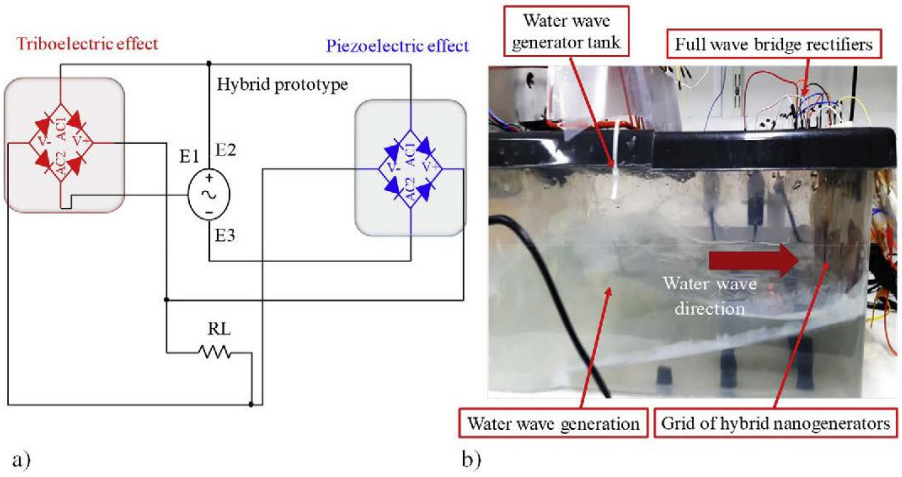

Fig. 4. a) Circuit diagram of the hybrid nanogenerators for the load matching and capacitor charging experiments. b) Grid of hybrid nanogenerators placed in the water wave generator tank for its output performance measurements.

impacts, and connected to a 1 MΩ load resistance, respectively. Furthermore, the enhancement was verified with the charging performance of the energy harvesters charging a capacitor of 2.2 μF for 80 s, where the hybrid nanogenerators reached a maximum voltage of 5.4 V as shown in Fig. 6 b.

Furthermore, the maximum average output power and power density of ~15.92 mW and ~0.99 mW/cm^2, respectively was generated with a load resistance of 8 MΩ through the load resistance matching practical experiment (Fig. 6 c). This is compared with the maximum generated output power of ~19.76 mW with a load resistance of 10 MΩ reached through the simulated model of the hybrid prototypes (L = 4 cm) (see Supplementary Information document). Such output performance difference results from assuming the maximum surface charge density between the triboelectric materials in contact, and piezoelectric polarization under ideal conditions.

Additionally, the maximum voltage reached by the grid of hybrid devices was 12.87 V, compared with a single unit that reached a maximum value of 5.4 V charging a capacitor of 2.2 μF for 80 s as depicted in Fig. 7 a, and Fig. 7 b. The grid of hybrid devices connected in parallel with a total active area of 256 cm^2 resulted in an enhancement factor of 2.43 in the output power (Fig. 7 f) and output performance enhancement in charging different capacitors compared with a single hybrid nanogenerator. Such a grid of four energy harvesters generated a maximum average instantaneous output current, voltage and charge transferred, which rises steadily under the different frequencies (0.7 Hz–3 Hz) from ~89.05 μA to ~314.13 μA, ~185 V–~631 V, and ~346.38 nC–~1095.62 nC (Fig. 7 c-e), respectively. As a result, the maximum generated output power and power density were between ~10.70 mW and ~46.58 mW, and ~0.042 mW/m^2 to ~ 0.18 mW/m^2 with a load resistance of 8 MΩ, respectively as depicted in Fig. 7 f. Furthermore, to calculate the average energy conversion efficiency (ECE) η of the grid of hybrid device system, defined as the ratio between the electric energy ($E_{electric}$) delivered to the load resistor of 8 MΩ and the mechanical energy ($E_{waterwave}$) applied by the water wave impact over a period (t) of 30 s with the different frequencies. The $E_{electric}$ released by the grid of hybrid nanogenerators was calculated by Eq. (6):

$$E_{electric} = \int_{t1}^{t2} RI^2 dt = 16.10\ J \quad (6)$$

where I is the average instantaneous current and R is the load resistance. The total average energy (potential energy and kinetic energy) produced by the water wave generator tank was calculated as Eq. (7)[32]:

$$E_{waterwave} = \frac{1}{2}\rho g A^2 = 59.36\ J \quad (7)$$

where g is the acceleration of gravity ($g = 9.8$ m/s^2), ρ is the density of water ($\rho = 1000$ kg/m^3), and A is the wave amplitude (between ~10 cm and ~12 cm, frequencies = 0.7 Hz–3 Hz). Consequently, the overall η of the grid of hybrid devices was 27.12% calculated by Eq. (8) [33]:

$$\eta = \frac{E_{electric}}{E_{waterwave}} x100\% = 27.12\% \quad (8)$$

Moreover, due to the improvement of the water wave impact energy harvesting, and good performance storing energy in different capacitors using the grid of hybrid nanogenerators, an application was demonstrated.

The grid of hybrid nanogenerators was used to power a one way wireless 433 MHz transmitter (Seed 113990010) and sent a signal to the receiver to turn on 4 Kingbright L-7104PWC-A 3 mm white LEDs (1200 mcd), with a transmission distance from 2 m to 8 m as shown in Fig. 8 a and Fig. 8 b. This was achieved after charging a capacitor of 47 μF between 312 s and 857 s, the voltage reached was within 2.95 V–8.51 V and the switch was open to power up the transmitter as depicted in Fig. 8 c. Furthermore, as the transmission distance increases, more energy was required with a longer charging time required for the capacitor. The energy stored in the capacitor for the grid of hybrid devices, and the power generated for the capacitor during the discharging process for powering the wireless transmitter were between 204.51 μJ and 1.54 mJ, and 340.85 μW to 2.57 mW, respectively (Fig. 8 d). Besides, it was demonstrated that the grid of hybrid energy harvesters show the capacity to drive small electronic devices by the achieved output power levels (see Supplementary Video S1).

Finally, we consider the scale up the capability of a grid of these hybrid energy harvesters by constructing large water-hybrid nanogenerators-structure interfaces (Fig. 9) with an area of 18 m^2 that receives wave sizes among 0.3 m–4 m [34]. If the interface is integrated with 11,250 hybrid devices connected in parallel, it is estimated to generate an average output power, and energy of ~21.61 W, and ~23.70 kJ. Considering a water wave impact over the proposed interface with a maximum amplitude of 4 m, it is calculated to generate a total energy of 78.4 kJ using (7). Using (8), it is calculated that the large-scale hybrid nanogenerators could have an energy conversion efficiency of 30.22%, harvesting the impact energy of water waves in large scale.

As a result, with the enhancement of the water wave impact energy harvesting performance, the grid of hybrid nanogenerators is suitable

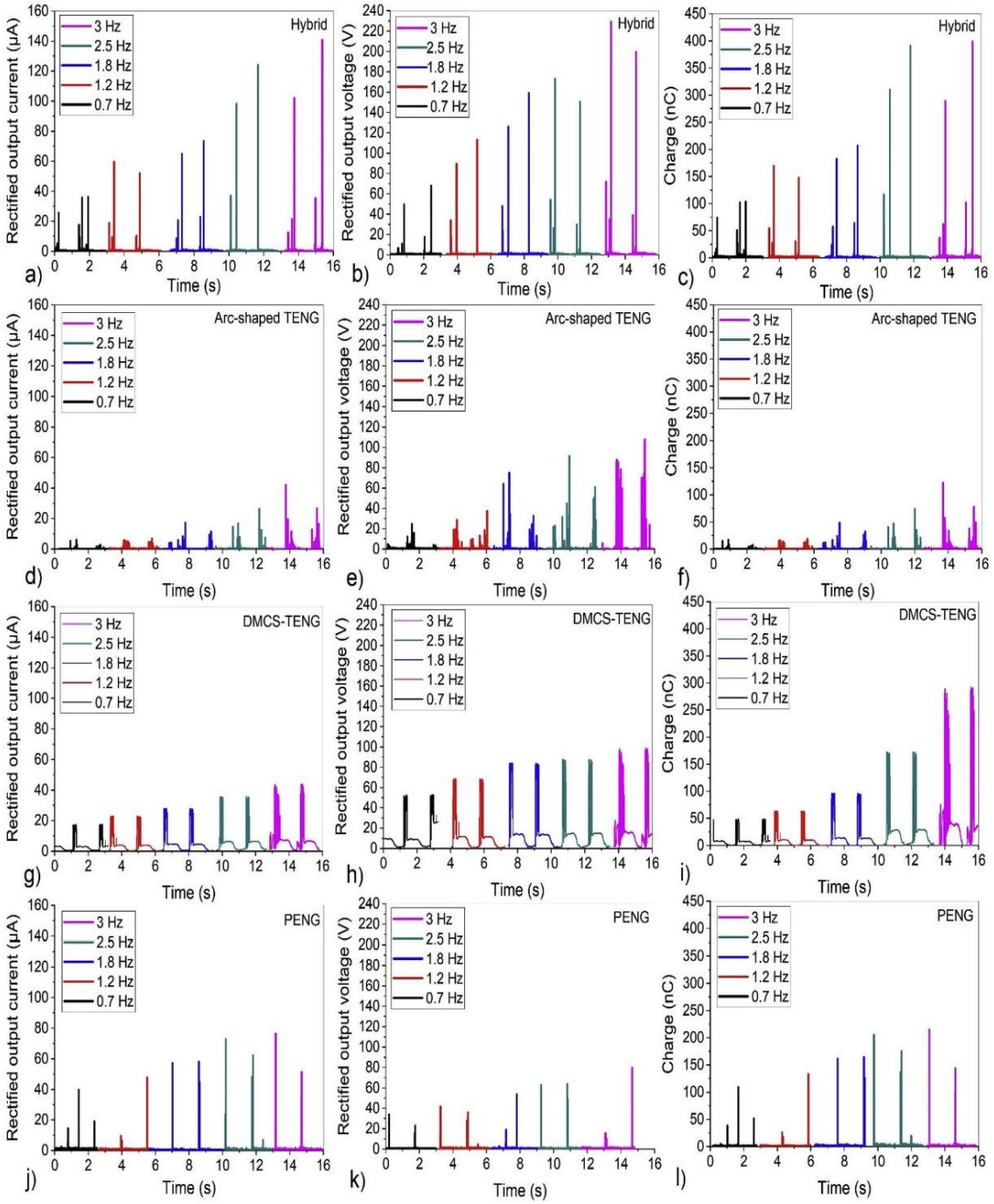

Fig. 5. a) Average rectified instantaneous output current, b) output voltage, and c) transferred charges of hybrid nanogenerator. In comparison with (d–f) arc-shaped TENG, (g–i) DMCS-TENG, and (j–l) PENG average rectified instantaneous output current, output voltage, and transferred charges connected to a 1 MΩ load resistor tested in a water wave impact generator tank under different frequencies of impact between 0.7 Hz and 3 Hz.

for powering a variety of battery-less systems as wireless nodes for coastal sensing applications.

6. Conclusion

In this study, the improvement in the output performance of prototype devices for ocean wave, impact force energy harvesting was achieved by simultaneously coupling triboelectric-piezoelectric effects, and also by the attribution of an electrical parallel connection of a grid of such devices. This was verified by measuring the output current, voltage, charge transferred, output power, and examining the ability to charge a selection of capacitors with a grid of four hybrid devices connected in parallel and tested under simulated wave conditions at low frequencies. As a result the output performance response of the hybrid devices increases linearly, as the frequency between 0.7 Hz and 3 Hz and amplitude between 10 cm and 12 cm of breaking wave impact rises. Moreover, the grid of hybrid nanogenerators has the potential to drive low-power electronic devices. This was demonstrated by using the

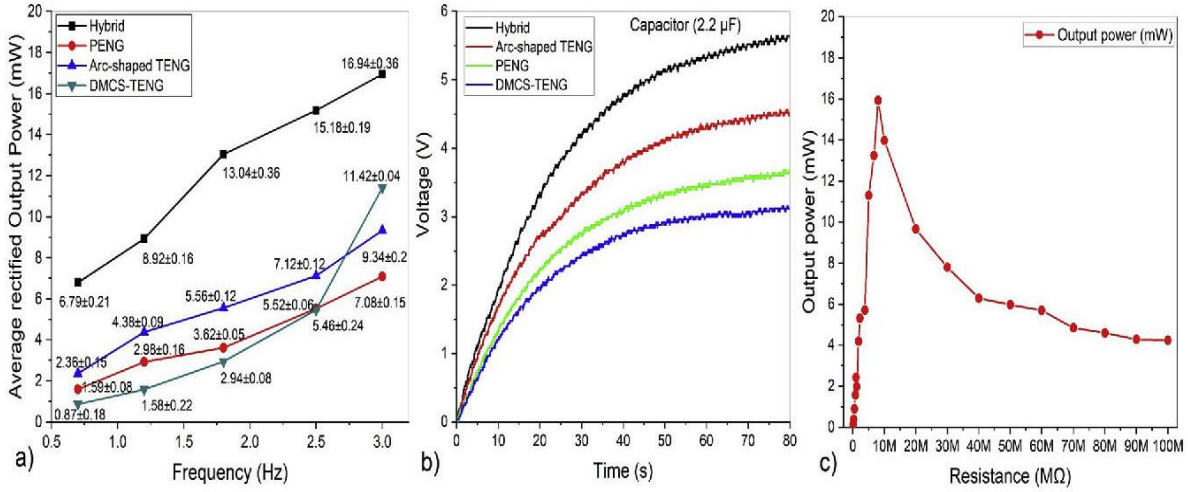

Fig. 6. a) Rectified average instantaneous output power and its standard deviation analysis calculated (10 measurements performed for each sample) of Hybrid device compared with TENG and PENG devices connected to a 1 MΩ resistor under water wave impact (0.7 Hz–3 Hz). b) Charging performance of a single hybrid device, arc-shaped TENG, PENG, and DMCS TENG connected to a 2.2 μF capacitor. c) Load resistance matching analysis to reach the highest output power performance of the 4 hybrid devices tested in the water generator tank.

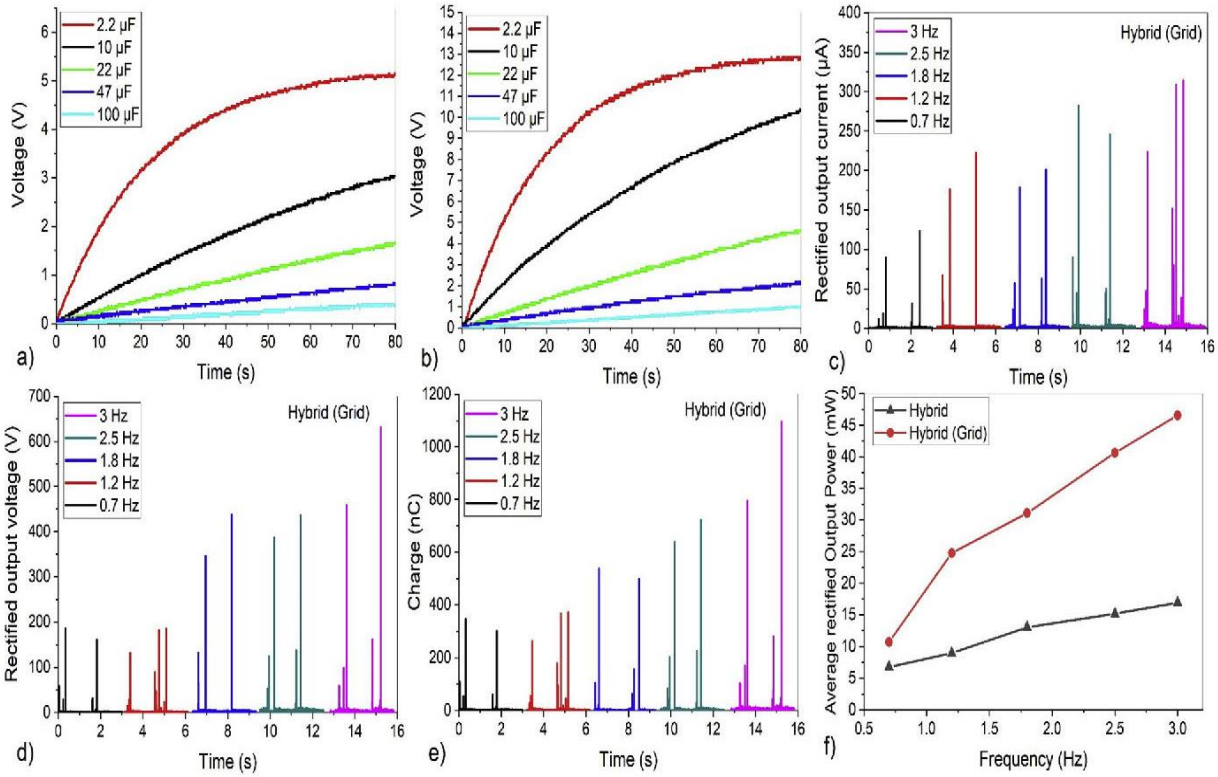

Fig. 7. a) Charging performance of a single hybrid device, and b) a grid of 4 hybrid devices connected in parallel to different capacitors (2.2 μF–100 μF). c) Rectified instantaneous output current, d) output voltage, e) transferred charges, and f) output power of a grid of hybrid devices compared with a single hybrid device unit connected to a 1 MΩ load resistor.

stored energy in a capacitor charged over different periods of time. The devices were capable of powering a wireless transmitter and sending a signal to a receiver at varying distances. Finally, the high output power obtained, shows that the integrated grid of devices offers a promising innovative approach for the production of high-performance energy harvesting mechanisms focused on harvesting water wave impact energy. These are capable of energizing self-powered marine sensing systems for environmental monitoring requiring an average power consumption in the range from 1 mW to 100 mW [36,37]. Further, it is estimated that with the construction of large water-hybrid nanogenerator-structure interfaces for the generation of electricity on a larger scale, harvesting the impact of the water waves for powering networks of self-powered sensing systems for smart fish farms having an average power consumption from 100 W to 1 kW [38]. This research work provides a promising alternative approach to harvest breaking water wave impact energy that contributes to the previous blue energy

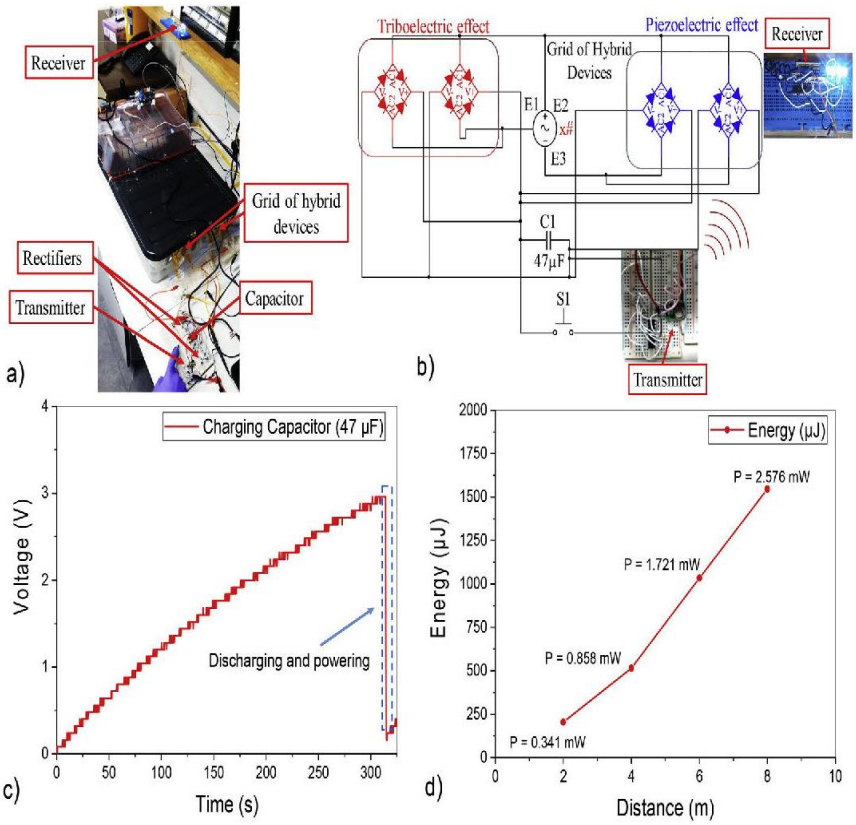

Fig. 8. a) Set-up for powering the wireless transmitter with the grid of hybrid nanogenerators under the water wave impact. b) Electrical circuit diagram of the hybrid nanogenerators to charge the 47 μF capacitor for powering the wireless transmitter. c) Capacitor charging and discharging process for powering the wireless transmitter under the water wave impact with a frequency of 1.2 Hz. d) Energy stored in the 47 μF capacitor for the grid of hybrid devices, and the power generated for the capacitor during the discharging process for powering the wireless transmitter to send a signal to a receiver with a transmission distance from 2 m to 8 m.

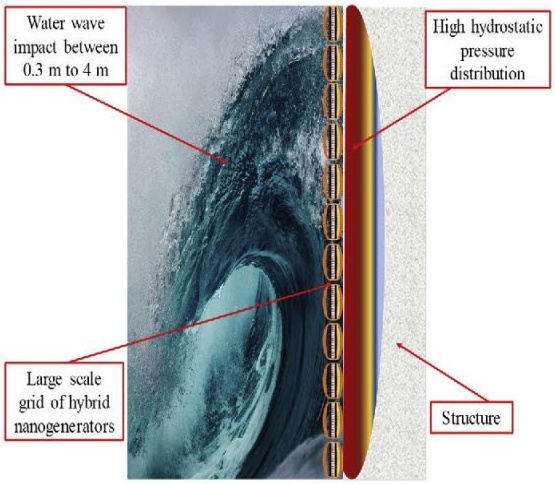

Fig. 9. Two-dimensional schematic illustration of the configuration of the proposed large water-hybrid nanogenerators-structure interfaces to escalate the energy harvesting of water wave impact (Ocean water wave adapted from Refs. [35]).

harvesting studies, which are focused on harvesting shallow water wave energy [2–10].

Declaration of competing interest

The authors declare that they have no known competing financial interests or personal relationships that could have appeared to influence the work reported in this paper.

CRediT authorship contribution statement

Ulises Tronco Jurado: Conceptualization, Methodology, Software, Investigation, Validation, Data curation, Formal analysis, Writing - original draft, Writing - review & editing, Visualization, Project administration. **Suan Hui Pu:** Resources, Conceptualization, Writing - review & editing, Supervision. **Neil M. White:** Resources, Conceptualization, Writing - review & editing, Supervision.

Acknowledgements

The authors thank CONACYT for the fellowship awarded to Ulises Tronco Jurado.

Appendix A. Supplementary data

Supplementary data to this article can be found online at https://doi.org/10.1016/j.nanoen.2020.104701.

References

[1] N. Elvin, A. Erturk, Advances in Energy Harvesting Methods, Springer, New York Heidelberg Dordrecht London, 2013.
[2] T.X. Xiao, X. Liang, T. Jiang, L. Xu, J.J. Shao, J.H. Nie, et al., Spherical triboelectric nanogenerators based on spring-assisted multilayered structure for efficient water wave energy harvesting, Adv. Funct. Mater. 28 (2018) 1802634.
[3] X. Li, J. Tao, X. Wang, J. Zhu, C. Pan, Z.L. Wang, Networks of high performance triboelectric nanogenerators based on liquid–solid interface contact electrification for harvesting low-frequency blue energy, Adv. Energy Mater. 8 (2018) 1800705.
[4] X. Zhang, M. Yu, Z. Ma, H. Ouyang, Y. Zou, S.L. Zhang, et al., Self-powered distributed water level sensors based on liquid–solid triboelectric nanogenerators for ship draft detecting, Adv. Funct. Mater. 29 (2019) 1900327.
[5] M. Xu, T. Zhao, C. Wang, S.L. Zhang, Z. Li, X. Pan, et al., High power density tower-like triboelectric nanogenerator for harvesting arbitrary directional water wave energy, ACS Nano 13 (2019) 1932–1939.

Appendix A

[6] S.L. Zhang, M. Xu, C. Zhang, Y.-C. Wang, H. Zou, X. He, et al., Rationally designed sea snake structure based triboelectric nanogenerators for effectively and efficiently harvesting ocean wave energy with minimized water screening effect, Nano Energy 48 (2018) 421–429.
[7] F. Xi, Y. Pang, G. Liu, S. Wang, W. Li, C. Zhang, et al., Self-powered intelligent buoy system by water wave energy for sustainable and autonomous wireless sensing and data transmission, Nano Energy 61 (2019) 1–9.
[8] X. Yang, L. Xu, P. Lin, W. Zhong, Y. Bai, J. Luo, et al., Macroscopic self-assembly network of encapsulated high-performance triboelectric nanogenerators for water wave energy harvesting, Nano Energy 60 (2019) 404–412.
[9] Y. Wu, Q. Zeng, Q. Tang, W. Liu, G. Liu, Y. Zhang, et al., A teeterboard-like hybrid nanogenerator for efficient harvesting of low-frequency ocean wave energy, Nano Energy 67 (2020) 104205.
[10] L. Feng, G. Liu, H. Guo, Q. Tang, X. Pu, J. Chen, et al., Hybridized nanogenerator based on honeycomb-like three electrodes for efficient ocean wave energy harvesting, Nano Energy 47 (2018) 217–223.
[11] R.B. Mayon, Investigation of Wave Impacts on Porous Structures for Coastal Defences, University of Southampton, 2017.
[12] U.T. Jurado, S.H. Pu, N.M. White, A contact-separation mode triboelectric nanogenerator for ocean wave impact energy harvesting, in: 2017 IEEE SENSORS, 2017, pp. 1–3.
[13] U.T. Jurado, S.H. Pu, N.M. White, Dielectric-metal triboelectric nanogenerators for ocean wave impact self-powered applications, IEEE Sensors Journal 19 (2019) 6778–6785, https://doi.org/10.1109/JSEN.2019.2912070.
[14] U.T. Jurado, S.H. Pu, N.M. White, Water-dielectric single electrode mode triboelectric nanogenerators for ocean wave impact energy harvesting, in: Multidisciplinary Digital Publishing Institute Proceedings, 2018, p. 714.
[15] U. Khan, S.-W. Kim, Triboelectric nanogenerators for blue energy harvesting, ACS Nano 10 (2016) 6429–6432.
[16] C. Chang, V.H. Tran, J. Wang, Y.-K. Fuh, L. Lin, Direct-write piezoelectric polymeric nanogenerator with high energy conversion efficiency, Nano Lett. 10 (2010) 726–731.
[17] P. Ueberschlag, PVDF piezoelectric polymer, Sens. Rev. 21 (2001) 118–126.
[18] J. Lowell, A. Rose-Innes, Contact electrification, Adv. Phys. 29 (1980) 947–1023.
[19] A. Diaz, R. Felix-Navarro, A semi-quantitative tribo-electric series for polymeric materials: the influence of chemical structure and properties, J. Electrost. 62 (2004) 277–290.
[20] Y. Yu, X. Wang, Chemical modification of polymer surfaces for advanced triboelectric nanogenerator development, Extreme Mech. Lett. 9 (2016) 514–530.
[21] P. Bai, G. Zhu, Y.S. Zhou, S. Wang, J. Ma, G. Zhang, et al., Dipole-moment-induced effect on contact electrification for triboelectric nanogenerators, Nano Res. 7 (2014) 990–997.
[22] Q. Nguyen, B.H. Kim, J.W. Kwon, Based ZnO nanogenerator using contact electrification and piezoelectric effects, J. Microelectromech. Syst. 24 (2015) 519–521.
[23] M. Han, X. Zhang, W. Liu, X. Sun, X. Peng, H. Zhang, Low-frequency wide-band hybrid energy harvester based on piezoelectric and triboelectric mechanism, Sci. China Technol. Sci. 56 (2013) 1835–1841.
[24] Z.L. Wang, T. Jiang, L. Xu, Toward the blue energy dream by triboelectric nanogenerator networks, Nano Energy 39 (2017) 9–23.
[25] L. Xu, T. Jiang, P. Lin, J.J. Shao, C. He, W. Zhong, et al., Coupled triboelectric nanogenerator networks for efficient water wave energy harvesting, ACS Nano 12 (2018) 1849–1858.
[26] J. Chen, J. Yang, Z. Li, X. Fan, Y. Zi, Q. Jing, et al., Networks of triboelectric nanogenerators for harvesting water wave energy: a potential approach toward blue energy, ACS Nano 9 (2015) 3324–3331.
[27] S. Park, Y. Kim, H. Jung, J.-Y. Park, N. Lee, Y. Seo, Energy harvesting efficiency of piezoelectric polymer film with graphene and metal electrodes, Sci. Rep. 7 (2017) 17290.
[28] Z.L. Wang, L. Lin, J. Chen, S. Niu, Y. Zi, Theoretical modeling of triboelectric nanogenerators, in: Triboelectric Nanogenerators, Springer, 2016, pp. 155–183.
[29] S. Niu, S. Wang, L. Lin, Y. Liu, Y.S. Zhou, Y. Hu, et al., Theoretical study of contact-mode triboelectric nanogenerators as an effective power source, Energy Environ. Sci. 6 (2013) 3576–3583.
[30] F. Lu, H. Lee, S. Lim, Modeling and analysis of micro piezoelectric power generators for micro-electromechanical-systems applications, Smart Mater. Struct. 13 (2003) 57.
[31] S. Wang, Y. Xie, S. Niu, L. Lin, C. Liu, Y.S. Zhou, et al., Maximum surface charge density for triboelectric nanogenerators achieved by ionized-air injection: methodology and theoretical understanding, Adv. Mater. 26 (2014) 6720–6728.
[32] A. Khaligh, O.C. Onar, Energy Harvesting: Solar, Wind, and Ocean Energy Conversion Systems, CRC press, 2009.
[33] W. Tang, T. Jiang, F.R. Fan, A.F. Yu, C. Zhang, X. Cao, et al., Liquid-metal electrode for high-performance triboelectric nanogenerator at an instantaneous energy conversion efficiency of 70.6%, Adv. Funct. Mater. 25 (2015) 3718–3725.
[34] Oceanweathercom, Current Marine Data, Oceanweather Inc, 2018, 2018, http://www.oceanweather.com/data/index.html. (Accessed 30 October 2018).
[35] E. Arano, Ocean Water Wave Photo, 2016. https://www.pexels.com/photo/ocean-water-wave-photo-1295138/.
[36] D. Steingart, Power sources for wireless sensor networks, in: Energy Harvesting Technologies, Springer, 2009, pp. 267–286.
[37] Z.L. Wang, W. Wu, Nanotechnology-enabled energy harvesting for self-powered micro-/nanosystems, Angew. Chem. Int. Ed. 51 (2012) 11700–11721.
[38] M.M. Damien Toner, The Potential for Renewable Energy Usage in Aquaculture, 2002. http://www.aquacultureinitiative.eu.

Ulises Tronco Jurado received the M.Sc. degree in materials science from University of Guadalajara, Mexico, in 2015. He was a MEMS lab researcher at University of Texas at San Antonio, U.S., in 2014, working on modeling, synthesis, fabrication and characterization of quantum dots applied to c-silicon solar cells.

He is currently pursuing the PhD. Degree in Engineering and the Environment with the Mechatronics Research Group, and the Smart Electronic Materials and Systems Research Group, School of Electronics and Computer Science, University of Southampton, U.K. His current research interest include triboelectric nanogenerators for ocean wave monitoring applications that required self-powering.

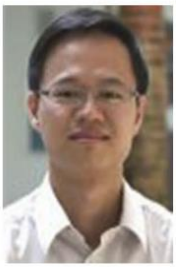

Suan Hui Pu received Ph.D. degree in electrical and electronic engineering from Imperial College London, U.K. in 2010. He is currently an Associate Professor at University of Southampton at Johor, Malaysia.

He is a visiting academic in the Schools of Engineering, and Electronics and Computer Science, at the University of Southampton, U.K. His current research interests include NEMS/MEMS sensors and actuators, graphene/graphite sensors and printed electronics.

He has served as a reviewer for IEEE Journal of Microelectromechanical Systems, IEEE Electron Device Letters, IEEE Transactions on Components, Packaging and Manufacturing Technology, IOP Nanotechnology, IOP Journal of Micromechanics and Microengineering, amongst others.

Neil M. White obtained a PhD from the University of Southampton in 1988. Neil was promoted to Senior Lecturer in 1999. His research interests include thick-film sensors, intelligent instrumentation, MEMS, self-powered microsensors and sensor networks. He is a Chartered Engineer, Senior Member of the IEEE, and a Chartered Physicist. He is a member of the Peer Review College for the EPSRC and is on the Editorial Board of the international journals Sensor Review and Journal of Materials Science: Materials in Electronics. Professor White is also a Series Editor for the Integrated Microsystems series for Artech House.

Nano Energy 78 (2020) 105204

Contents lists available at ScienceDirect

Nano Energy

journal homepage: http://www.elsevier.com/locate/nanoen

Wave impact energy harvesting through water-dielectric triboelectrification with single-electrode triboelectric nanogenerators for battery-less systems

Ulises Tronco Jurado [a,b,*], Suan Hui Pu [a,c], Neil M. White [b]

[a] Mechatronics Research Group, University of Southampton, Southampton, SO17 1BJ, UK
[b] Smart Electronic Materials and Systems Research Group, University of Southampton, Southampton, SO17 1BJ, UK
[c] University of Southampton Malaysia, Iskandar Puteri, 79200, Johor, Malaysia

ARTICLE INFO

Keywords:
Water-dielectric
Breaking wave impact
Triboelectrification
Liquid environments
Battery-less

ABSTRACT

This paper evaluates the effect of water-dielectric interfaces for wave impact energy harvesting at low frequencies (0.7 Hz–3 Hz) on the output performance of Water-Dielectric Single Electrode Mode Triboelectric Nanogenerators (WDSE-TENG). The triboelectric effect is generated between water (with a net positive charge) and a hydrophobic dielectric layer (with a net negative charge). Different WDSE-TENG configurations were tested using distinct hydrophobic materials. The water-fluorinated ethylene propylene (FEP) combination resulted in the best output performance. On the contrary, an output performance reduction by a factor of 3.53 was measured with seawater-dielectric interfaces. This can be compensated by increasing the contact area, with the best performance obtained using silicone rubber compound (Acetoxy, Elastomer) utilizing a WDSE-TENG with two-dielectric layer configuration. Employing seawater as a triboelectric material, the highest electrical output power and power density of 79.18 mW and 0.344 mW/cm^2 was generated with a grid of WDSE-TENG, comprising five devices connected in parallel. The output voltage, current, transferred charge, stored energy and energy conversion efficiency (ECE) values of the grid of connected WDSE-TENG devices were compared against a single device. Such energy harvesters were able to power an ultrasonic range sensor and a one-way wireless transmitter for motion detection, distance measurement, and monitoring weather conditions. The stored energy and generated power were −5.96 mJ and −5.18 mW, respectively. Furthermore, the integration of the grid of WDSE-TENG with a power management control circuit (PMCC) is able to increase the output power and hence offer the potential to power up electronic devices with power consumption requirements between 1 mW and 100 mW. The results demonstrate that the grid of WDSE-TENG offers an innovative energy harvesting approach using water as a triboelectric material. The device can be used as an energy source for smart battery-less wireless sensing systems at water-structure interfaces in aquaculture (e.g. for fish detection or water level measurement) and weather condition monitoring.

1. Introduction

The harvesting of renewable hydropower sources, generated from water motion, has attracted great interest for many years [1,2]. In particular, previous work has focused on collecting the energy generated by the random motion of shallow ocean waves at low frequencies ranging from 0.5 Hz to 10 Hz, using hybrid devices combined with triboelectric nanogenerators (TENG)-electromagnetic generators (EMG) [3,4], and different TENG with solid-solid material interfaces in contact under dry conditions [5–11], and water-solid interfaces [12–21]. Besides, harvesting breaking wave impact energy [22] have been reported previously through the use of dielectric-metal contact-separation mode triboelectric nanogenerators (DMCS-TENG) [23–25] with solid materials in contact over a wide frequency range between 0.7 Hz and 252 Hz. Water-dielectric single electrode mode triboelectric nanogenerator (WDSE-TENG) operating under breaking wave contact at 1.2 Hz has also been demonstrated [26]. Consequently, as triboelectricity exists when liquids are flowing or in contact with solid insulated materials [17,27–35], which creates an electric double layer (EDL) in two steps called the Wang model [30,33]. Electron exchange between

* Corresponding author. Mechatronics Research Group, University of Southampton, Southampton, SO17 1BJ, UK.
E-mail addresses: utj1n15@soton.ac.uk (U.T. Jurado), SuanHui.Pu@soton.ac.uk (S.H. Pu), nmw@ecs.soton.ac.uk (N.M. White).

https://doi.org/10.1016/j.nanoen.2020.105204
Received 2 June 2020; Received in revised form 16 July 2020; Accepted 17 July 2020
Available online 14 August 2020

Appendix A

liquid-solid interface due to contact electrification as the first step that makes the atoms on the solid surface to be ions. The interaction between the solid-liquid interface ions as the second step, resulting in a gradient distribution of cations and anions near the interface [30,33]. Practically, electron exchange and ion adsorption occur simultaneously and coexist in the liquid-solid interaction [30,32]. Specifically, the contact electrification between hydrophobic surfaces and liquid solutions is more likely to be dominated by electron transfer and the contact electrification between hydrophilic surfaces and liquid solutions is likely dominated by ion transfer [31]. This research work is aimed at an extended experimental study, analysis and optimization to exploit the liquid-solid contact electrification for harvesting breaking wave impact energy, at low frequencies (0.7 Hz–3 Hz). Such energy can be potentially harvested, exploited and improved using a grid of water-dielectric single electrode mode triboelectric nanogenerators (WDSE-TENG). Such an energy harvester converts the external mechanical energy into electricity by a combination of the triboelectric effect and electrostatic induction, based on contact electrification between water and selected hydrophobic dielectric polymer layers due to their high negativity in the triboelectric series [36,37]. Such as polydimethylsiloxane (PDMS, with silicon-oxygen bonds), polytetrafluoroethylene (PTFE, with carbon-fluoride bonds), silicone rubber compound (acetoxy elastomer, with silicon-oxygen bonds), fluorinated ethylene propylene (FEP, with carbon-fluoride bonds) and Polyimide (Kapton, with two acyl groups (C═O), bonded to nitrogen).

First, in order to evaluate the use of water as a triboelectric material for TENG, single-electrode and split-electrode TENG prototypes were fabricated and characterized. The generated output voltage, output current, transferred charge and output power were measured to study the contact electrification between water and the aforementioned dielectric polymer films. Tap water, deionized (DI) water and sodium chloride (NaCl) solution with a concentration of 0.6 M, which is similar to that in seawater, were compared when in contact with the hydrophobic polymer films. This was achieved in a wave tank that generates breaking water wave impacts at frequencies and amplitudes between 0.7 Hz and 3 Hz and 10 cm–12 cm, respectively. The aim was to find the optimum dielectric material to reach the highest output power from the water wave impact. Second, a load resistance matching experiment was performed with the objective being to obtain maximum output power from the WDSE-TENG with a suitable selection of solid materials that gives the highest performance from the proposed prototypes. Third, the produced output performance and ability to charge a variety of capacitors with a single, and also a grid of five, WDSE-TENG prototypes in a multi-unit parallel connection [38–40] to increase the current output were characterized in seawater under breaking water wave impact at the aforementioned frequencies. An enhancement in the performance was achieved using a grid of energy harvesters. Finally, it was demonstrated that the grid of WDSE-TENG has the potential to drive small electronic devices, such as an ultrasonic range sensor for detecting objects during a short period (~1 s). Furthermore, we aim to solve the challenge that this system and many self-powered systems based on TENG have, in that they are not able to work continuously. A power management control circuit (PMCC) was used, which allows the output power performance of the grid of WDSE-TENG to meet the power consumption requirements from 1 mW to 100 mW [41,42] for electronic devices. This demonstrates an alternative and novel approach for energy harvesting of ocean wave impact for autonomous monitoring applications requiring self-powered systems in liquid environments. Potential use cases include systems at structure-water interfaces in aquaculture for fish detection, measurement of the water levels at smart fish farms at small and big scales harvesting breaking water wave energy in areas between ~145 cm^2 to ~18 m^2, and sensor systems that monitor erosion in coastal defence systems.

2. WDSE-TENG prototypes fabrication and electrical characterization measurements set-up

2.1. Fabrication

The fabricated WDSE-TENG prototypes have a triboelectric active area of 7 cm × 4 cm and three different configurations, as depicted in Fig. 1, using hydrophobic dielectric layers with high negativity in the triboelectric series [36]. For the first sample of a WDSE-TENG, a dielectric layer was bonded onto a copper electrode (thickness (t) = 100 μm) with conductive acrylic glue (Electrical resistance through glue = 0.003 Ω, and t = 25 μm). The other exposed side of the copper layer was insulated with black PTFE tape to protect it from the water to prevent a short circuit (Fig. 1 a). With this device configuration, the contact electrification occurs at the face of the dielectric layer in contact with water. A number of different dielectric layers were tested, namely PTFE (t = 100 μm), FEP (t = 25 μm), Silicone rubber compound (t = 150 μm), Kapton (t = 127 μm), and PDMS (t = 125 μm). For the second configuration, a Cu layer (t = 100 μm) was completely insulated within silicone rubber layers on both sides to protect it from the water (Fig. 1 b) and to increase the contact area to produce contact electrification on both faces of the device when water contacts it. Additionally, using the second configuration, a copper layer was insulated on one side with a layer of PDMS and the other side with a layer of PTFE using conductive acrylic adhesive to test the combination of two different materials in contact electrification with water at the same time. For the electrical characterization, the electrode of each sample was connected to an external load of 10 MΩ.

The third configuration comprised two copper layers (split electrode) with an active area of 2.5 cm × 3 cm per layer, and a separation distance of 3 mm, which were bonded with conductive acrylic adhesive on a dielectric layer of either PTFE (t = 100 μm) or PDMS (t = 125 μm). The other face of the device was insulated with a layer of silicone rubber to protect it from short-circuit in contact with water (Fig. 1 c). The contact electrification is produced on both faces of the device when it contacts the water and the two electrodes (E1 and E2) were connected to an external load of 10 MΩ for electrical characterization. The objective of implementing a split electrode design commonly called the freestanding mode [43] is to increase the overall charge transfer relative to a WDSE-TENG.

2.2. Electrical characterisation

The WDSE-TENG output voltage, output current, charge transfer and output power of the prototypes were characterized in a breaking water wave generator tank in order to replicate the conditions of the mechanical energy generated by ocean wave impact. A hybrid stepper motor (RS Pro 535-0502) attached with an acrylic panel of 20 cm × 20 cm (t = 3 mm) is used to generate the wave motion in the water tank at different frequencies. The water wave breaks with frequencies from 0.7 Hz to 3 Hz and amplitudes between 10 cm and 12 cm (See Fig. S1 in the supplementary information document). The WDSE-TENG devices were placed at the wall on the right side of the tank where the water wave breaks against the dielectric triboelectric layer, which generates interchange of triboelectric charges between both surfaces as shown in Fig. 2 a and Fig. 2 c. DI water, tap water and 0.6 M NaCl solution (artificial seawater) were used in contact with the WDSE-TENG devices. Therefore, a practical load resistance matching analysis with load resistances varying between 100 Ω and 100 MΩ connected to the energy harvester prototype was performed to obtain the maximum output power as depicted in Fig. 2 b.

Additionally, the rectified output performance and the ability to charge a variety of capacitors varying from 4.7 μF to 470 μF for 85 s with a single device (Fig. 2 a), and a grid of five WDSE-TENG devices connected in parallel were tested as illustrated in Figs. 2 c and Fig. 10 a. Every WDSE-TENG device was connected to a full wave bridge rectifier

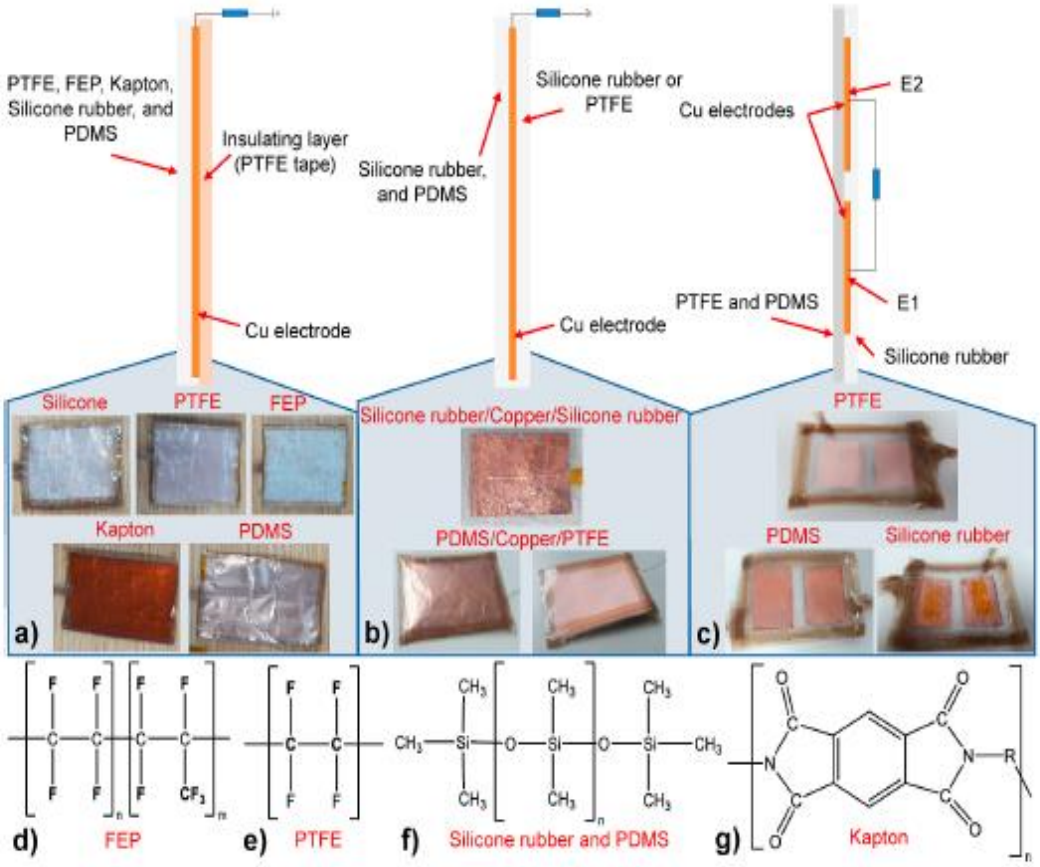

Fig. 1. Two-dimensional schematic and digital images of the three configurations of fabricated WDSE-TENG prototypes a) WDSE-TENG with one dielectric layer, b) full device covered with two dielectric layers and c) split electrode-two dielectric layers. Molecular structure of d) FEP, e) PTFE, f) Silicone rubber (Acetoxy, elastomer) and PDMS and g) Kapton.

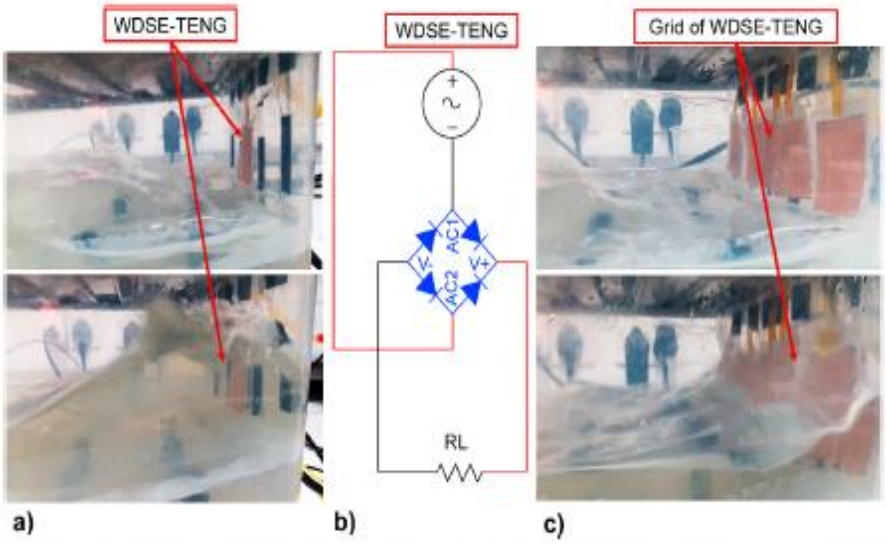

Fig. 2. a) Digital image of the single WDSE-TENG attached and under breaking water wave impact in the water wave impact generator tank. b) Circuit diagram of the WDSE-TENG for the load matching and charging of different capacitors. c) Digital image of the grid of five WDSE-TENG devices attached and under breaking water wave impact in the water wave impact generator tank.

(using BAS 40 diodes) for the electrical characterization of the grid of such devices. Furthermore, a durability test was performed to the WDSE-TENG energy harvester under breaking water wave impact through different periods from 30 min to 210 min and number of cycles of operation. Moreover, the grid of energy harvesters was used to drive electronic devices including an HC-SR04 ultrasonic ranger by storing

Appendix A

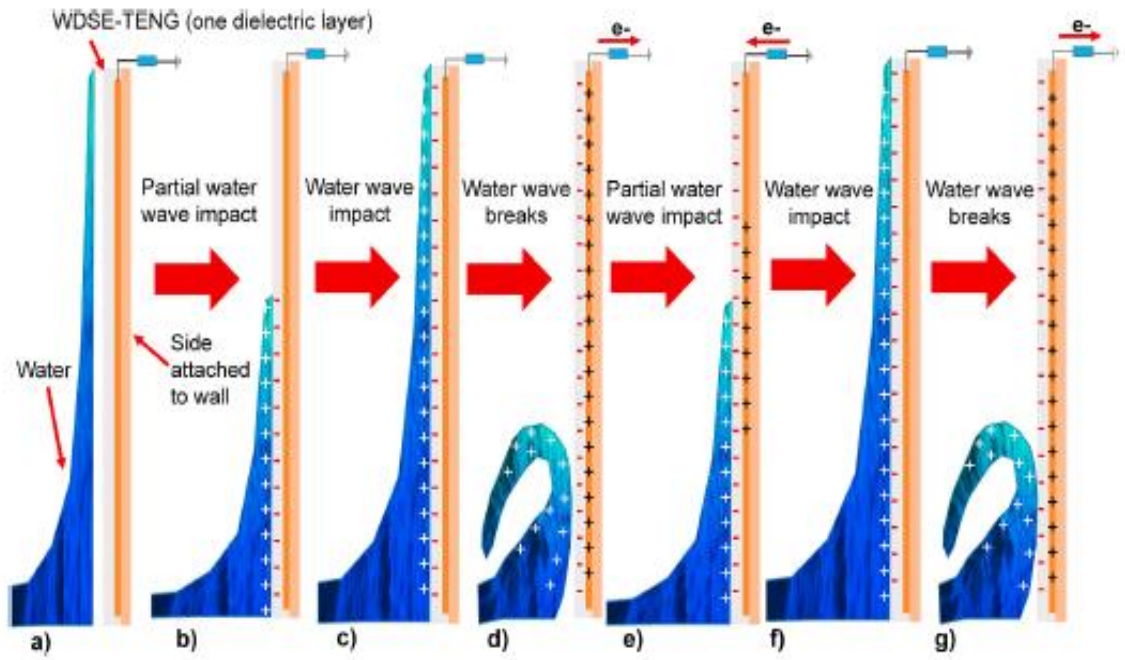

Fig. 3. a–g. Working mechanism of the WDSE-TENG with one-dielectric layer by the contact electrification of dielectric layers with breaking water wave impact.

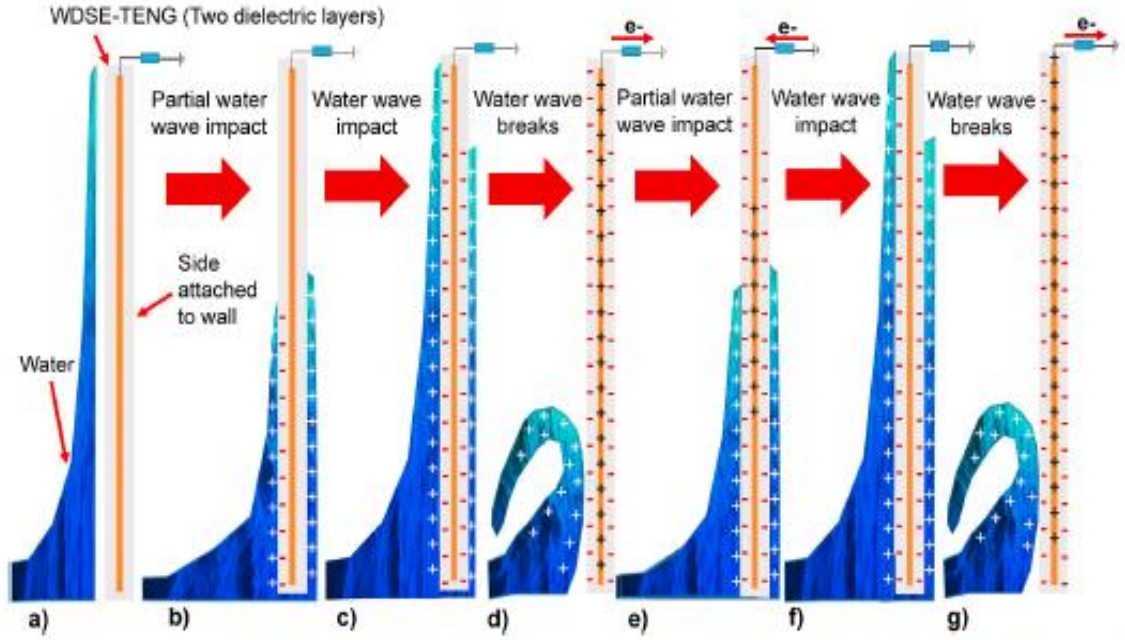

Fig. 4. a–g. Working mechanism of the WDSE-TENG with two-dielectric layers by the contact electrification of dielectric layers with breaking water wave impact.

and discharging electrical energy using capacitors. Finally, a PMCC unit was developed using the grid of WDSE-TENG as a source and this improved its energy extraction to have a direct wave impact-to-electrical conversion.

All the WDSE-TENG prototypes and connection wires were insulated to avoid short circuit conditions when the devices are in contact with water. The output voltage and current measurements of the WDSE-TENG energy harvesters were performed using an Agilent Technologies N6705B Power analyzer (10 measurements performed for each sample). The output power was calculated from these measurements. Furthermore, the transferred charges were calculated by integrating the output current peaks generated during the impact of the water waves over the devices, and the charge of different capacitors (4.7 μF–470 μF) by the energy harvesters were obtained with a Tektronix TDS 2014C digital oscilloscope (10 measurements performed for each sample).

3. WDSE-TENG working mechanism through water-dielectric interfaces for electricity generation

Fig. 3 a-g and Fig. 4 a-g illustrates the working mechanism of the WDSE-TENG with one-dielectric layer and two-dielectric layers configuration due to contact electrification and ion interaction between the breaking water wave and the hydrophobic dielectric layers. Before the dielectric layers make contact with water (Fig. 3 a and Fig. 4 a), no charge transfer and ion adsorption occur. When the water wave starts to make partially contact against the dielectric layers (Fig. 3 b and Fig. 4 b),

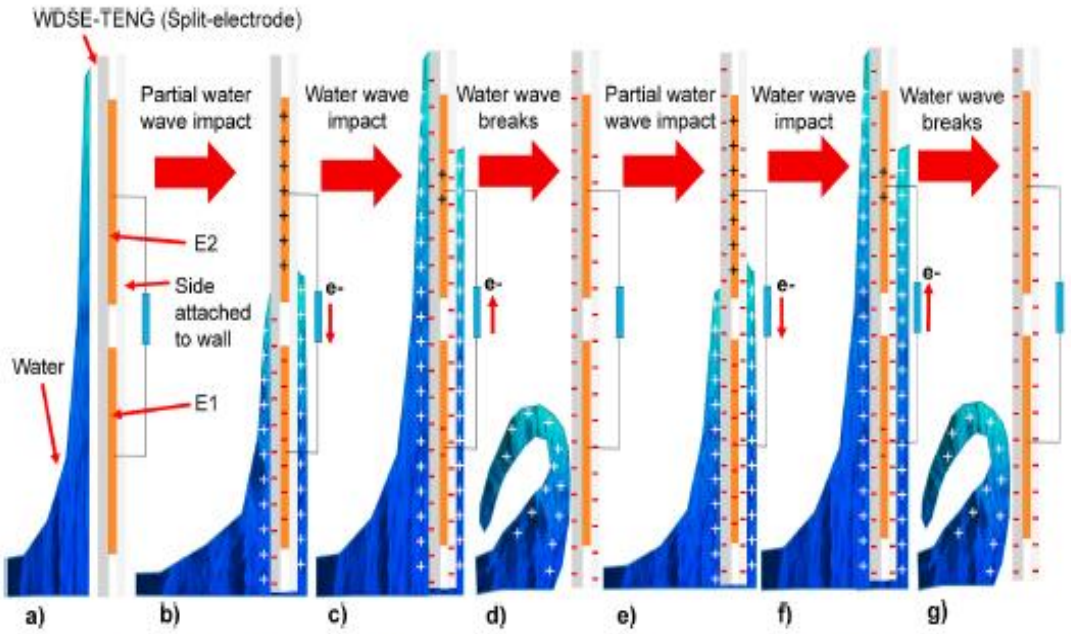

Fig. 5. a–g. Working mechanism of the split-electrode WDSE-TENG with two-dielectric layers by the contact electrification of dielectric layers from breaking water wave impact.

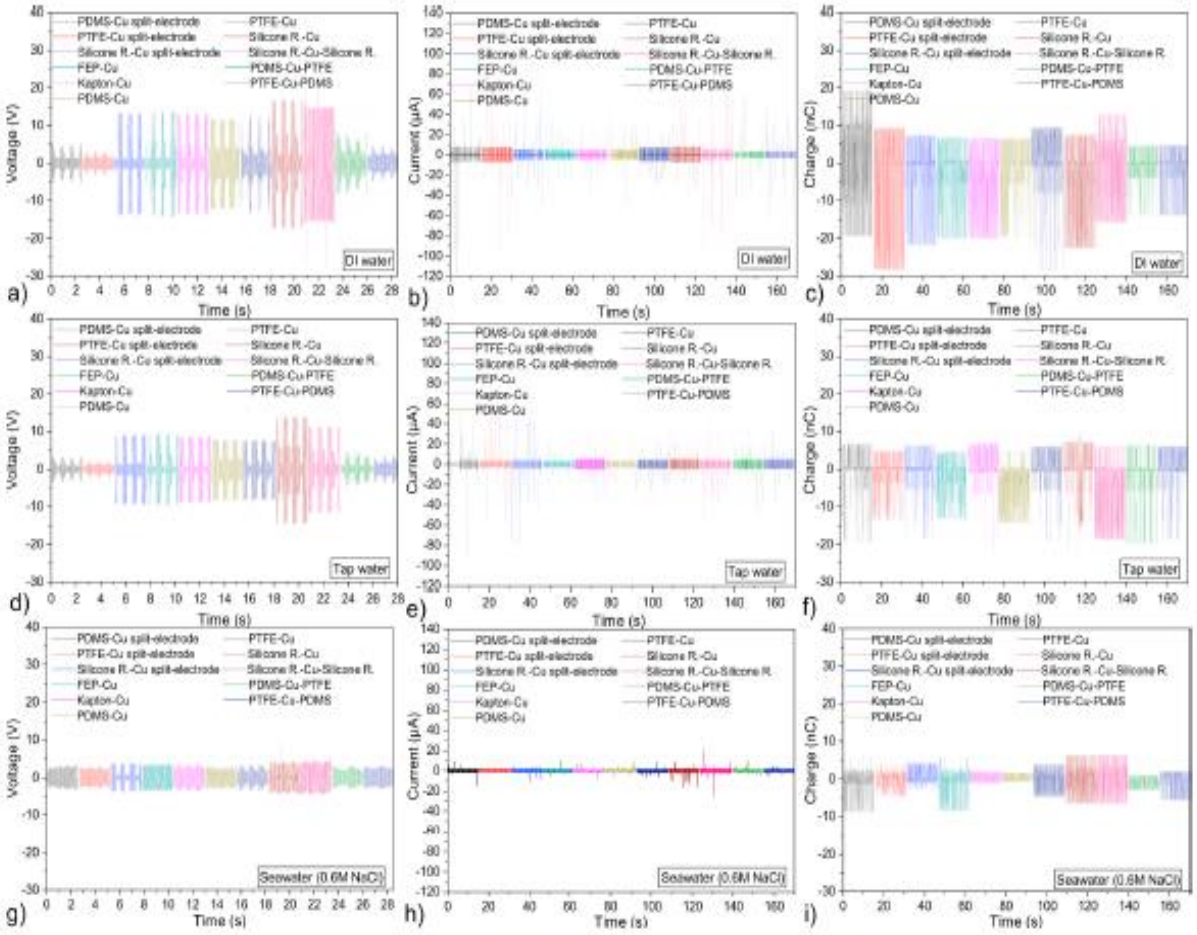

Fig. 6. The average instantaneous output voltage, output current and transferred charges of the WDSE-TENG with different configurations and materials in contact with (a–c) DI water, (d–f) tap water and (g–i) artificial seawater.

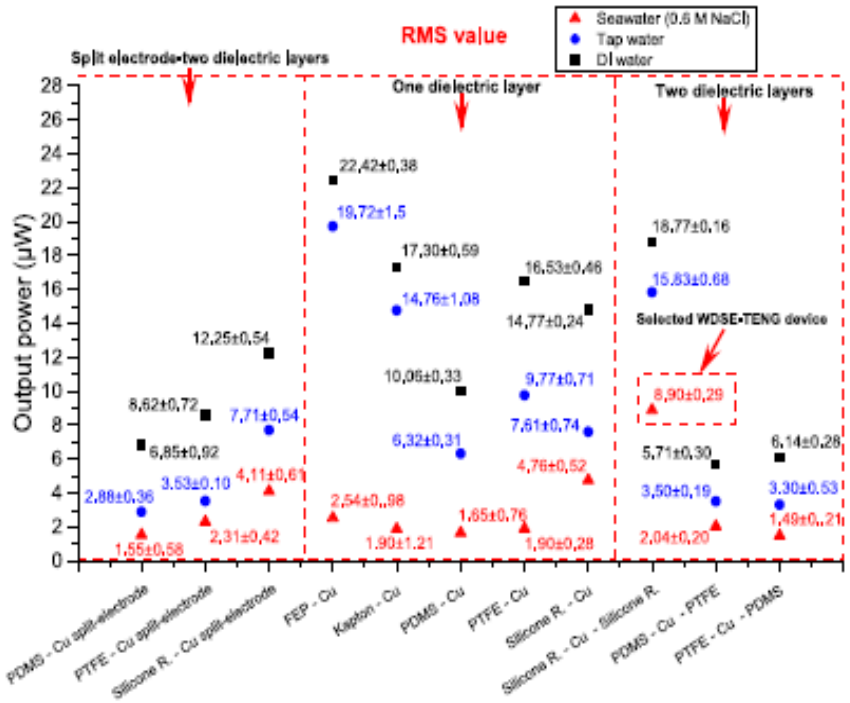

Fig. 7. Comparison of the output power calculated for each of the three WDSE-TENG prototypes when exposed to 10.5 cm amplitude waves at 1.2 Hz (with a 10 MΩ load).

the electron exchange and ionization of the surface groups on the dielectric layers will cause the dielectric layer to be negatively charged [44] and create a positively charged EDL on the contact surface of the water wave to maintain electrical neutrality [30–33,45,46] (Fig. 3 c and Fig. 4 c). As the water wave breaks down and moves off the dielectric layers, the positive charges in the EDL can be carried away with the water and the negative charges can remain on the surface of the dielectric layers. The negative electric potential difference between the electrode and the load resistor to ground attains equilibrium as electrons flow to ground (Fig. 3 d and Fig. 4 d) due to the triboelectric charges on the dielectric layers, which can be retained for hours or even days [47]. When another water wave is partially impacting/contacting the negatively charged dielectric layers in a short period (−0.0008 s) of the impact motion process (See Fig. S2 in the supplementary information document), the negative charges will attract counter ions from the water to form another positively charge EDL, and establishes a positive electric potential difference. Therefore, electrons will flow from ground and load resistor to the electrode (Fig. 3e and Fig. 4 e) that produces an instantaneous current peak until a new equilibrium is reached (−0.29 s, Fig. 3 f and Fig. 4 f) (See Fig. S3 in the supplementary information document). When the water wave breaks down (−0.0103 s) and leaves the dielectric layers, a negative electric potential difference will be established between the electrode and load resistor to the ground and another new equilibrium is achieved (Fig. 3 g and Fig. 4 g). Once the following water wave contacts with the dielectric layers of the WDSE-TENG (Fig. 3 a-g and Fig. 4 a-g), power generation cycle repeats itself.

Additionally, the working mechanism of the WDSE-TENG with split-electrode and two-dielectric layers configuration is depicted in Fig. 5 a-g. No charge transfer and ion adsorption take place before the contact electrification between the dielectric layers and water (Fig. 5 a). Subsequently, the water wave starts its contact over the WDSE-TENG, and this results in electrical neutrality with negative charges on the dielectric layer surface, which also creates a positively charged EDL on the water (Fig. 5 b). This generates an unbalanced electric potential difference between E1 and E2 that drives the movement of electrons from E2, through the load resistance to E1 as the water wave is partially impacting the WDSE-TENG energy harvester (Fig. 5 b). This process produces an instantaneous negative current (Fig. 5 b). Therefore, once the water wave fully impacts the device dielectric layers, induced electrons move back from E1 to E2, through the load resistance as the electric potential distribution changes toward equilibrium which produces an instantaneous positive current (Fig. 5 c). As the water wave breaks down and moves off the dielectric layers, the positive charges in the EDL can be carried away with the water and the negative charges can remain on the surface of the dielectric layers (Fig. 5 d). Once the following water wave starts impacting with the dielectric layers of the split-electrode WDSE-TENG with two-dielectric layers (Fig. 5 e), another cycle of operation is completed (Fig. 5 f-g). The water wave after the impact with the dielectric layers of the WDSE-TENG prototypes should not leave residual water on the dielectric hydrophobic layers surface, in an ideal situation to generate the maximum electrical output.

4. Experimental results and discussion

4.1. Water-dielectric triboelectric materials selection and optimisation

The comparison of the three configurations for the WDSE-TENG energy harvester prototypes according to their electrical output performance measurements in contact with DI water, tap water and seawater with a frequency and amplitude of impact of 1.2 Hz and 10.5 cm is shown in Fig. 6 a-i (See Fig. S2 in the supplementary information document). In contact with DI water, the devices had a maximum output voltage (V_{RMS}), output current (I_{RMS}) and transferred charges ranging from 3.06 V to 7.36 V, 1.87 μA–5.06 μA and 5.41 nC–13.70 nC (Fig. 6 a-c), respectively. As a result, a maximum output power between 5.71 μW and 22.42 μW was calculated (Fig. 7). In contact with tap water, the maximum output power was between 2.88 μW and 19.72 μW and this was calculated from the measured V_{RMS} (1.47 V–5.76 V) and I_{RMS} (1.04 μA–4.80 μA), along with transferred charges of 4.98 nC–9.93 nC (Fig. 6 d-f). The output performance using tap water was reduced by a factor of 1.46 compared with the DI water (Fig. 7).

The WDSE-TENG with one dielectric layer using FEP (t = 25 μm) in

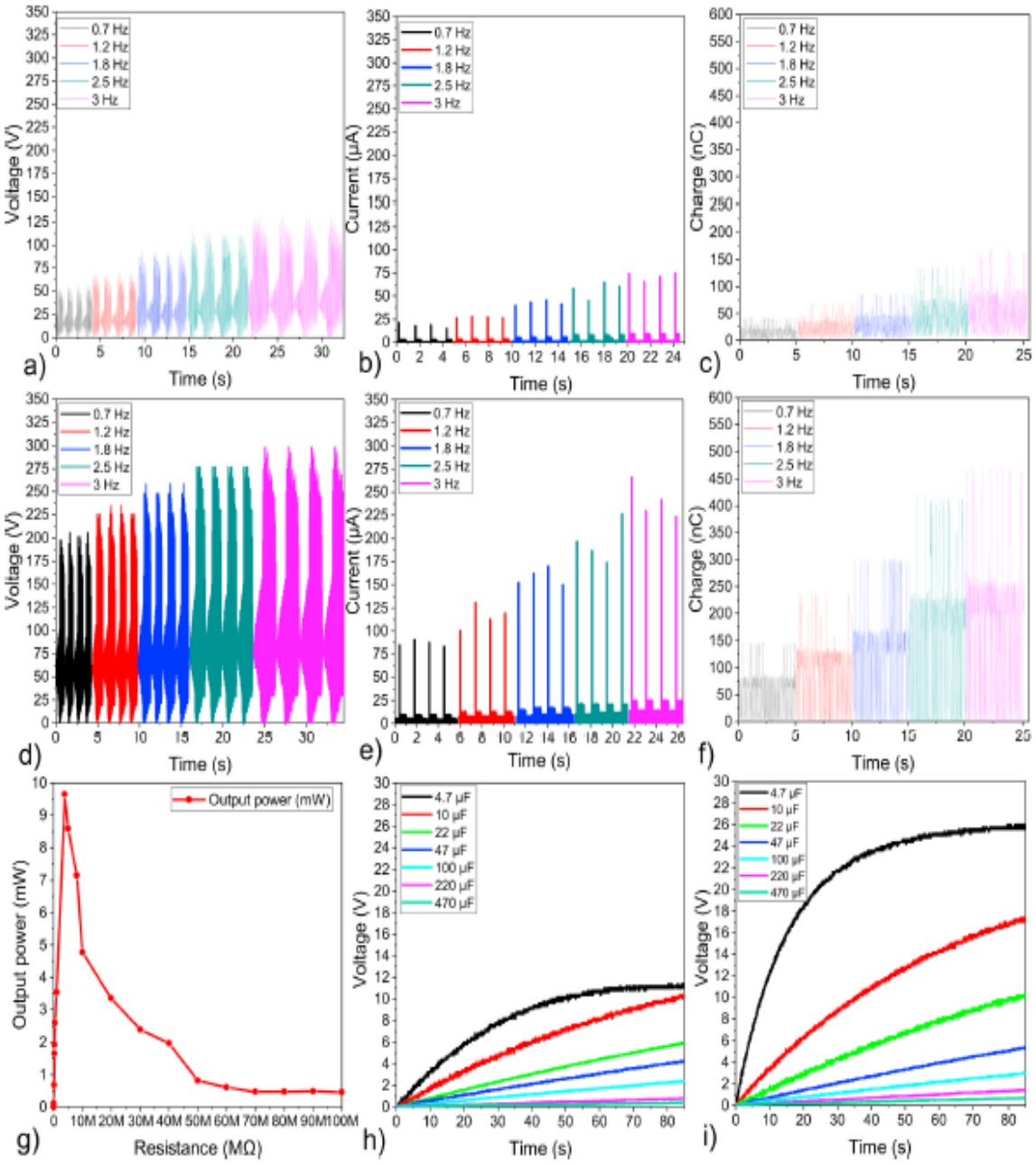

Fig. 8. a) Instantaneous output voltage, b) current and c) transferred charges of a single WDSE-TENG with two-dielectric layers of silicone rubber compound. d) Instantaneous output voltage, e) current and f) transferred charges of the grid of five WDSE-TENG devices through different breaking wave impact frequencies (0.7 Hz–3 Hz) with a load resistance of 3.8 MΩ. g) Load resistance matching analysis to obtain the highest output power performance with the WDSE-TENG devices. h) Charging performance of a single WDSE-TENG energy harvester, and i) a grid of five WDSE-TENG energy harvesters connected in parallel to different capacitors (4.7 μF–470 μF) tested in the water generator tank.

contact with tap water and DI water produced the highest output performance (Fig. 7). The prototype with two dielectric layers of silicone rubber produced the next highest output performance, likely due to the large contact area (V_{RMS}, I_{RMS} and power of 5.76 V–6.21 V, 2.74 μA–3.04 μA and 15.83 μW–18.77 μW, respectively). However, the output performance decreased for the WDSE-TENG with split-electrode with two dielectric layers due to the reduced active area of 2.5 cm × 3 cm. Furthermore, the configuration of the WDSE-TENG with two distinct dielectric layers of PDMS and PTFE have shown relatively poor output power performance from 3.30 μW to 6.14 μW (Fig. 7).

Moreover, the output power for the water-dielectric energy harvesters was reduced by a factor of 4.20 and 2.86 when they were in contact with seawater compared with the DI and tap water, respectively (Fig. 7). The maximum output voltage, current, transferred charge and output power values were 3.75 V, 2.37 μA, 4.63 nC and 8.89 μW with the two dielectric layer configuration using silicone rubber compound (t = 150 μm) with a Cu electrode as depicted in Fig. 6 g-i and Fig. 7. For the one dielectric layer configuration using silicone rubber, a maximum output power of 4.76 μW (Fig. 7) was obtained, with corresponding output voltage, current and transferred charge values of 4.93 V, 0.96 μA and 3.98 nC, respectively. The reduction in the performance of the WDSE-TENG energy harvesters indicated that they are affected by the

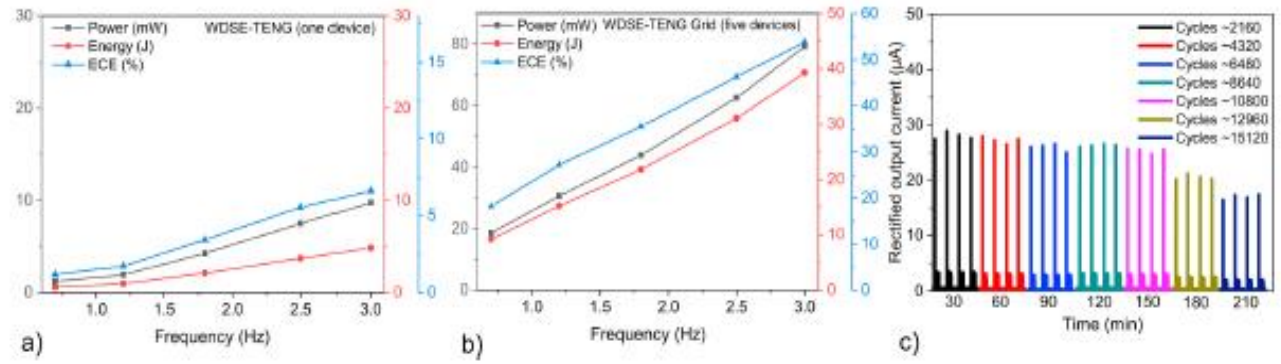

Fig. 9. a) Average instantaneous output power, energy and energy conversion efficiency of a single WDSE-TENG with two-dielectric layers of silicone rubber compound over 15 seconds. b) Average instantaneous output power, energy and energy conversion efficiency of the grid of five WDSE-TENG devices through different breaking wave impact frequencies (0.7 Hz–3 Hz) and amplitudes (10 cm–12 cm) with a load resistance of 3.8 MΩ, for 15 s. c) Maximum average instantaneous output current generated by the WDSE-TENG during different periods and cycles of operation from 30 min to 210 min and −2160 cycles to −15120 cycles under breaking water wave impact.

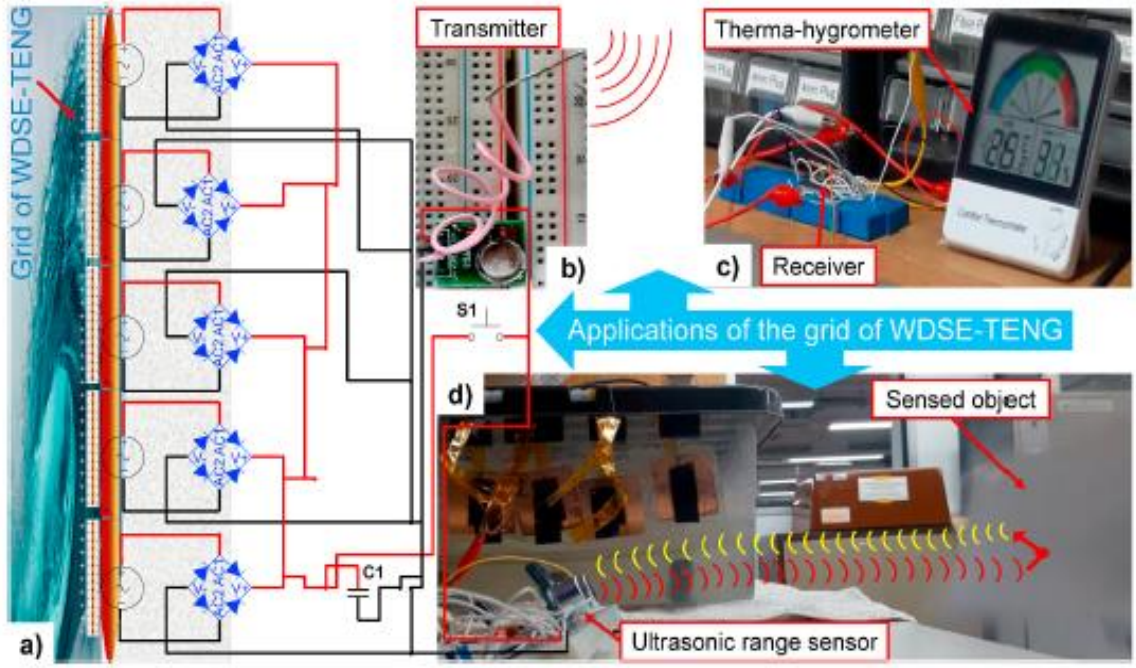

Fig. 10. a) Electrical circuit diagram of the grid of WDSE-TENG energy harvesters under breaking water wave impact to charge the 47 μF and 470 μF capacitors to power-up b) the wireless transmitter to turn on c) a therma-hygrometer and d) an ultrasonic range sensor (Ocean water wave adapted from Ref. [59]).

electrolytes in water. This is due to the fact that dielectric materials cannot completely elude the adhesion of water droplets after it is separated from the water wave impact. Once there are electrolytes in water, more positive charges including dissolved ions will remain on the dielectric films, resulting in the partial screening of the tribo-charges on the films [36,44,48–51]. In the near future, this issue could be solved by the creation of superhydrophobic dielectric layers or by changing the dielectric film with a specific functional group to counter the ions with opposite charges that remain on the contacted surfaces [49] during water wave impact.

The results show that the reduction in the performance of the WDSE-TENG can be compensated by increasing the contact area of the devices operating with seawater to obtain a better output performance (Fig. 7). Consequently, as the WDSE-TENG energy harvesters must be working in seawater conditions under breaking water wave impact, the selected devices for further characterization were the ones composed with two dielectric layers composed of silicone rubber (Fig. 7. The selected devices generated the highest power performance of 8.90 μW under seawater conditions due to the effective contact area of 46 cm^2 (Fig. 1 b), compared with the other energy harvesters with active areas of 23 cm^2 and 27.2 cm^2 (Fig. 1 a and 1 c). The performance of the triboelectric liquid-solid interfaces used for the WDSE-TENG energy harvesters, arranged according to the output performance under breaking water wave impact is summarized in Table 1. The most negative material generating significant electron transfer effect in contact with DI water and tap water was FEP (See Table S1 in the supplementary information document). On the contrary, the most negative dielectric material with the seawater-dielectric interface interaction was Silicone rubber compound (Fig. 7), which means that the charge transferred using this water-dielectric interface is the highest from the selected triboelectric materials, with the objective being to reach the highest electric output performance in the proposed WDSE-TENG energy harvesters in seawater conditions. Nevertheless, the WDSE-TENG devices comprising FEP, PTFE, Polyimide and PDMS layers in contact with seawater show weak electron

Table 1
Comparison of the level of positive and negative triboelectric water-dielectric interfaces in terms of ease of losing or gaining electrons through breaking seawater wave impact.

Triboelectric liquid–solid interfaces combination		
Liquid	Positive	DI water Tap water Seawater (0.6M NaCl)
Solid	Negative	Polydimethylsiloxane (PDMS) (125 μm) Polyimide (127 μm) Polytetrafluoroethylene (PTFE) (100 μm) Fluorinated ethylene propylene (FEP) (24 μm) Silicone rubber compound (Acetoxy, Elastomer) (150 μm)

transfer effect, which means that ion adsorption effect dominates the contact electrification with those polymers [34,35].

4.2. Grid/single WDSE-TENG output performance electrical characterisation under different breaking water wave impact frequencies and potential battery-less applications

The WDSE-TENG with two-dielectric layers comprising silicone rubber compound exhibit maximum output power and power density of 9.65 mW and 0.21 mW/cm^2, respectively. These values were obtained with a load resistance of 3.8 MΩ, selected from a load resistance matching characterization under breaking water wave impact at 3 Hz with an amplitude of 12 cm (Fig. 8 g). Further, the grid/single WDSE-TENG tested in seawater through different breaking water wave impact frequencies (0.7 Hz–3 Hz) and amplitudes (10 cm–12 cm) show a linear increase in their overall output performance by a factor of 3.29 and 2.54 as the frequency of impact increases as illustrated in Fig. 8 a-f (See Table S2 in the supplementary information document). Such increase is attributed and proportional to the total mechanical energy of the breaking water wave impact (2) consisting of potential and kinetic energy that contacts on the WDSE-TENG devices. Which rises from 50.76 J to 73.10 J that produces an increase in the friction between the liquid-solid interface [35,52–54] (Fig. 4 e) increasing the electron exchange and ion adsorption that occurs simultaneously [30–33] as the frequency and amplitude of impact rises (See Fig. S4 in the supplementary information document). The maximum rectified output power of the single WDSE-TENG device increases from 1.21 mW to 9.76 mW (Fig. 9 a-b), with corresponding maximum instantaneous output voltage, current and transferred charge values of 56.84 V–130 V, 21.31 μA–74.67 μA and 41.79 nC–169 nC, respectively (Fig. 8 a-c).

In comparison, the grid of five energy harvesters connected in parallel, with a total active area of 230 cm^2, showed an overall enhancement by a factor of 6.14 in the average rectified instantaneous output performance with an increasing output voltage, current and transferred charges from 205.63 V to 298 V, 90.52 μA–265.78 μA and 144.9 nC–469.70 nC, respectively (Fig. 8 d-f). Consequently, the grid of energy harvesters generated a maximum output power and power density of 18.61 mW–79.18 mW (Fig. 9 a-b) and 0.081 mW/cm^2 to 0.344 mW/cm^2 (3.8 MΩ load). Furthermore, the output performance enhancement was verified by charging different capacitors (4.7 μF–470 μF). The maximum voltage reached by the single unit of WDSE-TENG was 11.18 V, compared with the grid of WDSE-TENG devices that reached a maximum value of 25.73 V, when charging a capacitor of 4.7 μF for 85 s as illustrated in Fig. 8 h and Fig. 8 i.

Additionally, the average energy conversion efficiency (ECE) η of one WDSE-TENG energy harvester and a grid of WDSE-TENG composed of five devices was calculated. The ECE is defined as the ratio between the electric energy ($E_{electric}$) delivered to the load resistor of 3.8 MΩ and the mechanical energy ($E_{waterwave}$) applied by the breaking water wave impact on the single/grid of WDSE-TENG devices. A time period of 15 s was considered when calculating $E_{electric}$ for different frequencies (0.7 Hz–3 Hz) and amplitudes (10 cm–12 cm). The $E_{electric}$ released for the single and grid WDSE-TENG energy harvesters were from 0.6 J to 4.84 J and 9.23 J–39.28 J, respectively as shown in Fig. 9 a-b. These values were estimated using the following equation:

$$E_{electric} = \int_{t1}^{t2} RI^2 dt \quad (1)$$

where I is the average instantaneous current generated by the devices and R is the load resistance. The total mechanical energy of the water waves was between 50.76 J and 73.10 J consisting of potential energy and kinetic energy [55]:

$$E_{waterwave} = \frac{1}{2}\rho g A^2 \quad (2)$$

Where g is the acceleration of gravity, ρ is the density of seawater (1036 kg/m^3) [56], and A is the wave amplitude (from 10 cm to 12 cm. Consequently, the overall η of the single/grid of WDSE-TENG energy harvesters rise linearly between 1.18% and 6.62% and 18.19% and 53.74% as depicted in Fig. 9 a-b, calculated by Ref. [57]:

$$\eta = \frac{E_{electric}}{E_{waterwave}} x\,100\% \quad (3)$$

Moreover, analyzing the potential to scale up the energy harvesting of breaking water wave on an area of 18 m^2, where the water wave breaks with amplitudes between 0.3 m and 4 m [58] using a grid of WDSE-TENG. This could be possible with the fabrication of big water-dielectric triboelectric-structure interfaces composed with 7200 energy harvesters connected in parallel, which could have the potential to generate an average output power, and energy of −30.63 W and −15.20 kJ, respectively. Consequently, estimating the breaking of a water wave with an amplitude of 4 m that generates the energy of 78.4 kJ (2) impacting over the big proposed interface. The big-scale grid of WDSE-TENG could have an ECE of 19.38% (3), collecting breaking water wave impacts in big-scale with different amplitudes in the aforementioned area. Besides, a durability test was performed on the WDSE-TENG device composed of two silicone rubber dielectric layers under breaking water wave impact with a frequency and amplitude of −1.2 Hz and −10.5 cm, over different periods of 30, 60, 90, 120, 150 and 180 min. Based on the number of cycles of operation and the rectified output current of the WDSE-TENG energy harvester. The results show that the energy harvester maximum average output current is stable over 150 min and −10800 cycles of operation under the impact of water waves as illustrated in Fig. 9 c. Subsequently, the performance decreases linearly as the operation time increases from 150 min to 180 min and 210 min with a decrease by a factor of 1.27 and 1.55, respectively (Fig. 9 c). The average maximum instantaneous current decreased from −27.14 μA (60–150 min) to −21.21 μA and −17.41 μA (180–210 min) as the cycle of operation increases from −12960 to −15120, respectively. Although under −10800 cycles of operation, the WDSE-TENG performance was stable, further investigation is required to improve the energy conversion efficiency and device durability to withstand the harsh environmental conditions of the ocean and liquid environments.

Besides, due to the improvement of the breaking water wave energy harvesting through the implementation of the grid of WDSE-TENG devices charging different capacitors (Fig. 10 a), some applications were demonstrated. First, the grid of WDSE-TENG energy harvesters was used to power a one way wireless 433 MHz transmitter (Seeed Studio RF link kit part no. 113990010) to send a signal to the receiver to turn on a therma-hygrometer with a transmission distance from 2 m to 8 m as shown in Fig. 10 b-c. This was achieved after charging a 47 μF capacitor between 129 and 370 s, resulting in a voltage of 3.19 V–9.81 V across the capacitor, and then using the stored electrical energy to power up the transmitter. To transmit at longer distances, more energy can be stored by charging suitable capacitors for a longer time. The energy stored in the capacitor for the grid of WDSE-TENG devices, and the power

generated for the capacitor during the discharging process for powering the wireless transmitter were between 193.56 μJ and 2.24 mJ, and 322 μW to 3.73 mW, respectively (Fig. 11 a and Fig. 11 c).

Furthermore, an ultrasonic range sensor (HC-SR04) for detection of objects was powered by charging a 470 μF capacitor for 570 s (Figs. 10 d and Fig. 11 b) using the grid of energy harvesters. The range sensor was able to track the movement of a plastic sheet located at a distance of −30 cm over a short period (−1 s) as illustrated in Fig. 10 d. The energy stored in the capacitor for the grid of energy harvesters and the power supplied by the capacitor to power up the ultrasonic ranger sensor were 5.96 mJ and 5.18 mW, respectively. This demonstration confirmed that the grid of energy harvesters using a liquid-solid interface was able to drive typical electronic devices found in wireless sensor systems.

Finally, energy transfer with a pre-storage capacitor (Ct) was used to store the energy from the grid of WDSE-TENG and to maintain the optimal voltage across the diode rectifier bridge in order to optimize energy extraction. This was achieved using a flyback converter circuit that gives more design flexibility [60]. Therefore, a LT8303 micropower high-voltage insolated flyback converter was integrated to the grid of WDSE-TENG to form a power management control circuit (PMCC) [60] as shown in Fig. 11 d-e. The objective of the PMCC is to maintain the voltage constant across the diode rectifier, when the temporary capacitor (4.7 μF) reaches approximately 5 V after 12.8 s (Fig. 11 f). This is achieved by transferring one part of the energy stored in Ct to the storage capacitor (Cs, 100 μF) through the flyback converter (Fig. 11 f). Harvesting the breaking water wave impact for 200 s, the storage capacitor reached a maximum voltage of 2.64 V with a stored energy of 16.37 μJ, as shown in Fig. 11 f. This power conversion principle enables the utilization of multiple WDSE-TENG connected in parallel using one coupled inductor and only one PMCC (Fig. 11 d-e). This system is able to improve the output power of the water-dielectric energy harvesters with the potential to power up electronic devices such as autonomous wireless sensor nodes for detecting fish and measuring water levels at smart fish farms.

5. Conclusions

In summary, this research work has demonstrated the potential of WDSE-TENG devices as an innovative and alternative approach for harvesting mechanical energy from breaking wave impact forces at the structure-water interfaces using water as a triboelectric material. This contributes to existing energy harvesting studies that are focused on shallow water wave energy harvesting employing liquid-solid interfaces [3–21].

Firstly, by comparing WDSE-TENG composed of different device configurations and five hydrophobic dielectric materials in contact with DI water, tap water and seawater, the ideal energy harvester configuration and the liquid-solid interface was found in order to enhance the output performance of the proposed energy harvesters. The performance of the DI/tap water-FEP WDSE-TENG were the most promising. On the other hand, a reduction in the performance of the WDSE-TENG with seawater-dielectric interfaces was observed, but it was demonstrated that this can be compensated by increasing the contact area of the devices to enhance the output performance. Consequently, the WDSE-TENG energy harvester comprising two-hydrophobic silicone rubber compounds showed the highest electrical output working in seawater conditions under breaking water wave impact. Secondly, it was demonstrated that an improvement in the power output by a factor of

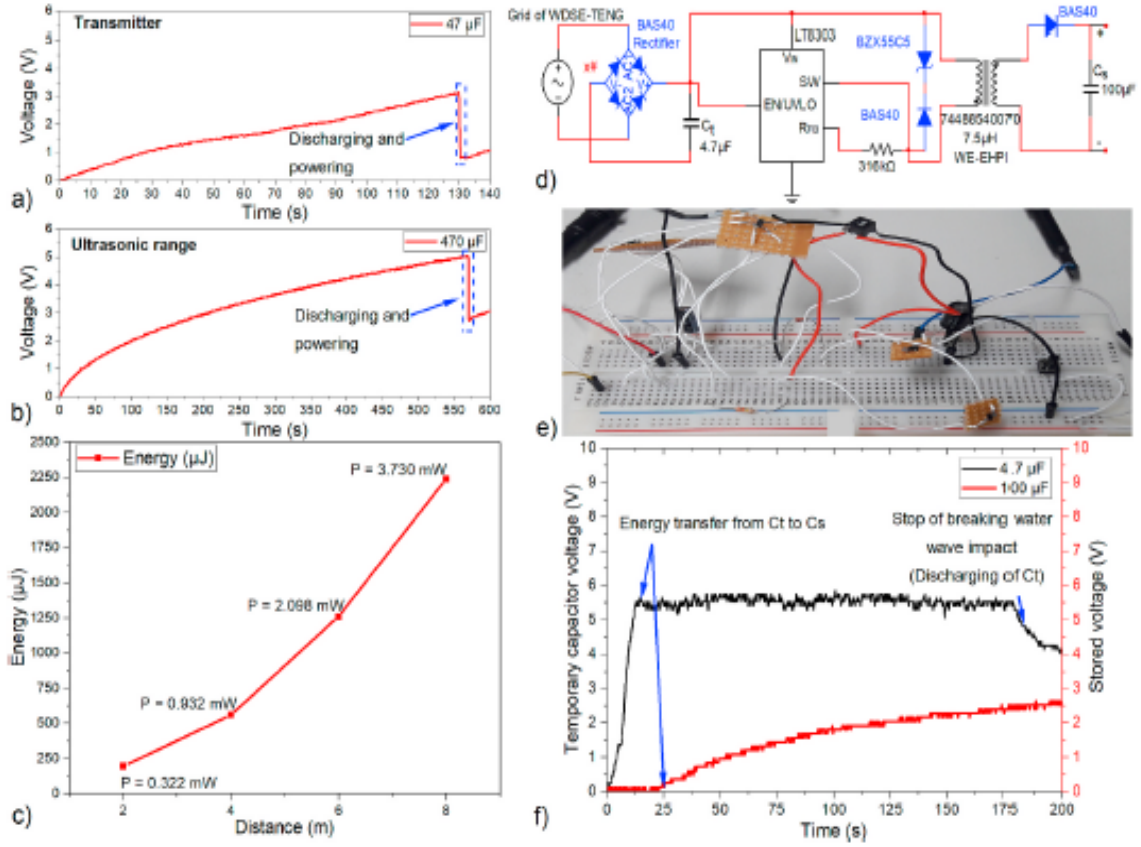

Fig. 11. Capacitor charging and discharging process for powering the a) wireless transmitter to power-up the therma-hygrometer, and b) ultrasonic range sensor under the breaking water wave impact with a frequency of 1.2 Hz. c) Energy stored in the 47 μF capacitor for the grid of WDSE-TENG devices, and the power supplied by the capacitor during the discharging process for powering the wireless transmitter to turn on a therma-hygrometer. d) Integration of the grid of WDSE-TENG with an LT8303 micropower high-voltage insolated flyback converter to form a power management control circuit (PMCC). e) Digital image of the PMCC circuit with the grid of WDSE-TENG. f) Energy transfer from Ct to Cs from harvesting the breaking water wave impact for 200 s.

6.14 for the seawater-dielectric energy harvesters was possible. This was achieved using a parallel connection of a grid of five WDSE-TENG devices with a coverage area of 230 cm^2 compared to a single WDSE-TENG device. The ability to charge different capacitors was demonstrated, and the output voltage, current, transferred charges, output power and ECE values respond with linear and proportional increase as the water wave impact energy rises, increasing the liquid-solid interface friction, electron exchange and ion adsorption [30–33,35,52–54] as the frequency varies from 0.7 Hz to 3 Hz, with amplitudes between 10 cm and 12 cm.

Thirdly, the grid of WDSE-TENG devices has the potential to drive low-power electronic devices with stored energy levels between 2.24 mJ and 5.96 mJ, and they generate power in the range 3.73 mW–5.18 mW, which is sufficient to power an ultrasonic range sensor, and also to power a wireless transmitter. Finally, the integration of the grid of WDSE-TENG devices with a PMCC allows the device to achieve power levels from 1 mW to 100 mW [41,42] for powering electronic devices continuously using a TENG. Further investigation is required to explore the integration of superhydrophobic materials, surface patterning modification to enhance hydrophobicity, utilization of normalized thickness values, and more efficient energy coupling to withstand the seawater conditions utilizing the WDSE-TENG energy harvesters that have a stable electrical output under ~10000 cycles of operation during 150 min, measured through a durability test. The integration of the grid of WDSE-TENG offers an innovative approach that is able to work in liquid environments and hence provide an energy source for self-powered wireless sensing systems at water-structure interfaces. Potential applications include fish detection for smart aquaculture, water level measurements, weather condition monitoring, and sensor systems that monitor erosion and weathering in coastal defence systems.

CRediT authorship contribution statement

Ulises Tronco Jurado: Conceptualization, Methodology, Software, Investigation, Validation, Data curation, Formal analysis, Writing - original draft, Writing - review & editing, Visualization, Project administration. **Suan Hui Pu:** Resources, Conceptualization, Writing - review & editing, Supervision. **Neil M. White:** Resources, Conceptualization, Writing - review & editing, Supervision.

Declaration of competing interest

The authors declare that they have no known competing financial interests or personal relationships that could have appeared to influence the work reported in this paper.

Acknowledgments

The authors thank CONACYT for the fellowship awarded to Ulises Tronco Jurado.

Appendix A. Supplementary data

Supplementary data to this article can be found online at https://doi.org/10.1016/j.nanoen.2020.105204.

References

[1] N. Elvin, A. Erturk, Advances in Energy Harvesting Methods, Springer Science & Business Media, 2013.
[2] D. Jiang, et al., Water-solid triboelectric nanogenerators: an alternative means for harvesting hydropower, Renew. Sustain. Energy Rev. 115 (2019) 109366.
[3] Y. Wu, et al., A teeterboard-like hybrid nanogenerator for efficient harvesting of low-frequency ocean wave energy, Nano Energy 67 (2020) 104205.
[4] L. Feng, et al., Hybridized nanogenerator based on honeycomb-like three electrodes for efficient ocean wave energy harvesting, Nano Energy 47 (2018) 217–223.
[5] F.-R. Fan, Z.-Q. Tian, Z.L. Wang, Flexible triboelectric generator, Nano energy 1 (2) (2012) 328–334.
[6] G. Zhu, et al., Toward large-scale energy harvesting by a nanoparticle-enhanced triboelectric nanogenerator, Nano Lett. 13 (2) (2013) 847–853.
[7] T.X. Xiao, et al., Spherical triboelectric nanogenerators based on spring-assisted multilayered structure for efficient water wave energy harvesting, Adv. Funct. Mater. 28 (35) (2018) 1802634.
[8] M. Xu, et al., High power density tower-like triboelectric nanogenerator for harvesting arbitrary directional water wave energy, ACS Nano 13 (2) (2019) 1932–1939.
[9] S.L. Zhang, et al., Rationally designed sea snake structure based triboelectric nanogenerators for effectively and efficiently harvesting ocean wave energy with minimized water screening effect, Nano Energy 48 (2018) 421–429.
[10] F. Xi, et al., Self-powered intelligent buoy system by water wave energy for sustainable and autonomous wireless sensing and data transmission, Nano Energy 61 (2019) 1–9.
[11] X. Yang, et al., Macroscopic self-assembly network of encapsulated high-performance triboelectric nanogenerators for water wave energy harvesting, Nano Energy 60 (2019) 404–412.
[12] B.K. Yun, H.S. Kim, Y.J. Ko, G. Murillo, J.H. Jung, Interdigital electrode based triboelectric nanogenerator for effective energy harvesting from water, Nano Energy 36 (2017) 233–240.
[13] X. Yang, S. Chan, L. Wang, W.A. Daoud, Water tank triboelectric nanogenerator for efficient harvesting of water wave energy over a broad frequency range, Nano Energy 44 (2018) 388–398.
[14] J.-W. Lee, W. Hwang, Theoretical study of micro/nano roughness effect on water-solid triboelectrification with experimental approach, Nano Energy 52 (2018) 315–322.
[15] X.J. Zhao, S.Y. Kuang, Z.L. Wang, G. Zhu, Highly adaptive solid–liquid interfacing triboelectric nanogenerator for harvesting diverse water wave energy, ACS Nano 12 (5) (2018) 4280–4285.
[16] X. Li, J. Tao, X. Wang, J. Zhu, C. Pan, Z.L. Wang, Networks of high performance triboelectric nanogenerators based on liquid–solid interface contact electrification for harvesting low-frequency blue energy, Adv. Energy Mater. 8 (21) (2018) 1800705.
[17] Z.H. Lin, G. Cheng, L. Lin, S. Lee, Z.L. Wang, Water–solid surface contact electrification and its use for harvesting liquid-wave energy, Angew. Chem. Int. Ed. 52 (48) (2013) 12545–12549.
[18] L. Pan, et al., Liquid-FEP-based U-tube triboelectric nanogenerator for harvesting water-wave energy, Nano Res. 11 (8) (2018) 4062–4073.
[19] G. Zhu, et al., Harvesting water wave energy by asymmetric screening of electrostatic charges on a nanostructured hydrophobic thin-film surface, ACS Nano 8 (6) (2014) 6031–6037.
[20] B. Zhang, et al., Self-powered acceleration sensor based on liquid metal triboelectric nanogenerator for vibration monitoring, ACS Nano 11 (7) (2017) 7440–7446.
[21] X. Zhang, et al., Self-powered distributed water level sensors based on liquid–solid triboelectric nanogenerators for ship draft detecting, Adv. Funct. Mater. 29 (41) (2019) 1900327.
[22] R.B. Mayon, Investigation of Wave Impacts on Porous Structures for Coastal Defences, Doctoral, University of Southampton, 2017 [Online]. Available, https://eprints.soton.ac.uk/422221/.
[23] U.T. Jurado, S.H. Pu, N.M. White, A contact-separation mode triboelectric nanogenerator for ocean wave impact energy harvesting, in: 2017 IEEE SENSORS, IEEE, 2017, pp. 1–3.
[24] U.T. Jurado, S.H. Pu, N.M. White, Dielectric-metal triboelectric nanogenerators for ocean wave impact self-powered applications, IEEE Sensor. J. 19 (16) (2019) 6778–6785.
[25] U.T. Jurado, S.H. Pu, N.M. White, Grid of hybrid nanogenerators for improving ocean wave impact energy harvesting self-powered applications, Nano Energy 72 (2020), 104701.
[26] U.T. Jurado, S.H. Pu, N.M. White, Water-dielectric single electrode mode triboelectric nanogenerators for ocean wave impact energy harvesting, Multidiscipl. Dig. Publ. Inst. Proc. 2 (13) (2018) 714.
[27] B. Ravelo, F. Duval, S. Kane, B. Nsom, Demonstration of the triboelectricity effect by the flow of liquid water in the insulating pipe, J. Electrost. 69 (6) (2011) 473–478.
[28] Y. Sun, X. Huang, S. Soh, Using the gravitational energy of water to generate power by separation of charge at interfaces, Chem. Sci. 6 (6) (2015) 3347–3353.
[29] U. Khan, S.-W. Kim, Triboelectric nanogenerators for blue energy harvesting, ACS Nano 10 (7) (2016) 6429–6432.
[30] Z.L. Wang, Triboelectric nanogenerator (TENG)—sparking an energy and sensor revolution, Adv. Energy Mater. 10 (17) (2020) 2000137.
[31] S. Lin, L. Xu, A.C. Wang, Z.L. Wang, Quantifying electron-transfer in liquid-solid contact electrification and the formation of electric double-layer, Nat. Commun. 11 (1) (2020) 1–8.
[32] L. Zhou, D. Liu, J. Wang, Z.L. Wang, Triboelectric nanogenerators: fundamental physics and potential applications, Friction (2020) 1–26.
[33] Z.L. Wang, A.C. Wang, On the origin of contact-electrification, Mater. Today 30 (2019) 34–51.
[34] J. Nie, et al., Probing contact-electrification-induced electron and ion transfers at a liquid–solid interface, Adv. Mater. 32 (2) (2020), 1905696.
[35] S. Li, et al., Contributions of different functional groups to contact electrification of polymers, Adv. Mater. 32 (25) (2020), 2001307.
[36] A. Diaz, R. Felix-Navarro, A semi-quantitative tribo-electric series for polymeric materials: the influence of chemical structure and properties, J. Electrost. 62 (4) (2004) 277–290.

Appendix A

[37] D. Davies, Charge generation on dielectric surfaces, J. Phys. Appl. Phys. 2 (11) (1969) 1533.
[38] Z.L. Wang, T. Jiang, L. Xu, Toward the blue energy dream by triboelectric nanogenerator networks, Nano Energy 39 (2017) 9–23.
[39] L. Xu, et al., Coupled triboelectric nanogenerator networks for efficient water wave energy harvesting, ACS Nano 12 (2) (2018) 1849–1858.
[40] J. Chen, et al., Networks of triboelectric nanogenerators for harvesting water wave energy: a potential approach toward blue energy, ACS Nano 9 (3) (2015) 3324–3331.
[41] D. Steingart, Power sources for wireless sensor networks, in: Energy Harvesting Technologies, Springer, 2009, pp. 267–286.
[42] Z.L. Wang, W. Wu, Nanotechnology-enabled energy harvesting for self-powered micro-/nanosystems, Angew. Chem. Int. Ed. 51 (47) (2012) 11700–11721.
[43] Z.L. Wang, L. Lin, J. Chen, S. Niu, Y. Zi, Triboelectric nanogenerator: freestanding triboelectric-layer mode, in: Triboelectric Nanogenerators, Springer, 2016, pp. 109–153.
[44] D. Choi, H. Lee, I.S. Kang, G. Lim, D.S. Kim, K.H. Kang, Spontaneous electrical charging of droplets by conventional pipetting, Sci. Rep. 3 (2013) 2037.
[45] J. Lyklema, Fundamentals of Interface and Colloid Science: Soft Colloids, Elsevier, 2005.
[46] Z.H. Lin, G. Cheng, S. Lee, K.C. Pradel, Z.L. Wang, Harvesting water drop energy by a sequential contact-electrification and electrostatic-induction process, Adv. Mater. 26 (27) (2014) 4690–4696.
[47] Y. Tada, Experimental characteristics of electret generator, using polymer film electrets, Jpn. J. Appl. Phys. 31 (3R) (1992) 846.
[48] B.J. Kirby, E.F. Hasselbrink Jr., Zeta potential of microfluidic substrates: 1. Theory, experimental techniques, and effects on separations, Electrophoresis 25 (2) (2004) 187–202.
[49] L.S. McCarty, G.M. Whitesides, Electrostatic charging due to separation of ions at interfaces: contact electrification of ionic electrets, Angew. Chem. Int. Ed. 47 (12) (2008) 2188–2207.
[50] W. Harper, Contact and Frictional Electrification, Morgan Hill, Laplacian Press, 1998.
[51] Y. Awakuni, J. Calderwood, Water vapour adsorption and surface conductivity in solids, J. Phys. Appl. Phys. 5 (5) (1972) 1038.
[52] L. Zhao, J. Sun, X. Wang, L. Zeng, C. Wang, Y. Tu, System-size effect on the friction at liquid-solid interfaces, Appl. Math. Mech. 41 (3) (2020) 471–478.
[53] F.-C. Wang, Y.-P. Zhao, Slip boundary conditions based on molecular kinetic theory: the critical shear stress and the energy dissipation at the liquid-solid interface, Soft Matter 7 (18) (2011) 8628–8634.
[54] Y. Zhang, et al., Combined effects of pinning and adhesion force on solid\liquid interfacial friction behaviors under applied voltage, Tribol. Int. 134 (2019) 102–108.
[55] A. Khaligh, O.C. Onar, Energy Harvesting: Solar, Wind, and Ocean Energy Conversion Systems, CRC press, 2009.
[56] R. Pawlowicz, Key physical variables in the ocean: temperature, salinity, and density, Nat. Educ. Knowl. 4 (4) (2013) 13.
[57] W. Tang, et al., Liquid-metal electrode for high-performance triboelectric nanogenerator at an instantaneous energy conversion efficiency of 70.6%, Adv. Funct. Mater. 25 (24) (2015) 3718–3725.
[58] Oceanweathercom, Current Marine Data, Oceanweather Inc, [Online]. Available, http://www.oceanweather.com/data/index.html. (Accessed 30 October 2018).
[59] E. Arano, Ocean water wave photo [Online]. Available, https://www.pexels.com/photo/ocean-water-wave-photo-1295138/, 2016.
[60] S. Boisseau, G. Despesse, B.A. Seddik, Electrostatic conversion for vibration energy harvesting, Small-Scale Energy Harvest. (2012) 1–39.

Ulises Tronco Jurado received the M.Sc. degree in materials science from University of Guadalajara, Mexico, in 2015. He was a MEMS lab researcher at the University of Texas at San Antonio, U.S., in 2014, working on modelling, synthesis, fabrication and characterization of quantum dots applied to c silicon solar cells. He is currently pursuing a PhD. Degree in Engineering and the Environment with the Mechatronic Research Group, and the Smart Electronic Materials and Systems Research Group, School of Electronics and Computer Science, University of Southampton, U.K. His current research interest includes triboelectric nanogenerators for ocean wave monitoring applications that required self-powering.

Suan Hui Pu received Ph.D. degree in electrical and electronic engineering from Imperial College London, U.K. in 2010. He is currently an Associate Professor at University of Southampton at Johor, Malaysia. He is a visiting academic in the Schools of Engineering, and Electronics and Computer Science, at the University of Southampton, U.K. His current research interests include NEMS/MEMS sensors and actuators, graphene, graphite sensors and printed electronics. He has served as a reviewer for IEEE Journal of Microelectromechanical Systems, IEEE Electron Device Letters, IEEE Transactions on Components, Packaging and Manufacturing Technology, IOP Nanotechnology, IOP Journal of Micromechanics and Microengineering, amongst others.

Neil M. White obtained a PhD from the University of Southampton in 1988. Neil was promoted to Senior Lecturer in 1999. His research interests include thick-film sensors, intelligent instrumentation, MEMS, self-powered microsensors and sensor networks. He is a Chartered Engineer, Senior Member of the IEEE, and a Chartered Physicist. He is a member of the Peer Review College for the EPSRC and is on the Editorial Board of the international journals Sensor Review and Journal of Materials Science: Materials in Electronics. Professor White is also a Series Editor for the Integrated Microsystems series for Artech House.

References

[1] N. Elvin and A. Erturk, *Advances in energy harvesting methods*. Springer Science & Business Media, 2013.

[2] C. McGowin, R. Bedard, and N. Lenssen, "Ocean tidal and wave energy," *Renewable Energy Technical Assessment Guide—TAG-RE. Palo Alto: Electrical Power Research Institute,* 2005.

[3] J. Fernández-Chozas, "Technical and Non-Technical issues towards the commercialisation of wave energy converters," *Aalborg: PhD Thesis (DCE Thesis no. 44), Aalborg University,* 2013.

[4] F. Mwasilu and J.-W. Jung, "Potential for power generation from ocean wave renewable energy source: a comprehensive review on state-of-the-art technology and future prospects," *IET Renewable Power Generation,* vol. 13, no. 3, pp. 363-375, 2018.

[5] S. N. Gosling *et al.*, "Climate: Observations, projections and impacts," ed: Met Office, 2011.

[6] A. S. Parris *et al.*, "Global sea level rise scenarios for the United States National Climate Assessment," 2012.

[7] H. Bredmose, D. Peregrine, and G. Bullock, "Violent breaking wave impacts. Part 2: modelling the effect of air," *Journal of Fluid Mechanics,* vol. 641, pp. 389-430, 2009.

[8] H. Oumeraci, P. Klammer, and H. Partenscky, "Classification of breaking wave loads on vertical structures," *Journal of waterway, port, coastal, and ocean engineering,* vol. 119, no. 4, pp. 381-397, 1993.

[9] M. Esteban, H. Takagi, and T. Shibayama, *Handbook of coastal disaster mitigation for engineers and planners*. Butterworth-Heinemann, 2015.

[10] Z. Sabeur, W. Roberts, and A. Cooper, "Development and use of an advanced numerical model using the volume of fluid method for the design of coastal structures," *Numerical Methods for Fluid Dynamics,* vol. 5, pp. 565-573, 1995.

[11] Z. Sabeur, J. Cohen, J. Stephens, and A. Veldman, "Investigation on free surface flow oscillatory impact pressures with the Volume of Fluid method," *Numerical Methods for Fluid Dynamics,* vol. 6, pp. 493-498, 1998.

[12] R. B. Mayon, "Investigation of wave impacts on porous structures for coastal defences," Doctoral dissertation, University of Southampton, 2017.

[13] R. Mayon, Z. Sabeur, M. Tan, and K. Djidjeli, "Analysis of fluid flow impact oscillatory pressures with air entrapment at structures," *COASTAL ENGINEERING,* p. 2, 2016.

[14] F.-R. Fan, Z.-Q. Tian, and Z. L. Wang, "Flexible triboelectric generator," *Nano energy,* vol. 1, no. 2, pp. 328-334, 2012.

[15] R. Hinchet, W. Seung, and S. W. Kim, "Recent progress on flexible triboelectric nanogenerators for selfpowered electronics," *ChemSusChem,* vol. 8, no. 14, pp. 2327-2344, 2015.

[16] Z. L. Wang, L. Lin, J. Chen, S. Niu, and Y. Zi, *Triboelectric nanogenerators*. Springer, 2016.

[17] Z. L. Wang, "Triboelectric nanogenerators as new energy technology and self-powered sensors–Principles, problems and perspectives," *Faraday discussions,* vol. 176, pp. 447-458, 2015.

[18] U. Khan and S.-W. Kim, "Triboelectric nanogenerators for blue energy harvesting," *ACS nano,* vol. 10, no. 7, pp. 6429-6432, 2016.

[19] T. X. Xiao *et al.*, "Spherical triboelectric nanogenerators based on spring-assisted multilayered structure for efficient water wave energy harvesting," *Advanced Functional Materials,* vol. 28, no. 35, p. 1802634, 2018.

[20] M. Xu *et al.*, "High power density tower-like triboelectric nanogenerator for harvesting arbitrary directional water wave energy," *ACS nano,* vol. 13, no. 2, pp. 1932-1939, 2019.

[21] S. L. Zhang *et al.*, "Rationally designed sea snake structure based triboelectric nanogenerators for effectively and efficiently harvesting ocean wave energy with minimized water screening effect," *Nano Energy,* vol. 48, pp. 421-429, 2018.

[22] F. Xi *et al.*, "Self-powered intelligent buoy system by water wave energy for sustainable and autonomous wireless sensing and data transmission," *Nano Energy,* vol. 61, pp. 1-9, 2019.

[23] X. Yang *et al.*, "Macroscopic self-assembly network of encapsulated high-performance triboelectric nanogenerators for water wave energy harvesting," *Nano Energy,* vol. 60, pp. 404-412, 2019.

[24] X. Wen, W. Yang, Q. Jing, and Z. L. Wang, "Harvesting broadband kinetic impact energy from mechanical triggering/vibration and water waves," *ACS nano,* vol. 8, no. 7, pp. 7405-7412, 2014.

[25] X. Wang, S. Niu, Y. Yin, F. Yi, Z. You, and Z. L. Wang, "Triboelectric nanogenerator based on fully enclosed rolling spherical structure for harvesting low-frequency water wave energy," *Advanced Energy Materials,* vol. 5, no. 24, p. 1501467, 2015.

[26] J. Chen *et al.*, "Networks of triboelectric nanogenerators for harvesting water wave energy: a potential approach toward blue energy," *ACS nano,* vol. 9, no. 3, pp. 3324-3331, 2015.

[27] W. Liu *et al.*, "Torus structured triboelectric nanogenerator array for water wave energy harvesting," *Nano Energy,* vol. 58, pp. 499-507, 2019.

[28] L. Xu *et al.*, "Integrated triboelectric nanogenerator array based on air-driven membrane structures for water wave energy harvesting," *Nano Energy,* vol. 31, pp. 351-358, 2017.

[29] X. Li, J. Tao, X. Wang, J. Zhu, C. Pan, and Z. L. Wang, "Networks of high performance triboelectric nanogenerators based on liquid–solid interface contact electrification for harvesting low-frequency blue energy," *Advanced Energy Materials,* vol. 8, no. 21, p. 1800705, 2018.

[30] X. Zhang *et al.*, "Self-Powered Distributed Water Level Sensors Based on Liquid–Solid Triboelectric Nanogenerators for Ship Draft Detecting," *Advanced Functional Materials,* vol. 29, no. 41, p. 1900327, 2019.

[31] B. K. Yun, H. S. Kim, Y. J. Ko, G. Murillo, and J. H. Jung, "Interdigital electrode based triboelectric nanogenerator for effective energy harvesting from water," *Nano Energy,* vol. 36, pp. 233-240, 2017.

[32] X. Yang, S. Chan, L. Wang, and W. A. Daoud, "Water tank triboelectric nanogenerator for efficient harvesting of water wave energy over a broad frequency range," *Nano Energy,* vol. 44, pp. 388-398, 2018.

[33] J.-W. Lee and W. Hwang, "Theoretical study of micro/nano roughness effect on water-solid triboelectrification with experimental approach," *Nano Energy,* vol. 52, pp. 315-322, 2018.

[34] X. J. Zhao, S. Y. Kuang, Z. L. Wang, and G. Zhu, "Highly adaptive solid–liquid interfacing triboelectric nanogenerator for harvesting diverse water wave energy," *ACS nano,* vol. 12, no. 5, pp. 4280-4285, 2018.

[35] Z. H. Lin, G. Cheng, L. Lin, S. Lee, and Z. L. Wang, "Water–solid surface contact electrification and its use for harvesting liquid-wave energy," *Angewandte Chemie International Edition,* vol. 52, no. 48, pp. 12545-12549, 2013.

[36] L. Pan *et al.*, "Liquid-FEP-based U-tube triboelectric nanogenerator for harvesting water-wave energy," *Nano Research,* vol. 11, no. 8, pp. 4062-4073, 2018.

[37] G. Zhu *et al.*, "Harvesting water wave energy by asymmetric screening of electrostatic charges on a nanostructured hydrophobic thin-film surface," *ACS nano,* vol. 8, no. 6, pp. 6031-6037, 2014.

[38] B. Zhang *et al.*, "Self-powered acceleration sensor based on liquid metal triboelectric nanogenerator for vibration monitoring," *ACS nano,* vol. 11, no. 7, pp. 7440-7446, 2017.

[39] Y. Wu *et al.*, "A teeterboard-like hybrid nanogenerator for efficient harvesting of low-frequency ocean wave energy," *Nano Energy,* vol. 67, p. 104205, 2020.

[40] L. Feng *et al.*, "Hybridized nanogenerator based on honeycomb-like three electrodes for efficient ocean wave energy harvesting," *Nano Energy,* vol. 47, pp. 217-223, 2018.

[41] H. C. Soerensen and A. Weinstein, "Ocean energy: position paper for IPCC," *Hohmeyer and Trittin,* pp. 93-102, 2008.

[42] A. Malik, "Assessment of the potential of renewables for Brunei Darussalam," *Renewable and Sustainable Energy Reviews,* vol. 15, no. 1, pp. 427-437, 2011.

[43] H. C. Soerensen and A. Weinstein, "Ocean energy: position paper for IPCC," in *Key Note Paper for the IPCC Scoping Conference on Renewable Energy, Lübeck, Germany, January*, 2008.

[44] K. Gunn and C. Stock-Williams, "Quantifying the global wave power resource," *Renewable Energy,* vol. 44, pp. 296-304, 2012.

[45] N. Santhosh, V. Baskaran, and A. Amarkarthik, "A review on front end conversion in ocean wave energy converters," *Frontiers in Energy,* vol. 9, no. 3, pp. 297-310, 2015.

[46] C. McGowin, "Ocean Tidal and Wave Energy: Renewable Energy Technical Assessment Guide," *Electric Power Research Institute, Palo Alto, CA, Paper No. TAG-RE,* 2005.

[47] M. Mustapa, O. Yaakob, Y. M. Ahmed, C.-K. Rheem, K. Koh, and F. A. Adnan, "Wave energy device and breakwater integration: A review," *Renewable and Sustainable Energy Reviews,* vol. 77, pp. 43-58, 2017.

[48] D. Vicinanza, J. H. Nørgaard, P. Contestabile, and T. L. Andersen, "Wave loadings acting on overtopping breakwater for energy conversion," *Journal of Coastal Research,* no. 65, pp. 1669-1674, 2013.

[49] P. Contestabile, V. Ferrante, E. Di Lauro, and D. Vicinanza, "Prototype overtopping breakwater for wave energy conversion at port of Naples," in *The 26th International Ocean and Polar Engineering Conference*, 2016: International Society of Offshore and Polar Engineers.

[50] M. T. Pontes, "Assessing the European wave energy resource," 1998.

[51] L. Gato, P. Justino, and A. d. O. Falcão, "Optimization of power take-off equipment for an oscillating-water column wave energy plant," in *Proceedings of 6th European Wave Tidal Energy Conference*, 2005, pp. 155-61.

[52] C.-Y. Yueh and S.-H. Chuang, "A piston-type porous wave energy converter theory," *Journal of Marine Science and Technology,* vol. 21, no. 3, pp. 309-317, 2013.

[53] Z. L. Wang, T. Jiang, and L. Xu, "Toward the blue energy dream by triboelectric nanogenerator networks," *Nano Energy,* vol. 39, pp. 9-23, 2017.

[54] Z. L. Wang and J. Song, "Piezoelectric nanogenerators based on zinc oxide nanowire arrays," *Science,* vol. 312, no. 5771, pp. 242-246, 2006.

[55] C. Chang, V. H. Tran, J. Wang, Y.-K. Fuh, and L. Lin, "Direct-write piezoelectric polymeric nanogenerator with high energy conversion efficiency," *Nano letters,* vol. 10, no. 2, pp. 726-731, 2010.

[56] S. Priya *et al.*, "A review on piezoelectric energy harvesting: materials, methods, and circuits," *Energy Harvesting and Systems,* vol. 4, no. 1, pp. 3-39, 2019.

[57] Z. L. Wang, G. Zhu, Y. Yang, S. Wang, and C. Pan, "Progress in nanogenerators for portable electronics," *Materials today,* vol. 15, no. 12, pp. 532-543, 2012.

[58] S. Roundy and P. K. Wright, "A piezoelectric vibration based generator for wireless electronics," *Smart Materials and structures,* vol. 13, no. 5, p. 1131, 2004.

[59] S. P. Beeby, M. J. Tudor, and N. White, "Energy harvesting vibration sources for microsystems applications," *Measurement science and technology,* vol. 17, no. 12, p. R175, 2006.

[60] S. P. Beeby *et al.*, "A micro electromagnetic generator for vibration energy harvesting," *Journal of Micromechanics and microengineering,* vol. 17, no. 7, p. 1257, 2007.

[61] R. Herb, D. Parkinson, and D. Kerst, "The development and performance of an electrostatic generator operating under high air pressure," *Physical review,* vol. 51, no. 2, p. 75, 1937.

[62] X.-S. Zhang *et al.*, "Frequency-multiplication high-output triboelectric nanogenerator for sustainably powering biomedical microsystems," *Nano letters,* vol. 13, no. 3, pp. 1168-1172, 2013.

[63] W. Yang *et al.*, "Harvesting energy from the natural vibration of human walking," *ACS nano,* vol. 7, no. 12, pp. 11317-11324, 2013.

[64] S. Niu *et al.*, "Theory of sliding-mode triboelectric nanogenerators," *Advanced materials,* vol. 25, no. 43, pp. 6184-6193, 2013.

[65] S. Niu *et al.*, "Theoretical study of contact-mode triboelectric nanogenerators as an effective power source," *Energy & Environmental Science,* vol. 6, no. 12, pp. 3576-3583, 2013.

[66] Z. L. Wang, L. Lin, J. Chen, S. Niu, and Y. Zi, "Theoretical modeling of triboelectric nanogenerators," in *Triboelectric Nanogenerators*: Springer, 2016, pp. 155-183.

[67] X. Wang, S. Niu, Y. Yin, F. Yi, Z. You, and Z. L. Wang, "Triboelectric Nanogenerator Based on Fully Enclosed Rolling Spherical Structure for Harvesting Low-Frequency Water Wave Energy," *Advanced Energy Materials,* vol. 5, no. 24, 2015.

[68] J. Chen and Z. L. Wang, "Reviving Vibration Energy Harvesting and Self-Powered Sensing by a Triboelectric Nanogenerator," *Joule,* 2017.

[69] Z. L. Wang, "Triboelectric nanogenerators as new energy technology for self-powered systems and as active mechanical and chemical sensors," *ACS nano,* vol. 7, no. 11, pp. 9533-9557, 2013.

[70] Z. Wen *et al.*, "Harvesting broad frequency band blue energy by a triboelectric–electromagnetic hybrid nanogenerator," *ACS nano,* vol. 10, no. 7, pp. 6526-6534, 2016.

[71] Y. Yang *et al.*, "Silicon-based hybrid energy cell for self-powered electrodegradation and personal electronics," *ACS nano,* vol. 7, no. 3, pp. 2808-2813, 2013.

[72] Y. Yang, H. Zhang, J. Chen, S. Lee, T.-C. Hou, and Z. L. Wang, "Simultaneously harvesting mechanical and chemical energies by a hybrid cell for self-powered biosensors and personal electronics," *Energy & Environmental Science,* vol. 6, no. 6, pp. 1744-1749, 2013.

[73] Z. L. Wang, "On Maxwell's displacement current for energy and sensors: the origin of nanogenerators," *Materials Today,* vol. 20, no. 2, pp. 74-82, 2017.

[74] S. Wang, L. Lin, Y. Xie, Q. Jing, S. Niu, and Z. L. Wang, "Sliding-triboelectric nanogenerators based on in-plane charge-separation mechanism," *Nano letters,* vol. 13, no. 5, pp. 2226-2233, 2013.

[75] G. Zhu *et al.*, "Linear-grating triboelectric generator based on sliding electrification," *Nano letters,* vol. 13, no. 5, pp. 2282-2289, 2013.

[76] S. Wang, Y. Xie, S. Niu, L. Lin, and Z. L. Wang, "Freestanding triboelectric-layer-based nanogenerators for harvesting energy from a moving object or human motion in contact and non-contact modes," *Advanced Materials,* vol. 26, no. 18, pp. 2818-2824, 2014.

[77] Z. L. Wang, "Triboelectric nanogenerators as new energy technology and self-powered sensors–Principles, problems and perspectives," *Faraday Discuss.,* vol. 176, pp. 447-458, 2015.

[78] H. Baytekin, A. Patashinski, M. Branicki, B. Baytekin, S. Soh, and B. A. Grzybowski, "The mosaic of surface charge in contact electrification," *Science,* vol. 333, no. 6040, pp. 308-312, 2011.

[79] R. G. Horn and D. T. Smith, "Contact electrification and adhesion between dissimilar materials," *Science,* vol. 256, no. 5055, pp. 362-364, 1992.

[80] K. L. Kelly, E. Coronado, L. L. Zhao, and G. C. Schatz, "The optical properties of metal nanoparticles: the influence of size, shape, and dielectric environment," ed: ACS Publications, 2003.

[81] G. Collins *et al.*, "The use of pulsed laser deposition to produce low-temperature barium titanate films on nickel tape and carbon fiber fabric," *Microsystem technologies,* vol. 17, no. 4, pp. 701-706, 2011.

[82] J. Lowell and A. Rose-Innes, "Contact electrification," *Advances in Physics,* vol. 29, no. 6, pp. 947-1023, 1980.

[83] A. Diaz and R. Felix-Navarro, "A semi-quantitative tribo-electric series for polymeric materials: the influence of chemical structure and properties," *Journal of Electrostatics,* vol. 62, no. 4, pp. 277-290, 2004.

[84] S. Wang, L. Lin, and Z. L. Wang, "Nanoscale triboelectric-effect-enabled energy conversion for sustainably powering portable electronics," *Nano letters,* vol. 12, no. 12, pp. 6339-6346, 2012.

[85] P. Bai *et al.*, "Cylindrical rotating triboelectric nanogenerator," *ACS nano,* vol. 7, no. 7, pp. 6361-6366, 2013.

[86] D. Davies, "Charge generation on dielectric surfaces," *Journal of Physics D: Applied Physics,* vol. 2, no. 11, p. 1533, 1969.

[87] C. D. Richards, M. J. Anderson, D. F. Bahr, and R. F. Richards, "Efficiency of energy conversion for devices containing a piezoelectric component," *Journal of Micromechanics and Microengineering,* vol. 14, no. 5, p. 717, 2004.

[88] S. Fujishima, "The history of ceramic filters," *ieee transactions on ultrasonics, ferroelectrics, and frequency control,* vol. 47, no. 1, pp. 1-7, 2000.

[89] H. Kawai, "The piezoelectricity of poly (vinylidene fluoride)," *Japanese Journal of Applied Physics,* vol. 8, no. 7, p. 975, 1969.

[90] A. Jain, P. KJ, A. K. Sharma, A. Jain, and R. PN, "Dielectric and piezoelectric properties of PVDF/PZT composites: a review," *Polymer Engineering & Science,* vol. 55, no. 7, pp. 1589-1616, 2015.

[91] A. Jbaily and R. W. Yeung, "Piezoelectric devices for ocean energy: a brief survey," *Journal of Ocean Engineering and Marine Energy,* vol. 1, no. 1, pp. 101-118, 2015.

[92] D. T. Akcabay and Y. L. Young, "Hydroelastic response and energy harvesting potential of flexible piezoelectric beams in viscous flow," *Physics of Fluids,* vol. 24, no. 5, p. 054106, 2012.

[93] R. Murray and J. Rastegar, "Novel two-stage piezoelectric-based ocean wave energy harvesters for moored or unmoored buoys," in *Active and Passive Smart Structures and Integrated Systems 2009*, 2009, vol. 7288: International Society for Optics and Photonics, p. 72880E.

[94] J. Rastegar, C. Pereira, and H.-L. Nguyen, "Piezoelectric-based power sources for harvesting energy from platforms with low-frequency vibration," in *Smart Structures and Materials 2006: Industrial and Commercial Applications of Smart Structures Technologies*, 2006, vol. 6171: International Society for Optics and Photonics, p. 617101.

[95] A. Zurkinden, F. Campanile, and L. Martinelli, "Wave energy converter through piezoelectric polymers," in *Proceedings of the COMSOL Users Conference (Grenoble)*, 2007.

[96] X. Xie, Q. Wang, and N. Wu, "Potential of a piezoelectric energy harvester from sea waves," *Journal of Sound and Vibration,* vol. 333, no. 5, pp. 1421-1429, 2014.

[97] S. Pobering and N. Schwesinger, "A novel hydropower harvesting device," in *2004 International Conference on MEMS, NANO and Smart Systems (ICMENS'04)*, 2004: IEEE, pp. 480-485.

[98] D.-A. Wang and H.-H. Ko, "Piezoelectric energy harvesting from flow-induced vibration," *Journal of Micromechanics and Microengineering,* vol. 20, no. 2, p. 025019, 2010.

[99] G. Athanassoulis and K. Mamis, "Modeling and analysis of a cliff-mounted piezoelectric sea-wave energy absorption system," *Coupled Syst Mech,* vol. 2, no. 1, pp. 53-83, 2013.

[100] G. K. Ottman, H. F. Hofmann, and G. A. Lesieutre, "Optimized piezoelectric energy harvesting circuit using step-down converter in discontinuous conduction mode," *IEEE Transactions on Power Electronics,* vol. 18, no. 2, pp. 696-703, 2003.

[101] E. Lefeuvre, A. Badel, C. Richard, and D. Guyomar, "Piezoelectric energy harvesting device optimization by synchronous electric charge extraction," *Journal of Intelligent Material Systems and Structures,* vol. 16, no. 10, pp. 865-876, 2005.

[102] Y.-C. Shu and I. Lien, "Efficiency of energy conversion for a piezoelectric power harvesting system," *Journal of micromechanics and microengineering,* vol. 16, no. 11, p. 2429, 2006.

[103] E. Lefeuvre, A. Badel, C. Richard, and D. Guyomar, "Energy harvesting using piezoelectric materials: case of random vibrations," *Journal of Electroceramics,* vol. 19, no. 4, pp. 349-355, 2007.

[104] P. H. Nakasone and E. C. Silva, "Design of piezoelectric energy harvesting devices and laminate structures by applying topology optimization," in *SPIE Smart Structures and Materials+ Nondestructive Evaluation and Health Monitoring*, 2009: International Society for Optics and Photonics, pp. 728603-728603-11.

[105] S. Niu *et al.*, "Theoretical Investigation and Structural Optimization of Single-Electrode Triboelectric Nanogenerators," *Advanced Functional Materials,* vol. 24, no. 22, pp. 3332-3340, 2014.

[106] S. Niu *et al.*, "Simulation method for optimizing the performance of an integrated triboelectric nanogenerator energy harvesting system," *Nano Energy,* vol. 8, pp. 150-156, 2014.

[107] S. Niu and Z. L. Wang, "Theoretical systems of triboelectric nanogenerators," *Nano Energy,* vol. 14, pp. 161-192, 2015.

[108] D. J. Lacks and R. M. Sankaran, "Contact electrification of insulating materials," *Journal of Physics D: Applied Physics,* vol. 44, no. 45, p. 453001, 2011.

[109] S. Wang *et al.*, "Maximum Surface Charge Density for Triboelectric Nanogenerators Achieved by Ionized-Air Injection: Methodology and Theoretical Understanding," *Advanced Materials,* vol. 26, no. 39, pp. 6720-6728, 2014.

[110] F. Saurenbach, D. Wollmann, B. Terris, and A. Diaz, "Force microscopy of ion-containing polymer surfaces: morphology and charge structure," *Langmuir,* vol. 8, no. 4, pp. 1199-1203, 1992.

[111] F. Lu, H. Lee, and S. Lim, "Modeling and analysis of micro piezoelectric power generators for micro-electromechanical-systems applications," *Smart Materials and Structures,* vol. 13, no. 1, p. 57, 2003.

[112] Z. L. Wang, L. Lin, J. Chen, S. Niu, and Y. Zi, "Applications in Self-powered Systems and Processes," in *Triboelectric Nanogenerators*: Springer, 2016, pp. 351-398.

[113] Z. L. Wang, L. Lin, J. Chen, S. Niu, and Y. Zi, "Harvesting Large-Scale Blue Energy," in *Triboelectric Nanogenerators*: Springer, 2016, pp. 283-306.

[114] W. Tang *et al.*, "Liquid-metal electrode for high-performance triboelectric nanogenerator at an instantaneous energy conversion efficiency of 70.6%," *Advanced Functional Materials,* vol. 25, no. 24, pp. 3718-3725, 2015.

[115] J. Chen *et al.*, "Automatic mode transition enabled robust triboelectric nanogenerators," *ACS nano,* vol. 9, no. 12, pp. 12334-12343, 2015.

[116] Y. Yu and X. Wang, "Chemical modification of polymer surfaces for advanced triboelectric nanogenerator development," *Extreme Mechanics Letters,* vol. 9, pp. 514-530, 2016.

[117] R. V. Dukkipati, *Vibration analysis*. Alpha Science Int'l Ltd., 2004.

[118] J. Chen *et al.*, "Harmonic-resonator-based triboelectric nanogenerator as a sustainable power source and a self-powered active vibration sensor," *Advanced materials,* vol. 25, no. 42, pp. 6094-6099, 2013.

[119] Oceanweathercom, "Current Marine Data," *Oceanweather Inc,* Accessed 30 October 2018. [Online]. Available: http://www.oceanweather.com/data/index.html.

[120] A. Khaligh and O. C. Onar, *Energy harvesting: solar, wind, and ocean energy conversion systems*. CRC press, 2009.

[121] H. Zou *et al.*, "Quantifying the triboelectric series," *Nature communications,* vol. 10, no. 1, pp. 1-9, 2019.

[122] S. Li *et al.*, "Contributions of Different Functional Groups to Contact Electrification of Polymers," *Advanced Materials,* p. 2001307, 2020.

[123] Z. L. Wang and A. C. Wang, "On the origin of contact-electrification," *Materials Today,* 2019.

[124] U. T. Jurado, S. H. Pu, and N. M. White, "A contact-separation mode triboelectric nanogenerator for ocean wave impact energy harvesting," in *2017 IEEE SENSORS*, 2017: IEEE, pp. 1-3.

[125] U. T. Jurado, S. H. Pu, and N. M. White, "Dielectric-metal triboelectric nanogenerators for ocean wave impact self-powered applications," *IEEE Sensors Journal,* vol. 19, no. 16, pp. 6778-6785, 2019.

[126] P. Ueberschlag, "PVDF piezoelectric polymer," *Sensor review,* vol. 21, no. 2, pp. 118-126, 2001.

[127] P. Bai *et al.*, "Dipole-moment-induced effect on contact electrification for triboelectric nanogenerators," *Nano Research,* vol. 7, no. 7, pp. 990-997, 2014.

[128] Q. Nguyen, B. H. Kim, and J. W. Kwon, "based ZnO nanogenerator using contact electrification and piezoelectric effects," *Journal of Microelectromechanical Systems,* vol. 24, no. 3, pp. 519-521, 2015.

[129] M. Han, X. Zhang, W. Liu, X. Sun, X. Peng, and H. Zhang, "Low-frequency wide-band hybrid energy harvester based on piezoelectric and triboelectric mechanism," *Science China Technological Sciences,* vol. 56, no. 8, pp. 1835-1841, 2013.

[130] L. Xu *et al.*, "Coupled triboelectric nanogenerator networks for efficient water wave energy harvesting," *ACS nano,* vol. 12, no. 2, pp. 1849-1858, 2018.

[131] S. Park, Y. Kim, H. Jung, J.-Y. Park, N. Lee, and Y. Seo, "Energy harvesting efficiency of piezoelectric polymer film with graphene and metal electrodes," *Scientific reports,* vol. 7, no. 1, p. 17290, 2017.

[132] E. Arano, "Ocean Water Wave Photo " *https://www.pexels.com/photo/ocean-water-wave-photo-1295138/*, 2016.

[133] D. Steingart, "Power sources for wireless sensor networks," in *Energy harvesting technologies*: Springer, 2009, pp. 267-286.

[134] Z. L. Wang and W. Wu, "Nanotechnology-enabled energy harvesting for self-powered micro-/nanosystems," *Angewandte Chemie International Edition,* vol. 51, no. 47, pp. 11700-11721, 2012.

[135] M. M. Damien Toner, "The Potential for Renewable Energy Usage in Aquaculture," *http://www.aquacultureinitiative.eu*, 2002.

[136] U. T. Jurado, S. H. Pu, and N. M. White, "Grid of hybrid nanogenerators for improving ocean wave impact energy harvesting self-powered applications," *Nano Energy,* vol. 72, p. 104701, 2020.

[137] B. Ravelo, F. Duval, S. Kane, and B. Nsom, "Demonstration of the triboelectricity effect by the flow of liquid water in the insulating pipe," *Journal of Electrostatics,* vol. 69, no. 6, pp. 473-478, 2011.

[138] T. Paillat and G. Touchard, "Electrical charges and liquids motion," *Journal of electrostatics,* vol. 67, no. 2-3, pp. 326-334, 2009.

[139] Y. Sun, X. Huang, and S. Soh, "Using the gravitational energy of water to generate power by separation of charge at interfaces," *Chemical science,* vol. 6, no. 6, pp. 3347-3353, 2015.

[140] Z. L. Wang, "Triboelectric Nanogenerator (TENG)—Sparking an Energy and Sensor Revolution," *Advanced Energy Materials,* vol. 10, no. 17, p. 2000137, 2020.

[141] S. Lin, L. Xu, A. C. Wang, and Z. L. Wang, "Quantifying electron-transfer in liquid-solid contact electrification and the formation of electric double-layer," *Nature communications,* vol. 11, no. 1, pp. 1-8, 2020.

[142] L. Zhou, D. Liu, J. Wang, and Z. L. Wang, "Triboelectric nanogenerators: Fundamental physics and potential applications," *Friction,* pp. 1-26, 2020.

[143] J. Nie *et al.*, "Probing Contact-Electrification-Induced Electron and Ion Transfers at a Liquid–Solid Interface," *Advanced Materials,* vol. 32, no. 2, p. 1905696, 2020.

[144] D. Choi, H. Lee, I. S. Kang, G. Lim, D. S. Kim, and K. H. Kang, "Spontaneous electrical charging of droplets by conventional pipetting," *Scientific reports,* vol. 3, p. 2037, 2013.

[145] J. Lyklema, *Fundamentals of interface and colloid science: soft colloids*. Elsevier, 2005.

[146] Z. H. Lin, G. Cheng, S. Lee, K. C. Pradel, and Z. L. Wang, "Harvesting Water Drop Energy by a Sequential Contact-Electrification and Electrostatic-Induction Process," *Advanced Materials,* vol. 26, no. 27, pp. 4690-4696, 2014.

[147] Y. Tada, "Experimental characteristics of electret generator, using polymer film electrets," *Japanese journal of applied physics,* vol. 31, no. 3R, p. 846, 1992.

[148] B. J. Kirby and E. F. Hasselbrink Jr, "Zeta potential of microfluidic substrates: 1. Theory, experimental techniques, and effects on separations," *Electrophoresis,* vol. 25, no. 2, pp. 187-202, 2004.

[149] L. S. McCarty and G. M. Whitesides, "Electrostatic charging due to separation of ions at interfaces: contact electrification of ionic electrets," *Angewandte Chemie International Edition,* vol. 47, no. 12, pp. 2188-2207, 2008.

[150] W. Harper, "Contact and Frictional Electrification (Morgan Hill," ed: Laplacian Press, 1998.

[151] Y. Awakuni and J. Calderwood, "Water vapour adsorption and surface conductivity in solids," *Journal of Physics D: Applied Physics,* vol. 5, no. 5, p. 1038, 1972.

[152] L. Zhao, J. Sun, X. Wang, L. Zeng, C. Wang, and Y. Tu, "System-size effect on the friction at liquid-solid interfaces," *Applied Mathematics and Mechanics,* vol. 41, no. 3, pp. 471-478, 2020.

[153] F.-C. Wang and Y.-P. Zhao, "Slip boundary conditions based on molecular kinetic theory: The critical shear stress and the energy dissipation at the liquid–solid interface," *Soft Matter,* vol. 7, no. 18, pp. 8628-8634, 2011.

[154] Y. Zhang *et al.*, "Combined effects of pinning and adhesion force on solid\liquid interfacial friction behaviors under applied voltage," *Tribology International,* vol. 134, pp. 102-108, 2019.

[155] R. Pawlowicz, "Key physical variables in the ocean: temperature, salinity, and density," *Nature Education Knowledge,* vol. 4, no. 4, p. 13, 2013.

[156] S. Wang *et al.*, "Motion charged battery as sustainable flexible-power-unit," *Acs Nano,* vol. 7, no. 12, pp. 11263-11271, 2013.

[157] S. Boisseau, G. Despesse, and B. A. Seddik, "Electrostatic conversion for vibration energy harvesting," *Small-Scale Energy Harvesting,* pp. 1-39, 2012.

[158] U. T. Jurado, S. H. Pu, and N. M. White, "Water-dielectric single electrode mode triboelectric nanogenerators for ocean wave impact energy harvesting," in *Multidisciplinary Digital Publishing Institute Proceedings*, 2018, vol. 2, no. 13, p. 714.

[159] U. T. Jurado, S. H. Pu, and N. M. White, "Wave impact energy harvesting through water-dielectric triboelectrification with single-electrode triboelectric nanogenerators for battery-less systems," *Nano Energy,* vol. 78, p. 105204, 2020.